

INTRODUCTION
TO
NEURODYNAMICAL SYSTEMS

Lecture Notes by X.-J. Wang

Department of Mathematics and the James Franck Institute
University of Chicago

(July 1993)

TABLE OF CONTENT

1. Overview of the mammalian brain
2. Neurons and neural nets
3. Cable theory
4. Cable theory II: transient solutions
5. Hodgkin-Huxley theory of action potentials
6. Bifurcations and oscillations: the FitzHugh-Nagumo system
7. Action potential propagation
8. Bursting
9. Population dynamics: the Wilson-Cowan equation
10. Synchronization of the integrate-and-fire neurons
11. Coupled oscillators: reduction to phase models
12. Coupled oscillators II: examples
13. Coupled oscillators III: synchrony, clustering, and effects of heterogeneity
14. Rhythmic oscillations in a network of inhibitory neurons
15. Large neural networks with random connectivity
16. Activity-dependent synaptic plasticity
17. Development of visual maps: Linsker's model
18. Associative memory: Hopfield's net. Willshaw's net.
19. The problem of the cortical code

Lecture 1: Overview of the mammalian brain

Fig. 1: Local regions of the mammalian brain.

The central nerve system consists of discrete, well-identified cells (neurons) (Ramon y Cajal ~1898). A neuron receives inputs by synapses located on a dendritic tree, and sends its output signal to other cells through an axon (figs. 2-3). The dendritic tree can be very elaborated (e.g. Purkinje cell of cerebellum, fig. 2).

The pyramidal cell, which constitute about 85% of all cells in the neocortex, typically have one apical dendrite and one basal dendrite. Most of the synapses are located on spines (fig. 3).

Neurons communicate with each other via chemicals called neurotransmitters. The effect of a transmitter on a postsynaptic cell is either to depolarize or hyperpolarize the membrane potential, then it is said to excite or inhibit the postsynaptic cell. A presynaptic cell either excites or inhibits all the postsynaptic cells it is connected to.

There are two aspects to the functioning of the CNS

(A) Input-output computation

e.g. sensorimotor system

- ISSUES:
- sensory code
 - feature detection
 - topographic map
 - motor generation and control
 - memory and learning

(B) intrinsic organization and dynamics

- positive feedback abound in the CNS. In the neocortex, excitatory pyramidal cells interact with each other through axonal collaterals (Lorente de Nò, 1930s). More than 4/5 of all synapses in rat neocortex have cortical neuron as presynaptic element.
- a multitude of nonlinear ion channels exist in individual cells (Hodgkin-Huxley, 1940-50s; Wins 1980s).
- nonlinear phenomena like instabilities, oscillation and synchronization, population rhythmic activities. This latter may be involved in information processing, but is also important in characterizing different awake and sleep states as well as diseases (e.g. epilepsy) (fig. 4).

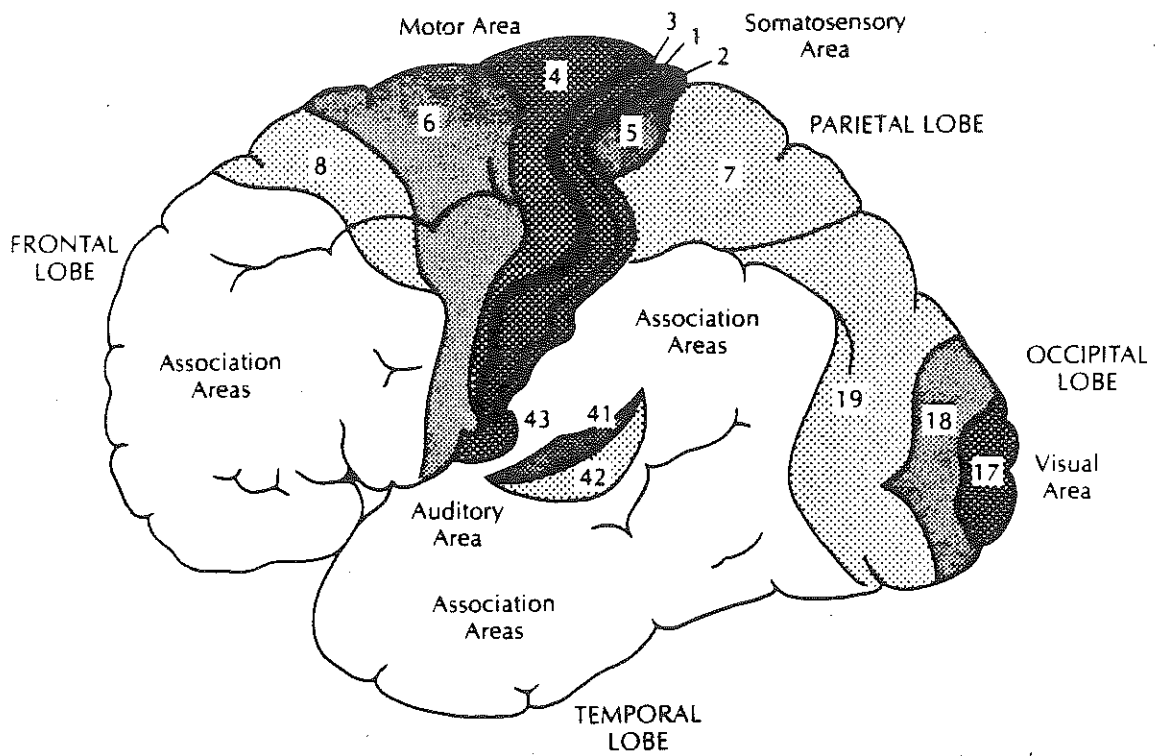


FIG. 15.1. Neocortex of the human brain and its main anatomical and functional areas. (Adapted from Brodmann, in Fulton, 1938.)

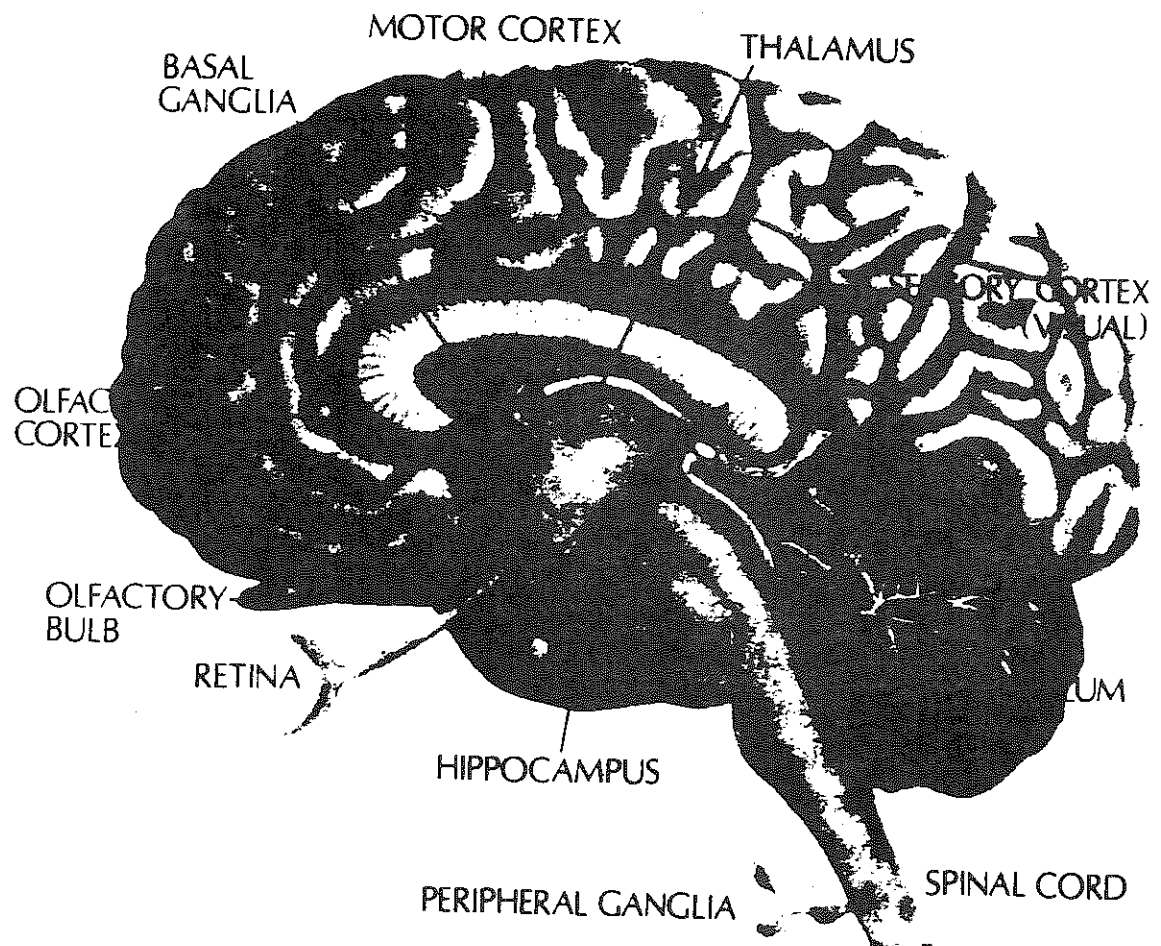


fig.1.1

FIG. 1.2. Local regions for which synaptic organization will be described in this book.

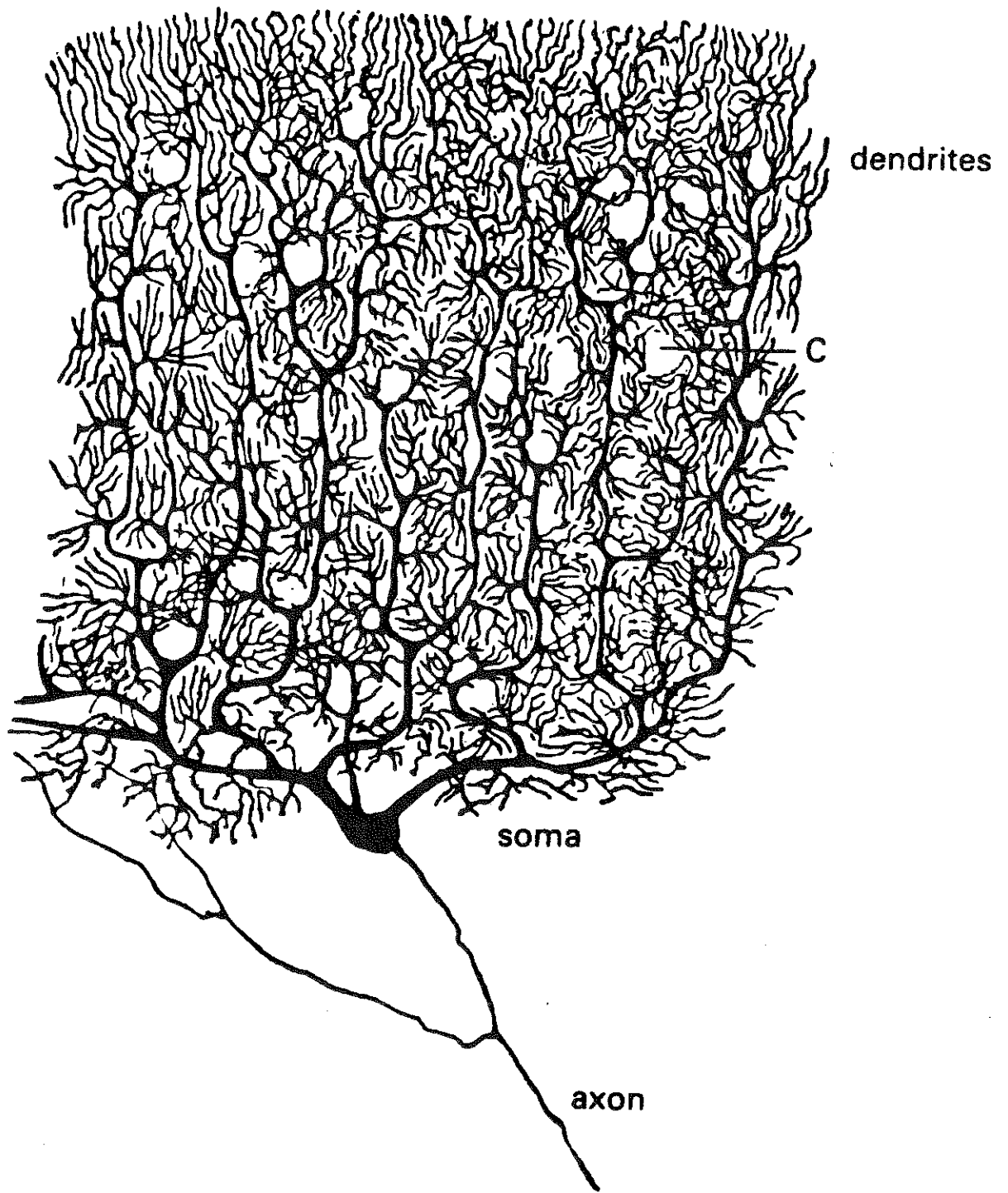


Fig. 1.2

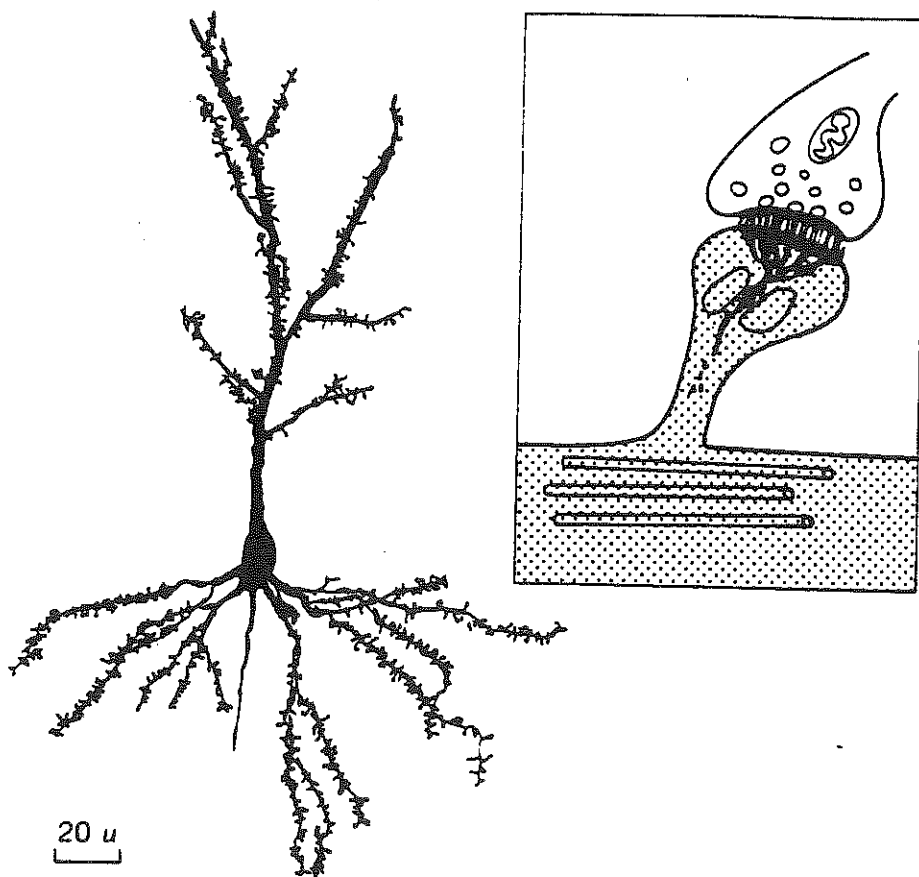


Figure 5.7 Dendritic spines may be strategic loci for morphological changes that subserve long-term memory. (Left) Drawing of a pyramidal neuron from the rat cortex, with a typically large number of dendritic spines. (Right) Schematic representation of a dendritic spine (shaded) with the characteristic filaments and sacs constituting the spine apparatus, and the postsynaptic density. The elongated tubes in the dendritic shaft are microtubules that participate in the formation of spines. Spines usually bear one excitatory synapse. (From Dudai 1989.)

fig. 1-3

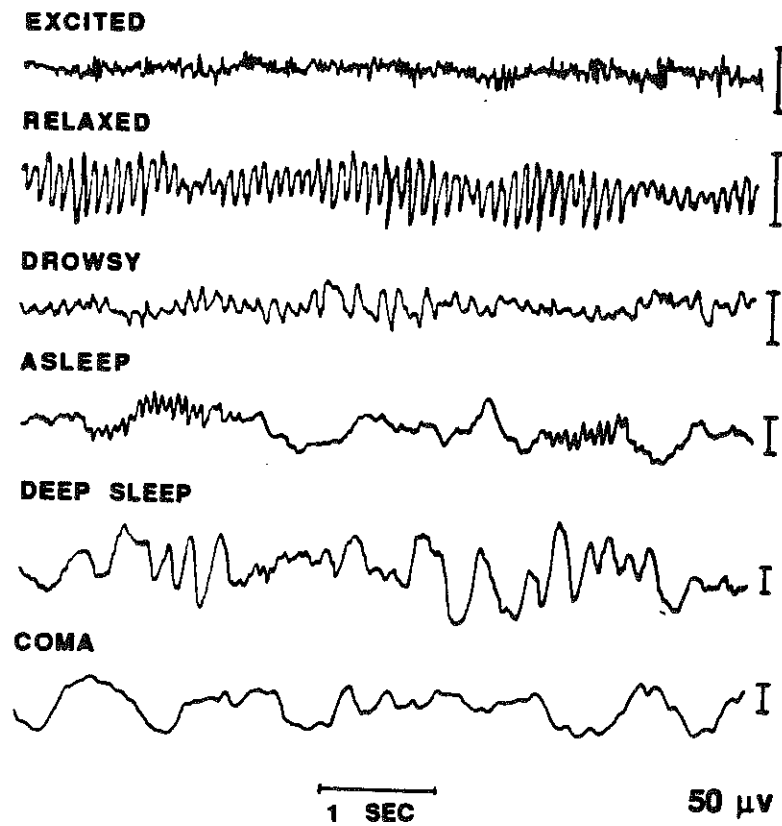


Figure A.6 Characteristic electroencephalogram (EEG) traces during variations in states of consciousness. (From Penfield and Jasper 1954.)

fig. 1-4

Lecture 2: neurons and neural nets

(2.1)

Single neuron.

The main state variable to describe a neuron is its transmembrane potential. Its output is in the form of a stereotyped electrical signal called "action potential". There are different levels of modeling for a single neuron.

(1) McCulloch-Pitts, because the action potential is an all-or-none event, a neuron may be assigned a binary state variable $x = 0$ or 1 . For a population of such units, a simple description would be to write

$$x_i(t^+) = H\left(\sum_j w_{ij} x_j(t) - \theta_j\right) \quad \text{where } H(x) = \begin{cases} 1 & \text{if } x > 1 \\ 0 & \text{otherwise} \end{cases}$$

so, a cell i sums over the inputs $\{x_j(t)\}$ with the synaptic weight w_{ij} and fires if $\sum_j w_{ij} x_j(t)$ reaches a threshold θ_j . One time unit $\approx 1 \text{ ms}$. The connectivity w_{ij} remain unspecified for the moment.

(2) integrate-and-fire

Continuous x and time t

$$\frac{dx}{dt} = -\lambda x + I(t) \quad \text{if } x(t) = 0 \text{ then } x(t^+) = 0$$

e.g. $I(t) = I_0 > \lambda \Theta$

$$\rightarrow x(t) = \frac{I_0}{\lambda} - (\frac{I_0}{\lambda} - x_0) e^{-\lambda t}$$

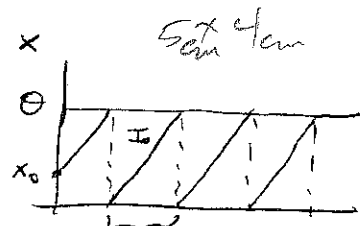
for a network,

$$\frac{dx_i}{dt}$$

$$= -\lambda x_i + I_i(t) + \sum_j w_{ij} H(x_j - \theta) ; \quad x_i(t^+) = 0 \text{ if } x_i(t) = \theta$$

(3) stochastic model.

(4) biophysical model, but the geometry of the cell is ignored.



$$T = \frac{1}{\lambda} \ln \left[1 - \frac{\theta \lambda}{I_0} \right]^{-1}$$

If a cell is electronically compact, one can assume that it is isopotential, thus can be described by a single $V(t)$ independent of its spatial location. We shall call it a space-clamped cell or a point cell.

A cell usually possesses a number of ionic channels, hence a point cell is described by a set of nonlinear ordinary differential equations (ODEs). A network is described by a large, discrete population of coupled ODEs.

(5) When the dendritic tree geometry is taken into account, a single cell must now be described by partial differential equations (PDEs). PDE description is also required for propagation of action potentials along the axonal cable and branching tree.

For biophysical modeling, (4) is often sufficiently appropriate as far as network behaviors are concerned; (5) is necessary when single cell dynamics is of main concern, or when local dendritic processes are investigated (e.g. cellular basis of learning & memory).

Connectivity within a network

Knowledge is at this moment quite insufficient. So in theoretical works one often assumes very simple form of connectivity between cells in a network. One general point is that the connectivity is not very local, certainly not such notion as "nearest-neighbour". "Coupling" is appropriate. One particular form of coupling, the global connectivity (every cell is coupled to every other cell), is of theoretical interest because it is adequate for mathematical analysis. A second point is that the connectivity is not rigid, indeed the plasticity of the nerve system underlying learning and memory is thought to be expressed as the modifiability of the connectivity strength w_{ij} . So there is a high degree of randomness in the connectivity.

Let us review briefly some main characteristics.

- (1) in the mouse neocortex, for instance, for 1 mm^3 there are
- | | | |
|--------------------------------------------------|------|---------------------------------------------------|
| 9×10^4 neurons | $\}$ | $\rightarrow \sim 7800 \text{ synapses / neuron}$ |
| 7×10^8 synapses | | |
| 4 km axon ($d \sim 0.3 \mu\text{m}$) | $\}$ | $\sim 1 \text{ synapse / } 5.7 \mu\text{m axon}$ |

If connection between cells is very specific, axonal buttons must be highly clustered and there should be long stretches of free axon. It is not what has been observed (fig. 1)

Pyramidal cells	$\sim 85\%$	$\sim 70\%$
stellate cells	$\sim 15\%$	$\sim 30\%$

Synapses type I ~ 90% (85% on spines)
type II ~ 10%

random consideration.

$$85\% \times 85\% = 72\% \quad \text{type I on spine}$$

$$85\% \times 15\% = 13\% \quad \text{type II on dendritic shaft}$$

$$15\% \times 85\% = 13\% \text{ type II on cell body}$$

$15^{\circ} \text{O} \times 15^{\circ} \text{O}$ = 2 $^{\circ} \text{O}$ type II on dendritic shaft

(2) axonal fibers can seem very random in some brain regions (e.g. neocortex), or quite ordered (e.g. parallel fibers in cerebellum) (figs. 2-3).

In the neocortex, if complete randomness is assumed, then every pair of cells talk to each other at most birecursively. (if $\exists 5000$ synapses / cell. $5000 \times 5000 = 2.5 \times 10^7 \geq$ total # of cells)

However, one should bear in mind the columnar organization found in the somatosensory, visual and motor cortex (fig. 4). Laminar structure of the cortex also dictate a form of ordered organization (fig. 5).

(3) Even if the connectivity is widespread, it may be sparse. In a network of N neurons, a given neuron may be linked to all N neurons, or to a fraction of the population (# of synapses M proportional to N), or to a fixed number of neurons (M independent of N). How would M scale with N ?

Let us present an argument, due to C. Stevens which suggests that neither of the above three possibilities seems to be the case.

Consider a reference brain (e.g. mouse) with size n , and $M(n)$ synapses per cell. For a new brain of size N , let $s = N/n$.

Assume

$$M(N) = M(sn) = f(s) M(n) \quad \text{where } f(s) \text{ is a scaling function} \\ \rightarrow \text{homogeneous}$$

$$\rightarrow f(s) \sim s^\alpha. \quad \text{how to estimate } \alpha?$$

Observation: • density of synapses r is constant across cortical layers, regions and species $r = 0.6 \times 10^9$ synapses / mm^3 .

P is also constant across cortical regions (except visual cortex) and species, $P = 1.48 \times 10^5$ neurons / mm^2

(for primate A17, $P = 3.57 \times 10^5$ neurons / mm^2)

Let Q : total number of synapses

V : total volume

A : total surface area } of cortex

T : average cortical thickness

$$\rightarrow Q = rV \quad V = AT \quad N = pA \quad \rightarrow M(N) = Q/N = rT/p$$

from the scaling law, on the other hand

$$M(N) = M(n) (N/n)^\alpha = (r/p) (A/a)^\alpha$$

$$\rightarrow T/t = (A/a)^\alpha$$

$$\text{or } \log(T) = \alpha \log(A) + \{\log(t) - \alpha \log(a)\}$$

data \rightarrow $\alpha \approx 0.07$ very small.
(fig. 6)

$$\rightarrow M(N) \sim N^{0.07}$$
 connectivity is sparse

therefore, # of synapses / cell is almost independent of N , though this unusual scaling may have a significance we do not yet understand.

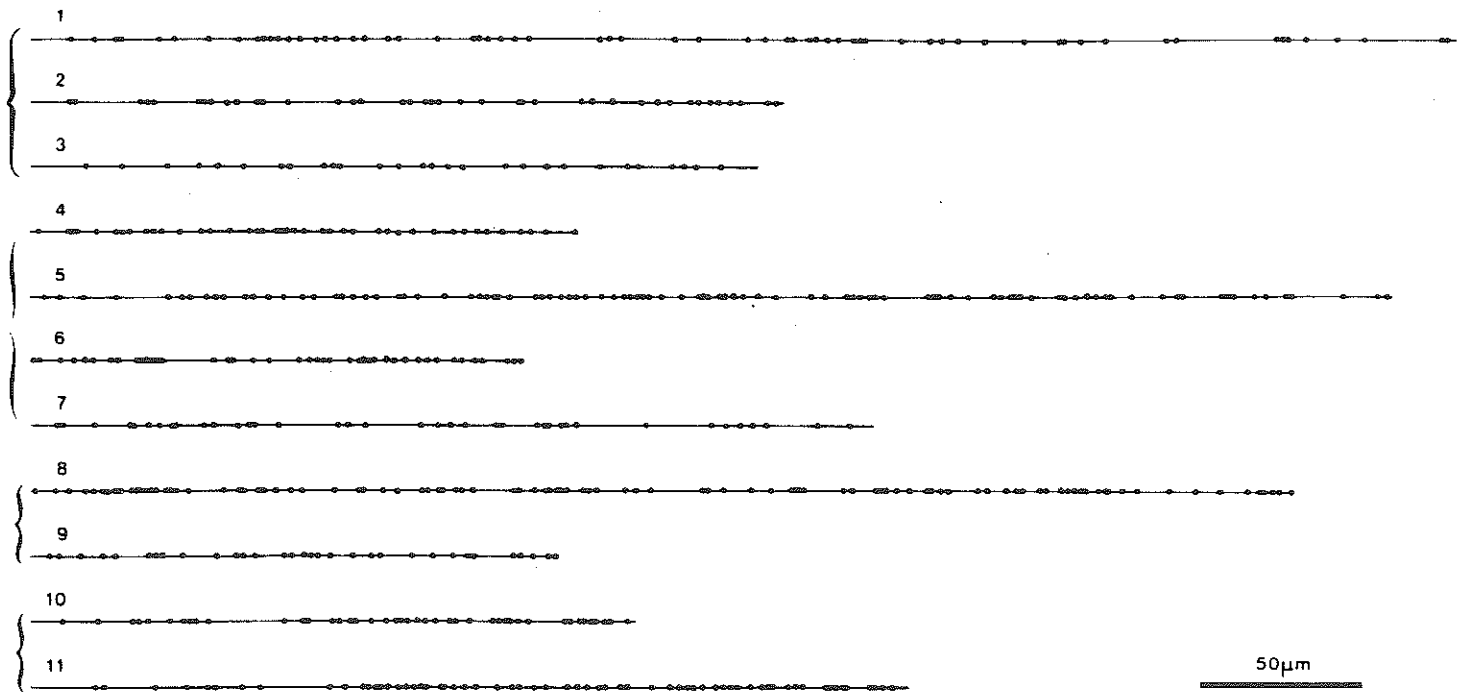


Fig. 23. Primary axon collaterals of pyramidal cells (numbered 1 to 11), straightened to show the distribution of boutons (dots). Brackets indicate collaterals which belong to one and the same cell. (Hellwig 1990)

fig. 2.1

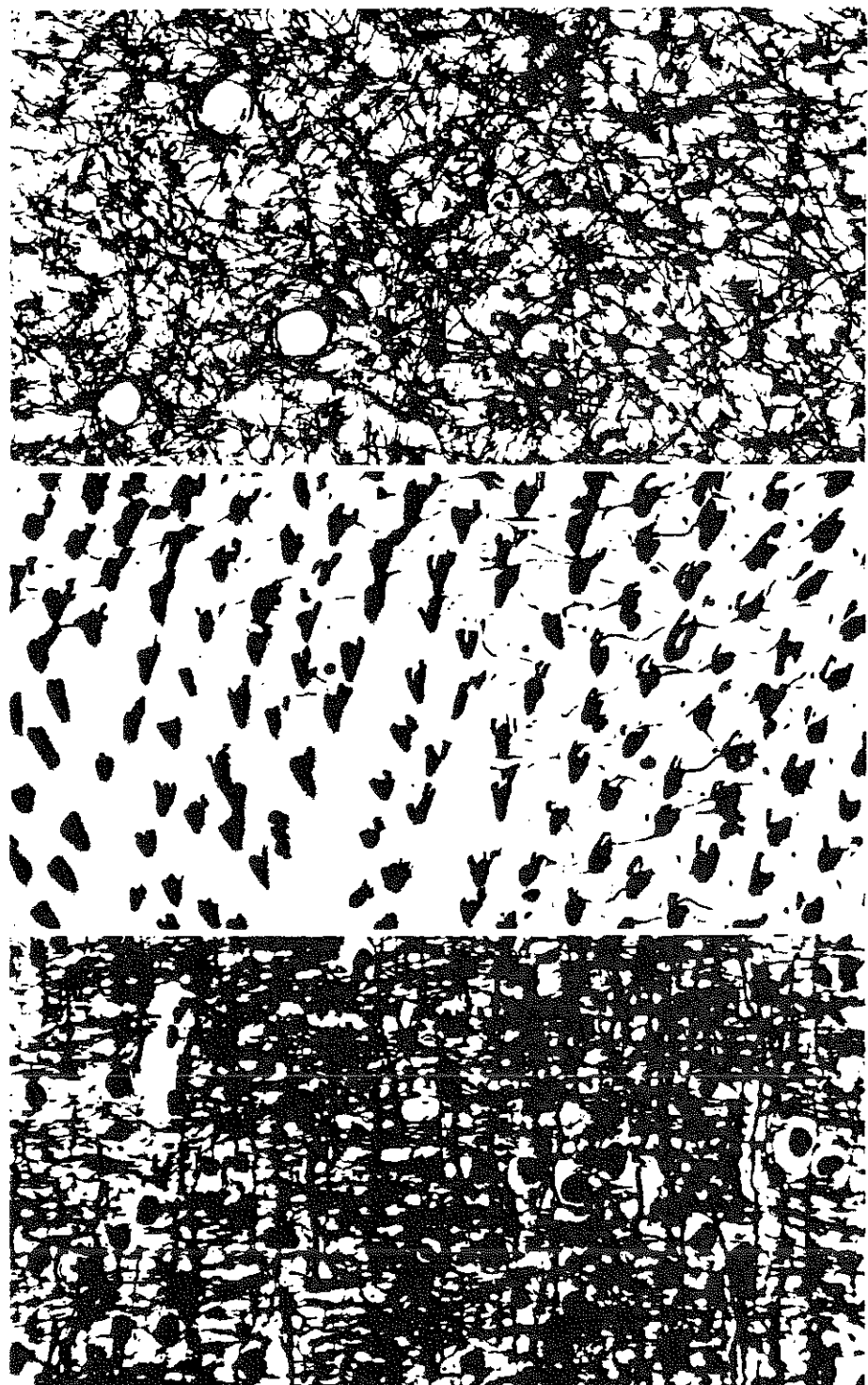


fig. 2, 2



Fig. 20. Reduced silver stain after Bielschowsky, modified by V. Staiger. Layer V of the mouse cortex. The staining of axons is fairly complete, while the staining of dendrites and neural cell bodies is suppressed, except for some lumps inside the nuclei. The density of axons on such preparations is higher than 1 km/mm^3 . Note that the enlargement is the same as in Fig. 17. (Braitenberg 1981)

fig. 2, 3

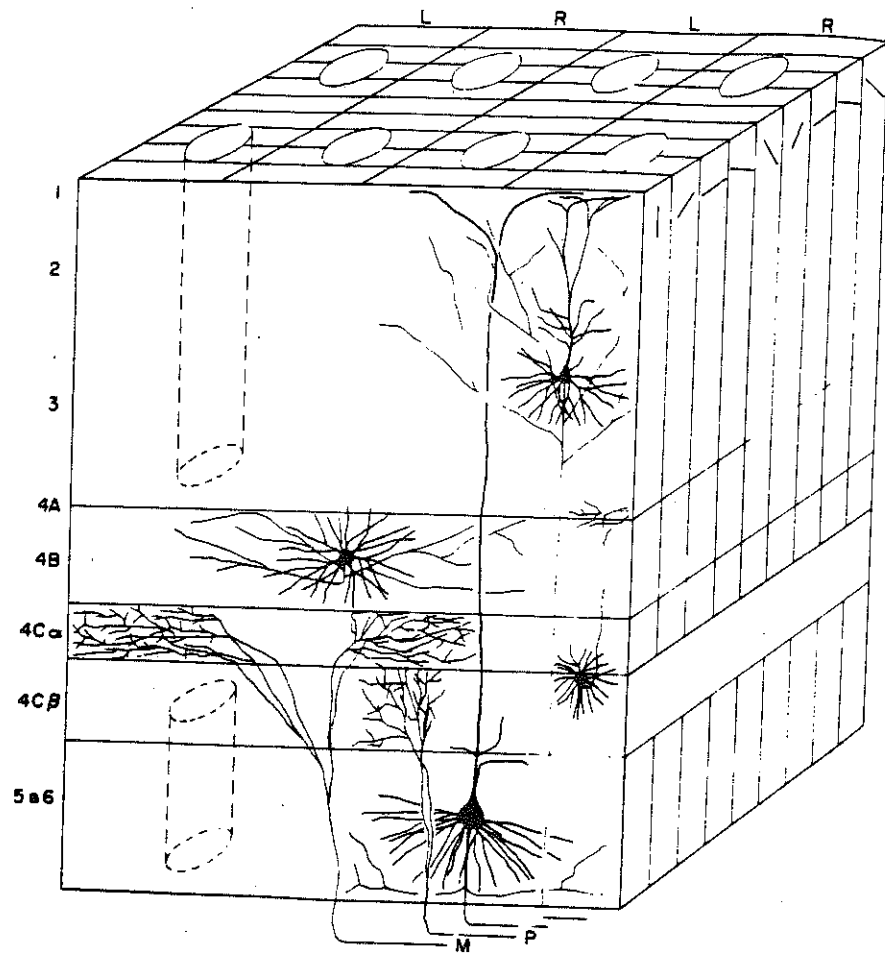
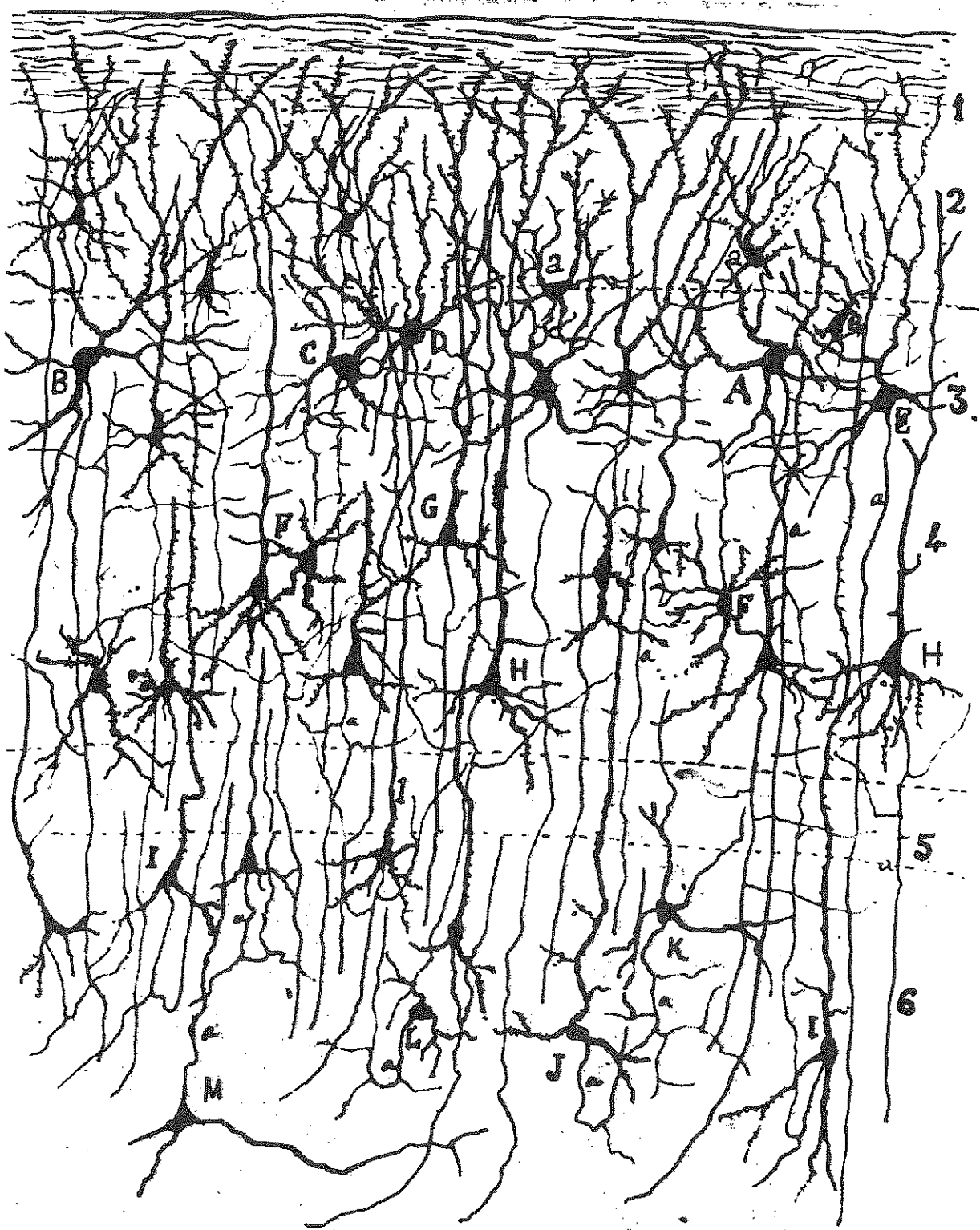


FIG. 12.6. "Ice-cube" model of visual cortex in the macaque monkey. L and R indicate ocular dominance "columns" or "slabs." The narrower orientation columns run orthogonally. The cytochrome oxidase rich "blobs" appear as cylinders in the center of ocular dominance columns. M, P: Thalamic afferents originating from the magno- and parvocellular layers of the lateral geniculate nucleus, respectively, and terminating in separate subdivisions of layer 4, within appropriate ocular dominance slabs.

fig. 2.4

2.6



GOLGI-STAINED NERVE TISSUE from the visual cortex of a rat was sketched by Cajal in 1888. The numbers along the right-hand margin identify cellular layers; the capital letters label individual neurons. One of Cajal's most important contributions to neurobiology was to establish the neuron as a discrete, well-defined cell rather than as part of a continuous network.

fig. 2.5

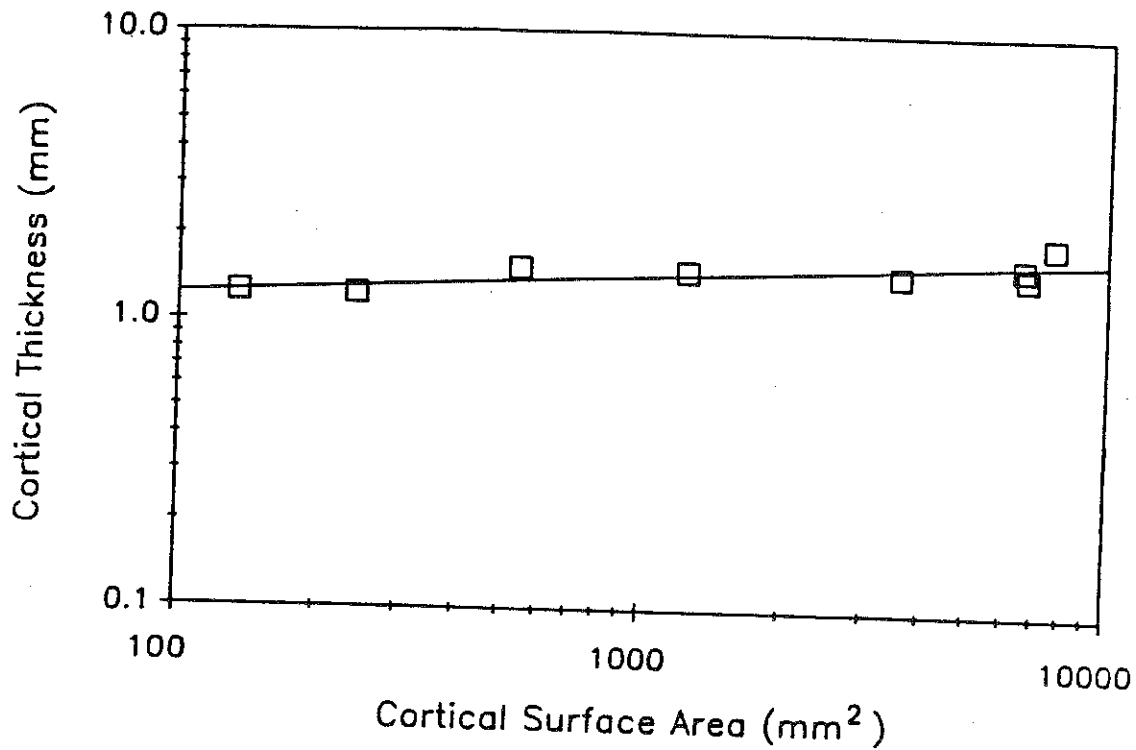


Figure 1: A double logarithmic plot of cortical thickness (in mm) as a function of cortical surface area (in mm^2) for area 17. Data derived from cortical volumes given by Frahm *et al.* (1984) and cortical thickness given by Rockel *et al.* (1980). Animals represented, in order of increasing cortical size, are tree shrew (Scandentia), galago (Prosimian), marmoset, squirrel monkey, macaque, baboon, chimpanzee, and man (Simians). The regression line is

$$\log(T) = 0.07 \log(A) - 0.047$$

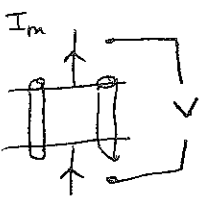
where T is cortical thickness (mm) and A the surface area (mm^2).

Fig. 2.6

Lecture 3: cable theory

neuron membrane: lipid bilayer

$$C_m = 1 \mu F/cm^2$$



with a number of ion channels, pumps etc

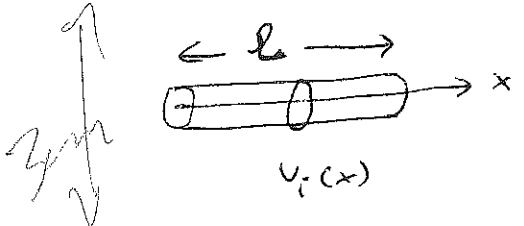
$V = E_i - E_o$, E_o is often assumed indep. of space and time. For a point cell,

$$I_m = C_m \frac{dV}{dt} + I_{ion} \quad \text{e.g. } I_{ion} = \frac{V - V_r}{R_m} = G_m(V - V_r)$$

for membrane parameters, we use superficial density: $[G_m] = S/cm^2$

$$\rightarrow [R_m] = \Omega \text{ cm}^2$$

Now, for a cable, e.g. a passive dendritic branch (fig. 1)



for cytoplasmatic parameters, we use

$$\underline{\text{axial density}} \quad [G_i] = S/cm$$

$$\rightarrow [R_i] = \Omega \text{ cm}$$

for a cable of diameter d , let

$$C_m = C_m(\pi d) \quad g_m = G_m(\pi d) \quad [g_m] = S/cm$$

$$r_m = \frac{1}{g_m} \quad r_i = \frac{1}{g_i}$$

$$g_i = G_i \pi \left(\frac{d}{2}\right)^2 \quad [g_i] = S/cm$$

Let $V = E_i - E_o$, we have

$$\frac{\partial V}{\partial x} = \frac{\partial E_i}{\partial x} = - I_i r_i, \quad \frac{\partial^2 V}{\partial x^2} = - r_i \frac{\partial I_i}{\partial x} = r_i i_m \quad (i_m = I_m(\pi d))$$

$$\rightarrow g_i \frac{\partial^2 V}{\partial x^2} = C_m \frac{\partial V}{\partial t} + \sum_k g_k (V - V_{rk}) \quad [g_k] = S/cm$$

We should be concerned with the passive properties, with only one passive current. and we can assume $V_p = 0$ ($V \rightarrow V - V_r$).

$$\rightarrow \frac{r_m}{r_i} \frac{\partial^2 V}{\partial x^2} = r_m C_m \frac{\partial V}{\partial t} + V$$

$$\rightarrow \text{characteristic time } T_m = r_m C_m = R_m C_m$$

$$\text{length } \lambda = \sqrt{\frac{r_m}{r_i}} = \sqrt{\frac{R_m}{R_i} \left(\frac{d}{4}\right)} \propto d^{1/2}$$

$$\text{In dimensionless variables } X = x/\lambda \quad T = t/T_m$$

$$\frac{\partial^2 V}{\partial X^2} = \frac{\partial V}{\partial T} + V \quad \text{cable equation (Kelvin)}$$

$$\text{steady state solution } V(X) = A_1 e^X + A_2 e^{-X}$$

$$\begin{array}{ll} \text{suppose the current flows} & \text{or } B_1 \cosh X + B_2 \sinh X \\ \text{only to the right at } X=0. & \\ \text{dfn: } G_{in} = \frac{-1}{\sqrt{r_i r_m}} \frac{1}{V} \frac{dV}{dX} \Big|_0 & \text{or } C_1 \cosh(L-X) + C_2 \sinh(L-X) \end{array}$$

$$\text{electrotropic length } L = \ell/\lambda$$

$$\text{examples: (1) } L = \infty \quad V = V_0 \text{ at } X = 0 \rightarrow V(X) = V_0 e^{-X}$$

(fig. 2)

$$G_{in} = \frac{1}{\sqrt{r_i r_m}} \equiv G_{\infty} \quad R_{\infty} = 1/G_{\infty}$$

$$G_{\infty} \propto d^{1/2}$$

input conductance at $X = 0$.

$$(2) \quad \text{voltage clamp } V = 0 \text{ at } X = L$$

$$V = V_0 \quad X = 0 \quad (A, B, D)$$

$$V(X) = \frac{V_0 \sinh(L-X)}{\sinh L}$$

$$G_{in} = G_{\infty} \coth L$$

$$B_0 = \frac{G_{in}}{G_{\infty}} = \coth L > 1$$

$$\text{or } V = V_L \text{ at } X = L \quad (I, K)$$

(3) sealed end $\frac{\partial V}{\partial x} = 0 \text{ at } x=L$
 $V = V_0 \text{ at } x=0$

$$V(x) = \frac{V_0 \cosh(L-x)}{\cosh L} \quad (F, H, J)$$

$$G_{in} = G_{ab} \tanh L \quad B_0 = \frac{G_{in}}{G_{ab}} = \tanh L < 1$$

(4) leaky condition $\left. \frac{\partial V}{\partial x} \right|_L = V_L \frac{G_L}{G_{ab}} \text{ at } x=L$

G_L : prescribed (C, G)

$$\frac{V(x)}{V_L} = \cosh(L-x) + \frac{G_L}{G_{ab}} \sinh(L-x) \quad V_L = \frac{V_0}{\cosh L + \frac{G_L}{G_{ab}} \sinh L}$$

$$\frac{G_{in}}{G_{ab}} = \frac{\tanh L + \frac{G_L}{G_{ab}}}{1 + \frac{G_L}{G_{ab}} \tanh L}$$

this is an important formula

$$\frac{df_n}{dx} = B_{out} = \frac{G_{out}}{G_{ab}}, \quad G_{out} = -\frac{1}{R_{in}m} \sqrt{\frac{dV}{dx}}$$

We shall mean $B=B_{out}$ except at $x=0$ where $B=B_{in}$.

dendritic tree: each branch is viewed as a cylinder with its only L, λ on G_{ab} . If R_m and R_i are constant, $\lambda \sim d^{1/2}$, $G_{ab} \sim d^{3/2}$.

Matching at branching point:

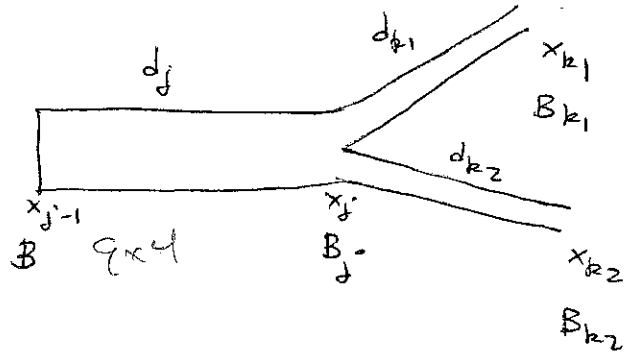
- V and $I_i = -\frac{1}{R_i} \frac{\partial V}{\partial x}$ continuous at branching points
- boundary condition at distal ends
- applied voltage or current at the electrode location.

example:

$$G_{injk_1} = G_{ak_1} \frac{\tanh L_{k_1} + B_{k_1}}{1 + B_{k_1} \tanh L_{k_1}}$$

$$L_{k_1} = \frac{x_{k_1} - x_j}{x_{k_1}} \quad B_{k_1} = \frac{G_{out k_1}}{G_{ak_1}}$$

ident for G_{injk_2}



(start with the terminal branches,
and work back ward)

Continuity $\rightarrow G_{out j} = G_{injk_1} + G_{injk_2} \quad B_j = \frac{G_{out j}}{G_{ak_1}}$

and $G_{inj-1} = G_{aj} \frac{\tanh L_j + B_j}{1 + B_j \tanh L_j}$

equivalent cylinder (Rall's 3/2 - law)

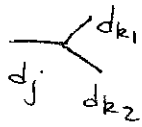
assumptions (for stationary state):

(1) R_m & R_i , same for all branches

(2) all terminal branches have the same boundary condition
(e.g. sealed)

(3) all terminal branches have the same electrotonic distance

(4)



$$d_j^{3/2} = d_{k_1}^{3/2} + d_{k_2}^{3/2}$$

example: thalamocortical relay cells of cat (fig. 3)

(5) proportional inputs have to be delivered so that an equal input voltage time course would be generated at all electrotonically equivalent dendritic locations.

→ a complicated-looking tree can be reduced to an equivalent cylinder. (3.3)
 (see fig. 4). For the ~~example~~ ^(simpler) above, if (1)-(5) are satisfied, let

us assume the sealed end at x_{k_1} & x_{k_2} . $\Rightarrow B_{k_1} = B_{k_2} = 0$

$$\rightarrow G_{\text{out},j} = G_{k_1} \tanh L_{k_1} + G_{k_2} \tanh L_{k_2}$$

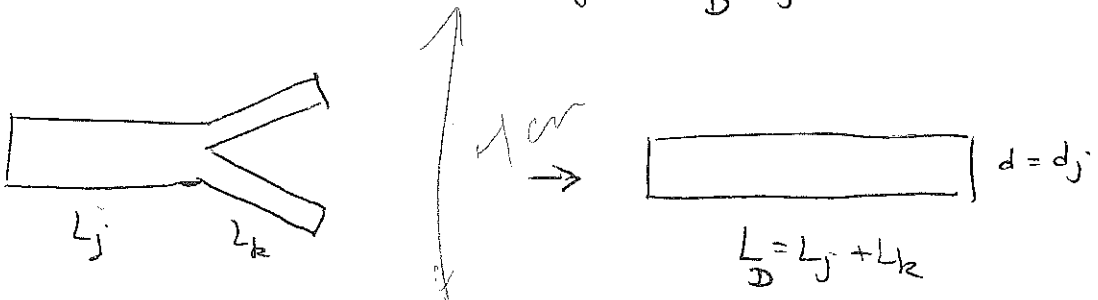
$$(3) \rightarrow L_{k_1} = L_{k_2} = L_k$$

$$(4) \rightarrow \frac{G_{k_1} + G_{k_2}}{G_{\text{out},j}} = \frac{d_{k_1}^{3/2} + d_{k_2}^{3/2}}{d_j^{3/2}} = 1$$

$$\rightarrow B_j = \frac{G_{\text{out},j}}{G_{k,j}} = \tanh L_k$$

$$\rightarrow B_o = \frac{\cancel{G_{\text{out},j-1}}}{G_{k,j}} = \frac{\tanh L_j + \tanh L_k}{1 + \tanh L_j \tanh L_k} = \tanh (L_j + L_k)$$

This input conductance ratio is thus the same as if we had an equivalent cylinder of electrotonic length $L_D = L_j + L_k$.



Note: if Rall's constraints are satisfied, the membrane area of the equivalent cylinder is the same as that of the original tree. (check)

$$\text{let } A_D = \pi l d = \pi \lambda L_D d$$

$$G_{\infty} = \lambda g_m = \lambda G_m (\pi d)$$

$$\rightarrow G_D = G_{\infty} \tanh L_D = G_m A_D \frac{\tanh L_D}{L_D} \sim \begin{cases} G_m A_D & \text{if } L_D \ll 1 \\ G_{\infty} & \text{if } L_D \gg 1 \end{cases}$$

total input conductance of the tree.

With a soma and an electrode, the input conductance of a nerve cell is

$$G_N = \sum_k G_{Dk} + G_S + G_{\text{shunt}}$$

several equivalent cylinders.

How to evaluate the various parameters from measurements? We shall need to consider transient solutions for this purpose. Let us only mention what we need here, and postpone a detailed discussion on transient solutions for arbitrary dendritic geometry, to the next lecture.

with the boundary condition $\frac{\partial V}{\partial x} = 0$ at 0 and L for a cylinder

$$V(x, T) = \sum_{n=0}^{\infty} B_n \cos \frac{n\pi x}{L} e^{-T/\tau_n}$$

$$\text{where } \tau_n = \frac{T_0}{1 + \left(\frac{n\pi}{L}\right)^2} \quad T_0 = \tau_m = R_m C_m$$

so for an equivalent cylinder, if one can measure $V(x, T)$ to deduce not only T_0 but also τ_1 , then

$$L_D = \frac{\pi}{\sqrt{\frac{T_0}{\tau_1} - 1}}$$

$$T_0 \rightarrow R_m = 1/G_m$$

if G_D can be measured directly $\rightarrow A_D$

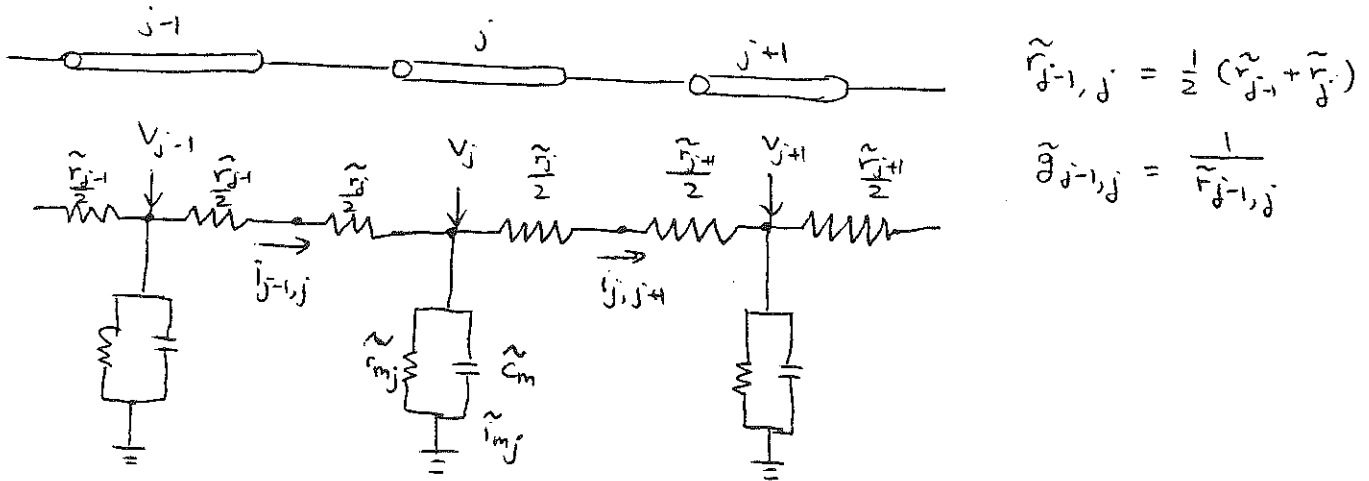
if R_i is measured separately, from A_D the diameter d may be deduced. But d can also be measured by anatomical methods.

Compartmental modeling. In practice, a dendritic tree is divided into a discrete number of "compartments", each is assumed isopotential.

$$\{d_j, l_j\}$$

Knowing $R_i, R_m, \{d_j, l_j\} \rightarrow \{\tilde{r}_j^-, \tilde{r}_{mj}^-\}$

$$\tilde{r}_j^- = R_i/l_j \quad \tilde{r}_{mj}^- = R_m/(\pi d_j l_j) \quad \tilde{C}_{mj} = C_m(\pi d_j l_j)$$



$$i_{mj} = i_{j-1,j} - i_{j,j+1} = \tilde{C}_{mj} \frac{dv_j}{dt} + \tilde{i}_{mj} \quad \tilde{g}_{mj} = g_{mj}(\pi d_j l_j)$$

$$\tilde{g}_{j-1} (v_{j-1} - v_j) \quad \tilde{g}_{j,j+1} (v_j - v_{j+1})$$

boundary condition: if sealed end $\rightarrow i_j^- = 0$

see fig. 5 for an example.

References: - JTB Jack, D Noble & RW Tsien, Oxford (1983)

« Electric current flow in excitable cells »

- W Rall in « Methods in neuronal modeling »

ed C Koch & I Segev MIT (1989)

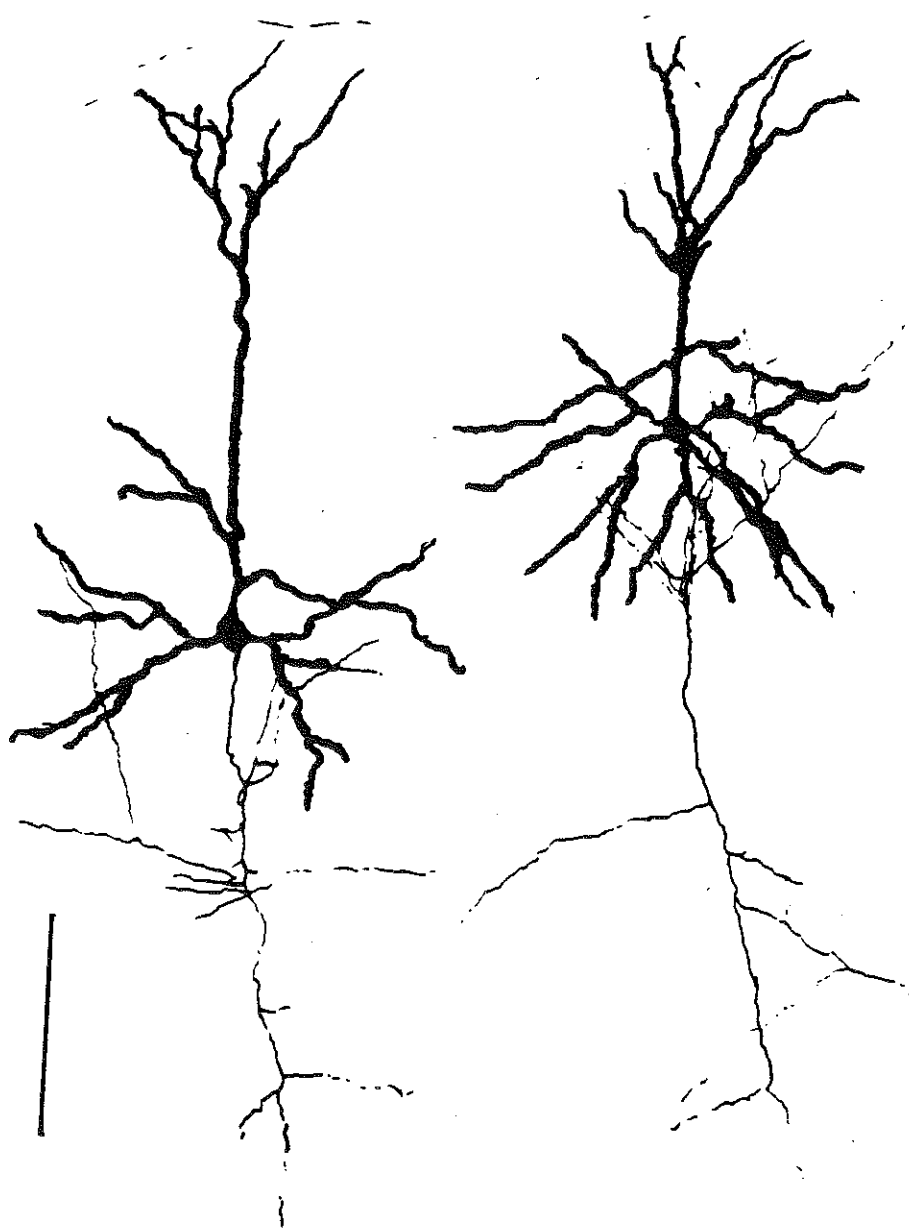


fig. 3.1

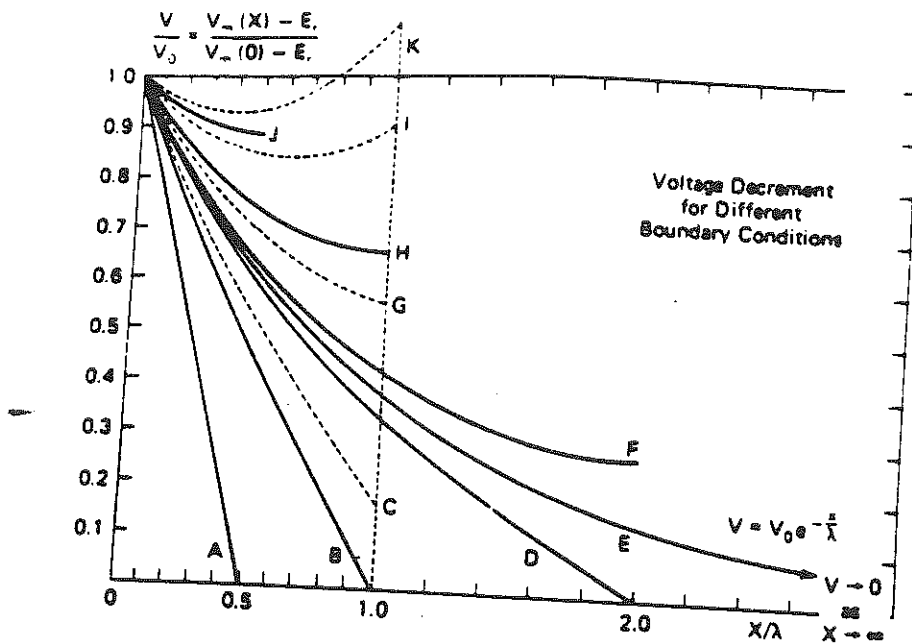


Figure 2.2

Examples of how steady voltage decrement with distance depends on the distal boundary condition. The applied voltage at $X = 0$ is normalized to 1.0 for all curves. Curve E shows an exponential decrement (eq. 2.19) for a semi-infinite length. Curves A, B, and D show steeper decrement (eq. 2.21) obtained when the most distal membrane is clamped to the resting potential, implying that $V = 0$ at $X = L$ for three different L values, 0.5, 1.0, and 2.0, respectively. Curves F, H, and J show less decrement (eq. 2.20) obtained for a sealed-end boundary condition, $dV/dX = 0$ at $X = L$, condition at $X = 1$; see eq. 2.25 and associated text. Curves I and K both have a voltage-clamped boundary condition at $X = 1$; see eq. 2.22 and associated text. (From Rall 1961.)

fig. 3.2

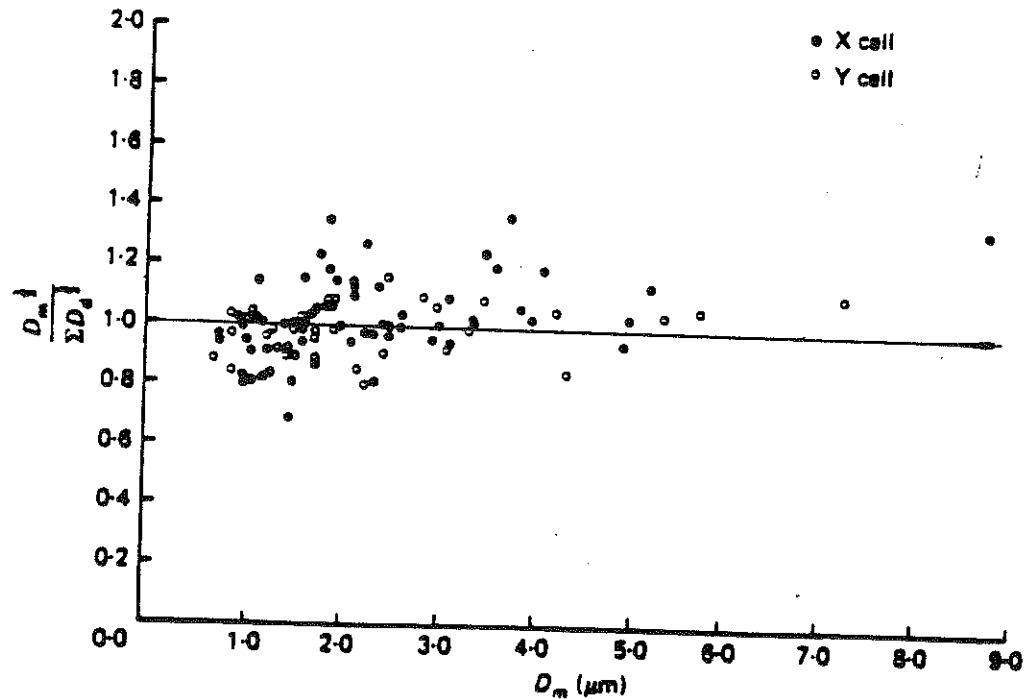


Fig. 1. Analysis of the $\frac{1}{2}$ power rule at ninety-seven dendritic branch points of ten different HRP-labelled geniculate neurones. The ordinate expresses the $\frac{1}{2}$ power relationship, and the abscissa reflects the diameter of the mother dendrite (D_m). Measurements of diameters of proximal dendrites were mostly made with the light microscope, whereas analysis of distal branch points were made from material reconstructed with the electron microscope (see text). Dendritic branch points of both X and Y cells satisfy the $\frac{1}{2}$ power rule remarkably well, exhibiting an average value of 0.99 ± 0.13 for this relationship.

fig. 3. 3.

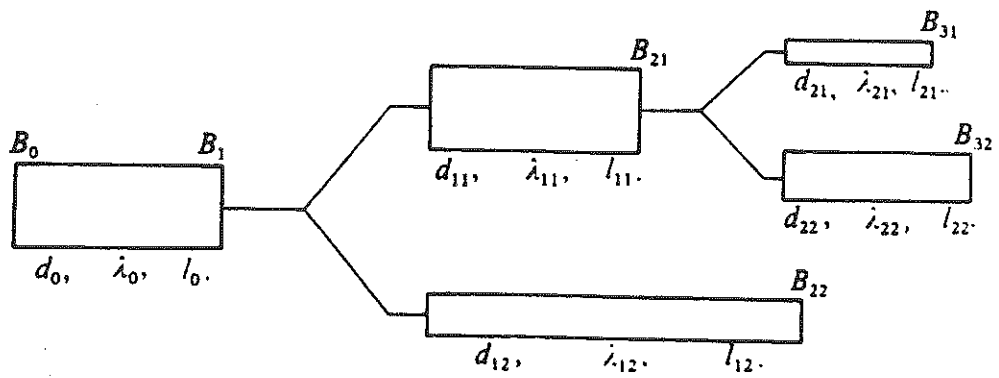


FIG. 7.6. The example treated in the text illustrating the significance of the symbols.

fig. 3.4

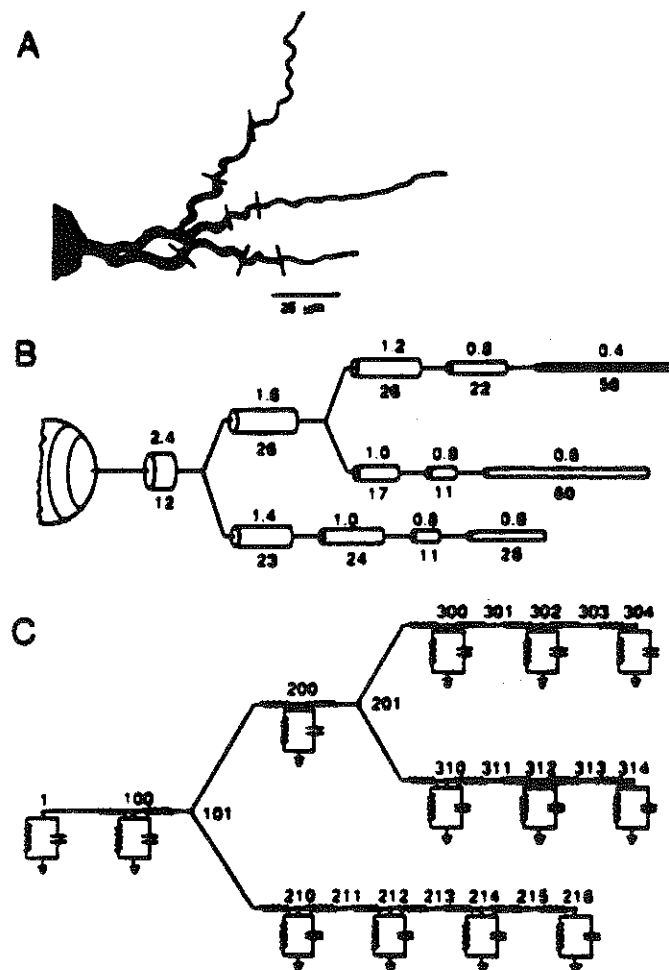


Figure 3.3

Stages in abstraction from an anatomical dendritic tree to an electrical circuit analog. (A) Two-dimensional projection of part of the soma and one dendrite of a vagus motoneuron in the guinea pig. Points at which unbranched dendrites were broken into successive cylindrical segments are indicated by lines. (B) Representation of the same dendrite as a branched system of cylindrical segments, indicating the length (below) and diameter (above) of each dendritic segment (in μm). Diameters are not drawn to the same scale as the lengths, but both are in the correct proportion. The motoneuron soma (shown partially) had a maximum diameter of $20 \mu\text{m}$ and minimum diameter of $15 \mu\text{m}$. (C) Circuit analog of B (see fig. 3.1) showing the positions of connections at branch points and the numbers assigned to circuit nodes within (even numbers) and between (odd numbers) successive segments.

fig. 3.5

Lecture 4: Cable theory II: transient solutions

(4.1)

The time-dependent solutions of the cable equation

$$\frac{\partial V}{\partial t} = \frac{\partial^2 V}{\partial x^2} - V + I(x, t) \quad \text{have been studied extensively.}$$

See J. Rinzel & W. Rall Biophys J 13, 648 (1974), 14, 759 (1974)

We shall summarize here a systematical procedure for obtaining transient solutions for a dendritic tree of arbitrary geometry and for an arbitrary input current $I(x, t)$. This formulation, due to

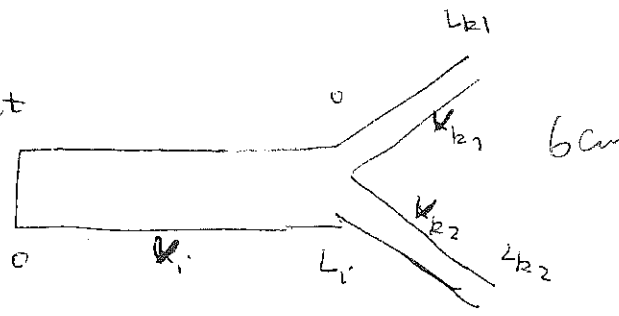
L. Abbott (Physica A 125, 343 (1992)), is expressed in the time domain. A complementary formulation, in terms of the Laplace transform of $V(x, t)$ can be found in E. Butz & J. Cowan, Biophys J. 14, 661 (1974).

The idea is to reduce the problem to an equation for the Green function of the system. Let us label the various segments of a given dendritic tree with an index i . Along each segment we label position with the coordinate x satisfying $0 \leq x \leq L_i$.

boundary condition at a branching point

$$V_i(L_i, t) = V_{k_1}(0, t) = V_{k_2}(0, t)$$

$$d_i^{3/2} \left. \frac{\partial V_i}{\partial x} \right|_{L_i} = d_{k_1}^{3/2} \left. \frac{\partial V_{k_1}}{\partial x} \right|_0 + d_{k_2}^{3/2} \left. \frac{\partial V_{k_2}}{\partial x} \right|_0$$



At the distal terminals, the boundary condition is either

$$V_i(L_i, t) = 0 \quad (\text{open-end})$$

$$\text{or } \left. \frac{\partial V_i}{\partial x} \right|_{L_i} = 0 \quad (\text{sealed-end}).$$

If $V_i(x, t)$ is the potential on segment i , $I_j(y, s)$ is the injected current (per unit area) at point y on segment j . Then we can write

$$\boxed{V_i(x, t) = \sum_j \left[\int_0^{L_j} dy G_{ij}(x, y, t) e^{-t} V_j(y, 0) + \int_0^t ds \int_0^{L_j} dy G_{ij}(x, y, t-s) e^{s-t} I_j(y, s) \right]}$$

where $G_{ij}(x, y, t)$ is the Green's function, defined for $t > 0$, and satisfying

$$\frac{\partial G_{ij}(x, y, t)}{\partial t} = \frac{\partial^2 G_{ij}(x, y, t)}{\partial x^2}$$

with the initial condition $G_{ij}(x, y, 0) = \delta_{ij} \delta(x-y)$. $G_{ij}(x, y, t)$ must also satisfy similar boundary conditions as $V_i(x, t)$, namely, at a branching point

$$G_{ij}(L_i, y, t) = G_{k_1 j}(0, y, t) = G_{k_2 j}(0, y, t) \quad \text{for all } j.$$

$$\left. d_i^{3/2} \frac{\partial G_{ij}(x, y, t)}{\partial x} \right|_{L_i} = \left. d_{k_1}^{3/2} \frac{\partial G_{ij}(x, y, t)}{\partial x} \right|_0 + \left. d_{k_2}^{3/2} \frac{\partial G_{ij}(x, y, t)}{\partial x} \right|_0$$

At a distal terminal

$$G_{ij}(L_i, y, t) = 0 \quad (\text{open-end})$$

$$\text{or} \quad \left. \frac{\partial G_{ij}(x, y, t)}{\partial x} \right|_{L_i} = 0 \quad (\text{sealed-end}).$$

Therefore, we need only to solve $G_{ij}(x, y, t)$. Once $G_{ij}(x, y, t)$ is known, $V_i(x, t)$ can be calculated for any initial condition and injected current distribution. $G_{ij}(x, y, t)$ obeys a diffusion equation and can be interpreted as the transition probability of a Brownian motion on a tree.

example: infinite cable

$$\rightarrow G_0(x-y, t) = \frac{1}{\sqrt{4\pi t}} e^{-\frac{(x-y)^2}{4t}}$$

this is the transition probability for a Brownian particle to move from y (at time 0) to x (at time t) in one-dimension.

for a semi-infinite cable ($x \geq 0$)

$$G(x, y, t) = \begin{cases} G_0(x-y, t) - G_0(x+y, t) & (\text{open end at } x=0) \\ G_0(x-y, t) + G_0(x+y, t) & (\text{sealed end at } x=0) \end{cases}$$

for an arbitrary tree,

$$G_{ij}(x, y, t) = \sum_{\text{trips}} A_{\text{trip}} G_0(L_{\text{trip}}, t)$$

where the sum is over all possible "trips" using the rules given below.

A trip is a path along the tree that starts at the point x on segment i and ends at the point y on segment j . Trips are constructed in accordance with the following rules.

- A trip may start out from x by traveling in either direction, but it may subsequently change direction only at a node or a terminal. A trip may pass through the points x and y an arbitrary number of times.
- When a trip arrives at a node, it may pass through the node to any segments radiating from the node.
- When it reaches a terminal, a trip always reflects back.

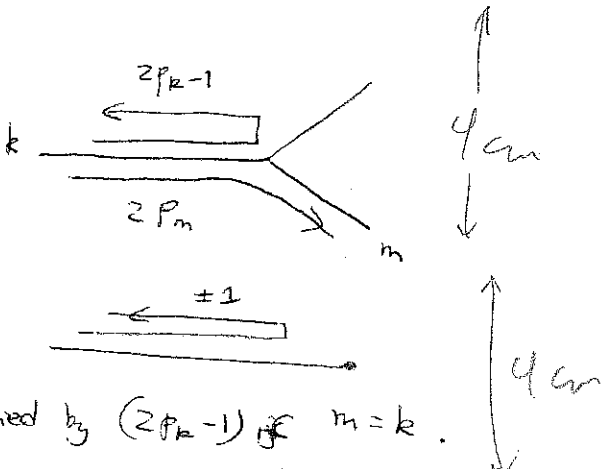
L_{trip} is the sum of the dimensionless lengths of all the steps taken along the course of the trip.

To compute the coefficients A_{trip} , let $P_k = \frac{d_k^{3/2}}{\sum_m d_m^{3/2}}$ be a factor associated to the segment k and to the node where the denominator is computed. Then

- Initially when the trip starts out from x , $A_{\text{trip}} = 1$
- A_{trip} is multiplied by $2P_m$ every time the trip crosses a node by going from segment k to segment m , $k \neq m$. A_{trip} is multiplied by $(2P_k - 1)$ if $m = k$.
- When the trip reflects off a sealed terminal, A_{trip} remains unchanged. When the trip reflects off an open terminal, A_{trip} is multiplied by -1 .

For a proof, see L. Abbott et al. Biol Cybern. 66, 49 (1991).

Balls' equivalent cylinder if $P_k = \frac{1}{2}$. ($\Rightarrow d_k^{3/2} = \sum_{m \neq k} d_m^{3/2}$).

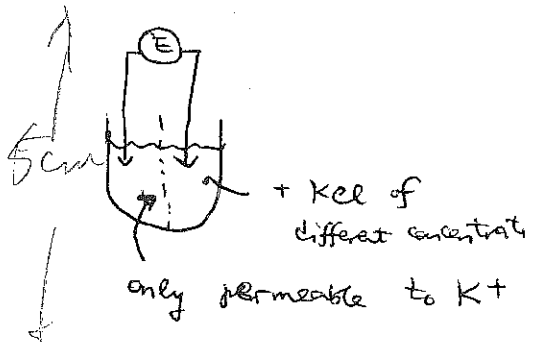


Lecture 5: Hodgkin-Huxley theory of action potentials

(1) equilibrium potential and the Nernst equation

equilibrium: thermal force by diffusion
(of concentration gradient)

= electrical force of charge gradient



Boltzmann: $\frac{P_1}{P_2} = e^{-\frac{U_2 - U_1}{kT}} \rightarrow \frac{c_1}{c_2} = e^{-\frac{U_1 - U_2}{kT}}$ $R = kN = 8.314$

$$U_1 - U_2 = \frac{F}{3} (E_1 - E_2) \quad F = 9.65 \times 10^4 \text{ C mol}^{-1}$$

charge / mole

$$\rightarrow E_1 - E_2 = \frac{RT}{3F} \ln \frac{c_2}{c_1}$$

$$V_{rev} = E_1 - E_0 = \frac{RT}{3F} \ln \frac{[C]_o}{[C]_i}$$

Example: $V_{Na} = 55 \text{ mV}$ in squid axon at 6.3°C

$$V_K = -72 \text{ mV}$$

$$\text{Ohm's law } I = gV \rightarrow I = g(V - V_{rev})$$

but this may not be exact. I may be nonlinear in V . (fig. 1)

(2) Goldman - Hodgkin - Katz theory

The transmembrane current due to both a concentration gradient and a gradient is expressed by the Nernst-Planck equation

$$I = -3FD \left(\frac{dc}{dx} + \frac{F\beta c}{RT} \frac{d\psi}{dx} \right)$$

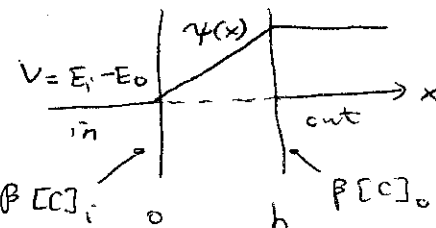
ψ : local potential

$$\psi(x) = V - \frac{Vx}{h} \text{ linear}$$

$$I = \text{const}$$

β = water-membrane partition

D = diffusion coefficient



$$\} P = \frac{D\beta}{h} \text{ permeability (cm/sec.)}$$

$$I = -\frac{3FD}{e^{\frac{3F\psi}{RT}}} \frac{d}{dx} (c e^{\frac{3F\psi}{RT}})$$

$$I \int_0^h e^{\frac{3F\psi}{RT}} dx = 3FD\beta ([C]_i e^{-\frac{3FV}{RT}} - [C]_o)$$

$$\rightarrow I = P \frac{3^2 F^2 V}{RT} \frac{[C]_i - [C]_o e^{-\frac{3FV}{RT}}}{1 - e^{-\frac{3FV}{RT}}}$$

GHK

note: equilibrium $I=0 \rightarrow V_{rev} = \frac{RT}{3F} \ln \frac{[C]_o}{[C]_i}$

$$I \rightarrow \begin{cases} P \frac{3^2 F^2 V}{RT} [C]_i & \text{as } V \rightarrow +\infty \\ P \frac{3^2 F^2 V}{RT} [C]_o & \text{as } V \rightarrow -\infty \end{cases}$$

quite

The nonlinearity is significant if $[C]_i \neq [C]_o$ are different.

e.g. $c = C_a^{2+}$ (fig. 2).

note: if $I = I_{Na^+} + I_K + I_L = 0 \rightarrow V_{rev} = \frac{RT}{F} \ln \frac{P_K [K]_o + P_{Na^+} [Na^+]_o + P_{Cl^-} [Cl^-]_i}{P_K [K]_i + P_{Na^+} [Na^+]_i + P_{Cl^-} [Cl^-]_o}$

(3) HH theory of action potentials

But the GHK description could not account for the very strongly nonlinear membrane properties observed by Hodgkin-Huxley on giant squid axon (fig. 3). HH demonstrated that the conductance g or permeability P for some ions is voltage-dependent, using newly developed voltage-clamp technique.

Giant squid axon: $d \approx 0.5 \text{ mm}$ $l > 5 \text{ cm}$

$$R_m = 700 \Omega \text{ cm}^2 \quad R_i = 30 \Omega \text{ cm}$$

$$\lambda = \sqrt{\frac{R_m d}{R_i}} / 4 = 5.4 \text{ mm} \quad (\text{so } l \gg \lambda).$$

Action potential (fig. 4). The propagation speed $\approx 20 \text{ m/s}$.

2 main currents I_{Na} & I_K ($\bar{g}_L = 0.3 \text{ mS/cm}^2$ is small)

Circuit (fig. 5). By changing the external sodium concentration in the solution, I_{Na} may be eliminated. Thus I_K can be characterized.

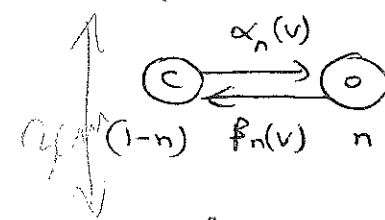
In a separate experiment, one records $I_{Na} + I_K$, then subtract from it the known I_K . Thus I_{Na} can be characterized in turn.

$$I_K = \bar{g}_K n P (V - V_K)$$

$$\bar{g}_K = \frac{I_K}{V - V_K}$$

$$T_n = \frac{1}{\alpha_n + \beta_n}$$

$$\dot{n} = \alpha_n(1-n) - \beta_n n = \frac{n_o(V) - n}{T_n(V)}$$



$$n_{\infty} = \frac{\alpha_n}{\alpha_n + \beta_n}$$

Note: all nonlinearity in V , so the system becomes linear in voltage-clamp preparations.

$$\rightarrow \text{solve } n(t) = n_{\infty}(v) - (n_{\infty}(v) - n_0(v_0)) e^{-t/\tau_n(v)}$$

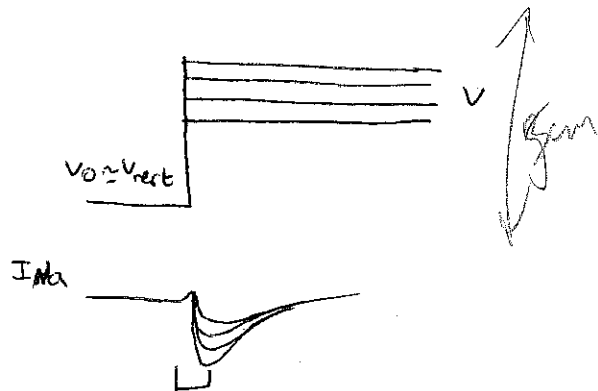
$$g_K = ((g_{K_\infty})^{\frac{1}{P}} - ((g_{K_\infty})^{\frac{1}{P}} - g_{K_0}^{\frac{1}{P}}) e^{-t/\tau_n(v)})^{\frac{1}{P}}$$

Curve fitting (fig. 6) $\rightarrow P=4$, $n_{\infty}(v)$ and $\tau_n(v)$.

$$I_{Na} = \bar{g}_{Na} m^P h^q (V - V_{Na})$$

m : activation . fast $P=3$

h : inactivation . slow $q=1$



again, we assume a first-order kinetics

for m and h :

$$m = \frac{m_{\infty}(v) - m}{\tau_m(v)}$$

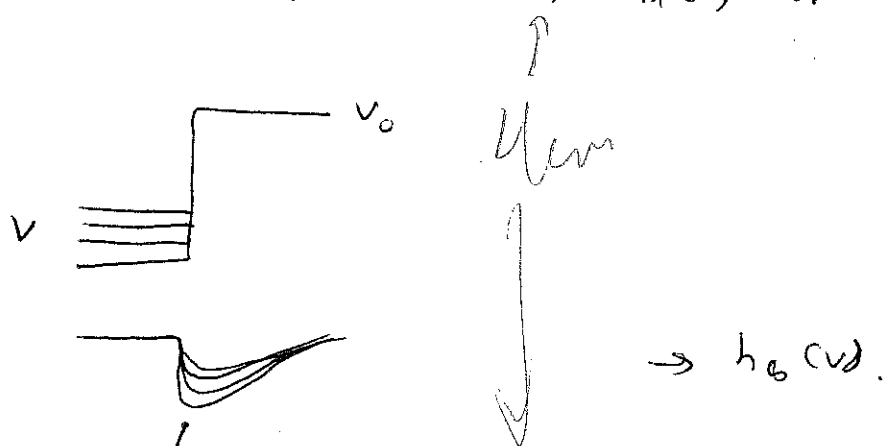
$$h = \frac{h_{\infty}(v) - h}{\tau_h(v)}$$

} solved explicitly
for fixed v

$h \approx h_0$ because it is slow

$$m_0 \approx 0 \quad h_{\infty}(v) \approx 0 \quad \rightarrow \quad g_{Na} = \bar{g}_{Na} m_{\infty}^3(v) h_0 [1 - e^{-t/\tau_m(v)}]^3 e^{-t/\tau_h(v)}$$

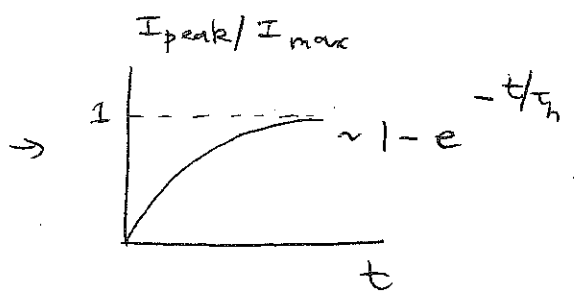
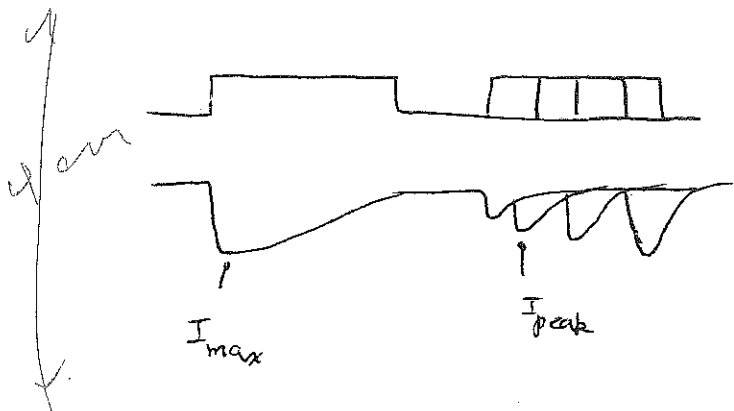
Curve fitting $\rightarrow m_{\infty}(v)$, $\tau_m(v)$ and τ_h .



$\rightarrow h_0(v)$.

$$I_{peak} \propto h_0(v)$$

an alternative way to measure $\tau_h(V)$: recovery experiment



Summary: $C \frac{dV}{dt} = -\bar{g}_{Na} m^3 h (V - V_{Na}) - \bar{g}_K n^4 (V - V_K) - \bar{g}_L (V - V_L) + I_{app}$

6.3 C°

$$\bar{g}_{Na} = 120 \text{ mS/cm}^2 \quad V_{Na} = 50 \text{ mV}$$

$$\frac{[Na]_o}{[Na]_i} = 8$$

$$Q_{10} = 3$$

$$\bar{g}_K = 36 \text{ mS/cm}^2 \quad V_K = -77 \text{ mV}$$

$$\frac{[K]_i}{[K]_o} = 25$$

$$\phi = 3 \frac{(T-6.3)/10}{(T-6.3)/10}$$

$$\bar{g}_L = 0.3 \text{ mS/cm}^2 \quad V_L = -54.4 \text{ mV}$$

$$\alpha_n = -0.01 (V + 55) / (e^{-\frac{V+55}{10}} - 1) \quad \beta_n = 0.125 e^{-\frac{(V+65)}{80}}$$

$$\alpha_m = -0.1 (V + 40) / (e^{-\frac{V+40}{10}} - 1) \quad \beta_m = 4 e^{-\frac{(V+65)}{18}}$$

$$\alpha_h = 0.07 e^{-\frac{(V+65)}{20}}$$

$$\beta_h = 1 / (e^{-\frac{(V+35)}{10}} + 1)$$

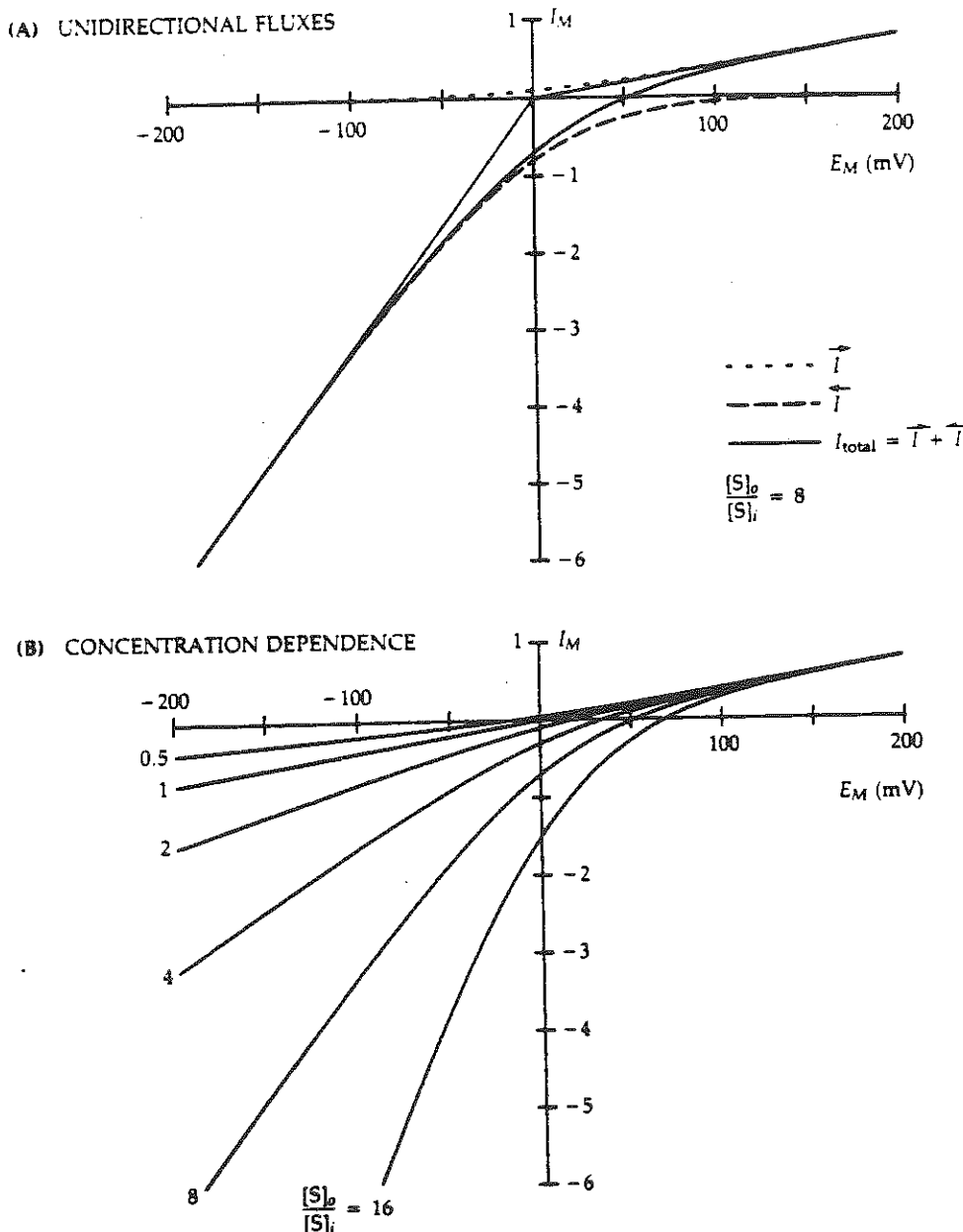
(see fig. 7). action potential reproduced (fig. 8).

remarks

- single channel gating (fig. 9) \rightarrow pharmacology / molecular biology
(complex stochastic kinetics)
- multiple ion channels (Llinás)
- $I_A \rightarrow$ small frequency \rightarrow spike coding
(Connors - Stevens) fig. 10

References

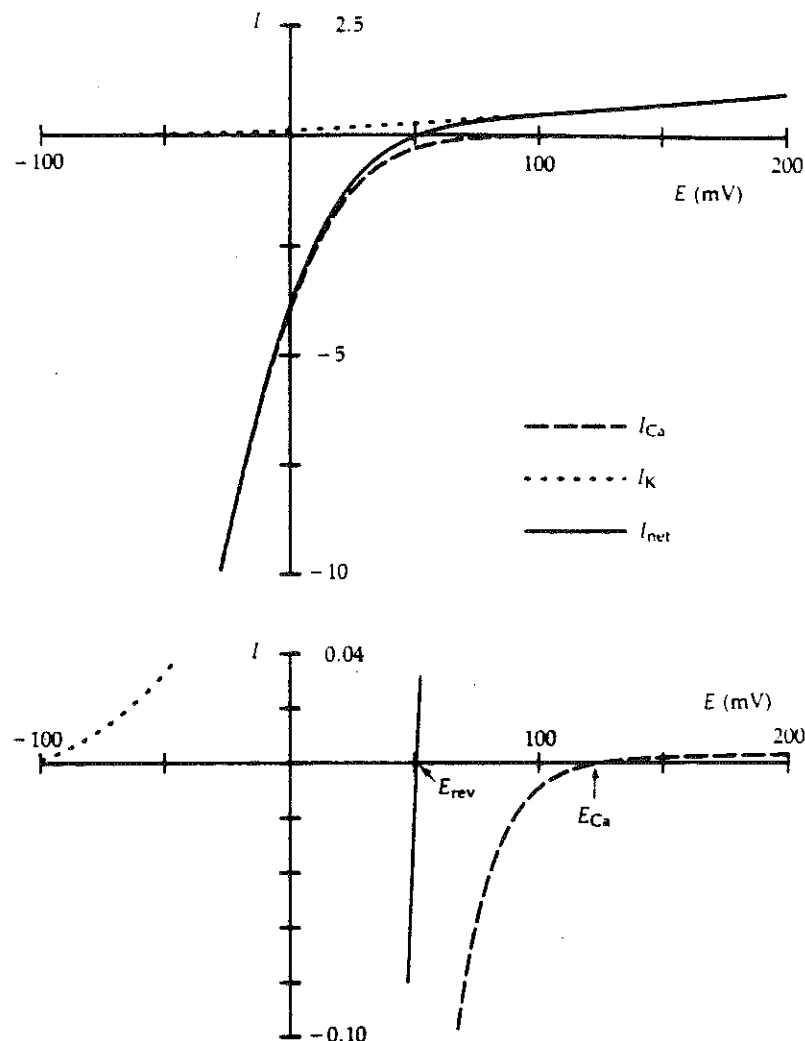
- A.L. Hodgkin and A.F. Huxley J Physiol. 117, 500 (1952)
- B. Katz (Nerve, muscle & synapse) McGraw-Hill (1966)
- B. Hille (Ionic channels of excitable membranes) Sinauer (1984)



2 CURRENT-VOLTAGE CURVES OF GHK THEORY

Theoretical $I-E$ relations for a homogeneous membrane obeying the Goldman (1943) and Hodgkin and Katz (1949) current equation for a single permeant, univalent cation. (A) Eightfold rectification with an eightfold concentration gradient, showing asymptotes extrapolating to the origin and showing the underlying unidirectional efflux and influx making up the total current. (B) Change of curvature and of reversal potential as the external concentration is varied from 0.5 to 16 while the internal concentration is kept constant at 1. (Current and concentration in arbitrary units.)

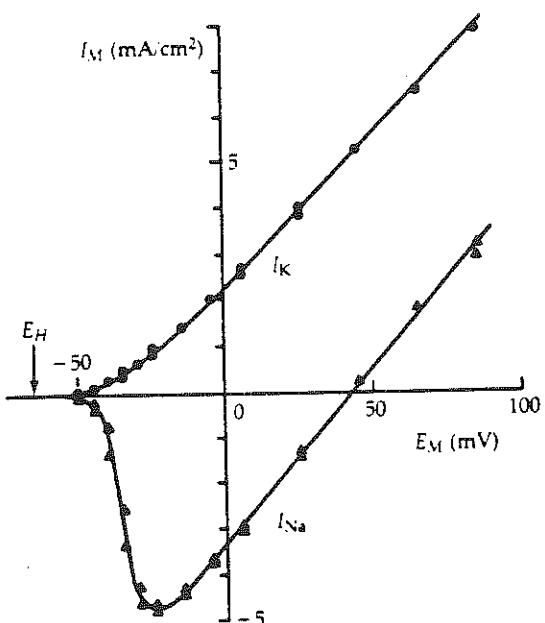
fig. 5.1



6 THEORETICAL I-E CURVE FOR Ca CHANNELS

The electrodiffusion theory of Goldman (1943) and Hodgkin and Katz (1949) gives $I-E$ relations for open ionic channels under simplifying assumptions given in Chapter 10. It predicts nonlinear $I-E$ relations when the concentration of permeant ion is unequal on the two sides of the membranes. The predicted rectification is most striking for Ca^{2+} ions because their concentration ratio is 10,000:1 and because for divalent ions, the rectification is completed over a narrower voltage range. Curves of I_{Ca} , I_{K} , and their sum are drawn with Equation 10-5 for a channel permeable to Ca^{2+} ions and very slightly permeable to K^+ ions as well ($P_{\text{K}}/P_{\text{Ca}} = 1/1000$). The assumed ionic concentrations are $[\text{Ca}^{2+}]_o = 2 \text{ mM}$, $[\text{Ca}^{2+}]_i = 100 \text{ nM}$, $[\text{K}^+]_o = 2 \text{ mM}$, $[\text{K}^+]_i = 100 \text{ mM}$. Although its permeability is low, the K^+ ion makes a significant contribution to the reversal potential of the Ca channel. The reversal potential (E_{rev}) here is at +52 mV, far less positive than the thermodynamic E_{Ca} , which is +124 mV.

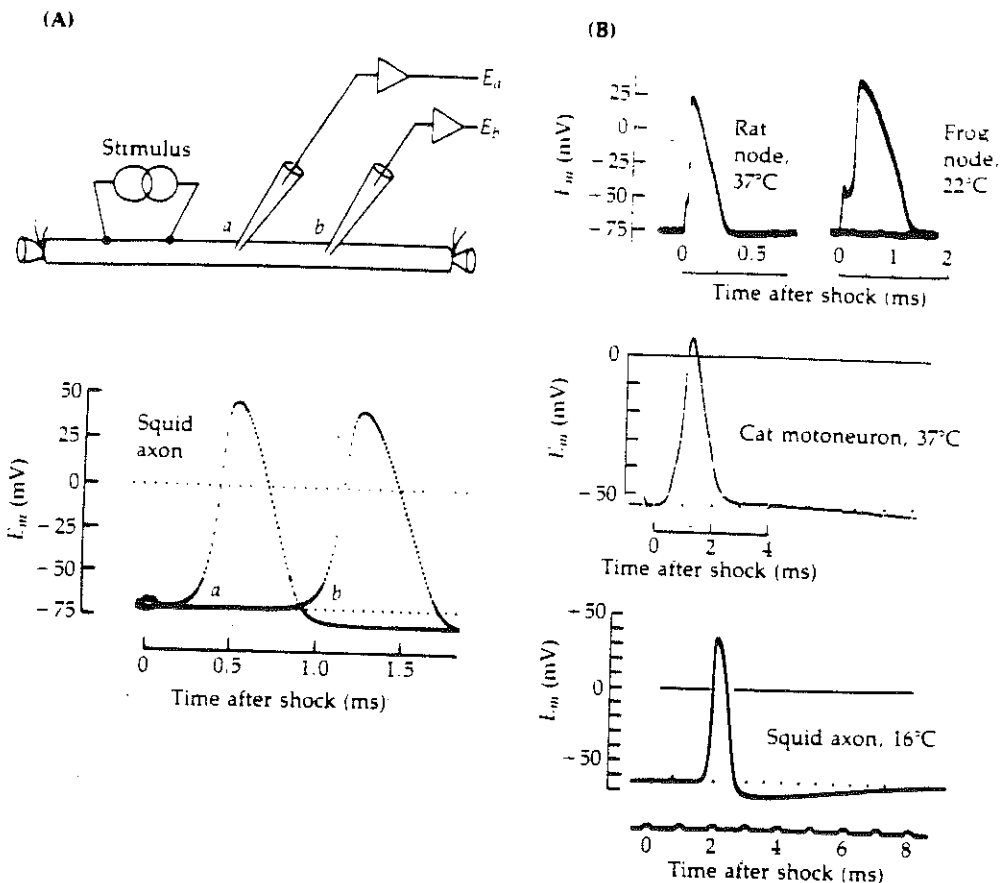
f.g. 5.2



9 CURRENT-VOLTAGE RELATIONS OF SQUID AXON

The axon membrane potential is stepped under voltage clamp from the negative holding potential (arrow) to various test potentials as in Figure 7. Peak transient sodium current (triangles) and steady-state potassium current (circles) from each trace are plotted against the test potential. The curvature of the two I - E relations between -50 and -20 mV reflects the voltage-dependent opening of Na and K channels, as explained in Figure 6 of Chapter 1. [From Cole and Moore, 1960.]

fig. 5, 3

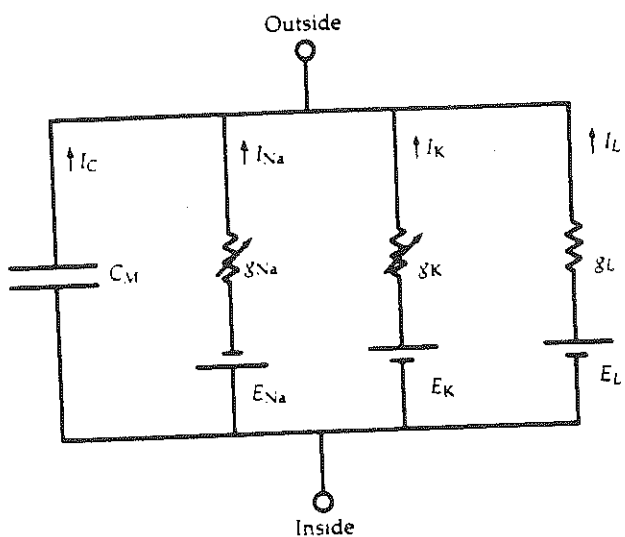


1 ACTION POTENTIALS IN NERVE MEMBRANES

(A) Propagated action potential recorded intracellularly from two points along a squid giant axon. The recording micropipettes *a* and *b* are separated by 16 mm, and a stimulator applies a shock to the axon. The two potential traces show the action potential sweeping by the two electrodes with a 0.75-ms propagation time between *a* and *b*, corresponding to a conduction velocity of 21.3 m/s. [Adapted from del Castillo and Moore, 1959.] (B) Comparison of action potentials from different cells. The recordings from nodes of Ranvier show the brief depolarization caused by the stimulating shock applied to the same node and followed by the regenerative action potential. [From Dodge, 1963; and courtesy of W. Nonner, M. Horácková, and R. Stampfli, unpublished.] In the other two recordings the stimulus (marked as a slight deflection) is delivered some distance away and the action potential has propagated to the recording site. [Courtesy of W.E. Crill, unpublished; and Baker et al., 1962.]

fig. 5.4

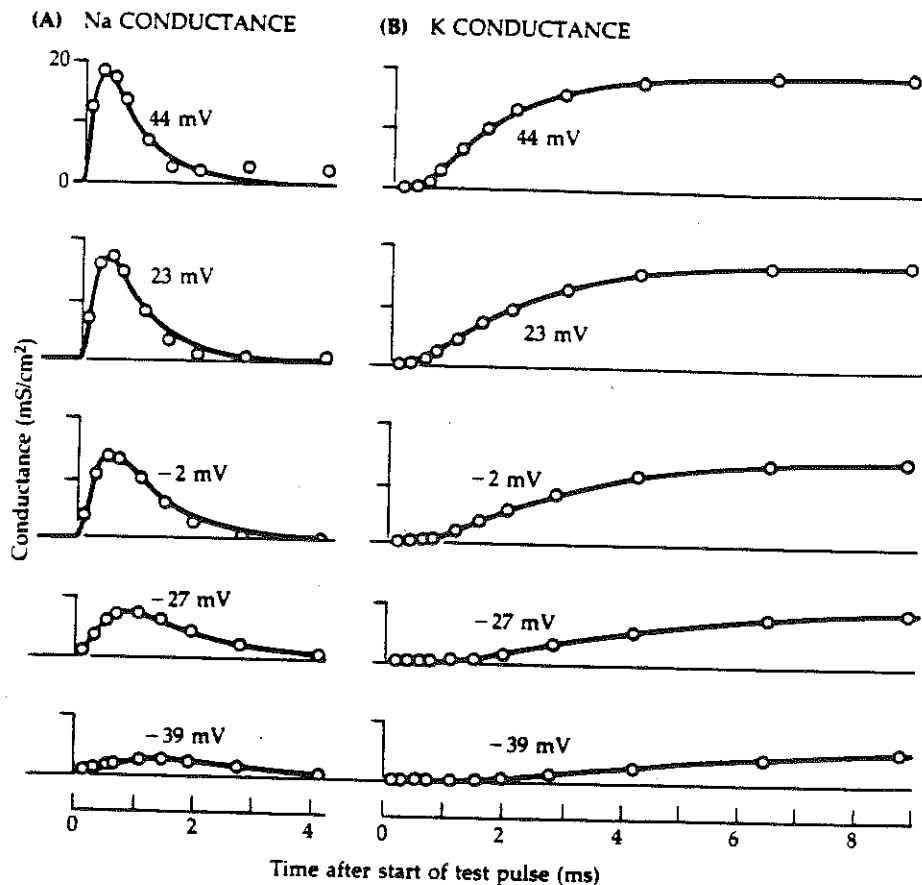
(5.6)



10 EQUIVALENT CIRCUIT OF AXON MEMBRANE

Hodgkin and Huxley described the axon membrane as an electrical circuit with four parallel branches. The capacitative branch represents the thin dielectric properties of the membrane. The three conductive branches represent sodium, potassium, and leak conductances with their different electromotive forces. The vertical arrows define the direction of positive current. The resistors with diagonal arrows through them denote time- and voltage-varying conductances arising from the opening and closing of ionic channels. [From Hodgkin and Huxley, 1952d.]

fig. 5.5



12 CONDUCTANCE CHANGES AT MANY VOLTAGES

Time courses of g_{Na} (A) and g_{K} (B) during depolarizing steps to the indicated voltages. Circles are the ionic conductances measured in a squid giant axon at 6.3°C . Smooth curves are the conductance changes calculated from the Hodgkin-Huxley model. [From Hodgkin, 1958; adapted from Hodgkin and Huxley, 1952d.]

fig. 5.6

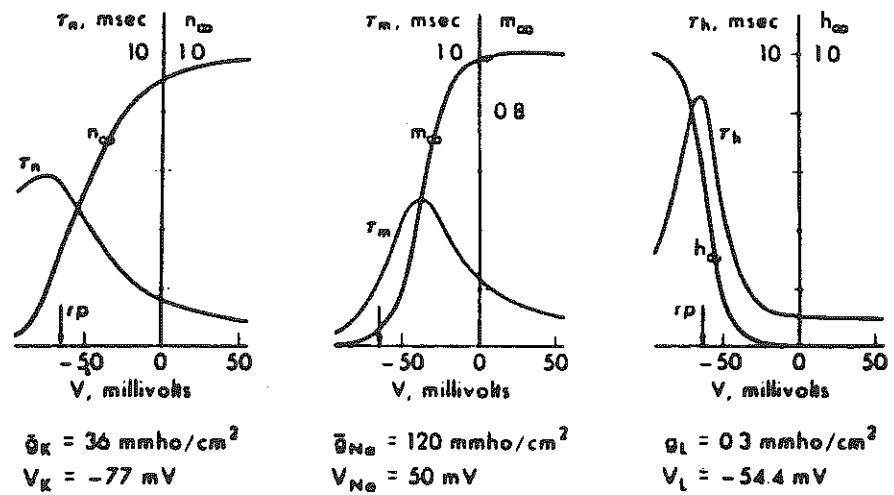


FIG. 12. Steady-state values of the variables n , m , and h and their time constants τ_n , τ_m , and τ_h as a function of membrane potential. Values from Hodgkin and Huxley (1952d) are replotted on an absolute membrane potential scale, taking the resting potential (r_p) in the experiments of Hodgkin and Huxley as -65 mV. Numerical values of \bar{g}_K , \bar{g}_{Na} , \bar{g}_L and the equilibrium potentials are at the bottom of the figure. (From Cole, 1968.)

fig. 5,7

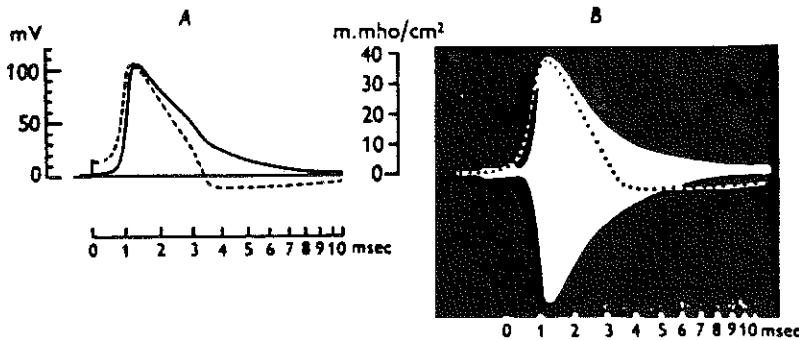


Fig. 16. A, solution of eqn. (26) for initial depolarization of 15 mV at a temperature of 6° C. The broken curve shows the membrane action potential in mV; the continuous curve shows the total membrane conductance ($g_{Na} + g_K + \bar{g}_I$) as a function of time. B, records of propagated action potential (dotted curve) and conductance change reproduced from Cole & Curtis (1939). The time scales are the same in A and B.

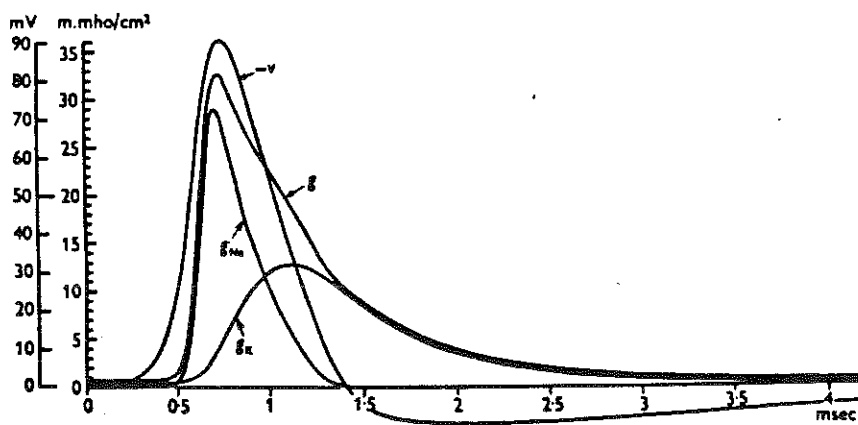
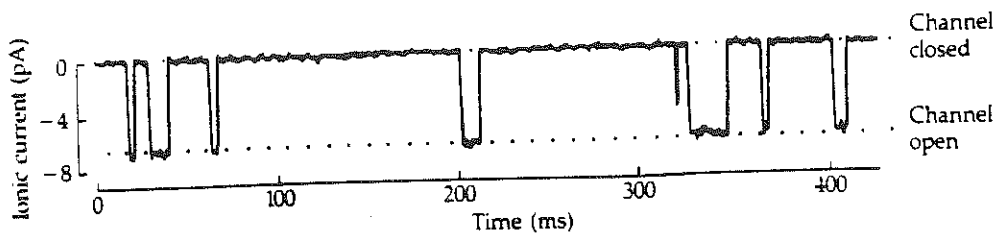


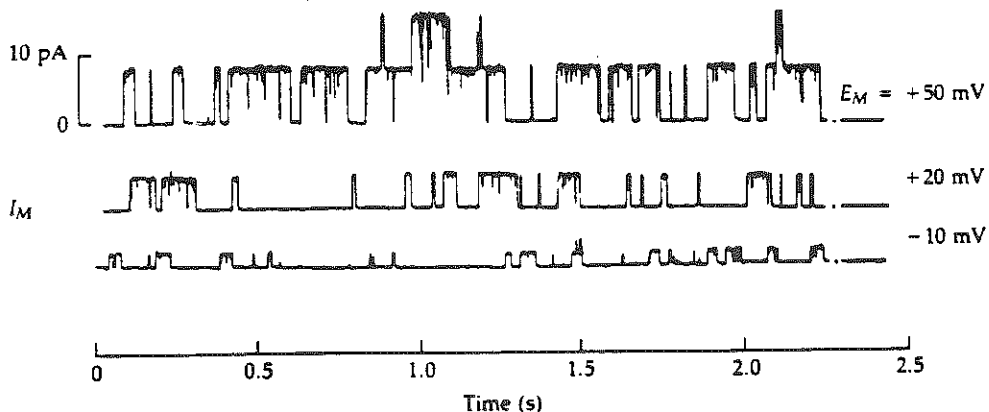
Fig. 17. Numerical solution of eqn. (31) showing components of membrane conductance (g) during propagated action potential ($-V$). Details of the analysis are as in Fig. 15.

fig. 5, 8



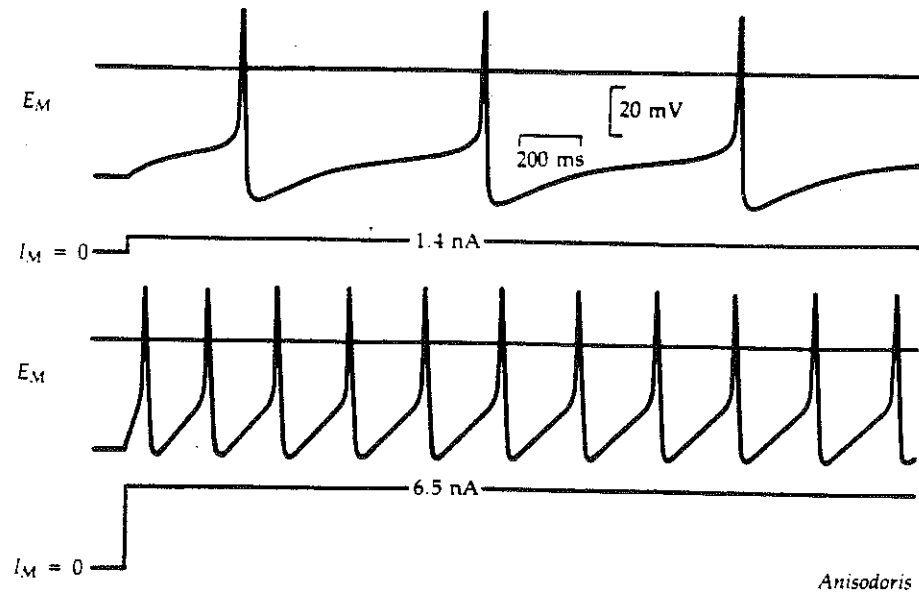
1 OPEN-SHUT GATING OF AN IONIC CHANNEL

Ionic current flowing across a tiny patch of excitable membrane showing eight brief openings (downward current deflections) of single ionic channels. The membrane patch has been excised from a cultured rat myotube and is bathed on both sides by Na salt solutions. Approximately 300 nM of the neurotransmitter, acetylcholine, applied to the extracellular membrane face is causing channels to open occasionally. At the -140 mV applied membrane potential, one open channel passes -6.6 pA, corresponding to a prodigious flow of 4.1×10^7 ions per second through a single pore. $T = 23^\circ\text{C}$. [Courtesy of D. Siemen, unpublished.]



7 OPENINGS OF SINGLE K(Ca) CHANNELS

Single-channel currents recorded from a small membrane patch of an intact rat myotube in culture. The records are stationary responses after the membrane has been held at the indicated potential for many seconds. The single-channel conductance is high, about 100 pS with normal, Na-containing extracellular solutions. Depolarization increases the probability and duration of channel opening and increases the unitary current size. $T = 20^\circ\text{C}$. [From Pallotta et al., 1981.]



1 REPETITIVE FIRING OF AN ISOLATED NEURON

Action potentials recorded with an intracellular microelectrode from a nudibranch (*Anisodoris*) ganglion cell whose axon has been tied off. A second intracellular microelectrode passes a step of current (I) across the soma membrane, initiating a train of action potentials. $T = 5^\circ\text{C}$. [From Connor and Stevens, 1971a.]

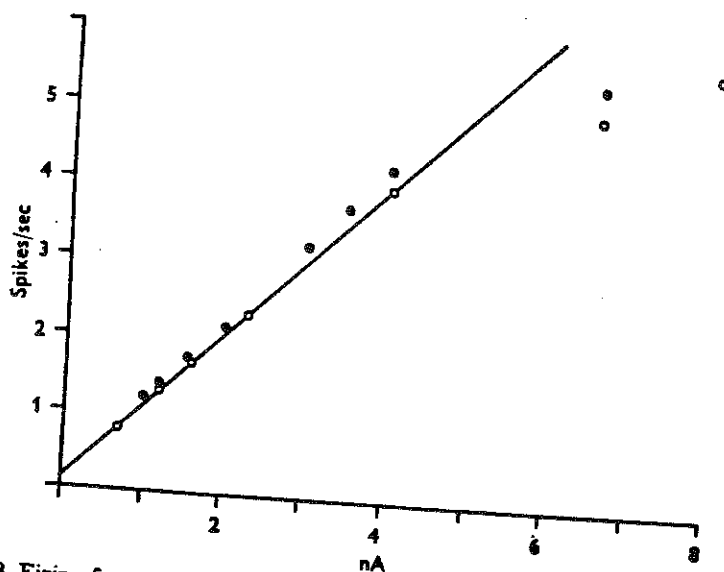


Fig. 8. Firing frequency (ordinate) plotted against transmembrane stimulus current (abscissa) for exemplar cell (open circles) and model (filled circles).

fig. 5.10

Lecture 6: Bifurcations and oscillations, the Fitz-Hugh-Nagumo system

In the Hodgkin-Huxley model, an action potential is followed by a "refractory period" when the membrane potential falls below the resting level and slowly recovers (repolarizes) back to V_{rest} (fig. 1). This phase coincides with a slow "deactivation" of I_{Na} (i.e. h drifts back to a high level) and "inactivation" of I_K (i.e. n or g_K decays to near zero). See fig. 1. The variables h and n have similar time constants, and are slower than m . The idea is thus to let $m = m_\infty(v)$, and define a "recovery variable" w which combines the effects of h, n . This is done based on voltage-clamp data. From fig. 2a we can assume that

$$\frac{dv}{dt} = -I_{ion}, \quad I_{ion} = f(v) + w(t, v) \quad \text{slow} \quad \frac{dw}{dt} = \frac{w_\infty - v}{\tau_w}.$$

instantaneous function of v

$$I_{peak}(v) = \lim_{t \rightarrow 0^+} I_{ion} = f(v) + w_\infty(v_{rest}) \stackrel{\approx}{=} f(v) = I_{peak}(v)$$

$$I_{ss}(v) = \lim_{t \rightarrow \infty} I_{ion} = f(v) + w_\infty(v) \rightarrow w_\infty(v) = I_{ss}(v) - I_{peak}(v)$$

from fig. 2.b $f(v)$ is approximated by a cubic function $f(v) = v(v-1)(v-a)$

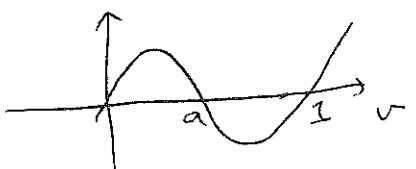
FHN:

$$\frac{dv}{dt} = -f(v) - w + I_{app}$$

$$\equiv F(v, w)$$

$$\frac{dw}{dt} = \epsilon(v - \delta w)$$

$$\equiv G(v, w)$$



2.5" x 1.5"

This is a 2-variable dynamical system, which can be analysed by the "phase plane" technique. (note: another way of reduction is based on $n+h=0, k \rightarrow (v, n)$ system)

Let $\frac{dv}{dt} = -I_{ion} + I = 0 \rightarrow I = I_{ion}$ or $w = -f(v) + I$. This curve on the (v, w) -plane is called the v -nullcline.

$$\frac{dw}{dt} = 0 \rightarrow w = \frac{v}{\gamma} \text{ if the } w\text{-nullcline.}$$

A steady state of the system is given (geometrically) by an intersection of the 2 nullclines. These are illustrated in fig. 3 with $I = 0$ ($b = \varepsilon$). Fig. 3 shows response to a brief stimulus of increasing intensity (subthreshold \rightarrow suprathreshold)

To study the stability of a s.s. (v_{ss}, w_{ss}) , let $v = v_{ss} + \delta v$, $w = w_{ss} + \delta w$, and we would like to know whether $(\delta v, \delta w)$ will grow or decay to zero with time. For small $(\delta v, \delta w)$ we have

$$\begin{pmatrix} \frac{d\delta v}{dt} \\ \frac{d\delta w}{dt} \end{pmatrix} = M \begin{pmatrix} \delta v \\ \delta w \end{pmatrix} \quad \text{where } M = \begin{pmatrix} \frac{\partial F}{\partial v} & \frac{\partial F}{\partial w} \\ \frac{\partial G}{\partial v} & \frac{\partial G}{\partial w} \end{pmatrix}_{v_{ss}, w_{ss}} = \begin{pmatrix} -f'(v_{ss}) - 1 \\ \varepsilon - \varepsilon \gamma \end{pmatrix}$$

+ higher order terms

$$\rightarrow \begin{pmatrix} \delta v(t) \\ \delta w(t) \end{pmatrix} = \underline{a}_1 e^{\lambda_1 t} + \underline{a}_2 e^{\lambda_2 t} \quad \text{where } \lambda_1, \lambda_2 \text{ are eigenvalues of } M.$$

$\rightarrow (v_{ss}, w_{ss})$ stable iff $\underline{\text{Re } \lambda_1, \text{Re } \lambda_2 < 0}$.

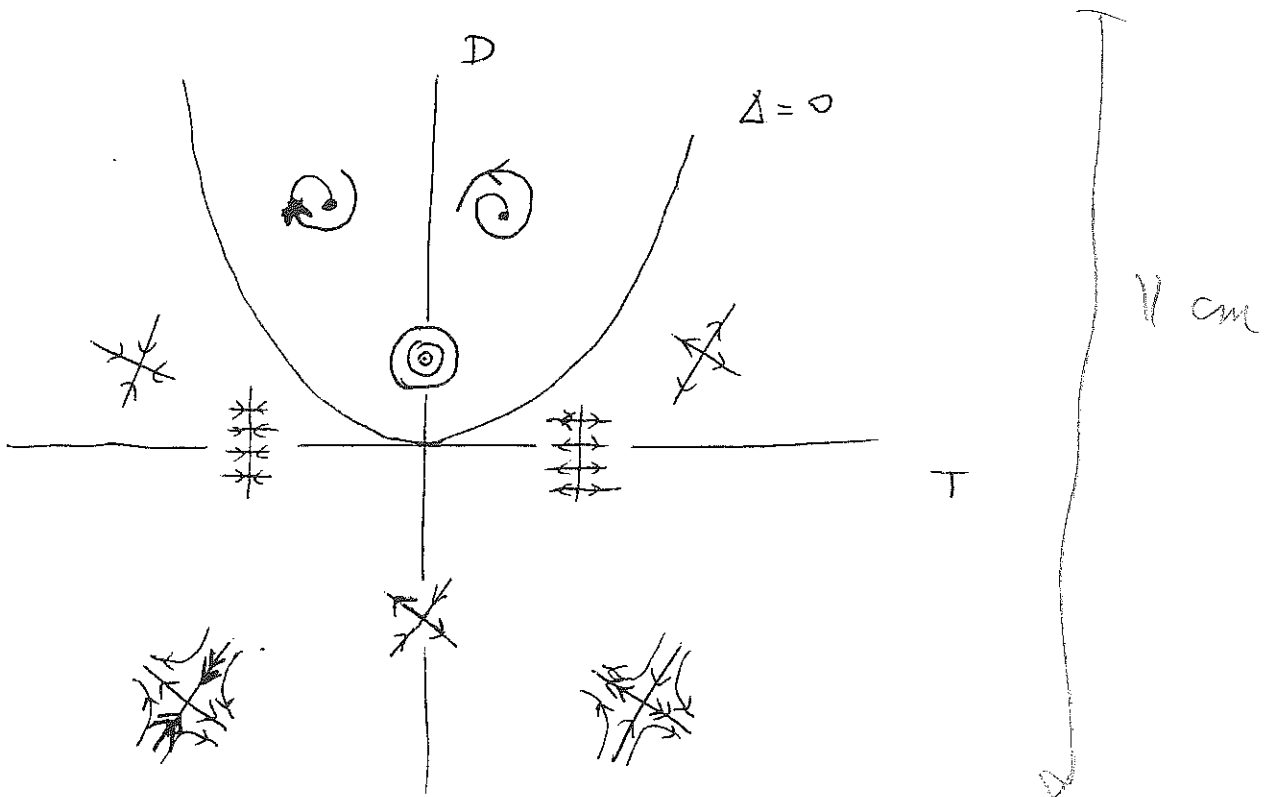
λ_1, λ_2 are solutions of $\det(M - \lambda I) = 0$.

In general, let $M = \begin{pmatrix} a_{11} & a_{12} \\ a_{21} & a_{22} \end{pmatrix}$, $T = \text{trace } M = a_{11} + a_{12}$,

$D = \det M = a_{11}a_{22} - a_{12}a_{21}$. Then $\underline{\lambda^2 - T\lambda + D = 0}$. The

solutions λ_1, λ_2 satisfy $\lambda_1 + \lambda_2 = T$ $\lambda_1 \lambda_2 = D$. Therefore, for instance, if $D > 0$ and $T < 0$, then (v_{ss}, w_{ss}) is stable.

Let $\Delta = T^2 - 4D$. The stability nature of the steady state as function of D and T are shown below



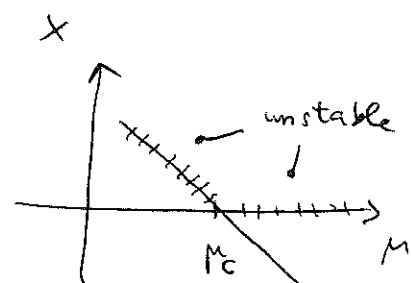
λ_1 and λ_2 , as well as (v_{ss}, w_{ss}) , are functions of the control parameters of the system. As a parameter is gradually varied, (v_{ss}, w_{ss}) may lose stability at a critical parameter value. Novel types of solutions may arise as a result of the instability, then we shall speak of a bifurcation phenomenon. We shall not be able to discuss the theory of stability and bifurcation systematically. Instead, let us give a few simple examples to illustrate what may happen in a two-variable dynamical system.

$$(1) \quad \frac{dx}{dt} = x(\mu - \mu_c) + cx^2$$

$$\text{S.S. } x_1 = 0 \text{ or } x_2 = \frac{\mu_c - \mu}{c}$$

$$\text{stability: } \lambda = \mu - \mu_c \text{ for } x_1$$

$$= \mu_c - \mu \text{ for } x_2$$



688
6cm x 5cm

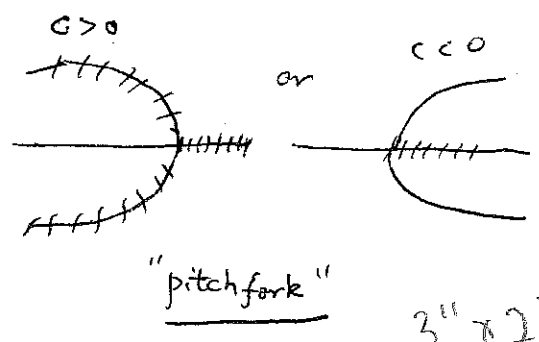
$$(2) \quad \frac{dx}{dt} = H_0(x, \mu) = x(\mu - \mu_c) + cx^3$$

$$H_0(x, \mu) = -H_0(-x, \mu)$$

$$\text{S.S. } x_1 = 0 \quad x_{2,3} = \pm \sqrt{\frac{\mu_c - \mu}{c}}$$

$$\text{stability } \lambda = \mu - \mu_c \text{ for } x_1$$

$$= 2(\mu_c - \mu) \text{ for } x_{2,3}$$



3" x 2"

$$(3) \quad \frac{dx}{dt} = H(x, \mu) = (\mu - \mu_c) + cx^2 \quad H_e(-x) = H(x)$$

S.S.: $x_{1,2} = \pm \sqrt{\frac{\mu_c - \mu}{c}}$



or



stability $\lambda = \pm 2\sqrt{c(\mu_c - \mu)}$

"saddle-node" $\exists^{(1) \times 2}$

$$(4) \quad \text{Hopf bifurcation} \quad \lambda_{1,2} = \sigma \pm i\omega \in \mathbb{C}, \quad \sigma \text{ changes sign}$$

e.g. $\dot{x} = -\omega y + (\mu - \mu_c)x + c(x^2 + y^2)$

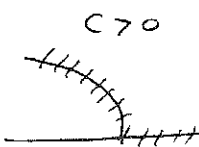
$$\dot{y} = \omega x + (\mu - \mu_c)y + cxy(x^2 + y^2)$$

let $x = r \cos \theta \quad y = r \sin \theta$

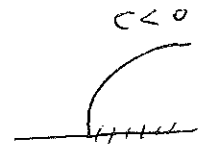
$$\rightarrow \begin{cases} \dot{r} = r(\mu - \mu_c) + cr^3 \\ \dot{\theta} = \omega \end{cases}$$

 $\exists^{(1) \times 1}$

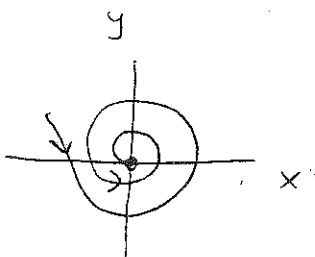
$$\dot{r} = 0 \rightarrow r_1 = 0 \quad \text{or} \quad r_2^2 = \frac{\mu_c - \mu}{c}$$



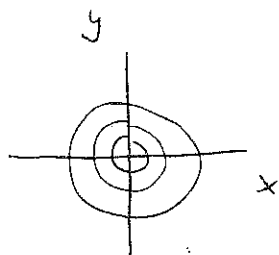
subcritical



supercritical

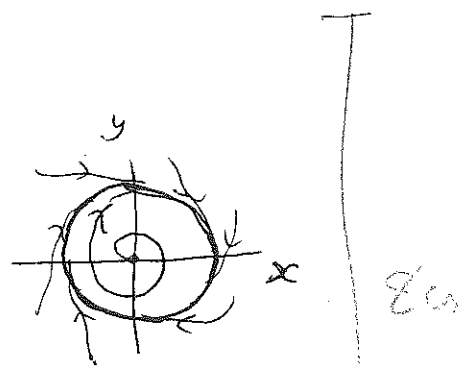


$$\mu < \mu_c$$



$$\mu = \mu_c$$

(but nonlinearly stable)



$$\mu > \mu_c$$

FHN: fig. 4

$\epsilon = 0.008$

Hopf bifurcation at $I \approx 0.055$ if $\delta=1$ $a=0.1$. supercritical

" at $I \approx 0.035$ if $\delta=2.54$ $a=0.14$ subcritical

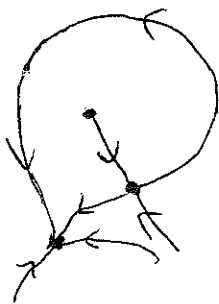
In this case, the oscillatory solution becomes stable after a saddle-node bifurcation of this oscillatory state. Therefore, there exists a range where a stable s.s. and a stable oscillatory state coexist (bistability). A perturbation to the system may induce a transition from one régime to another. This has been seen also in the original HH system, then observed experimentally on squid axon (fig. 5)

(5) homoclinic bifurcation

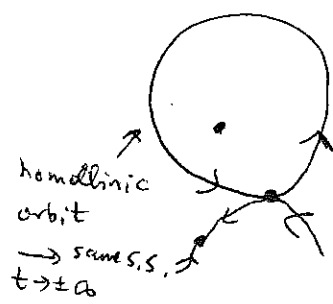
In contrast to the Hopf bifurcation, this is a mechanism of generating oscillations with frequency $\rightarrow 0$ at $\mu=\mu_c$. The period goes to infinity like

$$P \approx \ln\left(\frac{1}{|\mu-\mu_c|}\right) \quad \text{or} \quad \approx \frac{1}{|\mu-\mu_c|^{1/2}}$$

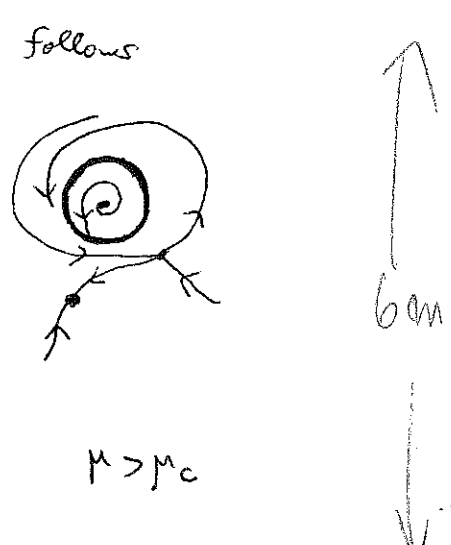
A geometric way to see such a scenario is as follows



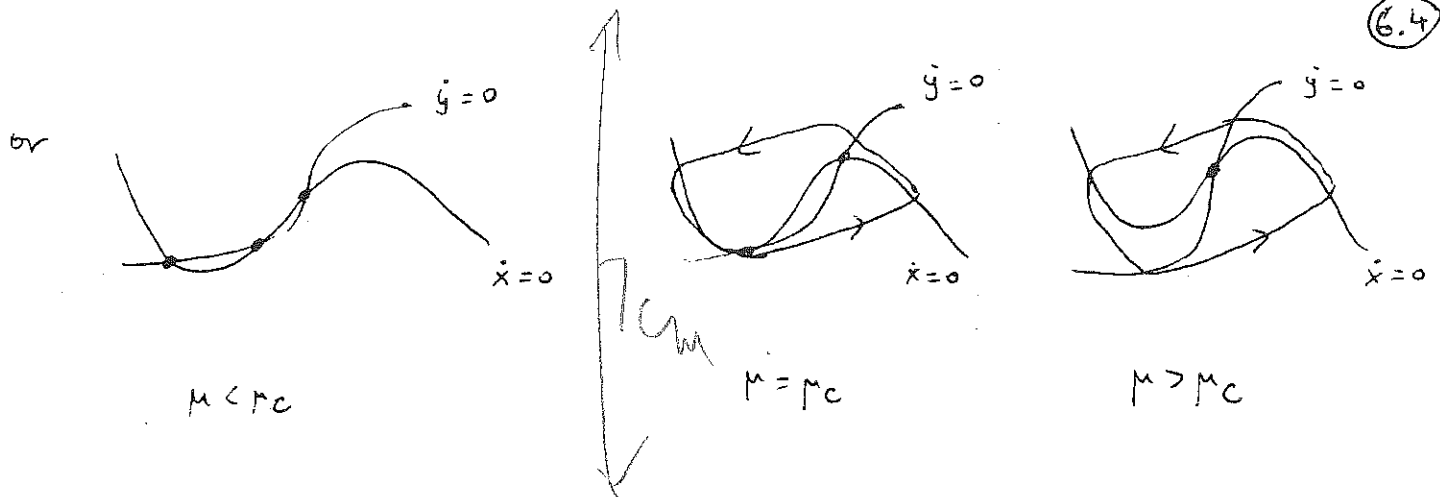
$$\mu < \mu_c$$



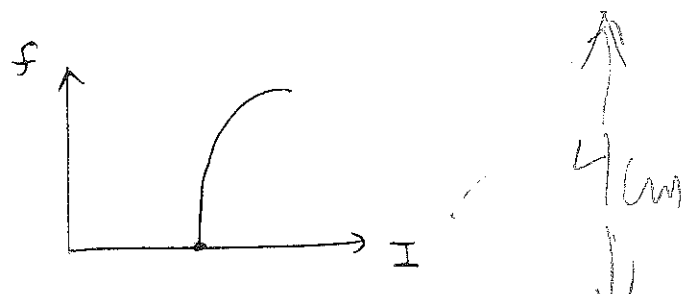
$$\mu = \mu_c$$



$$\mu > \mu_c$$



Note: this may be an explanation of the zero firing rate phenomenon in some neurons



Note: for higher dimensional systems, much more complicated bifurcations and dynamic behaviors (e.g. chaos) can occur.

References

- (1) L. Edelstein-Keshet, Random House 1988
« Mathematical Models in biology »
- (2) L. Glass & MC Mackay, Princeton Univ Press 1988
« From Clocks to Chaos: the rhythms of life »
- (3) M Hirsch & S Smale, Academic 1974
« Differential equations, dynamical systems & linear algebra »
- (4) J Guckenheimer & P Holmes, Springer 1983
« Nonlinear oscillations, dynamical systems & bifurcations of vector fields ».

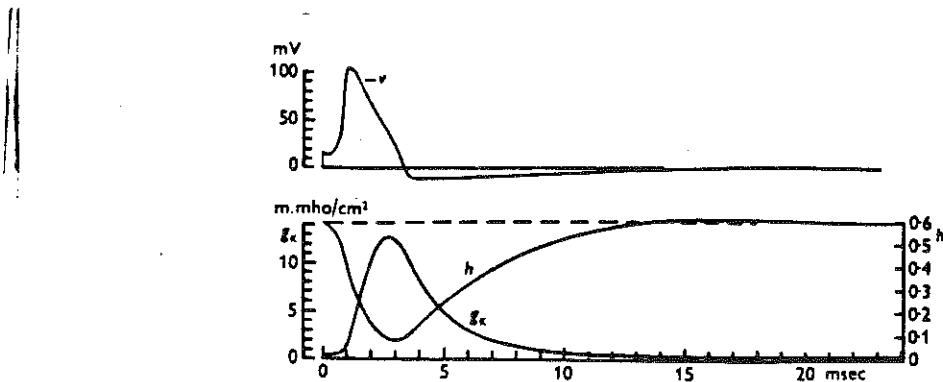


Fig. 19. Numerical solution of eqn. (26) for initial depolarization of 15 mV and temperature of 6° C. Upper curve: membrane potential, as in Fig. 13. Lower curves show time course of g_K and A during action potential and refractory period.

fig. 6. 1

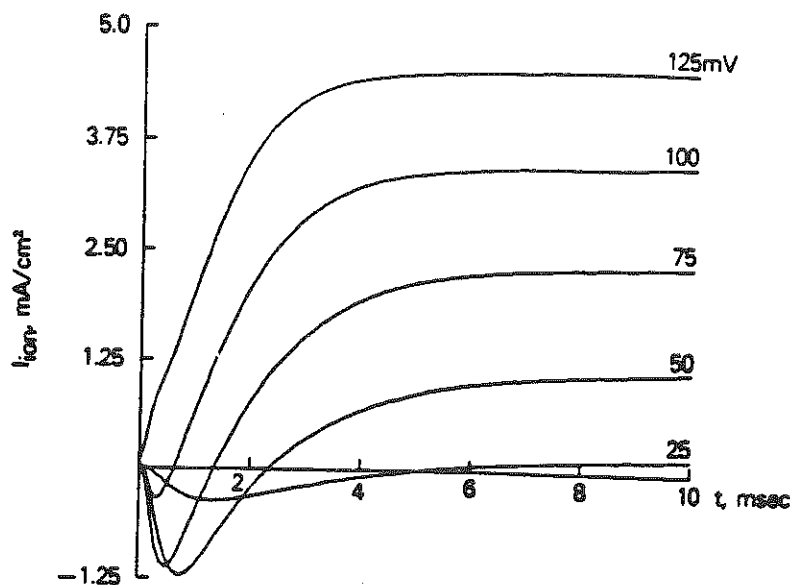


FIG. 2. Theoretical curves of voltage and space-clamped current, $I_{ss}(t; v)$ versus t , computed for the HH model. $I_{ss}(t; v)$ is evaluated, for constant v , from equations (4), (5), and the last three of (6).

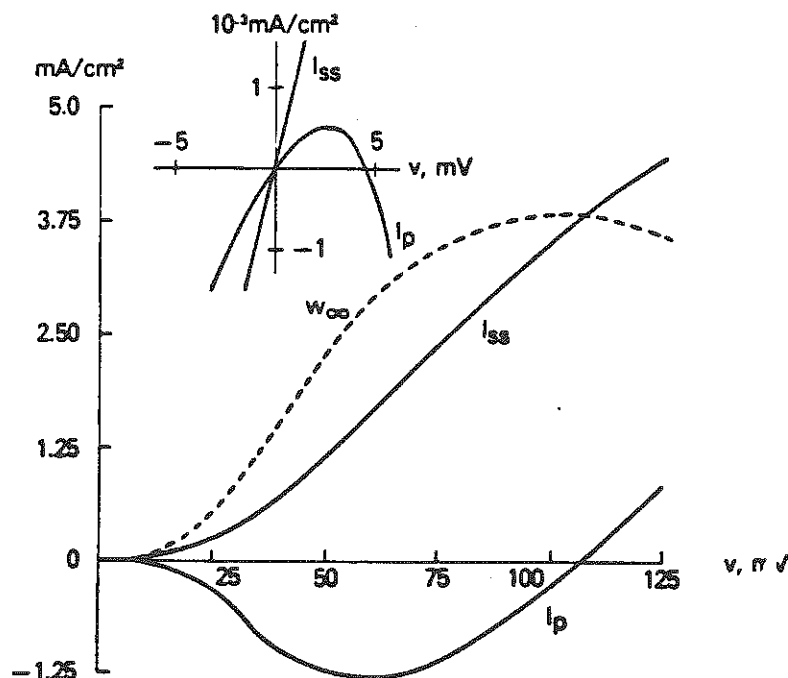


FIG. 5. Current-voltage curves from HH theoretical voltage clamp data (Fig. 2). Early transient peak current I_p and late steady state current I_{ss} are plotted versus clamp potential v . Upper inset expands region near the origin.

fig. 6. 2

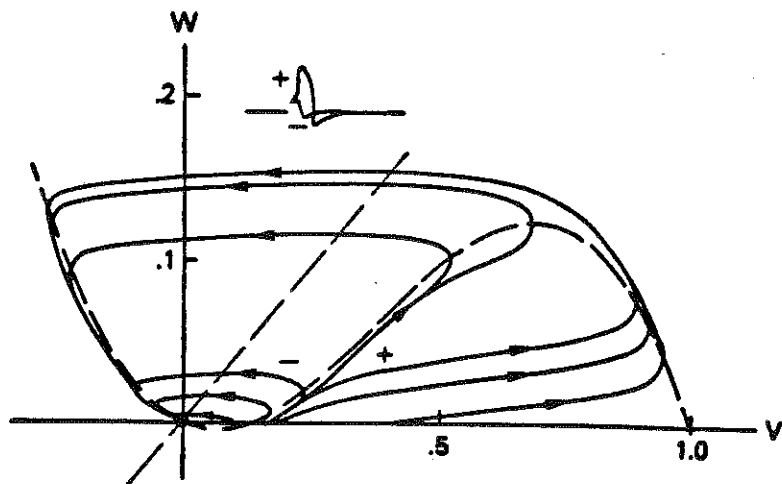


FIG. 7. Phase plane trajectories of space-clamped FHN equation (12) for an instantaneous current pulse (at $t = 0$) of various amplitudes. Each trajectory originates on the o -axis. Inset shows voltage waveforms, v versus t , for supra (+) and sub (-) threshold stimuli; the corresponding phase plane trajectories are labeled \pm . Model parameters are $a \approx .14$, $b \approx .008$, $\gamma \approx 2.54$. (Redrawn from FitzHugh [29].)

fig.6.3

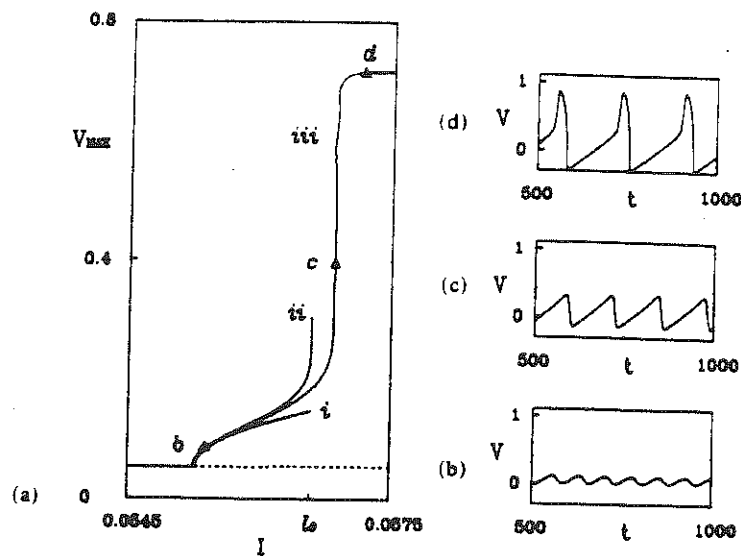


FIG. 4. (a) Comparison between the numerical branch of solutions and the asymptotic branch of solutions for a supercritical Hopf bifurcation of the FHN equations. The values of the parameters are $\epsilon = 0.008$, $\gamma = 1$ and $a = 0.1$. Solid and dashed curves represent stable and unstable solutions, respectively. (i) is an asymptotic approximation for small values of N , curve (ii) is an asymptotic approximation for all values of N and is obtained when (4.6) is computed numerically and curve (iii) is the numerical branch of solutions. The limit point is $I_0 = 0.05678$. The points b, c and d in Fig. 4a correspond to the periodic solutions given in Figs. 4b, c and d. They indicate the transition from small harmonic oscillations to large amplitude, relaxation oscillations. The values of the control parameter I corresponding to Figs. 4b, c and d are $I = 0.05527$, 0.05683 and 0.05740 , respectively.

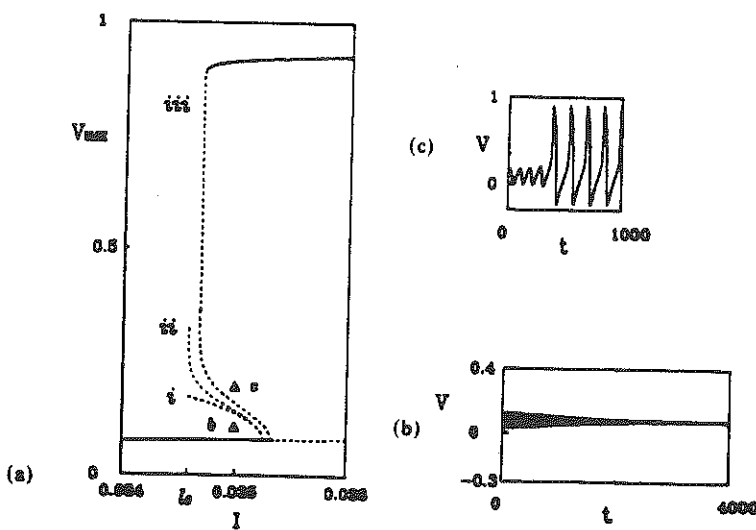


FIG. 5. Comparison between the numerical branch of solutions and the asymptotic branch of solutions for a subcritical Hopf bifurcation of the FHN equations. The values of the parameters are $\epsilon = 0.008$, $\gamma = 2.54$ and $a = 0.14$. Solid and dashed curves represent stable and unstable solutions, respectively. Curve (i) is an asymptotic approximation for small values of N , curve (ii) is an asymptotic approximation for all values of N when (4.6) is computed numerically and curve (iii) is the numerical branch of solutions. The limit point is $I_0 = 0.03457$. The points b and c in Fig. 5a correspond to the initial voltage perturbations from the steady state when $I = 0.035$. They are given by: $v(0) = 0.1200$, $w(0) = 0.03053$ (point b) and $v(0) = 0.1285$, $w(0) = 0.03053$ (point c). The trajectories emerging from these initial conditions are shown in Figs. 5b and 5c.

fig. C. 4

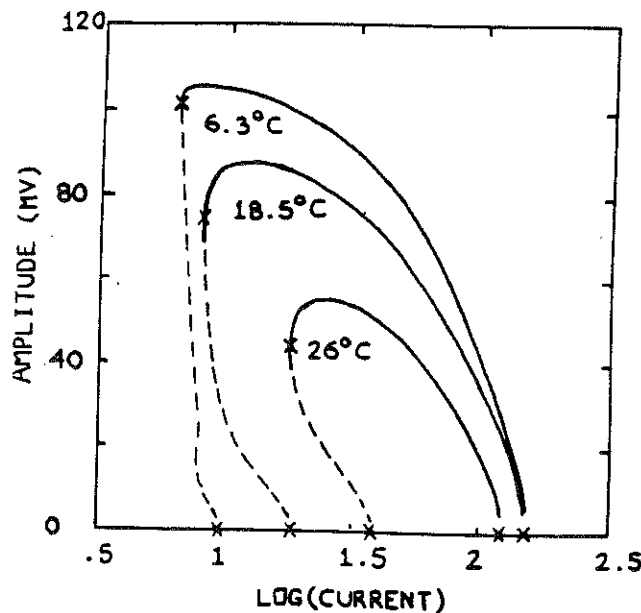


Fig. 2. Amplitude ($\max V - \min V$) of periodic solutions to HH equations as functions of applied current for three temperatures. Dashed portions correspond to unstable limit cycles. Points of Hopf bifurcation and knees on amplitude curves for neutrally stable limit cycles are indicated by X (from Rinzel and Miller [1980]).

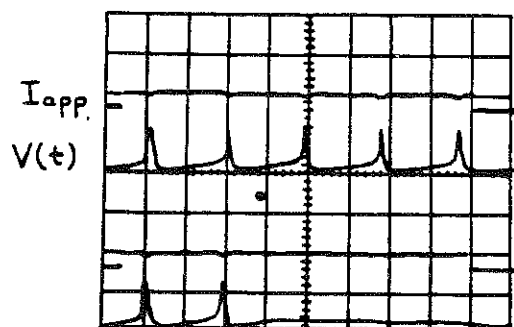


Fig. 3. Annihilation of repetitive firing of space-clamped squid axon membrane by a depolarizing shock. Upper two traces are control run without the shock (from Guttman et al [1980]).

fig. 6.5

Lecture 7: action potential propagation

Consider an active cable of diameter d .

$$\frac{d}{4R_i} \frac{\partial^2 V}{\partial x^2} = C_m \frac{\partial V}{\partial t} + I_{ion}, \quad I_{ion} = I_{Na} + I_K + I_L \quad (\text{HH 1952})$$

Constant velocity $\rightarrow z = x - ct \quad V(x, t) = V(z)$

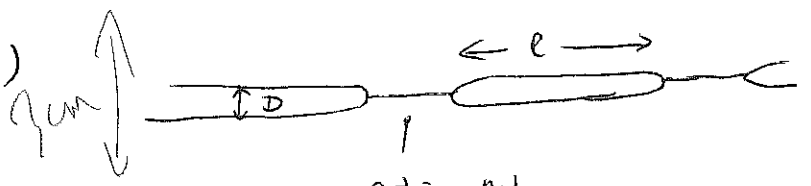
$$\rightarrow \frac{d}{4R_i} \frac{\partial^2 V}{\partial z^2} = -C_m c \frac{dV}{dz} + I_{ion} \quad \text{or} \quad \frac{d}{4R_i c^2} \frac{\partial^2 V}{\partial t^2} = C_m \frac{dV}{dt} + I_{ion}$$

at a cable point

If similar action potential form for $\neq d$

$$\rightarrow C \propto \sqrt{d/R_i} \quad (\text{unmyelinated axon})$$

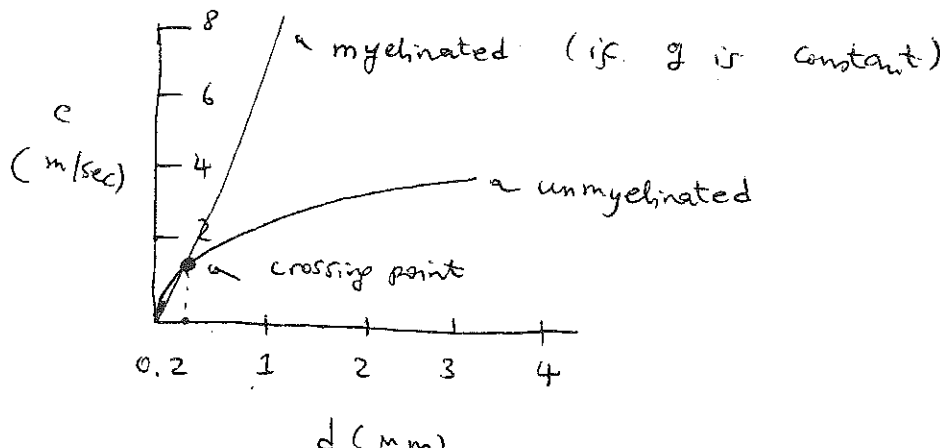
for myelinated axon (fig. 1)



$$C \propto d g \sqrt{l \cdot \ln g} \quad g = \frac{d}{D}$$

(fig. 2)

Cf. Jack - Noble - Tsien.



$\propto C$



How to compute a traveling wave solution and its stability? A rigorous treatment of this topic is not possible here. We shall instead discuss heuristically the general approach, based on the work by McKean, Rinzel and Keller.

Consider the FHN model of action potential:

$$\begin{cases} \frac{\partial v}{\partial t} = \frac{\partial^2 v}{\partial x^2} - f(v) - w & f(v) = v(v-a)(v-1) \\ \frac{\partial w}{\partial t} = \varepsilon(v - \delta w), & \text{if } \delta=0 \rightarrow \varepsilon \int_0^t v_t dt' = w(t) \end{cases}$$

The simplest case, when $\varepsilon=0$, corresponds to the absence of a refractory variable ($w=0$). It is not realistic and in fact without w no stable traveling wave solution is possible. However, it helps us to develop intuitions for such problems.

Looking for $v(x,t) = v(z)$ $z = x + ct$

$$\rightarrow [v'' - f(v) - cv' = 0] \quad \text{2d ODEs.}$$

let $v' = u$ $\begin{cases} v' = u \\ u' = f(v) + cu \end{cases}$ $\underline{\nabla F = +c > 0}$

f.p. $(0,0)$ $(a,0)$ $(1,0)$

Stability: $(0,0)$ and $(1,0)$ are saddle points

$$(a,0) \text{ is a } \begin{cases} \text{unstable node if } c \geq 2\sqrt{a(1-a)} \\ \text{unstable focus if } c < 2\sqrt{a(1-a)} \\ \text{center if } c=0. \end{cases}$$

- zero velocity $c=0$ (fig. 3)

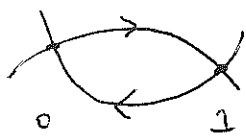
$$\alpha < \frac{1}{2}$$



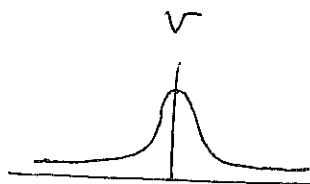
homoclinic orbit

$$\sqrt{2\alpha/\alpha}$$

$$\alpha = \frac{1}{2}$$

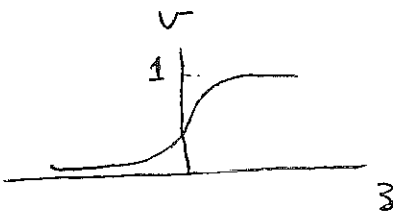


heteroclinic orbit



• Solitary "wave"

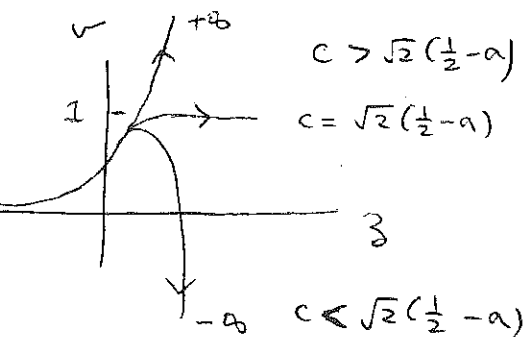
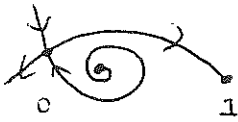
$$V(z) = \frac{3}{\sqrt{(2-\alpha)(\frac{1}{2}-\alpha)} \cosh \sqrt{\alpha} x + (\frac{1}{\alpha} + 1)}$$



a "front"

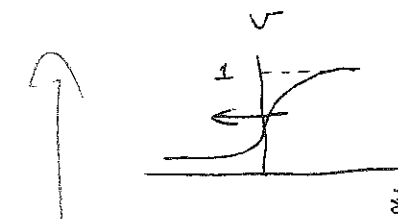
- finite velocity $c \neq 0$ (fig. 4)

$$c = \sqrt{2}(\frac{1}{2} - \alpha)$$



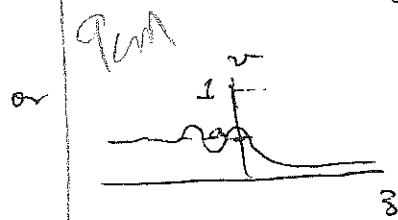
$$c = \sqrt{2}(\frac{1}{2} - \alpha)$$

$$c < \sqrt{2}(\frac{1}{2} - \alpha)$$



front wave
with finite
propagation speed

$$V(z) = \frac{1}{1 + e^{-z/\sqrt{2}}}$$



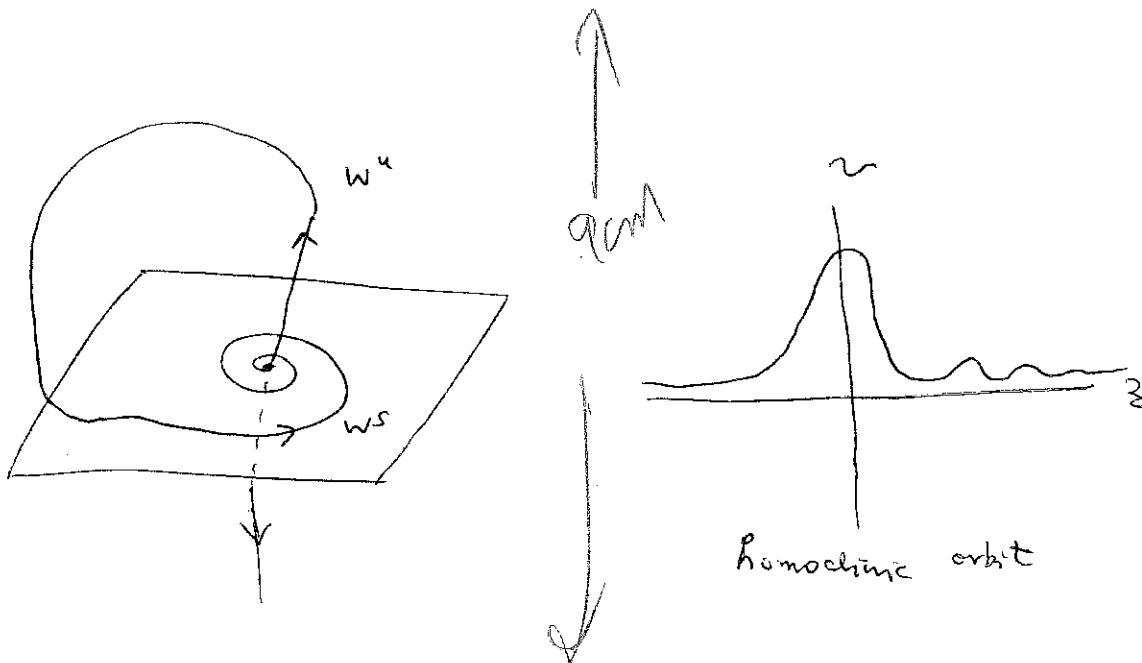
note: HH originally simulated their model on a computer, and calculated c by locating a solution which did not go to $\pm \infty$.

- Summary:
- a traveling wave solution can be studied as a homoclinic orbit of an ODE with independent variable ξ . Such an orbit exists only for particular values of c , hence c can be determined in this way.
 - without recovery variable w only a front solution is possible. (with finite c)

If $\varepsilon > 0$, the equation to be considered is

$$v''' - cv'' - f'(v)v' - \frac{b}{c}v = 0 \quad \text{3d ODE}$$

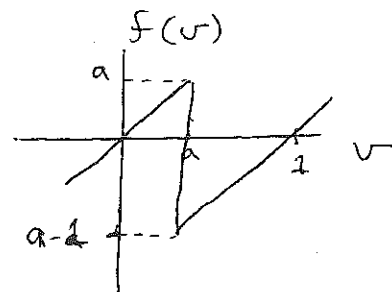
there is only one f.p. $(0, 0, 0)$.



Note: dynamics related to homoclinic orbits in multidimensional systems may be complex (\exists chaotic solutions, if the Shilnikov condition is fulfilled. And there may be a countably many solitary wave solutions with multiple pulses).

In order to be able to calculate analytic solutions, McKean introduced a piecewise linearization of the FHN model.

$$f(v) = -\Theta(v-a) + v$$



$$\rightarrow \boxed{v''' - cv'' - \alpha v' - \frac{b}{c} v = 0}$$

linear equation, except at $v=a$

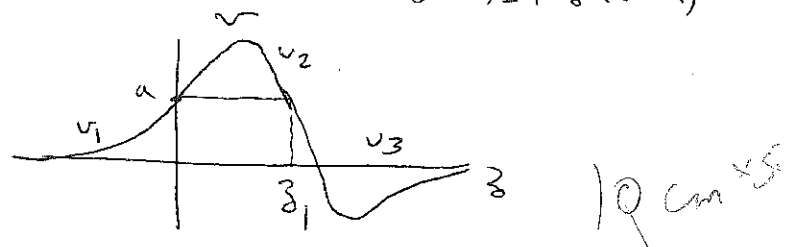
$$f'(v) = 1 - \delta(v-a)$$

$$v''(0^+) - v''(0^-) = -1$$

$$v''(\bar{z}_1^+) - v''(\bar{z}_1^-) = 1$$

$$v(z) \rightarrow 0$$

$$(z) \rightarrow 0$$



$$v(z) = \frac{b}{c} \int_{-\infty}^z v(z') dz' \xrightarrow[z \rightarrow +\infty]{} 0 \quad \rightarrow \int_{-\infty}^{\infty} v(z) dz = 0$$

Solution $v = \sum_{i=1}^3 a_i e^{\alpha_i z} \rightarrow p(\alpha) = \alpha^3 - c\alpha^2 - \alpha - \frac{b}{c} \quad \alpha = \infty$

$$\rightarrow \alpha_1 > 0 \quad \alpha_2, \alpha_3 < 0 \quad \text{or} \quad \alpha_2 = \bar{\alpha}_3 \quad \text{Re } \alpha_2, \alpha_3 < 0$$

$$v_1 = a_1 e^{\alpha_1 z} \quad v_2 = \sum_{i=1}^3 a_i e^{\alpha_i z} \quad v_3 = \sum_{i=2}^3 b_i e^{\alpha_i z}$$

unknowns: $a_1, a_2, a_3, b_2, b_3, z_1, c$.

Conditions: $v_2(0) = a_1, v_2(z_1) = a_2, v_3(z_1) = a_3, v_1'(0) = v_2'(0);$

$$v_2'(z_1) = v_3'(z_1); \quad v_2''(0) = v_2''(0) = -1; \quad v_3''(z_1) = v_2''(z_1) = 1$$

solutions (fig. 5): for each value of a , there are two solutions with different c . (artifact: $c \rightarrow \infty$ is due to linearization)

fig. 6: solution a as function of b . Recall that b is related to the temperature and fig. 6 may be compared with Huxley's computation from the HH model.

stability analysis (Evans): let $x = z - ct$, $v(x,t) = v(z-ct, t)$

$$\Rightarrow \begin{cases} v_t = v_{zz} - cv_z - f(v) - w \\ w_t = bw - cw_z \end{cases}$$

(v_c, w_c) a t -indep. solution. Let $v = v_c(z) + \delta v(z, t)$

$$w = w_c(z) + \delta w(z, t)$$

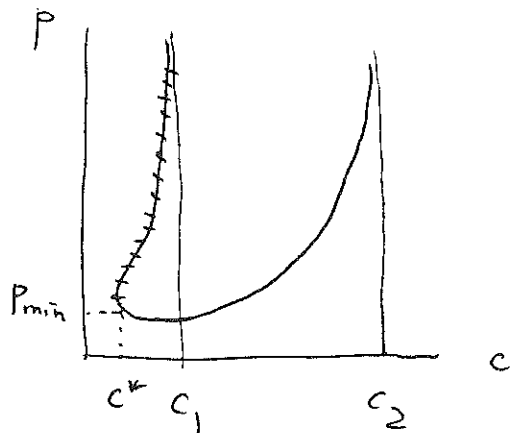
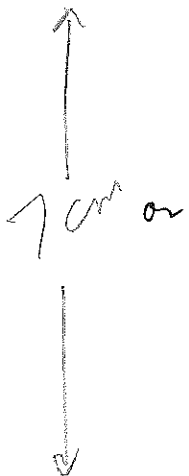
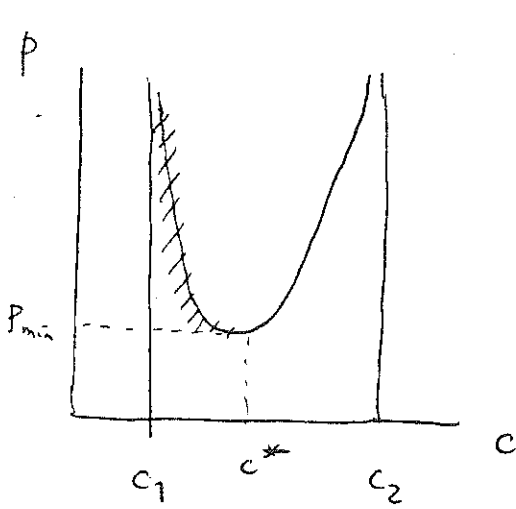
$$\Rightarrow \frac{d}{dz} \begin{pmatrix} \tilde{v} \\ \tilde{w} \end{pmatrix} = M(c, \lambda) \begin{pmatrix} \tilde{v} \\ \tilde{w} \end{pmatrix} \quad \text{then for } u = w \quad e^{\lambda t} \tilde{w}(z)$$

(v_c, w_c) is unstable if this equation admits bounded solution for (\tilde{v}, \tilde{w}) with $\operatorname{Re} \lambda > 0$.

Conclusion: the solution branch with smaller velocity of the (c, a) curve is unstable.

Note: For periodic wave trains, similar approach applies

with $\beta = kx + \omega t$. firing frequency = $\frac{c}{P}$ — velocity
— period in β .



(See fig. 7)

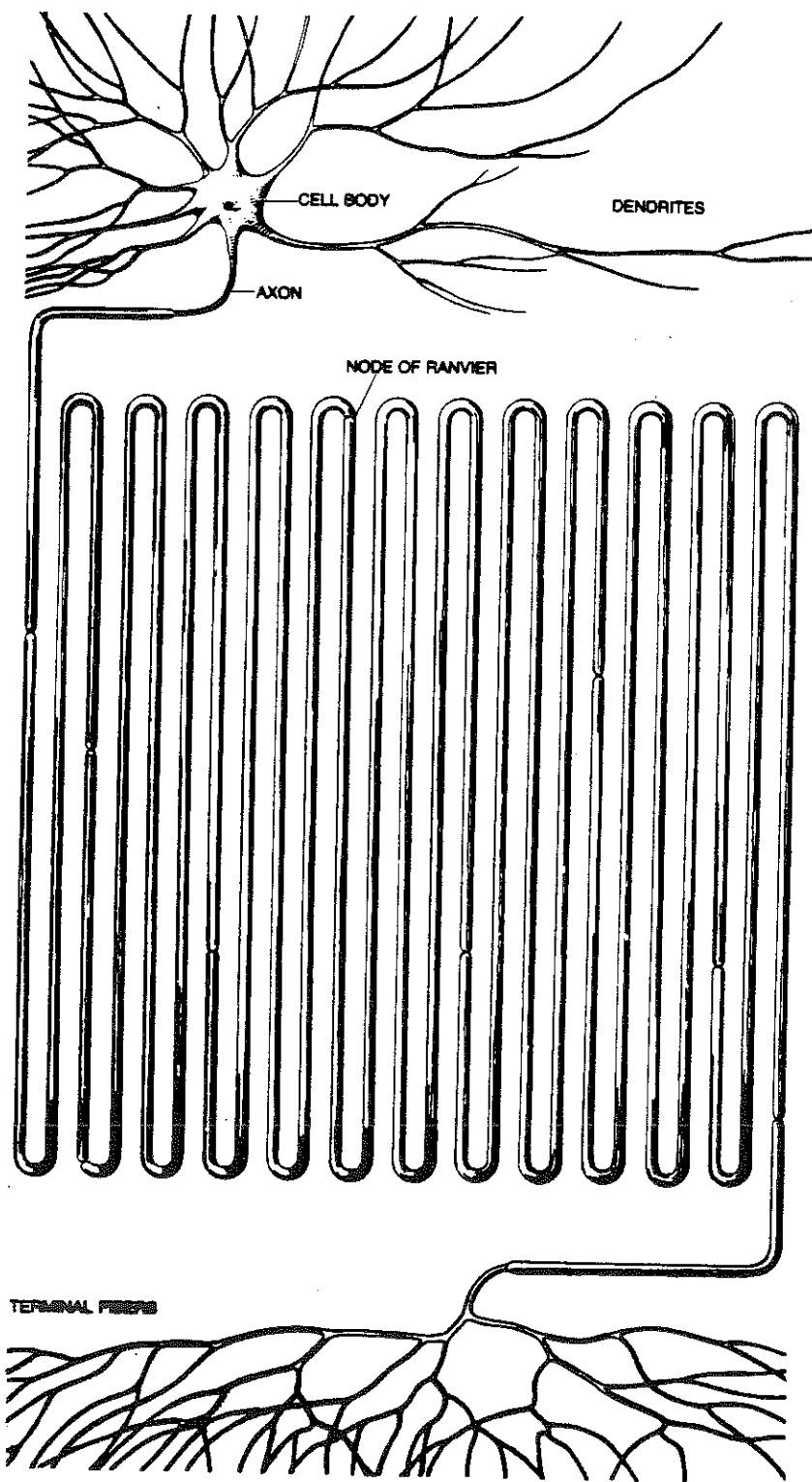


Figure 3 TYPICAL NEURON of a vertebrate animal (enlarged here 225 times) can carry nerve impulses for a considerable distance. The nerve impulses originate in the cell body and are propagated along the axon. This axon, folded for the diagram, would be a centimeter long at actual size, although some axons are more than a meter long. Many axons are insulated by a myelin sheath interrupted at intervals by the regions known as nodes of Ranvier.

Fig. 7.1

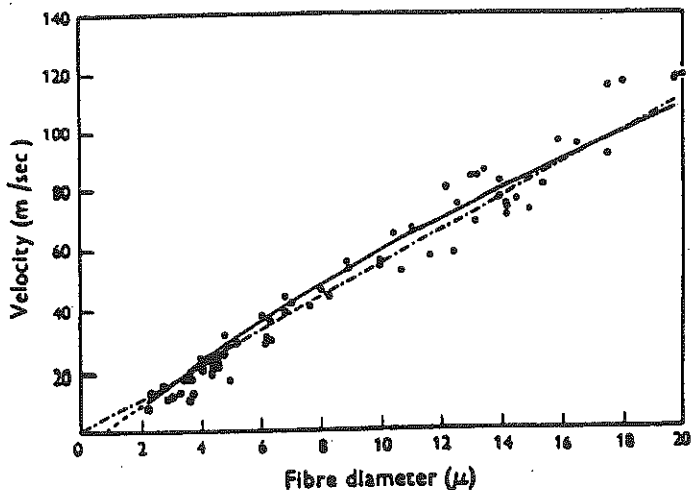


Fig. 2. Predicted relations between conduction velocity and fiber diameter for myelinated axons, modified from Rushton's (1951) Fig. 3. Open and closed circles represent Hursh's (1939) observations on conduction velocity of fibers from kittens and cats respectively. Rushton's relation computed using Sanders' measurements of g (the ratio of axon diameter to overall fiber diameter) is indicated by the solid curve with dashed extrapolation for small diameters. The linear relation based on the assumption of constant g is indicated by the broken line; its slope is $5.5 \text{ msec}^{-1} \mu\text{m}^{-1}$. From Waxman and Bennett, 1972.

Fig. 7. 2

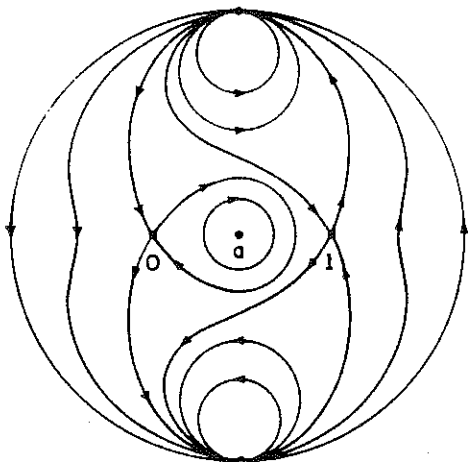
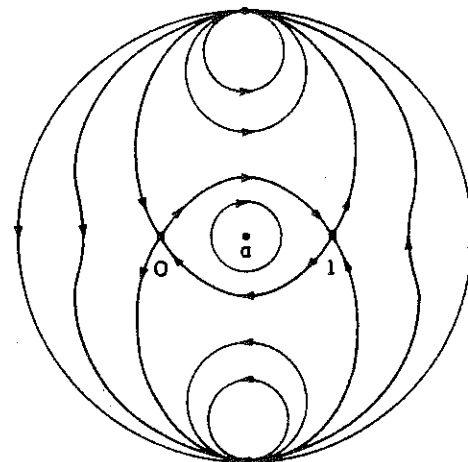
FIG. 6. $0 < a < \frac{1}{2}, b = 0, c = 0$ FIG. 7. $a = \frac{1}{2}, b = 0, c = 0$

fig. 7.3

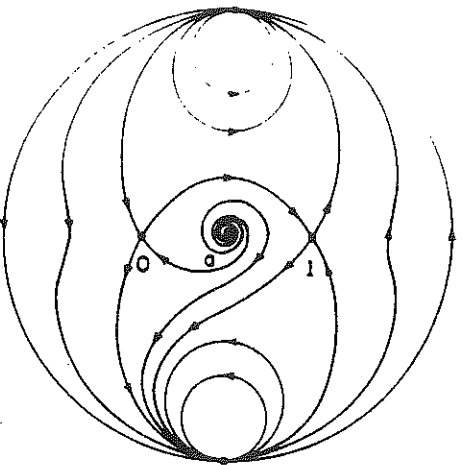


FIG. 8. $0 < a < \frac{1}{2}$, $b = 0$, $c = \sqrt{2}(\frac{1}{2} - a)$

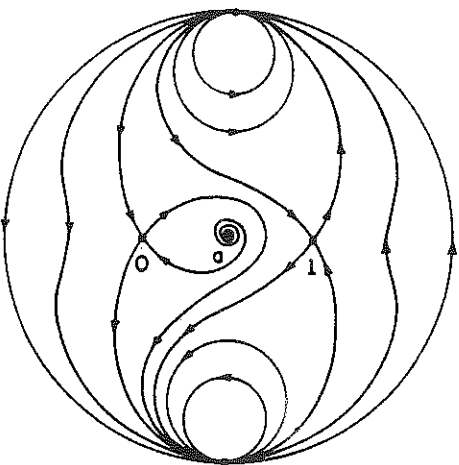


FIG. 9. $0 < a < \frac{1}{2}$, $b = 0$, $0 < c < \sqrt{2}(\frac{1}{2} - a)$

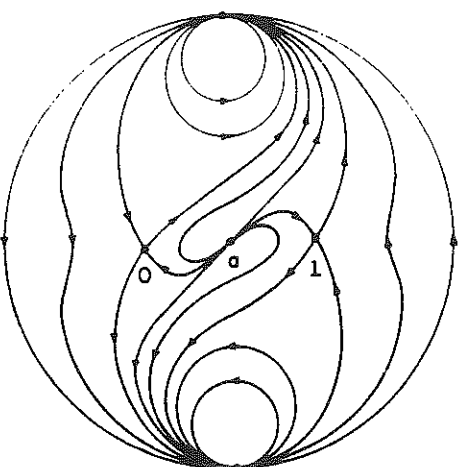


FIG. 10. $0 < a < \frac{1}{2}$, $b = 0$, $c > \sqrt{2}(\frac{1}{2} - a)$

fig. 7.4

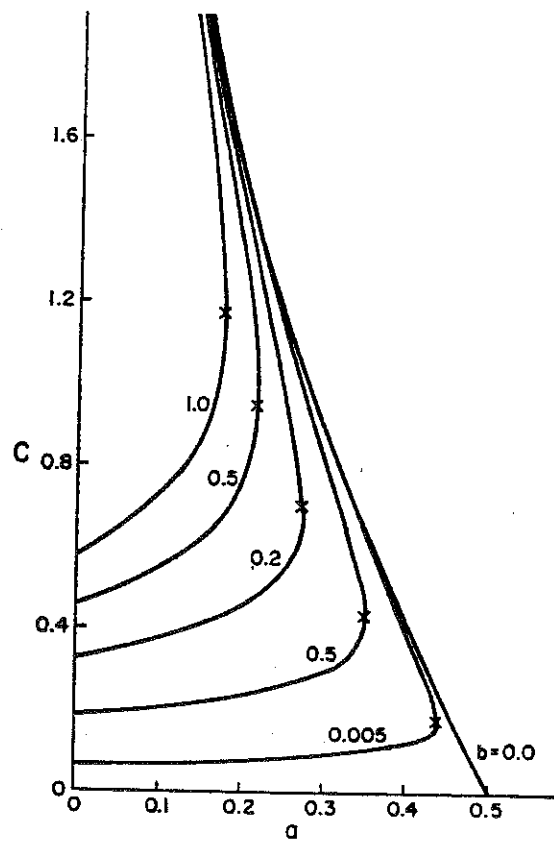
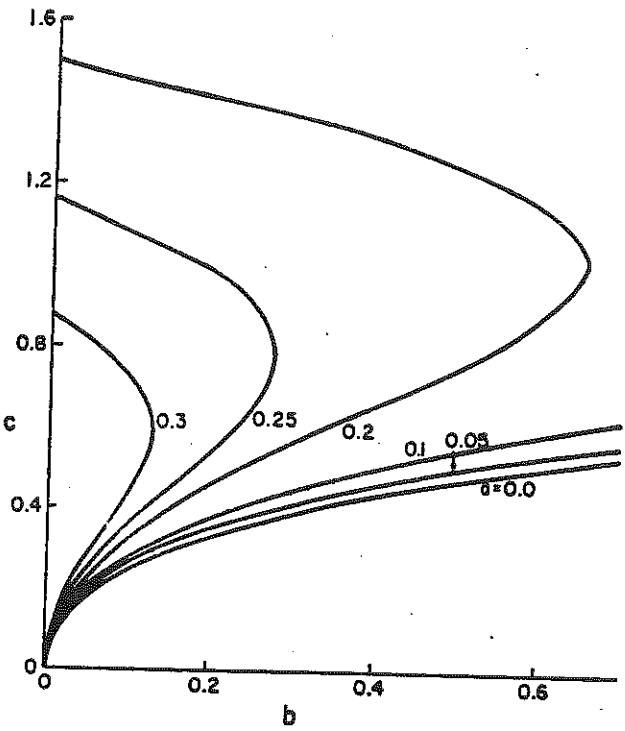


FIGURE 2 Propagation speed $c(a, b)$ of a pulse as a function of a for various positive values of b , determined numerically from Eqs. 13 and 14. The point a_*, c_* , determined by Eq. 19 is indicated by x . As $a \rightarrow 0$, the upper branch $c_*(a, b) \rightarrow \infty$. For $b = 0$, C is the speed of a transition waveform and is given by Eq. 55.

$$\phi = \varepsilon$$

Fig. 7.5

(7.7)



$$b = \varepsilon$$

FIGURE 5 Propagation speed $c(a, b)$ of a pulse versus b for various values of a . Only portions of the double branched curves for $a = 0.05, 0.1$ can be shown with the limits of b and c chosen here. For $a = 0$, $c = c_{\max}(b)$ and is given by Eq. 17.

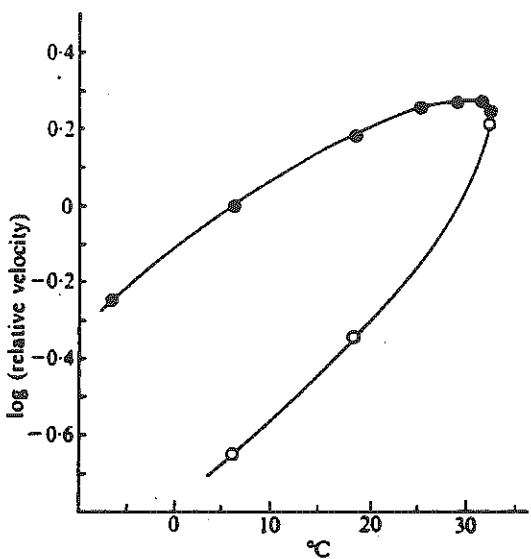


FIG. 10.5. Computed variation in conduction velocity with temperature. The filled circles are values for conduction velocity of the action potential expressed in terms of $\theta_1/\theta_{1,0}$, where $\theta_{1,0}$ is the conduction velocity (12.4 m s^{-1}) at 6.3°C . (From Huxley 1959a.) The open circles show values obtained by Huxley (1959b) for the conduction velocity of the sub-threshold wave.

fig. 7.6

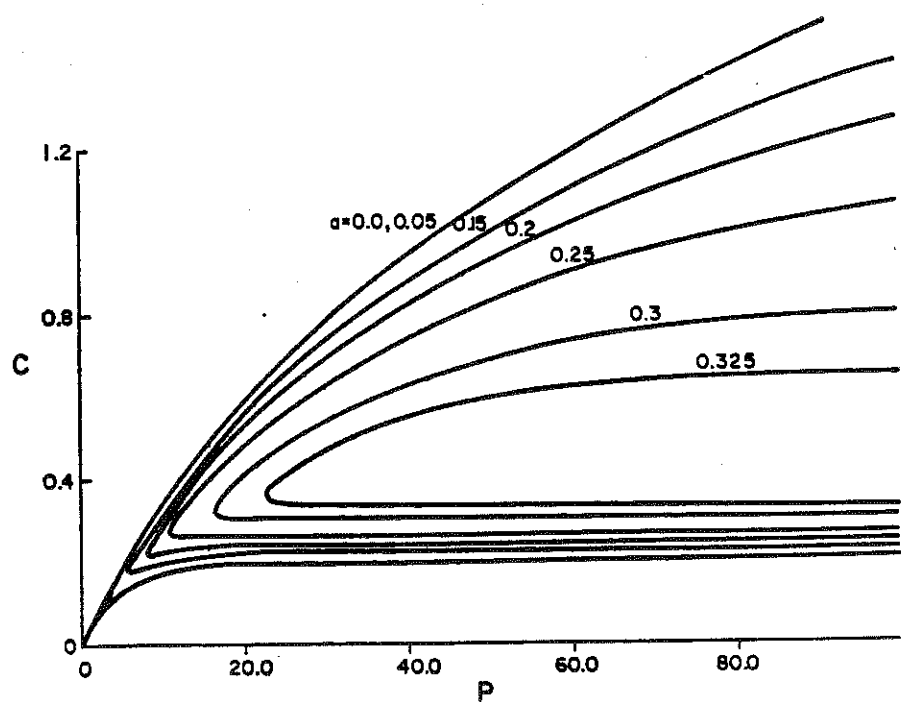


FIGURE 8 Propagation speed $c(a, b, P)$ of a periodic wave train as a function of its period P for $b = 0.05$ and various positive values of a , determined numerically from Eqs. 42 and 45-47. As $P \rightarrow \infty$, $c_f(a, b, P) \rightarrow c_f(a, b)$ and $c_s(a, b, P) \rightarrow c_s(a, b)$. For $a = 0$, $c_f(0, b, P)$ and $c_s(0, b, P)$ are determined numerically from E.2 and E.9 of Rinzel (16).

$$b = \epsilon$$

fig. 7.7

Lecture 8: Bursting

(1) Introduction

bursting is a common form of electrical activity involved in rhythmic dynamics.

example: - central pattern generators

e.g. Calabrese on leech heart (fig. 1)

or Getting on Tritonia (fig. 2)

- CNS

e.g. common bursting cells in neocortex (fig. 3)

epilepsy in hippocampus (fig. 4)

sleep waves & thalamus (fig. 5)

40 Hz in visual cortex (fig. 6)

In some cases the individual cells are endowed with ionic conductances so that isolated cells may be able to generate bursting oscillations.



not HH spiking but

at a slower time scale (100s)

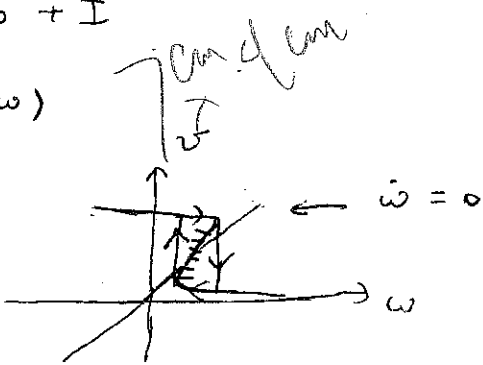
→ need to consider multi-dimensional system. Complex behaviors like chaos are possible.

key idea: separate disparate time scales.

example: FHN $\dot{v} = -f(v) - \omega + I$

$$\dot{\omega} = \epsilon(v - \delta\omega)$$

if $\epsilon = 0 \rightarrow \omega = \text{const}$



\exists bistability for the fast subsystem.

now if $\epsilon \neq 0$ but small \rightarrow consider slow shift of $\omega \rightarrow$ oscillation possible

This approach is applied to the study of bursting oscillations.

(2) Square-wave type bursting

If spikes are generated by $I_{Ca} + I_K$ instead of $I_{Na} + I_K$, then each spike induces an influx of Ca^{2+} into the cytosol. Now Ca^{2+} is a very special kind of ion and is involved in many 2nd messenger pathways and modulatory functions. Suppose that there is a

$$I_{KCa} = \bar{g}_{KCa} \frac{Ca}{B+Ca} (v - V_K) \rightarrow \text{an outward current slowly}$$

built up by spikes. Let the cell be described by

$$C \dot{v} = -\bar{g}_{Ca} m_\infty^3(v)(v - V_{Ca}) - \bar{g}_K n^4(v - V_K) - g_L(v - V_L)$$

$$- \bar{g}_{KCa} \frac{Ca}{B+Ca} (v - V_K) + I_{app}$$

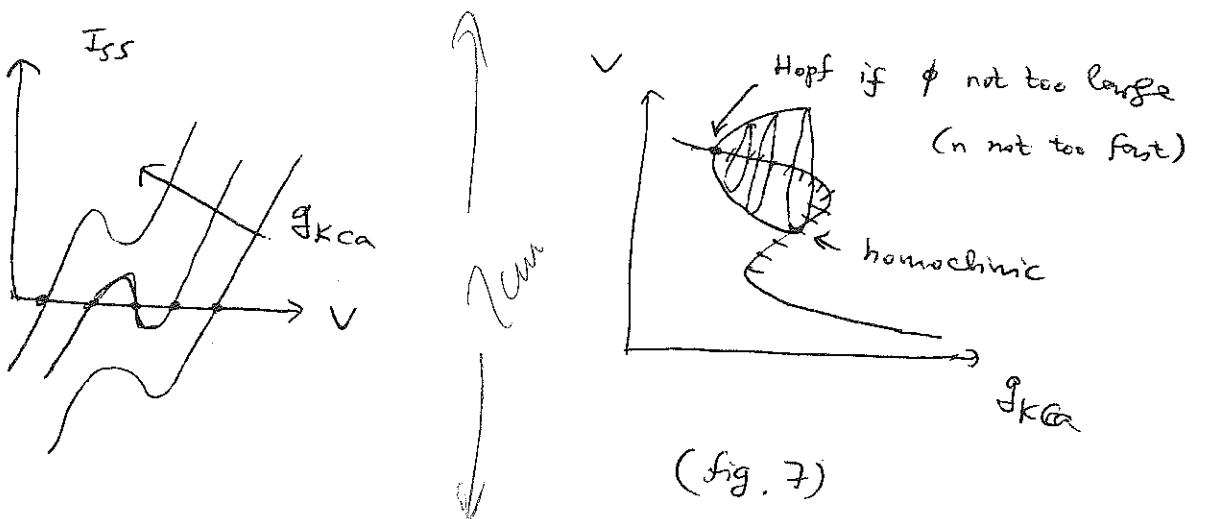
$$\dot{n} = \phi \frac{n_\infty(v) - n}{\tau_n(v)}$$

$$Ca = f \left[-\frac{\alpha}{A_d} I_{Ca}(v) - k_{Ca} Ca \right]$$

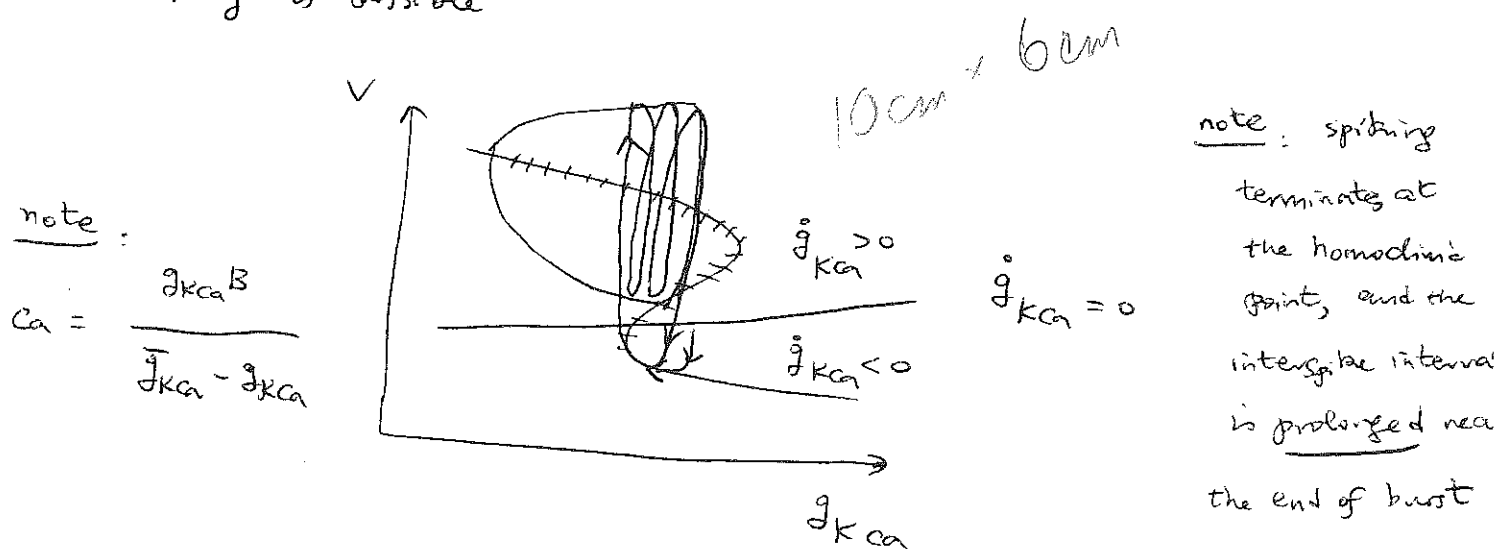
\downarrow conversion constant
 \downarrow thickness of a layer beneath the membrane

$$f \ll 1$$

$$f = 0 \rightarrow g_{KCa} = \text{const or parameter}$$



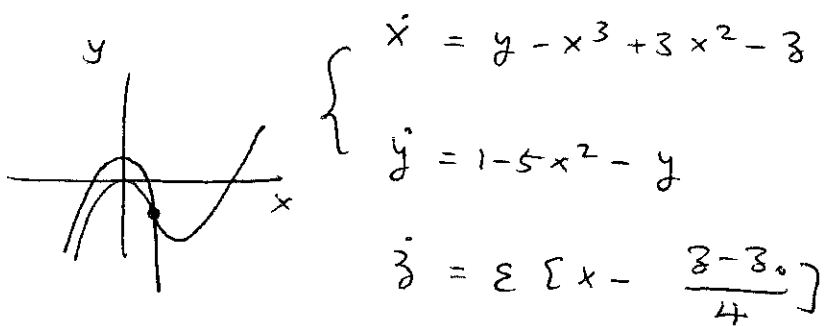
Now if $f < 1$ not zero. For appropriate K_{Ca} , the Ca -nullcline (hence g_{KCa} nullcline) may cross the s.s.-curve for the fast subsystem through the middle branch, below the homoclinic point.
 \rightarrow bursting is possible



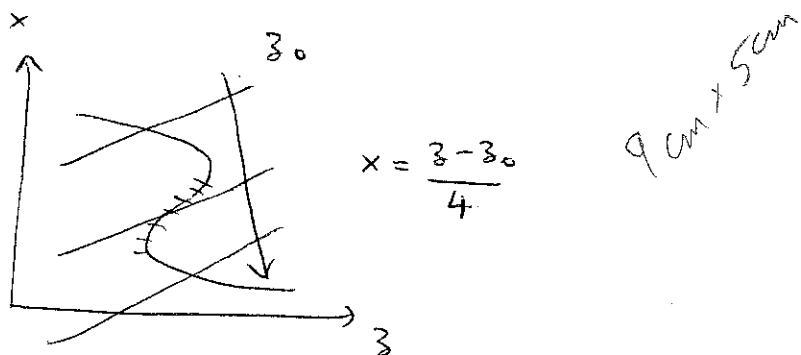
$$\frac{g_{KCa} B}{g_{KCa} - g_{KCa}}$$

note: With only one slow variable, bistability is required for the fast subsystem. Assuming g_{KCa} const. $\Rightarrow V = \bar{V} \equiv V_{ss}(g_{KCa})$ or $V = \bar{V}(g_{KCa}) = \frac{1}{T} \int_0^T v(t) dt$ for a limit cycle $\Rightarrow g_{KCa} = F(g_{KCa}, \bar{V})$ is an 1d system, hence cannot oscillate if \bar{V} is a unique function of g_{KCa} .

abstract model: Hindmarsh - Rose (Proc R Soc Lond B 221, 87 (1984))

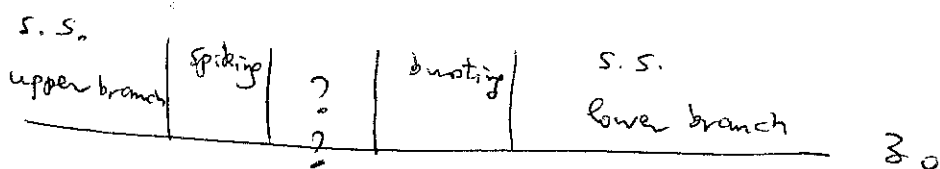


$$\varepsilon = 0 \rightarrow z = \text{const}$$



$$\varepsilon \ll 1$$

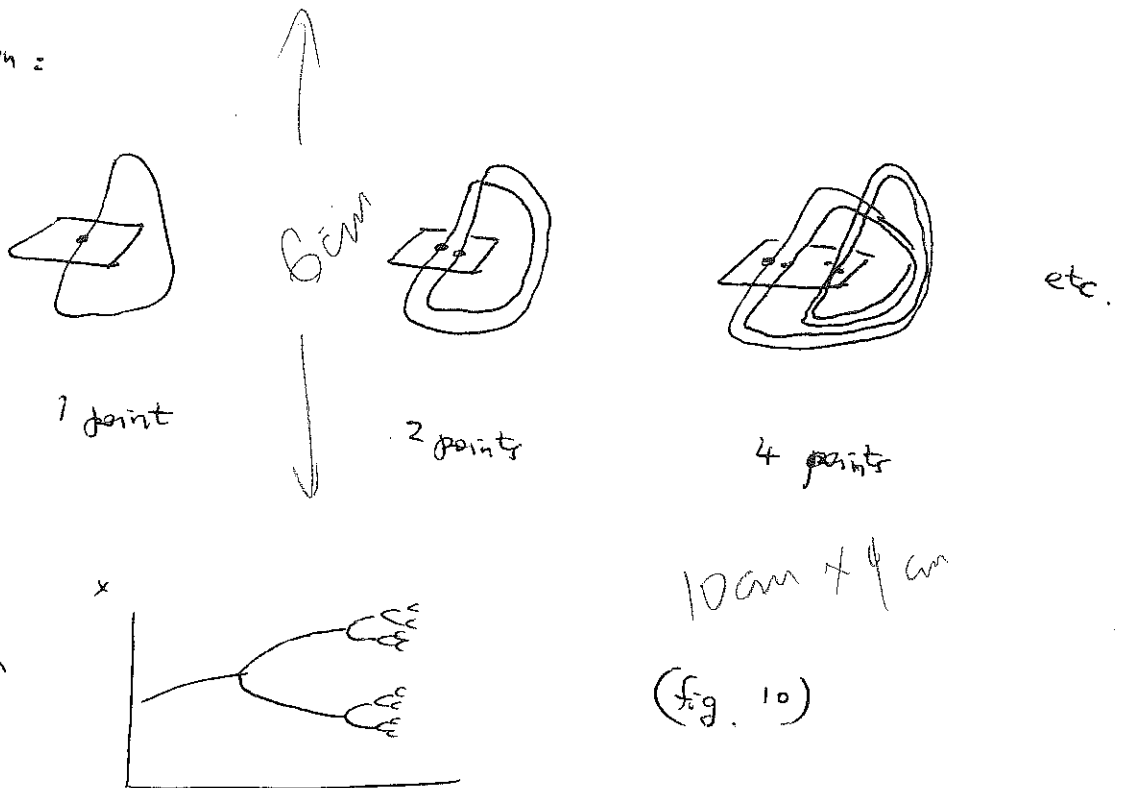
z_0 as parameter \rightarrow bursting (fig. 8)



Question: transition from spiking to bursting?

periodic doubling to chaos of the spiking state (fig. 9)

Poincaré section:



period doubling sequence of Feigenbaum

$$\frac{\mu_{n+1} - \mu_n}{\mu_n - \mu_{n-1}} \xrightarrow{n \rightarrow \infty} \boxed{\delta = 4.6692016091029909 \dots}$$

universal constant

or $(\mu_n - \mu_{n-1}) \sim \delta^{-n}$

fig. 10 Computed from a simple map

$$x_{n+1} = 4\mu x_n (1 - x_n) \quad (\text{originated from population dyna...})$$

chaos: - aperiodic

- sensitivity to initial conditions

$$|f^k x_0| = \prod_{k=0}^{n-1} |f'(f^k(x_0))| \quad |f^k x_0| \sim |f x_0| e^{\lambda n}, \quad \lambda > 0.$$

Bifurcation from spiking to bursting: the spiking state becomes chaotic which in turn is destabilized. Bursting is realized by homoclinicity to this unstable chaotic state.

cf. XJ Wang Physica D 62, 263 (1993)

(3) parabolic bursting. 2 - slow variables

e.g. Plant's model of R15 in Aplysia

$$C \dot{V} = -I_{Na} - I_K - I_{Ca} - I_{KCa} - I_L$$

q

$$\bar{g}_{Ca} \times (V - V_{Ca}) \quad \underline{x \text{ is slow}}$$

→ interplay of a slow inward current I_{Ca} and a slow outward current I_{KCa} generates slow oscillation which is independent of spikes. ¹ exists even if $\bar{g}_{Na} = 0$.

fig. 11 & fig. 12

$x, c_a \text{ const} \rightarrow$ fast subsystem bifurcation diagram. The slow subsystem can be obtained, by replacing V in the (x, c_a) equation by either its s.s. value or $\frac{1}{T} \int_0^T V(t) dt = \bar{V}$ for limit cycle.
 $\rightarrow V = V(x, c_a) \rightarrow \begin{cases} \dot{x} = (x_{ss}(v) - x)/\tau_x(v) \\ \dot{c}_a = f(-\frac{\alpha}{A_d} I_{Ca}(v) - k_{Ca} c_a) \end{cases} \quad v = V(x, c_a)$

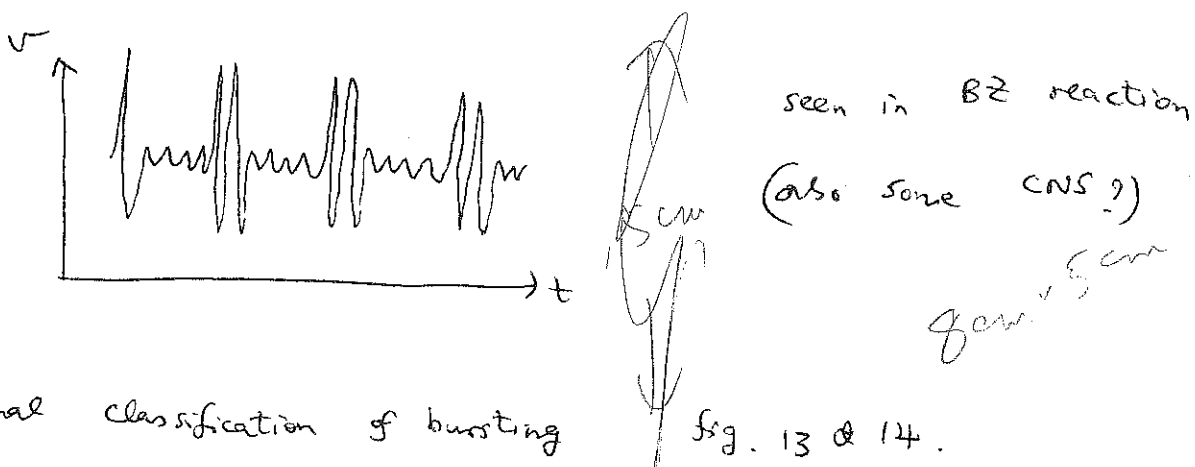
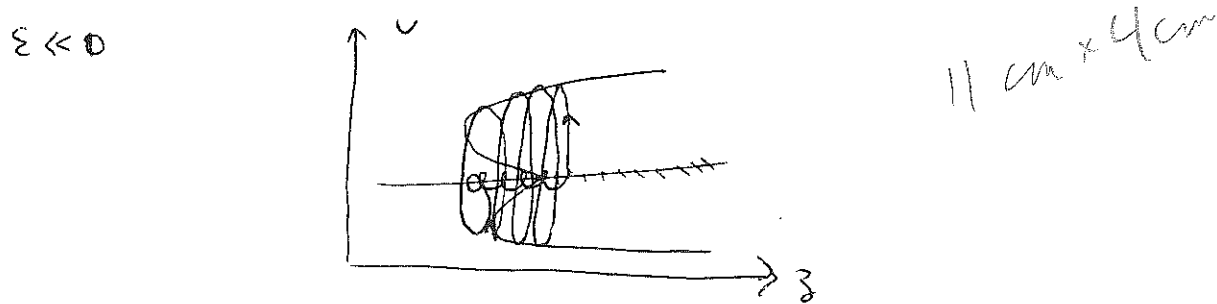
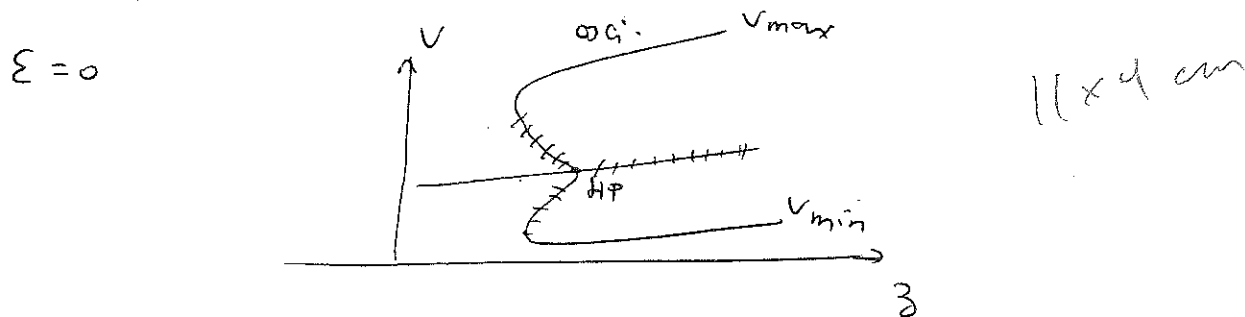
(4) mixed-mode bursting

FitzHugh-Rinzel

$$\dot{v} = -f(v) - w + \frac{z^2}{2} + I \quad f(v) = v^3/3 - v$$

$$\dot{w} = \phi(v + a - b w)$$

$$\dot{z} = \epsilon(-v + c - d z)$$



end.

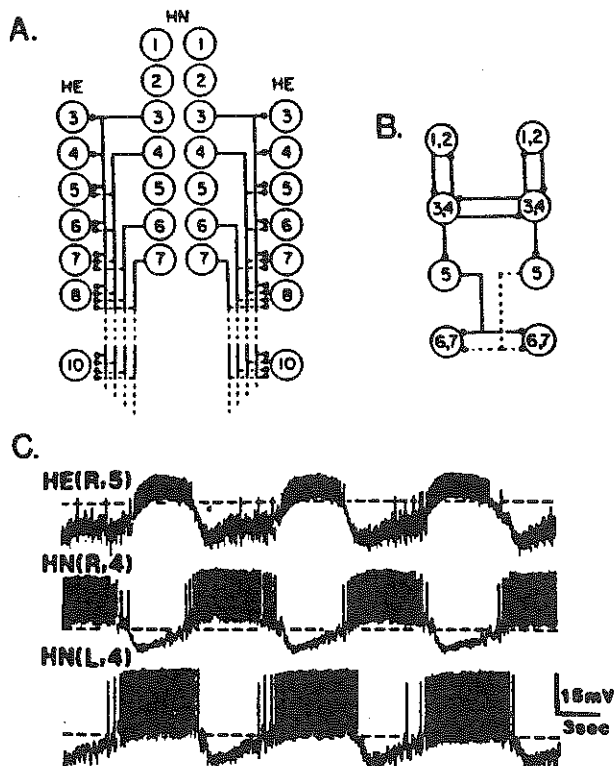


Fig. 1. Synaptic connectivity of heart (HE) motor neurons and heart (HN) interneurons. A: Circuit diagram showing the inhibitory synaptic connections from identified HN interneurons to HE motor neurons. B: Circuit diagram showing the inhibitory synaptic connections among all the identified HN interneurons. Neurons with identical input and output connections are lumped together. In circuit diagrams in this and the subsequent figure, large open circles represent neurons (each identified by the number of its ganglion) and lines represent major neurites or axons. Small, solid circles indicate inhibitory chemical synapses. C: Simultaneous intracellular recordings showing the normal rhythmic activity of two reciprocally inhibitory HN interneurons and an HE motor neuron postsynaptic to one of them in an isolated nerve cord. Dashed lines indicate a membrane potential of -50 mV. Heart interneurons are indexed by ganglion and body side from cell HN(L,1) to cell HN(R,7). Similar indexing applies to heart motor neurons. (Reproduced from Arbas and Calabrese, 1987a, with permission of the publisher.)

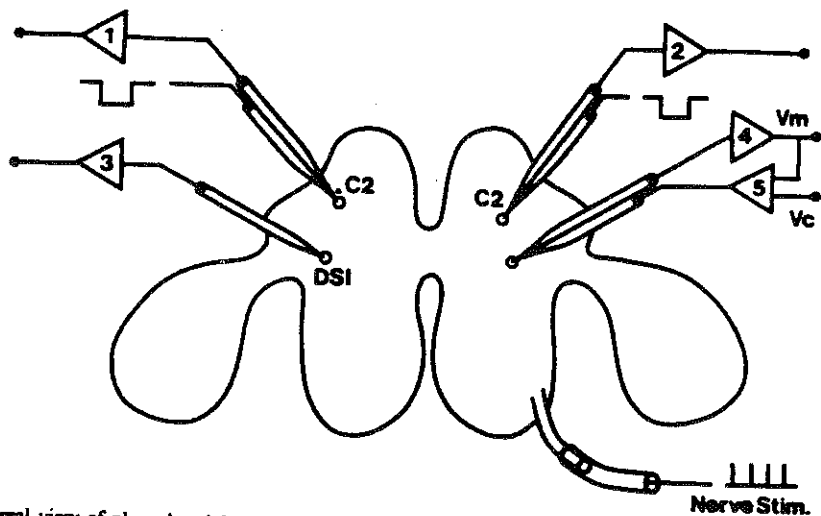


FIG. 1. Dorsal view of pleural-pedal-cerebral ganglion complex showing electrode placement for typical voltage clamp experiment. V_m , membrane potential; V_c , command voltage.

GATING OF PATTERN GENERATION

469

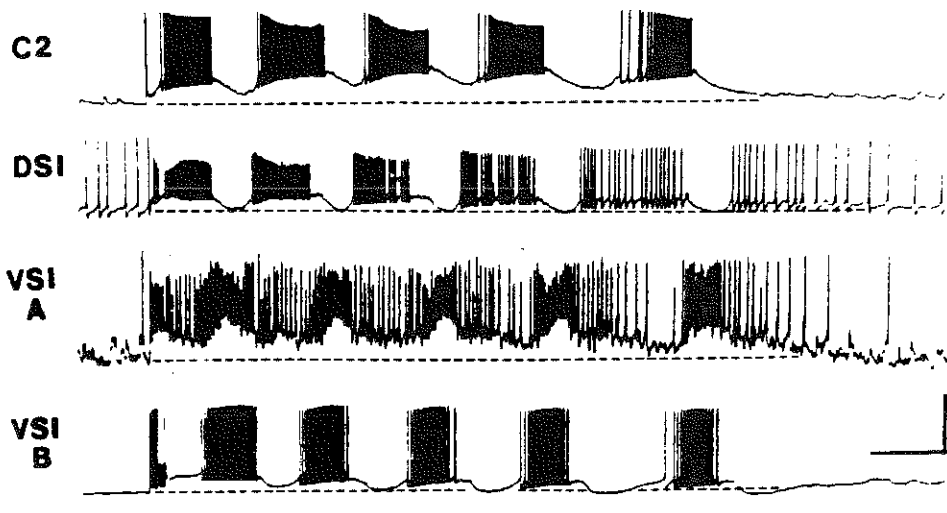


FIG. 2. Simultaneous intracellular recordings from cerebral cell 2 (C2), dorsal swim interneuron (DSI), and ventral swim interneurons (VSI-A and VSI-B) during swim activity initiated by electrical stimulation (bar below VSI-B trace). Dashed lines, resting potential. Calibrations: vertical, 50 mV for C2, DSI, and VSI-B; 25 mV for VSI-A; time scale, 5 s.

fig. 2

(8.6)

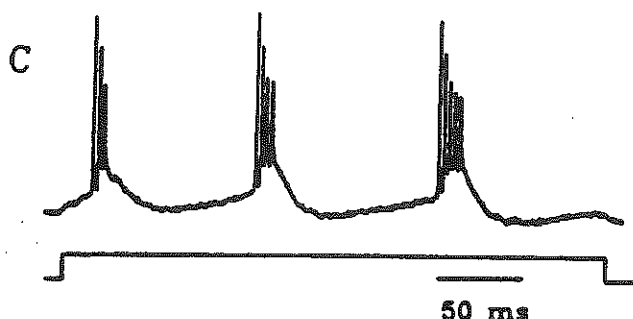
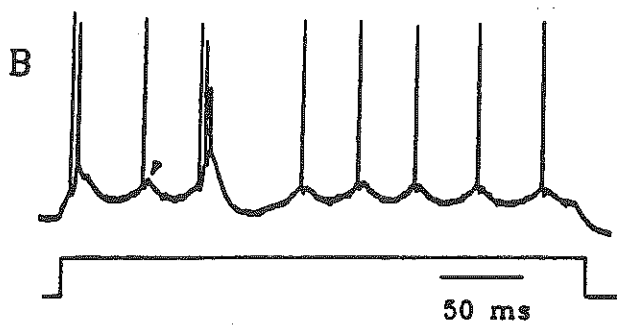
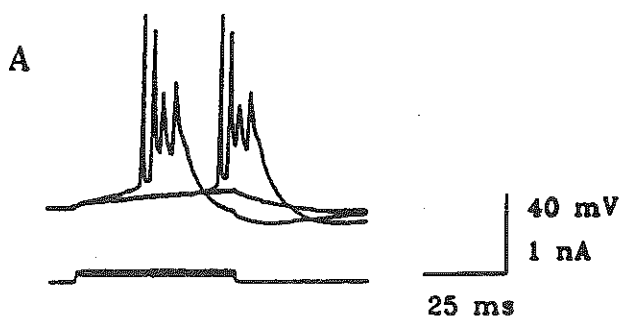
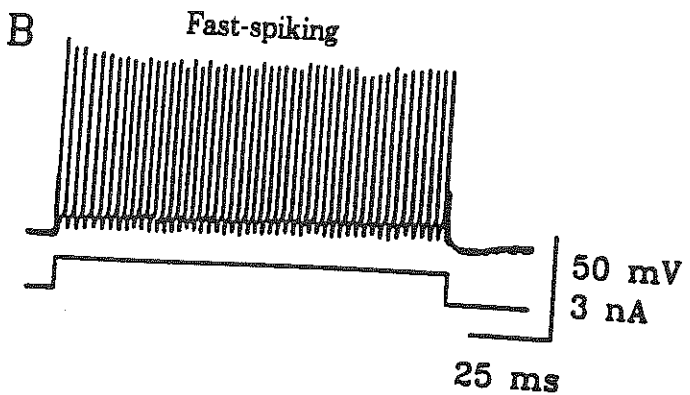
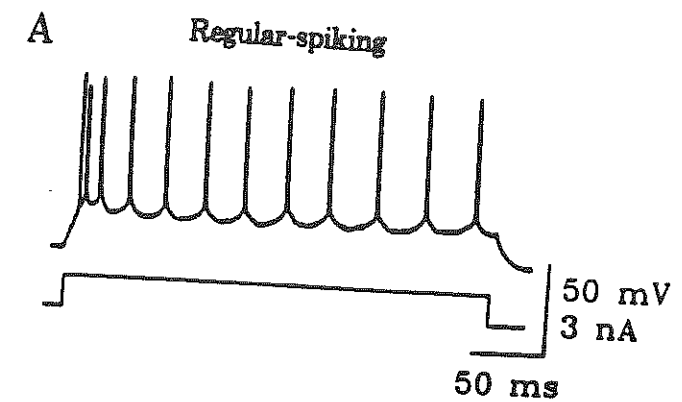


fig. 8.3

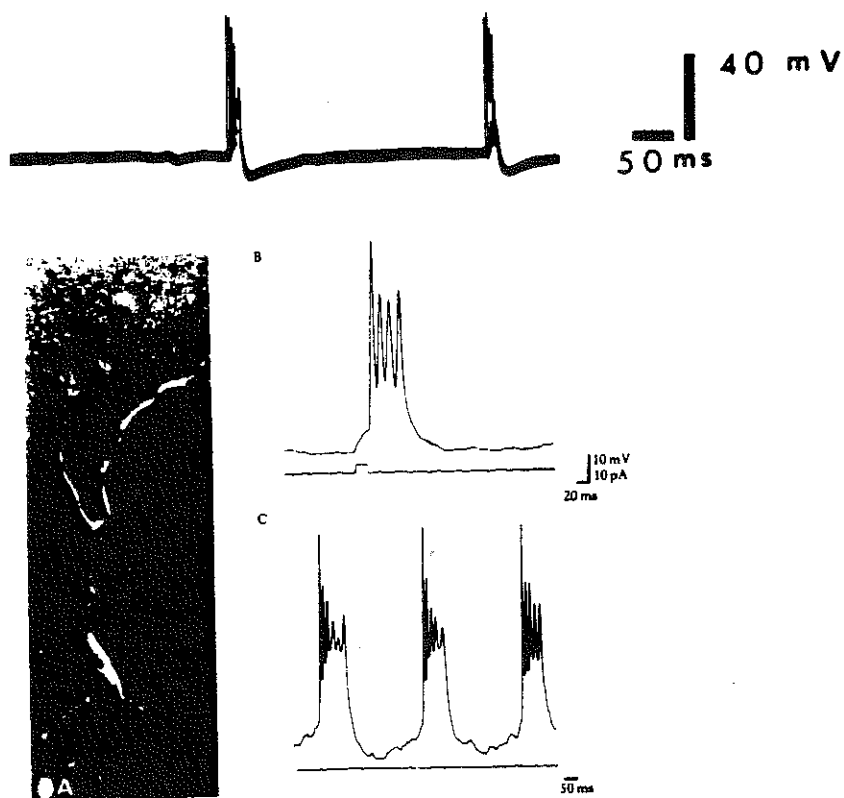


Figure 2.4. Intrinsic bursts in pyramidal cells in a slice (above) and in isolated pyramidal cells sheared of many of their dendrites (A-C). Note that the isolated cell can produce a burst after a brief current pulse (B), or it can produce a series of bursts during a sustained current injection (C), but Ca^{2+} spikes are not apparent. (Top from Wong and Prince, 1981; A-C from Wong, Traub, and Miles, 1986, with permission.)

fig. 2.4

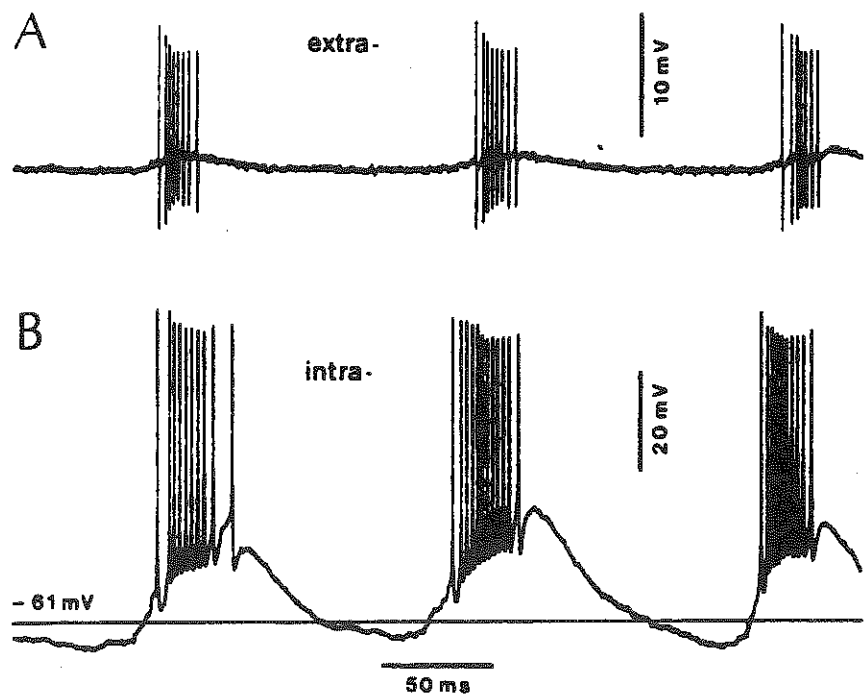


Figure 6.16. Episodes of rhythmic burst discharges recorded extracellularly (A) and then intracellularly (B) from the same RE neuron of a cat under barbiturate anesthesia. In A, positive is up. C: Spindle sequence of an RE neuron in a cat under barbiturate anesthesia. Membrane potential values refer to baseline levels. (Adapted from Mulle et al., 1986.)

fig. 8.5

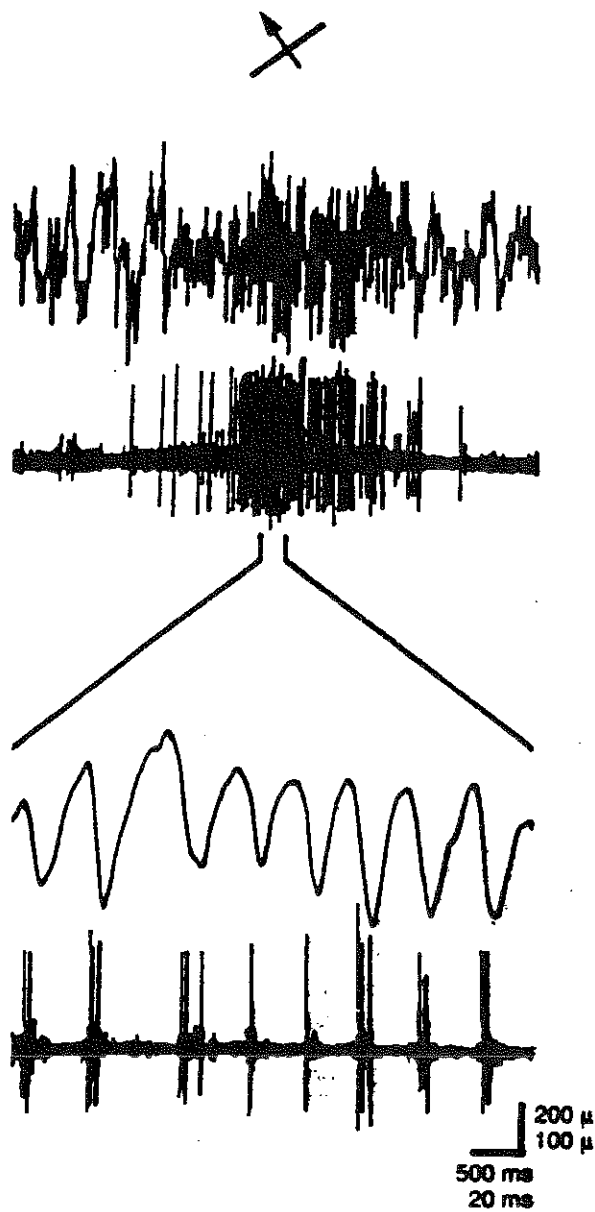
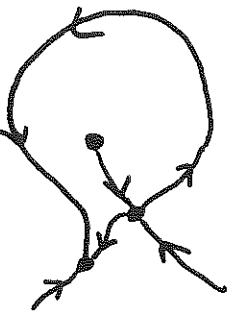


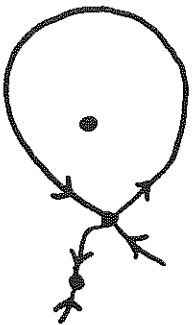
Fig. 1. Oscilloscope records of multi-unit activity and the local field potential from area 17 in an adult cat. The onset of the response to presentation of an optimally oriented light bar moving across the receptive field is shown at slow time scale in the upper two traces. The lower two traces display the activity at the peak of the response at an expanded time scale. The periodic spiking in the multi-unit activity is synchronized with the peak negativity of the local field potential oscillation in the gamma-frequency range. (Adapted, with permission, from Ref. 9.)

fig. 8.6

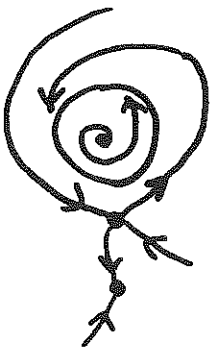


(8.8)

$$\mu < \mu_c$$



$$\mu = \mu_c$$



$$\mu > \mu_c$$

fig. 8.7

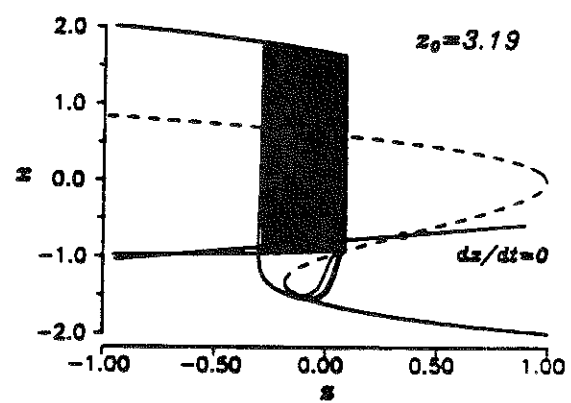
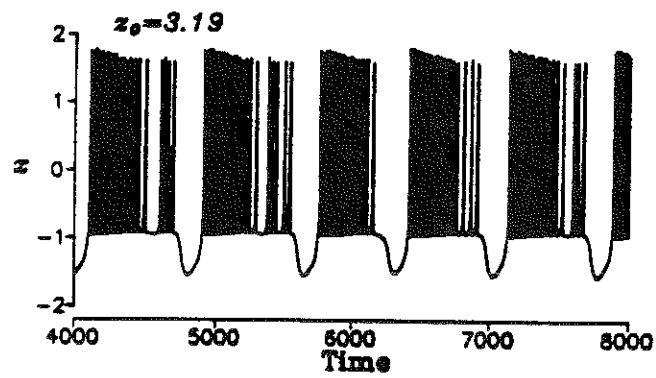
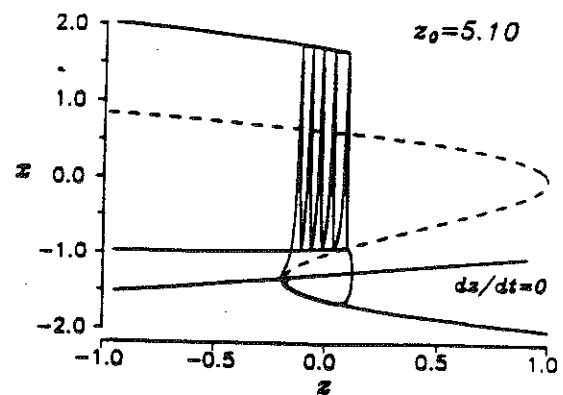
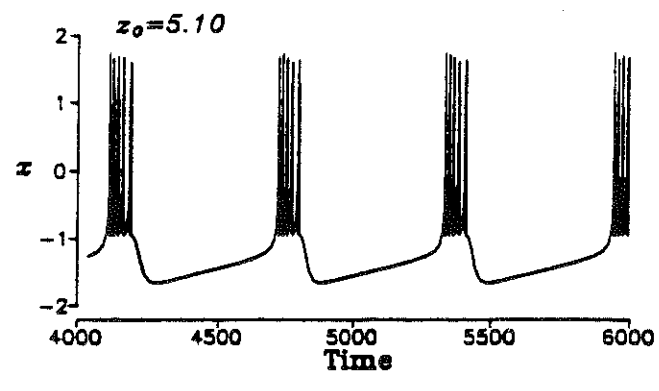


fig. 8.8

(8.9)

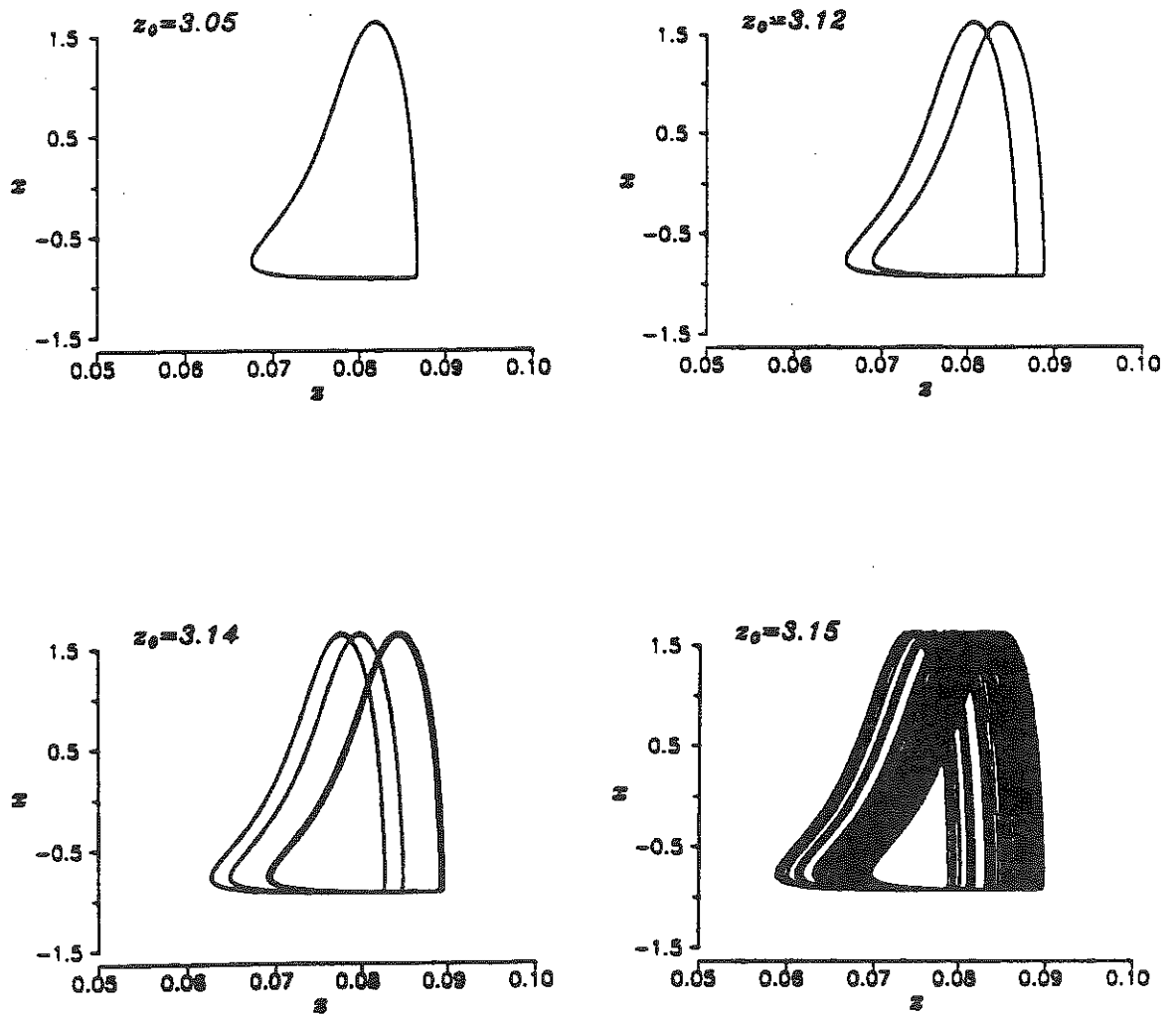


fig. 8.9

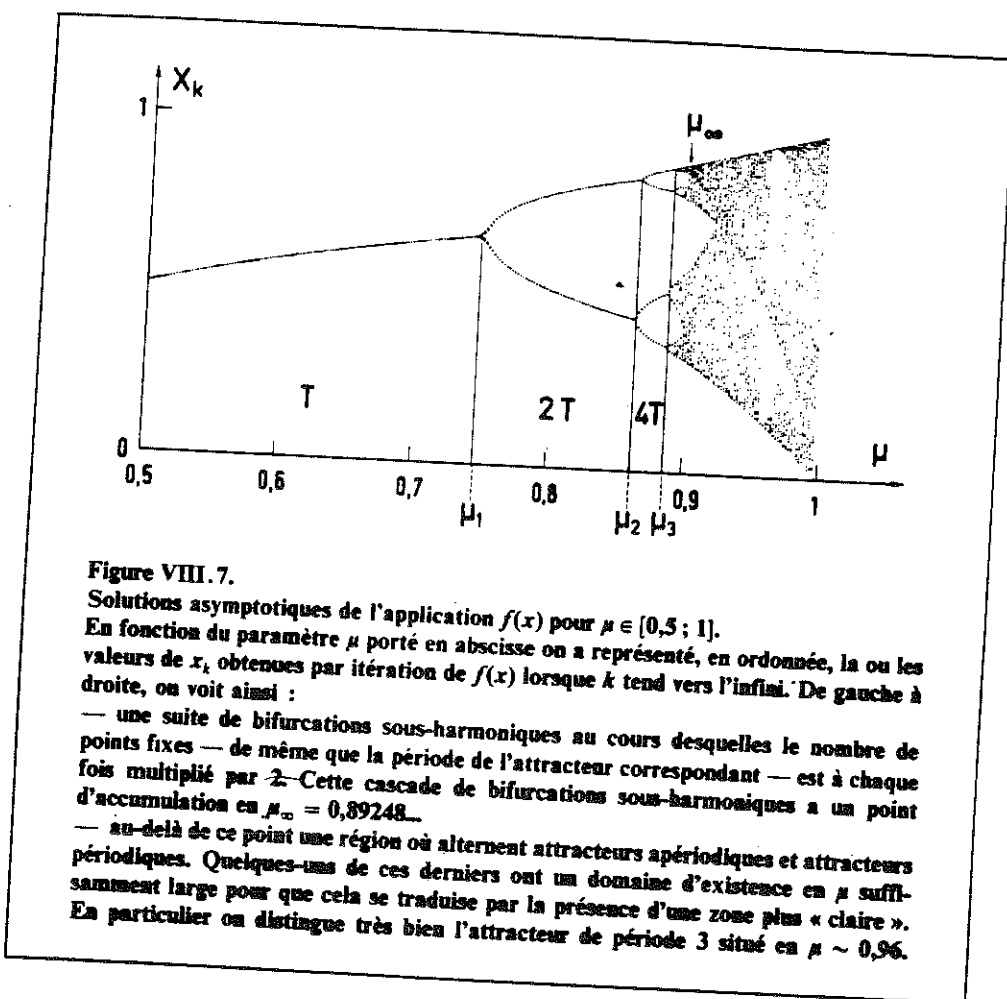


fig. 8.10

(8.10)

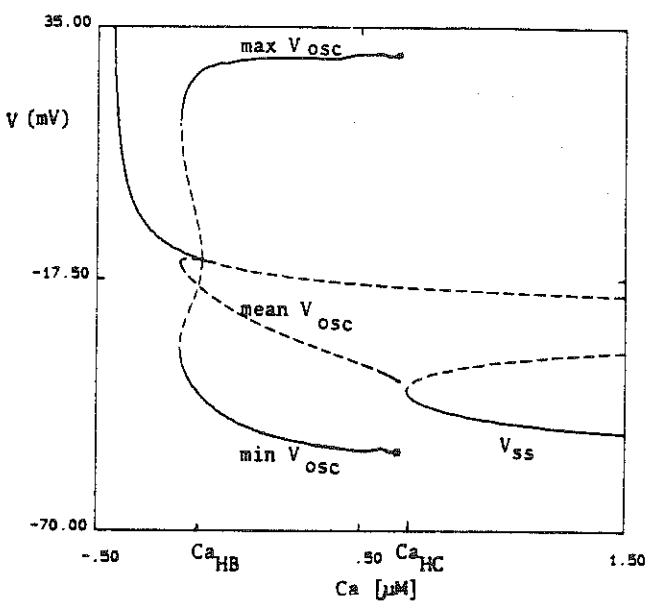


Fig. 5 Bifurcation diagram for fast subsystem, (3.1)-(3.3), of Plant's model with x fixed, $x = 0.7$. Steady state and periodic solution amplitudes plotted as function of Ca . Note, Hopf bifurcation at Ca_{HB} is subcritical and homoclinic connection at Ca_{HC} is degenerate (i.e., occurs at a saddle-node coalescence of two steady states).

fig. 8.11

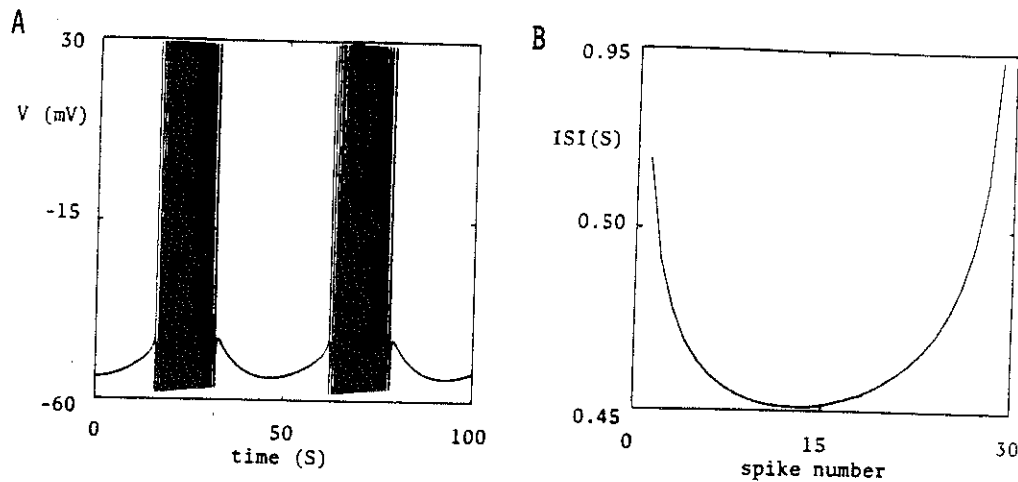


Fig. 7 (A) Parabolic burst pattern for Plant model, (3.1)-(3.5), obtained with parameter adjustments: ρ replaced by $\rho/4$, τ_x replaced by $40 \tau_x$, and, in $x_e(V)$ function, $A = 0.30$, $B = -40\text{mV}$. (B) Interspike interval (time between successive spike upstrokes) versus spike number for burst response in (A).

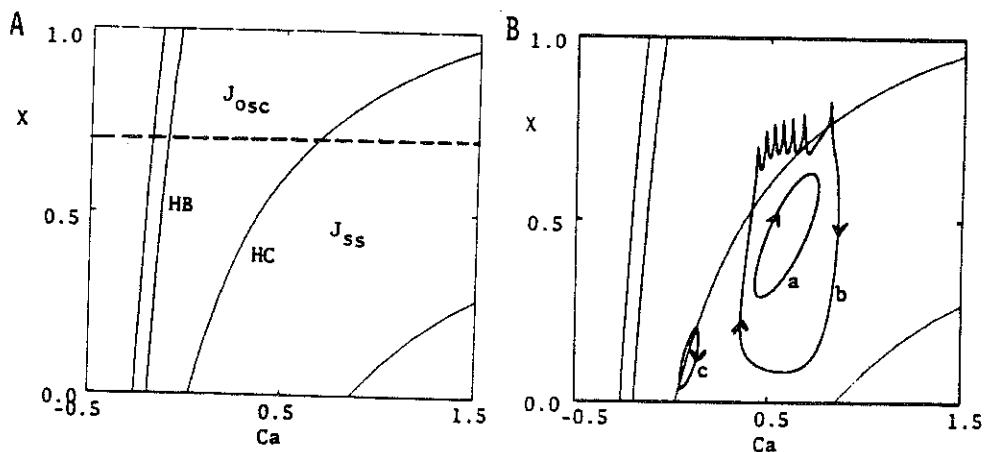


Fig. 6 Projection of bifurcation surface, V versus Ca and x , of fast subsystem, (3.1)-(3.3), for Plant's model. In A, lower right curve (unlabeled) corresponds to fold (i.e., limit points) where upper and middle branches of steady state surface coalesce. Lower fold is labeled HC because it coincides with (degenerate) homoclinic connection where branch of periodic solutions terminates. Leftmost curve (unlabeled) is for limit points of periodic solution branches which arise via subcritical Hopf bifurcation along curve HB . Curves in Fig. 5 represent a section through bifurcation surface for $x = 0.7$ (dashed line). Regions J_{ss} and J_{osc} of slow variables (described generally in Introduction) are shown explicitly here; J_{ss} is below HC and J_{osc} is between HC and leftmost curve. In B, solution trajectories of full model, (3.1)-(3.5), for three parameter sets, are projected onto $Ca-x$ plane. Case (b) is for burst response of Fig. 1B. For case (a), ρ is replaced by 5ρ and K_c by $0.8 K_c$ to generate a slow wave pattern without spikes. Case (c) corresponds to the parabolic burst pattern of Fig. 7A.

fig. 8.12

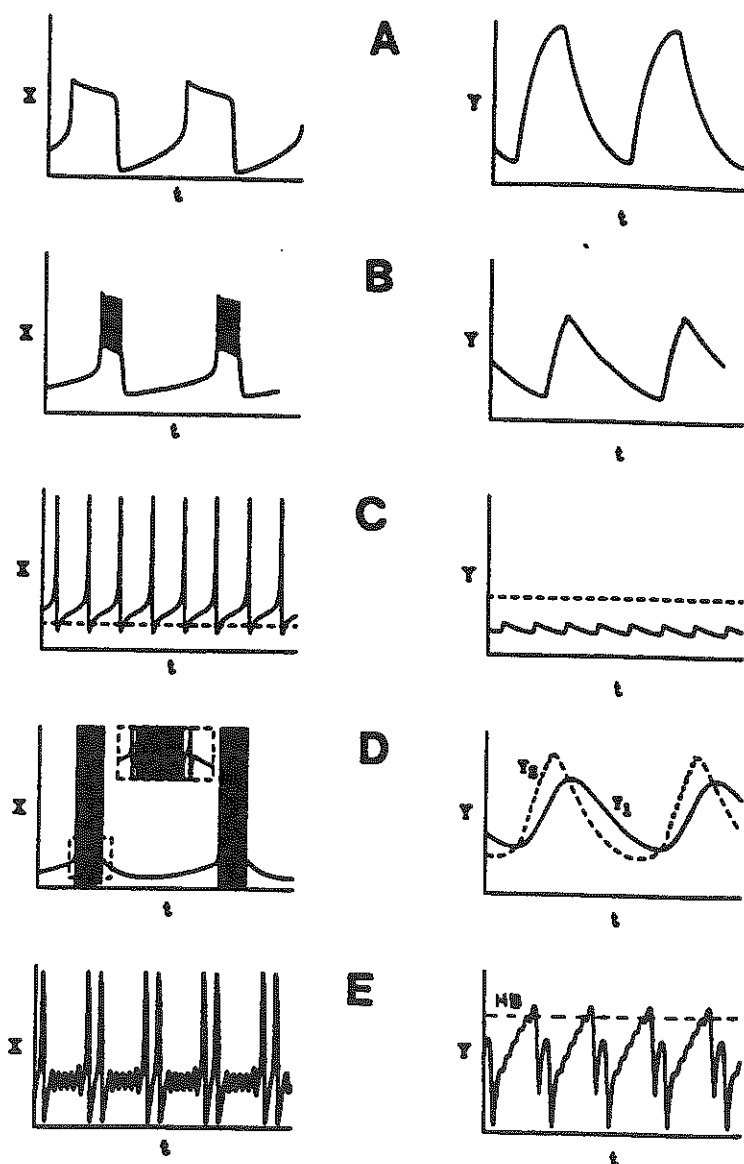


FIGURE 2. Time course of a fast (left) and slow (right) variable for corresponding schematics of Figure 1. These are for computed solutions of specific excitability membrane models. Cases A, B, C: V and Ca from (3.1)–(3.3) with parameter changes: $\lambda_n = 2.0, f = 0.08$ (A); $\lambda_n = 0.1$, and $k_{\text{Ca}} = 0.006$ (solid) or $k_{\text{Ca}} = 0.0006$ (dashed) (C). Case D: V , Ca (right, solid), and slow calcium conductance, z (right, dashed) for Plant's model (as given in [25] but with $\tau_z = 1.88 \times 10^4, K_C = 5.525 \times 10^{-3}, \rho = 0.9 \times 10^{-4}$). Case E: v and y for (3.4)–(3.6) with $\varepsilon = 0.0006$ (note, ε not too small here, so only 2 pulses per burst and y -increments not small).

fig. 8.13

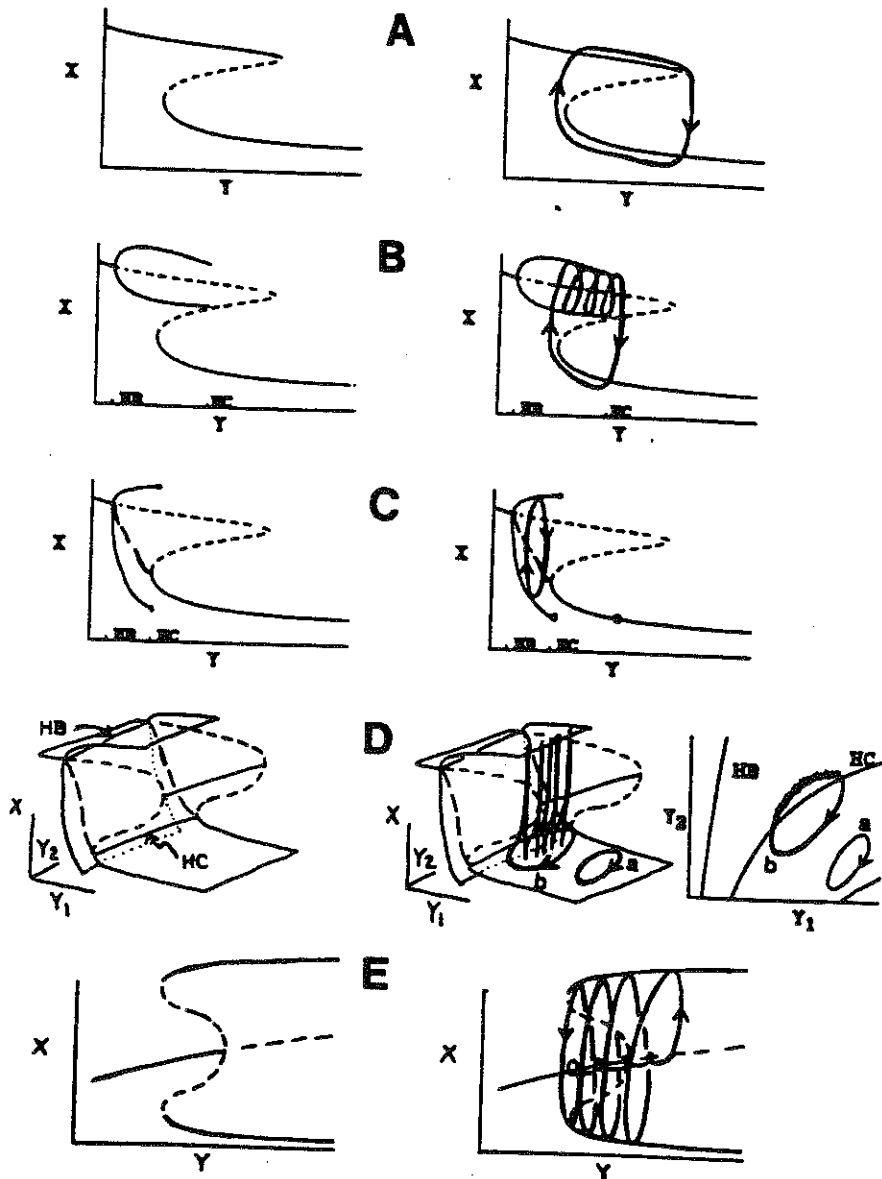


FIGURE 1. Left: Bifurcation diagram (compact description) of periodic and steady state solutions to fast subsystem (FAST) with slow variables as parameters. Maximum and minimum values of some solution component, or its time average over a period (long dashes), is plotted. Unstable solutions indicated by short dashes. Right: Schematic representation (heavy curves) of slow wave, burst, or continuous spiking trajectory as projected on bifurcation diagram (and its projection, case D, far right) of corresponding left panel.

fig. 8.14

Lecture 9 : Population neurodynamics: the Wilson-Cowan equation

Neural populations with many nonlinear units are fairly difficult to describe. A first attempt would be to seek a "statistical formulation" and obtain self-consistent equations for "macroscopic" quantities. Wilson and Cowan (1972, 1973) and Amari (1973) have independently pioneered such approach. We shall discuss here the simplest version of the Wilson-Cowan formulation, and be concerned with only averaged quantities (ignoring fluctuations). We shall see that such macroscopic description naturally yield such nonlinear phenomena as bistability and rhythmic oscillations.

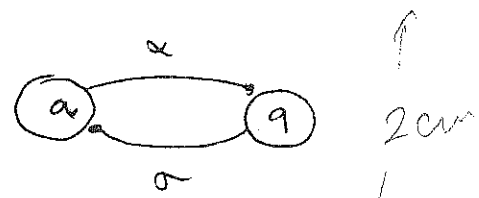
Consider first a population of similar cells. Suppose each cell is either in an active state or a quiescent state. Its dynamics is ruled by a simple stochastic kinetics: there is a transition rate α from the a state to the q state, and a transition rate σ from the q state back to the a state. Cells are assumed to statistically independent from one another.

Then, if the fraction of the population in the active state at time t is denoted by $a(t)$, we have
 (resp. quiescent) (resp. $q(t)$)

$$a(t) + q(t) = 1$$

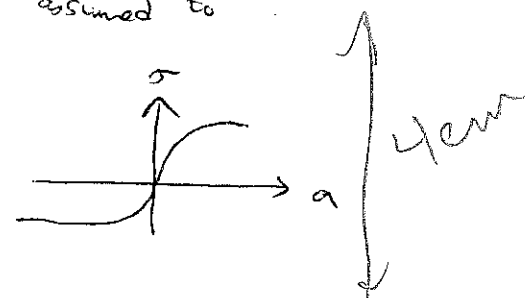
and $a(t)$ obeys a single equation

$$\frac{da}{dt} = (1-a)\sigma - \alpha a.$$



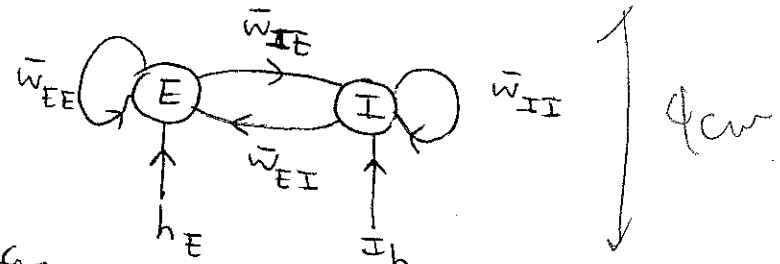
It is assumed that the transition rate from the q state to the a state represents the output of the population activity which in turn excites the cells. Hence σ should be a function of $a(t)$; $\sigma(a)$ usually assumed to a sigmoid form.

→ nonlinearity.



Now, let us consider two populations of neurons, one excitatory, the other one inhibitory. There are recurrent excitation within the E cells, mutual inhibition within the I cell, and cross-interactions between E cell and I cell.

Similar consideration as before allows us to write



$$\dot{a}_E = -\alpha_E a_E + (1-a_E) \sigma_E(v_E)$$

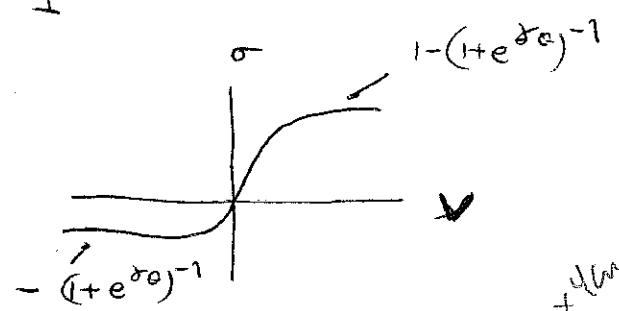
$$\dot{a}_I = -\alpha_I a_I + (1-a_I) \sigma_I(v_I)$$

where

$$v_E = \bar{w}_{EE} a_E - \bar{w}_{EI} a_I + h_E$$

$$v_I = \bar{w}_{IE} a_E - \bar{w}_{II} a_I + h_I$$

$$\sigma(v) = \frac{1}{1+e^{-\gamma(x-\theta)}} - \frac{1}{1+e^{\gamma\theta}}$$



v_{out} $+ v_{in}$

S.S. $\frac{a_E}{1-a_E} = \alpha_E^{-1} \sigma_E(v_E)$

$$\frac{a_I}{1-a_I} = \alpha_I^{-1} \sigma_I(v_I)$$

$\bar{w}_{EI}, \bar{w}_{IE} > 0$ is required for any interesting behaviors to exist.

3 fixed points, necessary condition: $\max \frac{da_I}{da_E} > 0$ in the a_E -nullcline.

Sufficient condition is that $\frac{d\alpha_I}{d\alpha_E} > 0$ at the inflection point of α_E^{-1} .

$$\Leftrightarrow \boxed{\bar{w}_{EE} > \frac{g}{\delta_E}}$$

→ bistable flip-flop

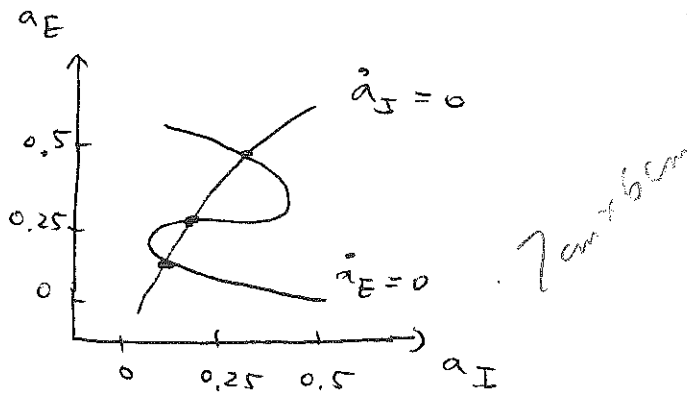
example: $h_E = h_I = 0$

$$\bar{w}_{EE} = 12 \quad \bar{w}_{IE} = 13$$

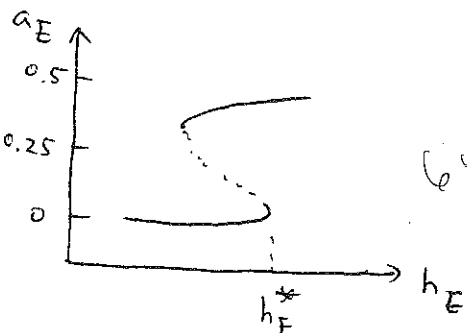
$$\bar{w}_{EI} = 4 \quad \bar{w}_{II} = 11$$

$$\delta_E = 1.2 \quad \theta_E = 2.8$$

$$\delta_I = 1 \quad \theta_I = 4$$



An external input, e.g. h_E , can switch the network from one state with low value of a_E to another state of high value of a_E .



note that the state with high a_E has also a high value of a_I .

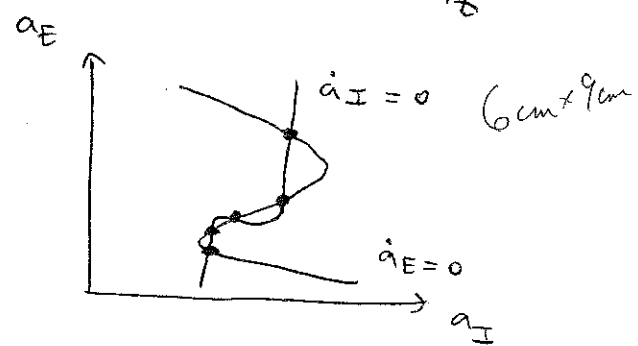
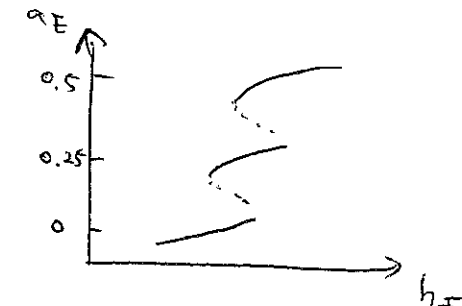
If \bar{w}_{EI} and \bar{w}_{II} are sufficiently weak, one can even have 5 fixed points, e.g. three stable states which coexist.

example: $\bar{w}_{EE} = 13$ $\bar{w}_{EI} = 4$

$\bar{w}_{IE} = 20$ $\bar{w}_{II} = 2$

$\delta_E = 1.2$ $\theta_E = 2.7$

$\delta_I = 5$ $\theta_I = 3.7$



On the other hand, if lateral inhibition is strong (\bar{w}_{EI} is large), then oscillations occurs. A necessary condition is

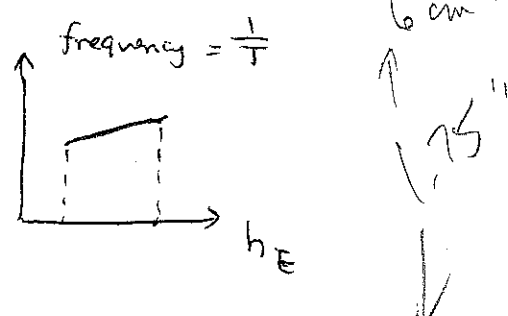
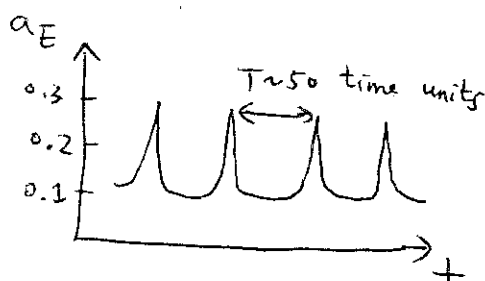
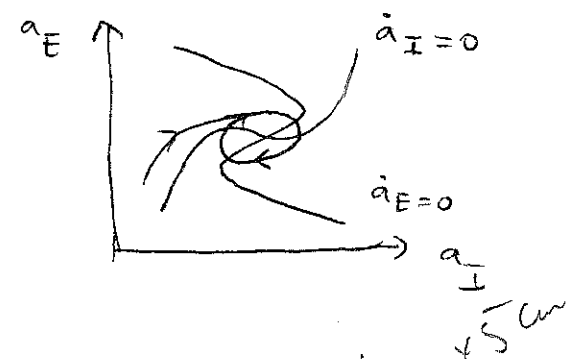
$$\frac{\delta_E \bar{w}_{EI}}{\delta_E \bar{w}_{EE} - 9} > \frac{\delta_I \bar{w}_{II} + 9}{\delta \bar{w}_{IE}}$$

example: $\bar{w}_{EE} = 16$ $\bar{w}_{EI} = 12$

$\bar{w}_{IE} = 15$ $\bar{w}_{II} = 3$

$\delta_E = 1.3$ $\theta_E = 1$

$\delta_I = 2$ $\theta_I = 3.7$



Lecture 10: Synchronization of integrate-and-fire neurons

It is desirable to be able to deal with a direct network of many neurons directly. We shall discuss some topics in that direction.

Consider N integrate-and-fire neurons coupled globally,

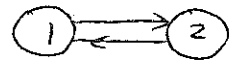
$$\dot{x}_k = -\lambda x_k + S_0 + \frac{\varepsilon}{N} \sum_j S(t-t_j) \quad \text{coupling is all-to-all.}$$

$$x_k(t) = 1 \rightarrow x_k(t^+) = 0$$

C. Peskkin: (Conjecture) (1) for \forall initial conditions, all oscillations are synchronized.
 (2) true even if \exists heterogeneities.

Case $N=2$

$$\varepsilon \ll 1$$



$$\therefore x_1 = 0 \quad x_2 = x_0$$

$$x_1(t) = \frac{S_0}{\lambda} (1 - e^{-\lambda t})$$

$$x_2(t) = \frac{S_0}{\lambda} (1 - e^{-\lambda t}) + \alpha_0 e^{-\lambda t}$$

$$\text{Let } t_A \text{ be the first firing time} \quad x_2(t_A) = 1 = \frac{S_0}{\lambda} - \left(\frac{S_0}{\lambda} - \alpha_0 \right) e^{-\lambda t_A}$$

$$\Rightarrow x_1(t_A^-) = S \frac{1-\alpha_0}{S-\alpha_0} \quad S = \frac{S_0}{\lambda}$$

$$x_1(t_A^+) = \frac{\varepsilon}{2} + S \frac{1-\alpha_0}{S-\alpha_0} \equiv \alpha_1 \quad x_2(t_A^+) = 0$$

$$\Rightarrow \alpha_{n+1} = \frac{\varepsilon}{2} + S \frac{1-\alpha_n}{S-\alpha_n}$$

$$\text{let } \beta = S^{-1} \quad \varepsilon_0 = \frac{\varepsilon}{2}$$

$$\alpha_{n+1} = \frac{1-\alpha_n}{1-\beta\alpha_n} + \varepsilon_0$$

$$\alpha_{n+2} = \alpha_{n+2}(\beta, \varepsilon_0)$$

$$= \alpha_n + A \beta \varepsilon_0 + O(\beta, \varepsilon_0)$$

$$\beta, \varepsilon_0 \ll 1$$

$$A = 1 - 2(1-\alpha_n) = 2\alpha_n - 1$$

so for $\epsilon, \beta \ll 1$

$$\alpha_{n+2} \approx \alpha_n + 2\epsilon\beta(\alpha_n - \frac{1}{2})$$

f.p. $\alpha_n = \frac{1}{2}$

$$\alpha_n > \frac{1}{2} \rightarrow \alpha_{n+2} > \alpha_n$$

$$\alpha_n < \frac{1}{2} \rightarrow \alpha_{n+2} < \alpha_n$$

thus $\alpha_n = \frac{1}{2}$ is a repeller $\alpha_n \rightarrow 0$ or 1

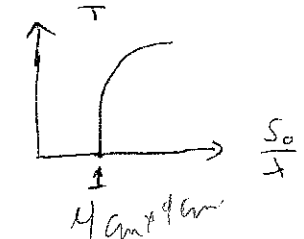
\Rightarrow 2 oscillators must be synchronized.

N-oscillators, proved by Mirollo & Strogatz (SIAM J Appl Math 50, 1645 (1990))

Assume that a free neuron evolves according to $x = f(\phi)$, $0 \leq \phi \leq 1$. e.g. for Pekin's case,

$$f(\phi) = \frac{s_0}{\tau} (1 - e^{-b\phi}) \quad b = \ln \frac{1}{1 - \frac{\lambda}{s_0}}$$

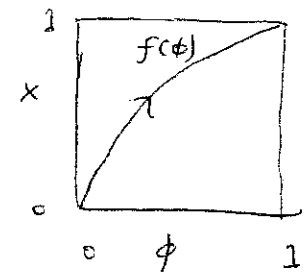
$$\frac{d\phi}{dt} = \frac{1}{\tau} \quad \tau = \frac{b}{\lambda} = \frac{1}{\lambda} \ln \frac{1}{1 - \frac{\lambda}{s_0}}.$$



But in general, assume that $f: [0, 1] \rightarrow [0, 1]$ is smooth, monotonically increasing and concave down

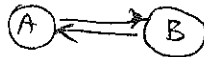
i.e. $f' > 0, f'' < 0$

$$f(0) = 0 \quad f(1) = 1$$

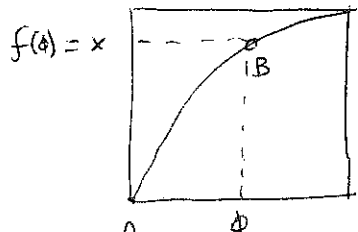


$$g = f^{-1} \quad g(0) = 0 \quad g(1) = 1$$

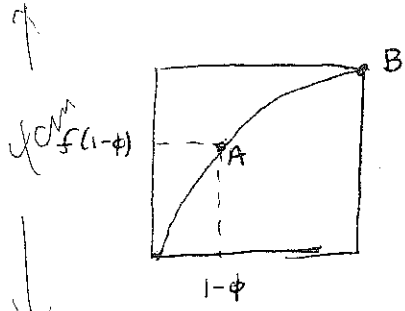
Consider 2 cells.



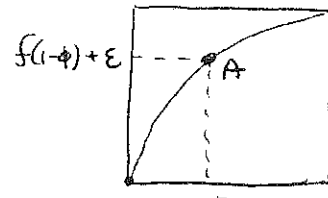
$$x_i(t) = 1 \rightarrow x_j^{+}(t) = \min(1, x_j(t) + \varepsilon)$$



(a)



(b)



(c)

$$A = (0, 0)$$

$$A = (1-\phi, f(1-\phi))$$

$$A = (\phi^*, f(1-\phi) + \varepsilon)$$

$$B = (\phi, f(\phi))$$

$$B = (1, 1)$$

$$B = (0, 0)$$

$$(\phi_A, \phi_B) = (0, \phi)$$

$$(\phi_A, \phi_B) = (1-\phi, 1)$$

$$(\phi_A, \phi_B) = (h(\phi), 0)$$

return map: let $\phi^* = g(f(1-\phi) + \varepsilon) \equiv h(\phi)$

$R(\phi) = \text{phase of } B \text{ immediately after the next firing of } A$
 $\equiv h(h(\phi))$

Lemma: $h'(\phi) < -1$ and $R'(\phi) > 1$ for $\forall \phi$.

Proof: $h'(\phi) = -g'(1-\phi) f'(1-\phi) = -\frac{g'(\varepsilon + f(1-\phi))}{g'(f(1-\phi))} < -1$

Since $g'' > 0$ so $g'(\varepsilon + x) > g'(0)$

and $R'(\phi) = h'(h(\phi)) h'(\phi)$

Proposition: there exists a unique fixed point for R and it is a repeller.

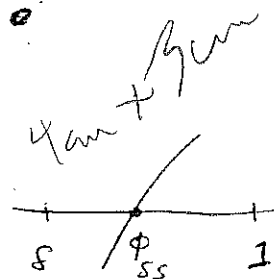
$$\varepsilon + f(1-\phi) < 1 \rightarrow \underline{\phi \in (\delta, 1)}, \quad \underline{\delta = 1 - g(1-\varepsilon)}$$

a s.p. for h is given by $F(\phi) = \phi - h(\phi) = 0$

one can easily check that $F(\delta) < 0$, $F(1) > 0$

moreover, $F'(\phi) = 1 - h'(\phi)$ $\frac{h(\delta)=1}{>2>0}$ $\frac{"}{1-g(\varepsilon)}$

$\rightarrow h$ has a unique f.p. ϕ_{ss}



since $R(\phi_{ss}) = \phi_{ss}$

and $R(\phi) > 1 \rightarrow \phi_{ss}$ is a repeller.

\rightarrow synchrony proved.

N-oscillators. Let $S = \{(\phi_1, \dots, \phi_n) \in \mathbb{R}^n \mid 0 < \phi_1 < \phi_2 < \dots < \phi_n < 1\}$

at $t=0 \quad \phi_0 = 1 \quad n=N-1$

$\rightarrow h(\phi) = \tau(\sigma(\phi))$ where

$$\sigma(\phi_1, \dots, \phi_n) = (1-\phi_n, \phi_1+1-\phi_n, \dots, \phi_{n-1}+1-\phi_n) \quad \begin{array}{l} \text{cells are relabeled} \\ \text{cell } 0 \rightarrow \text{cell } 1 \\ \text{cell } k \rightarrow \text{cell } k+1 \\ \text{cell } n \rightarrow \text{cell } 0 \end{array}$$

$$\tau(\sigma_1, \dots, \sigma_n) = (g(f(\sigma_1)+\varepsilon), \dots, g(f(\sigma_n)+\varepsilon))$$

let $R = h^n$

Absorption: the firing of oscillator n can bring the oscillator $n-1$ to threshold along with it.

Let $S_\varepsilon = \{(\phi_1, \dots, \phi_n) \in S \mid \varepsilon + f(\phi_{n-1}+1-\phi_n) < 1\}$

If $\phi \in S - S_\varepsilon$, an absorption will occur after one firing of strength ε .

When a group of neurons fire simultaneously, the pulse strength is the sum of individual pulse strengths, i.e. here $\epsilon \times \# \text{ of neurons of the group.}$

define: $A_i = \{\phi \in S \mid \phi^k(\phi) \in S_\epsilon, k=0, 1, \dots, i-1\} \quad A = \bigcap_{i=1}^{\infty} A_i$

then A is the set of i.c. that live forever without any absorptions

Theorem: the set A has zero Lebesgue measure.

Proof: by definition $R(A) \subset A$ for $\Phi = h^N$

on the other hand, explicit calculation shows that

$$\left| \det \left(\frac{\partial}{\partial \phi} R \right) \right| > 1 \quad (\text{again, using } g'' > 0, g' > 0)$$

Jacobian

$$\rightarrow \text{measure}(A) = 0.$$

Similar argument applies to initial conditions which, after a finite number of absorptions, live forever without reaching ultimate synchrony.

Simulations. recruitment (fig. 1)

Conjecture: if the coupling is space-dependent
or if oscillators are not identical $\} \rightarrow$ no total synchrony.

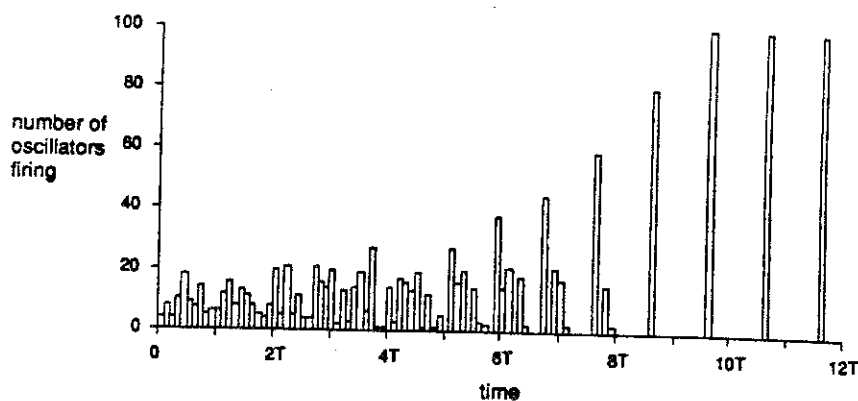


FIG. 5. Number of oscillators firing as a function of time, for the system (1.1) and (1.2), with $N = 100$, $S_0 = 2$, $\gamma = 1$, $\varepsilon = 0.3$, and random initial condition. Time is plotted in multiples of the natural period T of the oscillators. Each period is divided into 10 equal intervals, and the number of oscillators firing during each interval is plotted vertically.

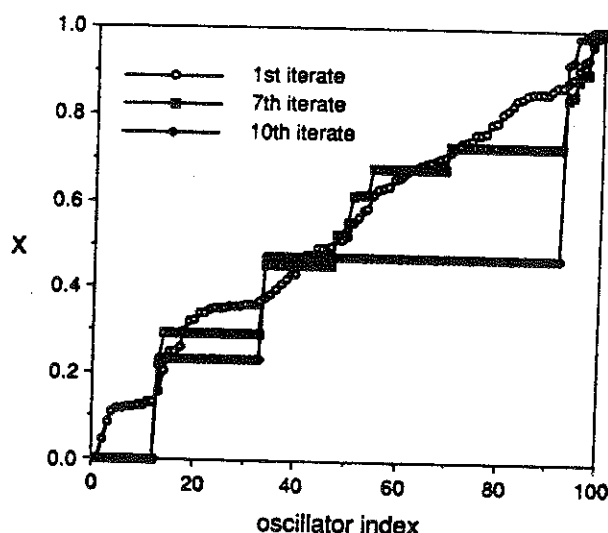


FIG. 6. The state of the system after the first, seventh, and tenth iterations of the return map. Same simulation as in Fig. 5. The flat sections of the graphs correspond to groups of oscillators that fire in unison.

fig. 10.1

Lecture 11: Coupled oscillators / reduction to phase model

(1) general procedure.

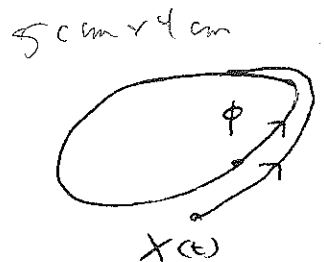
Consider first an oscillator

$$\frac{dx}{dt} = F(x) + \varepsilon G(x) \quad X \in \mathbb{R}^n.$$

$\varepsilon = 0 \rightarrow$ limit cycle $X_0(t) = X_0(t+T)$ which is assumed to be attractive.

choose phase $\frac{d\phi(X)}{dt} = \omega_0$ uniform. $T = \frac{2\pi}{\omega_0}$

$$\rightarrow X_0(\phi) = X_0(\phi + 2\pi).$$



for any point X outside the cycle, we define its phase as ϕ such

that

$$\lim_{t \rightarrow \infty} |X(t) - X_0(\phi(t))| = 0.$$

now $\varepsilon \neq 0$, $\frac{d\phi}{dt} = \nabla_X \phi \cdot (F(x) + \varepsilon G(x)) = \underbrace{\nabla_X \phi \cdot F}_{\omega_0} + \varepsilon \nabla_X \phi \cdot G(x)$

$$= \omega_0 + \varepsilon \mathcal{L}(\phi) + o(\varepsilon^2), \quad \boxed{\mathcal{L}(\phi) = (\nabla_X \phi) \Big|_{X=X_0(\phi)} \cdot G(X_0(\phi))}$$

Let $\phi = \omega_0 t + \gamma \rightarrow \frac{d\gamma}{dt} = \varepsilon \mathcal{L}(t + \gamma) = \varepsilon \omega, \quad \omega = \frac{1}{T} \int_0^T \mathcal{L}(t + \gamma) dt$

γ changes slowly in time.

average over one period

Similarly, consider 2 oscillators, with slightly different intrinsic frequencies

$$\frac{dx_1}{dt} = F(x_1) + \varepsilon f_1(x_1) + \varepsilon G_1(x_1, x_2)$$

$$\frac{dx_2}{dt} = F(x_2) + \varepsilon f_2(x_2) + \varepsilon G_2(x_2, x_1)$$

If $\varepsilon = 0$ each system has an attracting limit cycle, with $\frac{d\phi_i}{dt} = \omega_0$.

Now if $\varepsilon \neq 0$ but $\varepsilon \ll 1$. In the 1st order approximation

$$\frac{d\phi_i}{dt} = \nabla_{x_i} \phi_i \quad \frac{dx_i}{dt} = \omega_0 + \varepsilon (\nabla_{x_i} \phi_i) \Big|_{x_0} (f_i(x_0(\phi_i)) + G_i(x_0(\phi_i), x_0(\phi_i)))$$

Let $\gamma_i = \phi_i - \omega_0 t$ and average the right hand-side over $T = \frac{2\pi}{\omega_0}$

$$\Rightarrow \frac{d\gamma_i}{dt} = \varepsilon \Gamma_i (\gamma_i - \gamma_j) + \varepsilon \omega_i$$

where $\Gamma_i (\gamma_i - \gamma_j) = \frac{1}{T} \int_0^T dt (\nabla_{x_i} \phi_i)(x_0(\omega_0 t + \gamma_i)) G_i(\omega_0 t + \gamma_i, \omega_0 t + \gamma_j)$
 $\omega_i = \frac{1}{T} \int_0^T dt f_i(\omega_0 t + \gamma_i)$

example: $G_1 = G_2$ $f_1 = f_2 = 0$ (identical cells) $\rightarrow \Gamma_1 = \Gamma_2$

let $\gamma = \gamma_1 - \gamma_2$ $\omega_1 = \omega_2 = 0$

$$\rightarrow \frac{d\gamma}{dt} = \varepsilon H(\gamma)$$

$$H(\gamma) = \Gamma(\gamma) - \Gamma(-\gamma)$$

Since $H(\gamma + 2\pi) = H(\gamma)$, and $H(0) = 0$, we must have

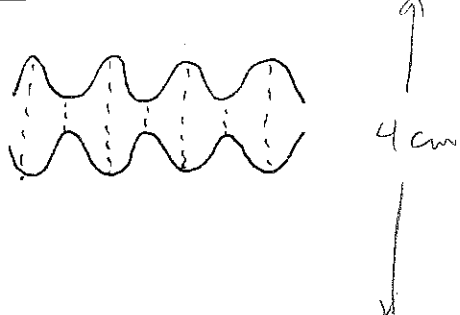
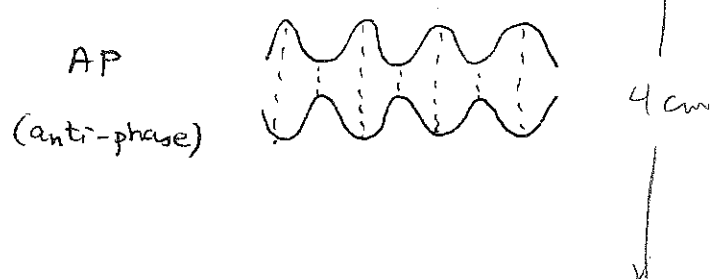
$$H(0) = H(\pi) = 0 \quad \text{but other } \gamma_{ss} \text{ may exist.}$$

Stability of $\gamma_{ss} = 0, \pi$? $H'(\gamma_{ss}) < 0 \rightarrow \gamma_{ss} \text{ stable}$

$> 0 \rightarrow \gamma_{ss} \text{ unstable.}$

One may say that the coupling is attractive if $H'(0) < 0$

and repulsive if $H'(\pi) < 0$



(2) Single example: integrate-and-fire model. We consider

$$\frac{dv_1}{dt} = -v_1 + s_0 + \epsilon \delta(t-t_2)$$

$$\frac{dv_2}{dt} = -v_2 + s_0 + \epsilon \delta(t-t_1)$$

the firing threshold is 2π , and 2π is identified with 0.

$\rightarrow v_i$ may be considered as phase-variables. If $\epsilon = 0 \rightarrow$

$$v_i(t) = s_0 - (s_0 - v_i(0)) e^{-t} \quad \text{"oscillator" if } s_0 > 2\pi$$

the period T is given by

$$\frac{2\pi}{s_0} = 1 - e^{-T}$$

$$T = \ln \frac{1}{1 - \frac{2\pi}{s_0}}$$

$$\text{Let } \phi_i = \omega_0 \ln \frac{1}{(1 - \frac{v_i}{S_0})} \quad \omega_0 = \frac{2\pi}{T}$$

$$\rightarrow \frac{d\phi_i}{dt} = \omega_0 \quad v_i = S_0 (1 - e^{-\phi_i/\omega_0})$$

Consider now 2-coupled oscillators ($\varepsilon \neq 0$). In terms of ϕ_i we have

$$\left\{ \begin{array}{l} \frac{d\phi_1}{dt} = \omega_0 + \frac{\omega_0 \varepsilon}{S_0} e^{\frac{\phi_1}{\omega_0}} s(t-t_2) \\ \frac{d\phi_2}{dt} = \omega_0 + \frac{\omega_0 \varepsilon}{S_0} e^{\frac{\phi_2}{\omega_0}} s(t-t_1) \end{array} \right. \quad \begin{array}{l} t_i \text{ is firing time of} \\ \text{the } i\text{th cell, thus} \\ v_i(t_i) = 0 \Leftrightarrow \phi_i(t_i) = 0 \end{array}$$

$$\text{let } \gamma_i = \phi_i - \omega_0 t$$

$$\rightarrow \frac{d\gamma_1}{dt} = \frac{\omega_0 \varepsilon}{S_0} e^{\frac{\gamma_1}{\omega_0} + t} s(t-t_2)$$

$$\boxed{\gamma_1(t_i) = -\omega_0 t_i}$$

$$\frac{d\gamma_2}{dt} = \frac{\omega_0 \varepsilon}{S_0} e^{\frac{\gamma_2}{\omega_0} + t} s(t-t_1)$$

substitute $e^t s(t-t_i)$ by

$$\frac{1}{T} \int_0^T e^t s(t-t_i) dt = e^{\frac{t_i}{\omega_0}} = e^{-\frac{\gamma_i}{\omega_0}}$$

$$\rightarrow \frac{d\gamma_1}{dt} = \varepsilon \Gamma(\gamma) \quad \frac{d\gamma_2}{dt} = \varepsilon \Gamma(-\gamma) \quad \boxed{\gamma = \gamma_1 - \gamma_2}$$

$$\Gamma(\gamma) = \frac{\omega_0}{S_0} e^{\frac{\gamma}{\omega_0}} \quad 0 \leq \gamma < 2\pi$$

$$\Gamma(-\gamma) = \frac{\omega_0}{S_0} e^{-\frac{\gamma+2\pi}{\omega_0}}$$

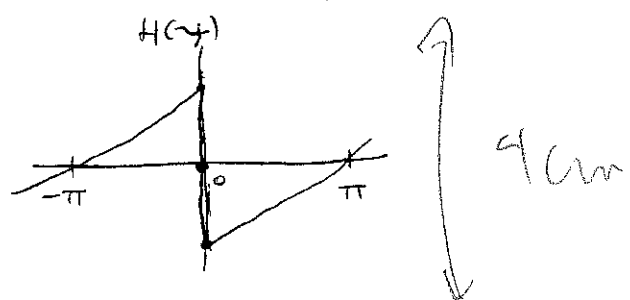
$$0 \leq \gamma < 2\pi$$

$$\frac{d\gamma}{dt} = \varepsilon H(\gamma)$$

$$= \frac{2\omega_0 \varepsilon}{S_0} e^{\frac{\gamma}{\omega_0}} \sinh\left(\frac{\gamma-\pi}{\omega_0}\right)$$

$$\rightarrow \gamma_{ss} = 0 \quad (\text{super})\text{stable}$$

$$H'(0) = -\infty.$$



(3) How to compute $(\nabla_x \phi)|_{x_0}$? we discuss here one approach.

Stability of a periodic solution: Floquet theory. Suppose $x_0(t)$ is a periodic solution of the system $\frac{dx}{dt} = F(x)$. Let $X(t) = x_0(t) + u(t)$

$$\rightarrow \frac{du}{dt} = L(t)u \quad L = \frac{\partial F}{\partial x}(x_0(t)) \quad L_{ij}(t+T) = L_{ij}(t).$$

A general solution of this linear equation with periodic coefficients can be expressed as

$$u(t) = S(t) e^{\Lambda t} u(0)$$

where Λ : t-independent matrix $S(t) = S(t+T) \quad S(0) = I$.

Inserting this into the equation we see that $S(t)$ must satisfy

$$\frac{dS}{dt} + S\Lambda - LS = 0$$

Let $\{\lambda_e\}$ be eigenvalues of Λ , $\{u_e\}$ $\{u_e^*\}$ left and right eigenvectors corresponding to $\{\lambda_e\}$. $\exists \lambda_0 = 0$ for periodic solution

$$\text{i.e. } \Lambda u_e = \lambda_e u_e \quad u_e^* \Lambda = \lambda_e u_e^*$$

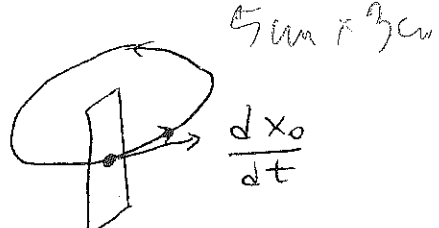
$$\text{assume } u_e^* u_m = \delta_{em}. \quad \Lambda u_0 = \lambda_0 u_0 = 0$$

$$\text{we can choose } u_0 = \left(\frac{dx_0}{dt}\right)_{t=0}.$$

$\frac{dx_0}{dt}$ is a solution of $\frac{du}{dt} = L(t)u \rightarrow \frac{dx_0}{dt} = S(t) e^{\Lambda(t)} u_0 = S(t) u_0$

but $\nabla_x \phi|_{x_0(t)} \cdot \frac{dx_0}{dt} = \omega_0$, therefore

$$\nabla_x \phi|_{x_0(t)} = \omega_0 u_0^* S^{-1}(t)$$



References:

- Y. Kuramoto & Chemical Oscillations, Waves & Turbulence>
Springer 1984
- N. Kopell and G.B. Ermentrout, Commun. Pure Appl. Math. 39, 623 (1986)
SIAM J Appl Math 50, 1014 (1990)
- T. Williams et al. J Neurophysiol. 64, 862 (1990)
- S. Grillner et al. Annu Rev Neurosci. 14, 163 (1991)

Lecture 12: phase model of coupled oscillators (examples)

We shall first discuss a pair of coupled oscillators; then a chain of oscillators in the context of central pattern generators for fish swimming.

Consider 2 identical oscillators ^{each} described by the following equations

$$\frac{d}{dt} \begin{pmatrix} x \\ y \end{pmatrix} = F(x, y) = \begin{pmatrix} x - (\omega_0 + \beta) y - (x - \beta y)(x^2 + y^2) \\ y + (\omega_0 + \beta) x - (y + \beta x)(x^2 + y^2) \end{pmatrix}$$

Let $z = x + iy$, the equation is simply $\frac{dz}{dt} = (1 + i(\omega_0 + \beta))z - ((1 + \beta)|z|^2)z$

limit cycle solution $z_0(t) = e^{i\omega_0 t}$ or $x_0 = \cos(\omega_0 t)$ $y_0 = \sin(\omega_0 t)$.

To study the stability of this solution, let $x = x_0 + \delta x$, $y = y_0 + \delta y$

$$\rightarrow \frac{d}{dt} \begin{pmatrix} \delta x \\ \delta y \end{pmatrix} = L(t) \begin{pmatrix} \delta x \\ \delta y \end{pmatrix} \quad L(t) = \begin{pmatrix} -2x_0(x_0 - \beta y_0) & -\omega_0 - 2y_0(x_0 - \beta y_0) \\ \omega_0 - 2x_0(y_0 + \beta x_0) & -2y_0(y_0 + \beta x_0) \end{pmatrix}$$

In terms of z -variable, let $z(t) = z_0(t)(1 + \delta(t))$

$$\rightarrow \begin{pmatrix} \delta x \\ \delta y \end{pmatrix} = S(t) \begin{pmatrix} \operatorname{Re} z \\ \operatorname{Im} z \end{pmatrix} \quad S(t) = \begin{pmatrix} x_0 & -y_0 \\ y_0 & x_0 \end{pmatrix}$$

We have

$$\frac{d\beta}{dt} = -(1+i\beta)(\beta + \bar{\beta}) \quad \text{or} \quad \frac{d}{dt} \begin{pmatrix} \operatorname{Re}\beta \\ \operatorname{Im}\beta \end{pmatrix} = \Lambda \begin{pmatrix} \operatorname{Re}\beta \\ \operatorname{Im}\beta \end{pmatrix}$$

$$\Lambda = -2 \begin{pmatrix} 1 & 0 \\ 0 & \beta \end{pmatrix}$$

$$\rightarrow \begin{pmatrix} \operatorname{Re}\beta(t) \\ \operatorname{Im}\beta(t) \end{pmatrix} = e^{\Lambda t} \begin{pmatrix} \operatorname{Re}\beta(0) \\ \operatorname{Im}\beta(0) \end{pmatrix}$$

the eigenvalues of Λ are $\lambda_0 = 0 \quad \lambda_1 = -2 \Rightarrow (x_0, y_0)$ stable.

$$u_0 = \omega_0 \begin{pmatrix} 0 \\ 1 \end{pmatrix} = \left. \frac{d x_0}{dt} \right|_{t=0} = F(x_0(t=0)), \quad \Lambda u_0 = 0.$$

$$u_0^* = \frac{1}{\omega_0} (-\beta, 1).$$

$$\begin{pmatrix} \delta x \\ \delta y \end{pmatrix} = S(t) e^{\Lambda t} \begin{pmatrix} \delta x(0) \\ \delta y(0) \end{pmatrix}$$

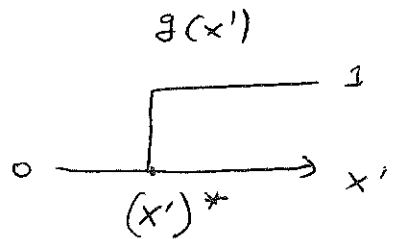
$$\rightarrow \boxed{\left. \frac{\partial}{\partial x} \phi \right|_{X_0(\phi)} = u_0^* S^{-1}(0) = \frac{1}{\omega_0} \begin{pmatrix} -y_0(\phi) - \beta x_0(\phi) \\ -\beta x_0(\phi) + y_0(\phi) \end{pmatrix} \quad \underline{\phi = \omega_0 t}.}$$

now, suppose 2 such oscillators are coupled through "synaptic" interactions. We shall consider 2 cases (type I & type II).

Type I:

$$\frac{d}{dt} \begin{pmatrix} x \\ y \end{pmatrix} = F(x, y) + \epsilon G(x, x') \quad 5 \text{ cm} \times 4 \text{ cm}$$

$$G(x, x') = \begin{pmatrix} g(x') \\ \vdots \\ 0 \end{pmatrix}$$



$g(x')$ is a step function (approximating a sigmoid function), with a threshold $(x')^*$. Let $(x')^* = \cos \alpha$, then $g(x') = 0$ if $\phi \notin (-\alpha, \alpha)$.

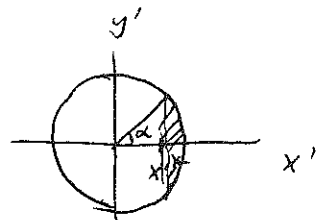
$\epsilon > 0$ excitatory coupling

$\epsilon < 0$ inhibitory coupling

Type II:

$$G(x, x') = \begin{pmatrix} g(x') (x_{\text{syn}} - x) \\ 0 \end{pmatrix} \quad 9 \text{ cm} \times 9 \text{ cm}$$

$\epsilon > 0$



here, we have a "reversal potential" x_{syn} . If x_{syn} is sufficiently positive, the coupling is said excitatory (resp. negative) (resp. inhibitory)

So, let us define $\gamma = \phi - \omega_0 t$ $\gamma' = \phi' - \omega_0 t$

$$\rightarrow \frac{d\gamma}{dt} = \epsilon \Gamma(\gamma - \gamma') \quad \frac{d\gamma'}{dt} = \epsilon \Gamma(\gamma' - \gamma)$$

where

$$\boxed{\Gamma(\gamma - \gamma') = \frac{1}{T} \int_0^T dt \left[\nabla_x \phi \right]_{x_0(\omega_0 t + \gamma)} \cdot G(\omega_0 t + \gamma, \omega_0 t + \gamma')}$$

for type I:

$$\Gamma(\gamma - \gamma') = \frac{-1}{\omega_0 T} \int_0^T dt g(\cos(\omega_0 t + \gamma')) [\sin(\omega_0 t + \gamma) + \beta \cos(\omega_0 t + \gamma)]$$

$$\text{let } \omega_0 t + \gamma' = t'$$

$$\Gamma(\gamma - \gamma') = \frac{-1}{2\pi} \int_{\gamma'}^{2\pi + \gamma} dt' g(\cos t') [\sin(t' + \gamma - \gamma') + \beta \cos(t' + \gamma - \gamma')]$$

$$= \frac{-1}{2\pi} \int_{-\pi}^{\pi} dt' [\sin(t' + \gamma - \gamma') + \beta \cos(t' + \gamma - \gamma')]$$

$$\rightarrow \boxed{\Gamma(\gamma - \gamma') = \frac{-1}{2\pi} \sin \alpha [\sin(\gamma - \gamma') + \beta \cos(\gamma - \gamma')]} \quad \gamma = \tilde{\gamma}$$

The phase difference $\phi - \phi' = \gamma - \gamma'$ between the 2 oscillations obey the following equation

$$\frac{d\tilde{\gamma}}{dt} = \epsilon H(\tilde{\gamma})$$

$$\boxed{H(\tilde{\gamma}) = \Gamma(\tilde{\gamma}) - \Gamma(-\tilde{\gamma})}$$

asymmetric part of $\Gamma(\tilde{\gamma})$.

$$= \frac{-1}{2\pi} \sin \alpha \sin \tilde{\gamma}$$

phase-locking solution

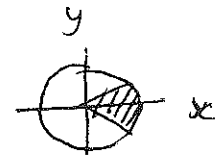
$$\frac{d\tilde{\psi}}{dt} = 0 \rightarrow H(\tilde{\psi}) = 0 \rightarrow \tilde{\psi} = 0, \pi$$

stability

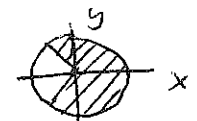
$$H'(0) = \frac{-1}{2\pi} \sin \alpha \quad H'(\pi) = \frac{+1}{2\pi} \sin \alpha$$

$H'(\psi)$ vs α

$$\rightarrow \text{if } \alpha < \frac{\pi}{2} \quad H'(0) < 0 \quad H'(\pi) > 0 \quad \text{IP}$$



$$\alpha > \frac{\pi}{2} \quad H'(0) > 0 \quad H'(\pi) > 0 \quad \text{AP}$$



Remark: $[H'(\tilde{\psi}) = P(\tilde{\psi}) + P(-\tilde{\psi})]$ describes the effect of the coupling

on phase change frequency, thus the "firing rate". For instance,

if the 2 oscillators are perfectly in phase, then $\tilde{\psi} = \psi'$

$$\frac{d\psi}{dt} = \varepsilon H'(0) = -\frac{\beta\varepsilon}{2\pi} \sin \alpha < 0 !$$

or $\frac{d\phi}{dt} = \omega_0 - \frac{\beta\varepsilon}{2\pi} \sin \alpha$. \rightarrow firing rate is decreased by excitatory coupling

if the coupling is weak ($\varepsilon \ll 1$).

Remark: The effect of a transmission delay τ can be readily accounted for.

If $g(x'(t))$ is replaced by $g(x'(t-\tau))$, the previous computation can be repeated without change, except that in the final result

$P(\pm\tilde{\psi})$ is replaced by $P(\pm\tilde{\psi} + \tau)$.

$$\begin{aligned}\rightarrow H(\tilde{\varphi}) &= \frac{-1}{2\pi} \sin \alpha [\sin(\tilde{\varphi} + \tau) + \beta \cos(\tilde{\varphi} + \tau)] \\ &\quad + \frac{1}{2\pi} \sin \alpha [\sin(-\tilde{\varphi} + \tau) + \beta \cos(-\tilde{\varphi} + \tau)] \\ &= \frac{-1}{\pi} \sin \alpha \sin \tilde{\varphi} [\cos \tau - \beta \sin \tau]\end{aligned}$$

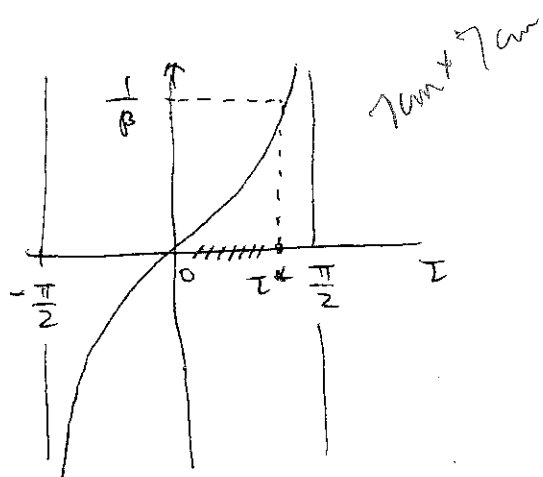
Suppose that $\sin \alpha > 0$ so that when $\tau = 0$, $\tilde{\varphi}_{ss} = 0$ is stable.

Now, if $\tau \neq 0$ we again have $\tilde{\varphi}_{ss} = 0, \pi$. the stability of the synchronized solution $\tilde{\varphi}_{ss} = 0$ is determined by

$$H'(0) = \frac{-1}{\pi} \sin \alpha [\cos \tau - \beta \sin \tau] < 0$$

$$\Leftrightarrow \cos \tau > \beta \sin \tau \Leftrightarrow \beta \tan \tau < 1$$

$$\Leftrightarrow \boxed{\tau < \tan^{-1} \frac{1}{\beta} = \tau^*} \quad \tau^* \rightarrow \frac{\pi}{2} \text{ if } \beta \rightarrow 0.$$



thus, the delay cannot be longer than a quarter of the natural period of solution, at maximum.

Type II: as exercise.

Suppose $G(x, x') = \begin{pmatrix} g(x') & (x_{syn} - x) \\ 0 & \end{pmatrix}$

Then, we can show that

$$\Gamma(\tilde{\gamma}) = -\frac{x_{syn}}{2\pi} \sin \alpha (\sin \tilde{\gamma} + \beta \cos \tilde{\gamma}) + \frac{1}{4\pi} \sin 2\alpha (\sin 2\tilde{\gamma} + \beta \cos 2\tilde{\gamma}) + \frac{\alpha \beta}{2\pi}$$

$$H(\tilde{\gamma}) = -\frac{x_{syn}}{\pi} \sin \alpha \sin \tilde{\gamma} + \frac{1}{2\pi} \sin 2\alpha \sin 2\tilde{\gamma}$$

$$H(\tilde{\gamma}_{ss}) = 0 \rightarrow \tilde{\gamma}_{ss} = 0, \pi \text{ or}$$

$$\cos \tilde{\gamma}_{ss} = \frac{x_{syn}}{2 \cos \alpha}$$

this extra solution exists if

$$\left| \frac{x_{syn}}{2 \cos \alpha} \right| < 1$$

$$H'(0) = \frac{\sin \alpha}{\pi} (2 \cos \alpha - x_{syn})$$

$$H'(\pi) = \frac{\sin \alpha}{\pi} (2 \cos \alpha + x_{syn})$$

Thus, there are 2 ways for $\tilde{\gamma}_{ss} = 0$ to become unstable (for $H'(0)$ to change sign), either $\sin \alpha$ changes sign, then $\tilde{\gamma}_{ss} = \pi$ becomes stable (in-phase $\tilde{\gamma}_{ss} = 0 \rightarrow$ anti-phase $\tilde{\gamma}_{ss} = \pi$); or $(2 \cos \alpha - x_{syn})$ changes sign, then $\tilde{\gamma}_{ss} = \cos^{-1} \frac{x_{syn}}{2 \cos \alpha}$ bifurcates (in-phase \rightarrow out-of-phase).

We now turn to a chain of coupled oscillators.

Lamprey is a simple vertebrate which has been studied extensively as an example of fish locomotion system. Its spinal cord-like can be isolated and maintained alive in laboratory, "fictive swimming" can be generated by stimulations.

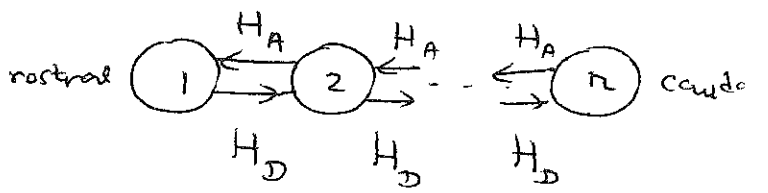
In vivo lamprey propels itself through water by rhythmic undulations that are caused by contractions passing down the axial muscles. The higher is the frequency of the contraction traveling wave along the body, the larger is the swimming speed. This frequency ranges from 0.25 to 10 Hz.

fig. 1
Lamprey's spinal cord has ~ 100 segments. No matter what is the traveling wave frequency of the neuronal activity along the cord, the intersegmental phase lag remains $\sim 1\%$ of the period, the body length is ~ 1 wavelength. This constant phase lag is thought to be very important for coordinated movement generation during swimming. Note that this phase lag varies with the period of the wave, if expressed in absolute unit of time rather than in fraction of the period, hence it cannot be explained by mechanisms such as synaptic delays.

Cohen - Holmes - Rand (1982) : phase model.

Suppose that each segment is described by an oscillator, or by its phase ϕ_k . Suppose that the connectivity is local and that ϕ_k obey the following questions

$$\frac{d\phi_1}{dt} = \omega_1 + H_A (\phi_2 - \phi_1)$$



$$\frac{d\phi_k}{dt} = \omega_k + H_A (\phi_{k+1} - \phi_k) + H_D (\phi_{k-1} - \phi_k) \quad 1 < k < n$$

$$\frac{d\phi_n}{dt} = \omega_n + H_D (\phi_{n-1} - \phi_n)$$

where H_A is the ascending coupling (caudal - rostral)

H_D " descending " (rostral - caudal)

CHR initially chose $H_A = H_D = \sin[(\phi_{k+1} - \phi_k)2\pi]$ and supposed a systematical frequency gradient. Travelling wave solution was found but phase lag $(\phi_{k+1} - \phi_k)$ is not independent of k .

Experimentally, Cohen concluded that there is no systematical frequency gradient along the spinal cord.

Kopell - Ermentrout (1985-1991)

$\omega_k \equiv \omega$ not frequency gradient.

problem: find conditions on H_A and H_D such that

(1) a phase-locking solution exists and is stable

$$\frac{d\phi_k}{dt} = \Omega \text{ for } \forall k$$

$$\Leftrightarrow \frac{d\gamma_k}{dt} = 0 \quad \gamma_k = \phi_{k+1} - \phi_k$$

(2) $\gamma_k > 0$ (rostral-caudal wave)

$$\gamma_k = \text{const. indep. } k$$

except for k near 1 and n .

phase-locking \rightarrow

$$\begin{aligned}\Omega &= \omega + H_A(\gamma_1) \\ \Omega &= \omega + H_A(\gamma_k) + H_D(-\gamma_{k-1}) \quad 1 < k < n \\ \Omega &= \omega + H_D(-\gamma_{n-1})\end{aligned}$$

The way to find such phase-locking solution is through a continuum limit as $n \rightarrow \infty$, and the spinal cord is parametrized by a continuous x $x = \frac{k}{n}$ varies from $x=0$ (rostral end) to $x=1$ (caudal end).

We shall not go into details, but only sketch the main conclusions.

Assumptions on H_A and H_D : (1) there exist a range of $\gamma < 0$ say J , such that $H_A(\gamma)$ and $H_D(-\gamma)$ have each a unique zero, i.e. $H_A(\gamma_R) = 0$ $H_D(-\gamma_L) = 0$.

→ the boundary condition is

$$\gamma = \gamma_L \text{ at the rostral end } x=0$$

$$= \gamma_R \text{ at the caudal end } x=1$$

(2) $H_A(\gamma)$ is monotonically increasing in γ

$H_D(\gamma)$ "decreasing in γ "

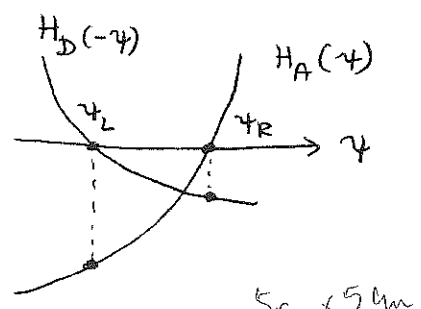
→ there is a unique solution to the phase-locking equations.

the form of the solution depends on which of the H_A and H_D "dominates".

We shall say that $H_A(\gamma)$ dominates if

$$|H_A(\gamma_L)| > |H_D(-\gamma_R)|$$

and $H_D(\gamma)$ dominates otherwise.



remark: if $H_A(\gamma) = \delta H_D(\gamma)$ proportional. then
 $(H_A \& H_D \text{ differ only by "synaptic strength"})$
 $H_A(\gamma_R) = \delta H_D(\gamma_R) = 0 \Rightarrow \gamma_L = -\gamma_R$

$$H_A(\gamma_L) = \delta H_D(\gamma_L) = \delta H_D(-\gamma_R)$$

→ H_A dominates iff $\delta > 1$

remark: $H_A \neq H_D$ otherwise no bias forces the wave unidirectional.

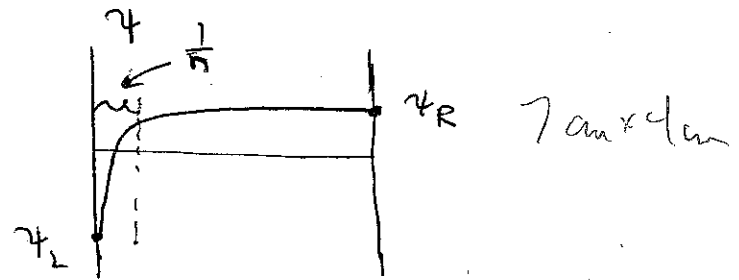
$H_A(0) \neq 0 \neq H_D(0) \rightarrow \text{no zero phase lag.}$

Theorem (Kopell-Ermentrout).

If H_A dominates \rightarrow

$$\gamma_k \approx \gamma_R$$

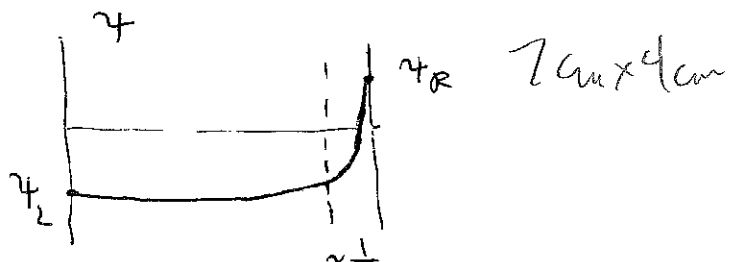
$$\Omega = \omega + H_b(-\gamma_R)$$



If H_D dominates \rightarrow

$$\gamma_k \approx \gamma_L$$

$$\Omega = \omega + H_A(\gamma_L)$$



(As a consequence, Ω is as closest as possible to the natural frequency ω .

which one to decide on? \rightarrow entrainment experiment.

further assumptions: let $f(\gamma) = H_A(\gamma) + H_D(-\gamma)$

- reasonable range of entrainment frequency $\left\{ \begin{array}{l} (3) f(\phi) = f(\phi_L) \text{ and } f(\phi) = f(\phi_R) \text{ each have 2 roots in J} \\ (4) f''(\phi) \neq 0 \text{ in J} \\ (5) f'(\phi_L) < 0 \text{ or } f'(\phi_R) > 0 \text{ holds.} \end{array} \right.$

Theorem: if H_A dominate, it is possible to entrain both above and (resp. H_D) below the rest frequency when forcing at the caudal end, but (resp. rostral) not at the rostral end.
(resp. caudal)

Specific experimental test seems to yield evidence supporting that H_A dominates.

fig. 2

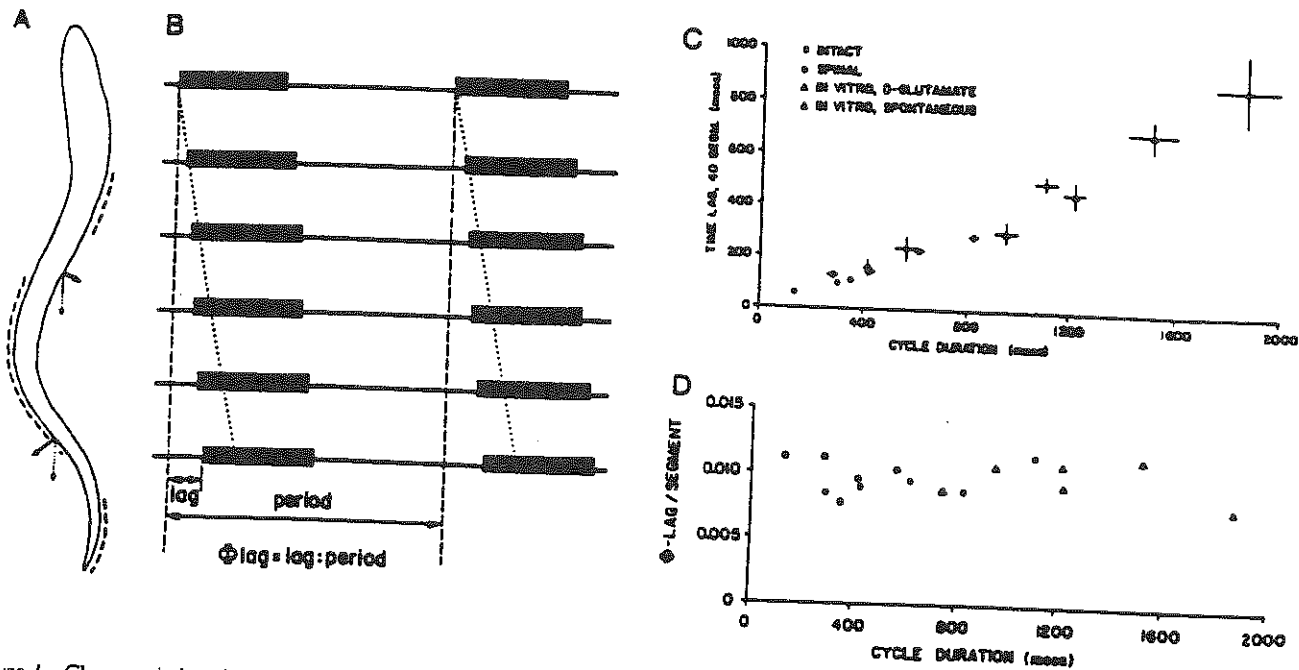


Figure 1 Characteristics of the actual swimming behavior in lamprey. A, body outline at one particular instance during swimming. Dotted lines denote regions of active muscle contraction. Arrows indicate forces being exerted against the water, with the caudally directed vector (dotted) propelling the animal forward. B, Schematic diagram indicating bursts of EMG activity in six segments in the rostral part of the body. There is a caudally directed electromyographical wave of contraction, resulting in a phase lag between consecutive segments. This intersegmental lag varies considerably in time with changing speed of locomotion (C; shown here for intact, spinal, and in vitro preparations), but constitutes a constant proportion of the cycle period (D), about 1% between adjacent segments, irrespective of the speed of swimming. (C,D: Modified from Wallén & Williams, 1984).

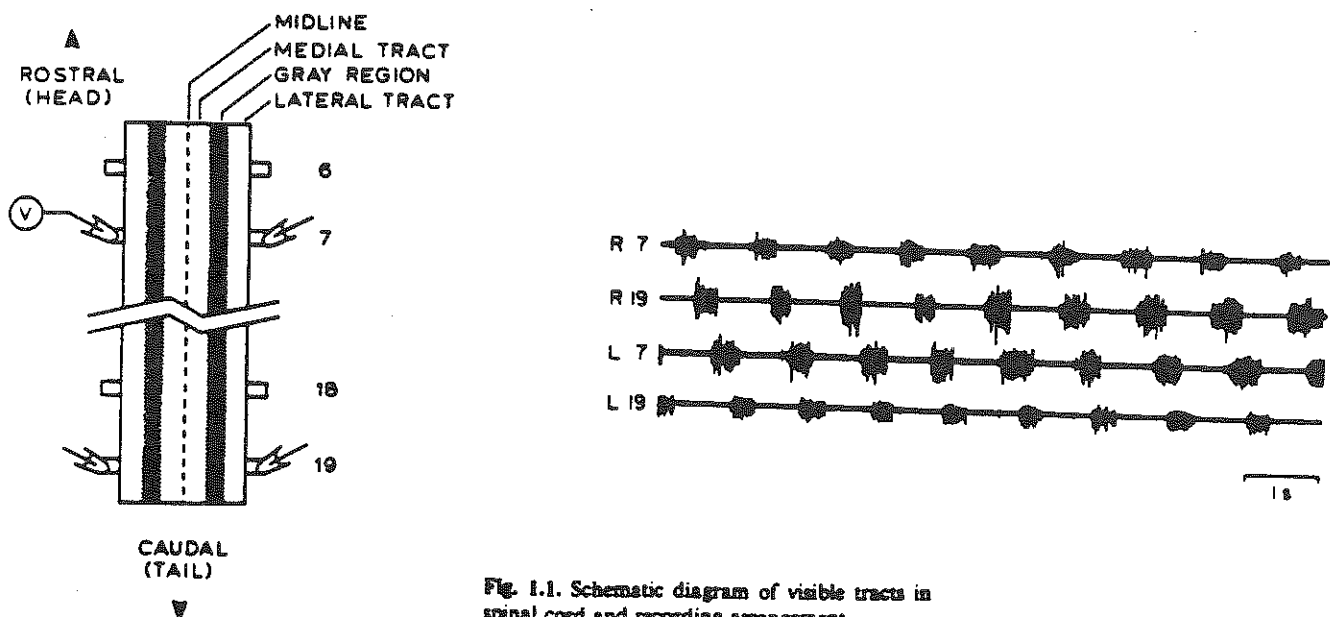


Fig. 1.1. Schematic diagram of visible tracts in spinal cord and recording arrangement

Fig. 12.1

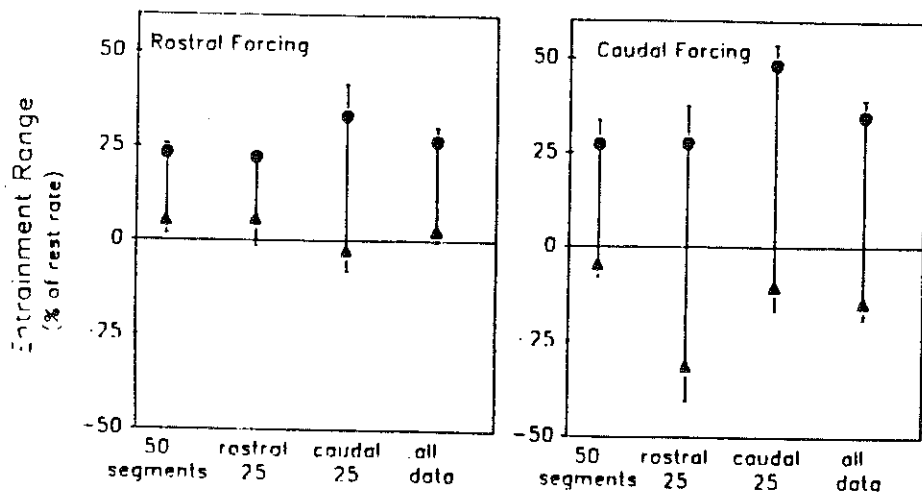


FIG. 7. Natural frequency provides the lower bound of the entrainment range for rostral forcing, whereas with caudal forcing entrainment can occur both above and below the natural frequency. Data from experiments listed in Table I. Natural frequency has been subtracted from the upper and lower limits of the entrainment range and divided by the rest rate. Hence zero represents the natural frequency. Each symbol represents the mean and standard error of the mean for each condition. "All data" represent the average of the 3 conditions for either rostral or caudal forcing. Filled circles, upper end of entrainment range; filled triangles, lower end. The difference between the lower limit of the entrainment range for rostral versus caudal forcing is statistically significant ($t = 3.35, P = 0.002$).

Fig. 12. 2

Lecture 13: Coupled oscillators III: Synchrony, clustering
 and effects of heterogeneity

Consider many oscillators as described by phase models which are coupled globally:

$$\frac{d\phi_i}{dt} = \omega_i + \frac{\epsilon}{N} \sum_{j=1}^N \Gamma(\phi_i - \phi_j) = F_i(\{\phi_j\})$$

The simplest choice for the coupling term is $\Gamma(\gamma) = -\sin \gamma$.

If $\epsilon > 0$ then the coupling favors bringing oscillators in phase by minimizing the phase differences $(\phi_i - \phi_j)$. If all oscillators are identical and have the same frequency $\omega_i = \omega$, then this network is quite trivial: all oscillators will be synchronized perfectly into a giant oscillator. Indeed, the solution exists such that

$$\phi_i^*(t) = \omega t + \phi_0 \quad \text{for } \forall i.$$

To study its stability, let $\gamma_i(t) = \phi_i(t) - \omega t$

$$\rightarrow \gamma_i^{ss} = \phi_i^*(t) - \omega t = \phi_0$$

The stability is given by the eigenvalues of the matrix

$$M = \left(\frac{\partial F_i}{\partial \gamma_j} \right) = \begin{pmatrix} a & & & & b \\ & a & & & \\ & & \ddots & & \\ b & & & \ddots & \\ & & & & a \end{pmatrix}$$

$\gamma_j = \gamma_j^*$

where $a = +\frac{\varepsilon(N-1)}{N} \Gamma'(0)$ and $b = -\frac{\varepsilon}{N} \Gamma'(0)$

$\det(M - \lambda I) = 0 \Rightarrow \lambda_1 = +\varepsilon \Gamma'(0)$ with multiplicity $(N-1)$

$\lambda_2 = 0$ (along the cycling direction)

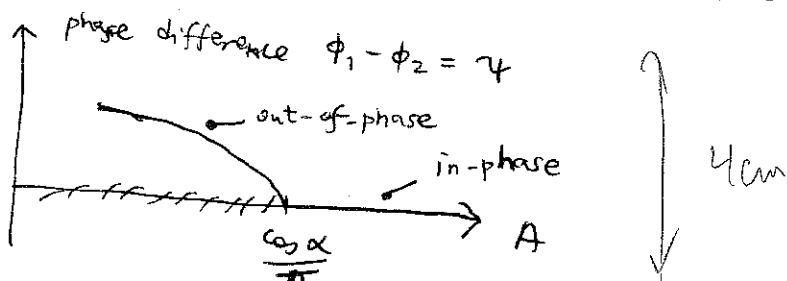
$\lambda_1 < 0 \Rightarrow$ stable.

However, if $\Gamma(\gamma)$ is not a sin-function, but a more general trigonometric function, then the situation is more interesting. For instance, in the type II case of the previous lecture, with $\beta = 0$, we have

$$\Gamma(\gamma) = -A \sin \alpha \sin \gamma + \frac{\sin 2\alpha}{4\pi} \sin 2\gamma$$

We have seen that with two oscillators, we have

either $\gamma_{ss} = 0, \pi$ or $\gamma_{ss} = \omega^{-1} \frac{A\pi}{\cos \alpha}$ if $\left| \frac{A\pi}{\cos \alpha} \right| < 1$



For N -oscillators, the in-phase state is stable as long as

$$A > A_C = \frac{\cos \alpha}{\pi} \quad \text{since}$$

$$\lambda_1 = \varepsilon \Gamma'(0) = \sin \alpha \left[-A + \frac{\cos \alpha}{\pi} \right]$$

But when A is decreased beyond A_C , the in-phase ("one-cluster") state becomes unstable and a "2-cluster" state appears, where the network splits into 2 clusters, oscillators in each cluster are in perfect synchrony but the 2 clusters have a phase shift, say Δ .

Suppose that the 2 clusters have respectively N_p and $N(1-p)$ oscillators, and described by 2 phases ϕ_1, ϕ_2 ($\Delta = \phi_1 - \phi_2$). Then the 2-cluster solution must satisfy

$$\frac{d\phi_1}{dt} = \omega + p \Gamma(\Delta) + (1-p) \Gamma(0)$$

$$\frac{d\phi_2}{dt} = \omega + p \Gamma(0) + (1-p) \Gamma(-\Delta)$$

$$\frac{d\Delta}{dt} = 0 \rightarrow p = \frac{\Gamma(0) - \Gamma(-\Delta)}{2\Gamma(0) - \Gamma(\Delta) - \Gamma(-\Delta)}$$

so there may be many such 2-cluster states.

One can study the stability of a 2-cluster state as in the case of the in-phase (1-cluster) state, and this yields

$$\begin{array}{lll}
 \lambda_1 = p \Gamma'(\alpha) + (1-p) \Gamma'(\Delta) & \text{multiplicity} & Np-1 \\
 \lambda_2 = (1-p) \Gamma'(\alpha) + p \Gamma'(-\Delta) & " & N(1-p)-1 \\
 \lambda_3 = p \Gamma'(-\Delta) + (p-1) \Gamma'(\Delta) & " & 1 \leftarrow \text{intercluster} \\
 \lambda_4 = 0 & " & \text{fluctuations} \\
 & & 1 \leftarrow \text{along the cycle}
 \end{array}$$

To further our discussions numerical simulations are needed.
 For more details see D Hansel et al (preprint 1993).

Exercise: consider

$\Gamma(\gamma) = -A \sin \alpha (\sin \gamma + \beta \cos \gamma) + \frac{1}{4\pi} \sin 2\alpha (\sin 2\gamma + \beta \cos 2\gamma)$.
 Analyse the 2-cluster state(s) and their eigenvalues both for
 $\beta = 0$ and $\beta \neq 0$. Under what conditions a 2-cluster state exists and is stable?

For a general coupling function $\Gamma(\gamma)$, there is usually a central parameter (like A in our simple case) which expresses the strength of "synchronizing interaction". As A is decreased, total synchrony will be lost, giving rise to phenomena of clustering (2-clusters, 3-clusters, etc.) ; and eventually to complete desynchronization (for small A).
 ↗

In the sense that every oscillator has a slightly different phase, and at each time instant the oscillators are uniformly distributed on the circle.

We shall now turn to the effects of heterogeneity, i.e.

when oscillators are not identical, each has its own ω_i . Assume that we have a well defined distribution $g(\omega)$ of frequencies, with

$$g(\omega + \omega_0) = g(\omega_0 - \omega).$$

Intuitively, the broader is the distribution $g(\omega)$, or the weaker is

the "synchronizing coupling" strength, the less

likely oscillators can be synchronized. It is a quite interesting

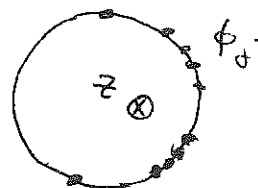
question to ask whether a population of such nonidentical oscillators can display a "macroscopic" synchronized rhythm.

Let us follow the original work of Y. Kuramoto and choose the simplest coupling form $\Gamma(\gamma) = -\sin \gamma$. The network is described by

$$\frac{d\phi_i}{dt} = \omega_i + \frac{\epsilon}{N} \sum_{j=1}^N \sin(\phi_j - \phi_i)$$

define

$$z = R e^{i\theta} = \frac{1}{N} \sum_{j=1}^N e^{i\phi_j}$$



then z is a "macroscopic variable" measuring the coherence. Due to the global character of the coupling, the network equation can be rewritten as

$$\boxed{\frac{d\phi_i}{dt} = \omega_i + \epsilon R \sin(\theta - \phi_i)}$$

Let $f(\omega, \phi, t)$ be the probability density for oscillators with frequency ω to be in the phase ϕ at time t ; $n(\phi, t)$ the number density of oscillators in the phase ϕ at time t .

$(\phi, \phi + d\phi)$

$$\rightarrow n(\phi, t) = \int_{-\infty}^{\infty} f(\omega, \phi, t) g(\omega) d\omega$$

$$\int_0^{2\pi} n(\phi) d\phi = 1$$

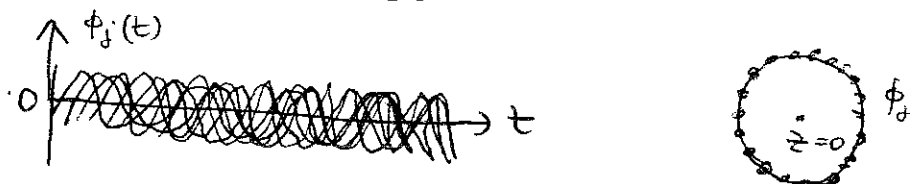
$$= \frac{1}{N} \sum_{j=1}^N \delta(\phi_j - \phi)$$

$$\& Z(t) = \int_0^{2\pi} n(\phi, t) e^{i\phi} d\phi.$$

We would like to seek a self-consistent equation for $Z(t)$.

Note that $n(\phi) = \frac{1}{2\pi}$ and $Z(t) \equiv 0$ is always a solution.

This corresponds to the incoherent state where oscillators are uniformly distributed over the circle.



On the other hand, for strong enough coupling strength ϵ , a novel solution with non-zero $Z(t)$ may exist. Due to the rotational invariance (under $\phi_j \rightarrow \phi_j + \phi_0$ for $\forall j$) of the original equation, this novel solution would have the simple form

$$Z(t) = R e^{i(\Omega t + \theta_0)}$$

where R is independent of time.

For this solution, we write

$$\frac{d\phi_i}{dt} = \omega_i + \epsilon R \sin(\theta_0 + \Omega t - \phi_i)$$

Let $\eta_i = \phi_i - \Omega t - \theta_0$

$\theta_0 \equiv 0$

$$\rightarrow \boxed{\frac{d\eta_i}{dt} = \Omega_i + \epsilon R \sin \eta_i} \quad \text{with } \Omega_i = \omega_i - \Omega.$$

We need to solve R and Ω . If η_i can be solved for each i , then we shall obtain $n(\eta, z, t)$ and a self-consistent equation

$$z = \int_0^{2\pi} n(\eta, z, t) e^{i\eta} d\eta.$$

Now, clearly the oscillators have to be divided into 2 categories.

(A)

$$\left| \frac{\Omega_i}{\epsilon R} \right| < 1 \rightarrow \eta_i^{ss} = \sin^{-1} \left(\frac{\Omega_i}{\epsilon R} \right)$$

which is stable whenever it exists.

(B)

$$\left| \frac{\Omega_i}{\epsilon R} \right| > 1 \rightarrow \eta_i(t) \text{ cannot be steady in time.}$$

Contributions from the two groups to n and z can be separated.

$$n = n_A + n_B$$

$$z = z_A + z_B$$

For group A, oscillators asymptotically have fixed phases ψ_i .

$$\rightarrow P_A(\psi, t) = \delta(\psi - \psi^{ss}) = \delta(\psi - \sin^{-1} \frac{\omega - \Omega}{\varepsilon R})$$

$$n_A = \int_{-\Omega + \varepsilon R}^{\Omega + \varepsilon R} \delta(\psi - \sin^{-1} \left(\frac{\omega - \Omega}{\varepsilon R} \right)) g(\omega) d\omega$$

$$= \varepsilon R \cos \psi g(\Omega + \varepsilon R \sin \psi) \quad |\psi| \leq \frac{\pi}{2}.$$

On the other hand, for group B, each oscillator moves with its own speed $\Omega_i = \varepsilon R \sin \psi_i$. So the motion for those oscillators is expected to be ergodic on a torus of dimension equal to the number of oscillators in this group.

$$\rightarrow P_B \propto \frac{F(\omega - \Omega)}{|\omega - \Omega - \varepsilon R \sin \psi|}$$

$$n_B = \int_{-\infty}^{-\Omega + \varepsilon R} + \int_{\Omega - \varepsilon R}^{+\infty} P_B g(\omega) d\omega$$

$$= \int_{\Omega - \varepsilon R}^{+\infty} g(\omega) \frac{F(\omega - \Omega)}{(\omega - \Omega)^2 - \varepsilon^2 R^2 \sin^2 \psi} d\omega$$

because $n_B(\psi + \pi) = n_B(\psi)$, $Z_B = \int_0^{2\pi} n_B(\psi) e^{i\psi} d\psi = 0$

hence does not contribute to Z .

$$\rightarrow R = \int_{-\frac{\pi}{2}}^{\frac{\pi}{2}} \varepsilon R \cos \psi g(\omega_0 + \varepsilon \sin \psi) e^{i\psi} d\psi$$

or $\int_{-\pi/2}^{\pi/2} d\psi g(\omega_0 + \varepsilon \sin \psi) \cos \psi \sin \psi = 0 \rightarrow \underline{\omega_0 = \omega_0}$

$$\varepsilon \int_{-\pi/2}^{\pi/2} d\psi g(\omega_0 + \varepsilon \sin \psi) \cos^2 \psi = 1$$

for small ε , we can expand $g(\omega_0 + \varepsilon \sin \psi)$ as

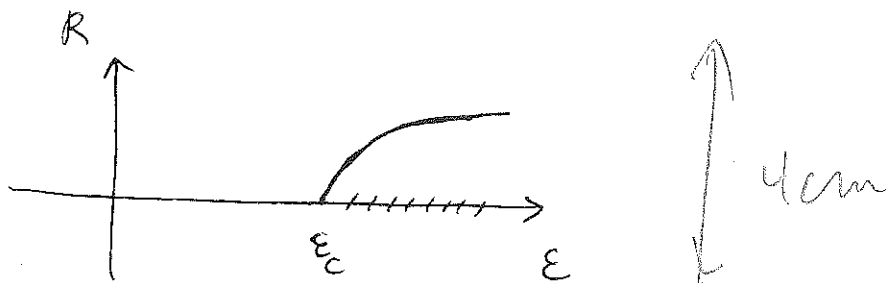
$$g(\omega_0 + \varepsilon \sin \psi) = g(\omega_0) + \frac{(\varepsilon)^2}{2} g''(\omega_0) \sin^2 \psi + \dots$$

$$\rightarrow 1 - \frac{\pi}{2} \varepsilon g(\omega_0) - \frac{\pi}{16} \varepsilon^3 g''(\omega_0) R^2 + \mathcal{O}(R^3) = 0$$

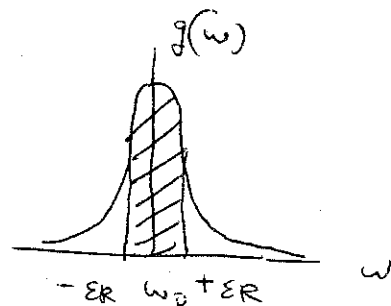
$$\rightarrow \text{solution exists if } \varepsilon > \varepsilon_c = \frac{2}{\pi g'(\omega_0)}$$

$$R = \left\{ \frac{1 - \frac{\pi}{2} \varepsilon g(\omega_0)}{\frac{\pi}{16} \varepsilon^3 g''(\omega_0)} \right\}^{1/2}$$

$$\underline{g''(\omega_0) < 0}$$



Therefore, for $\varepsilon > \varepsilon_c$, there exists a new solution where a subpopulation of oscillators with $\left| \frac{\omega - \omega_0}{\varepsilon R} \right| < 1$ become coherent, while the rest of the population (with $\left| \frac{\omega - \omega_0}{\varepsilon R} \right| > 1$) are incoherent and does not contribute to the "macroscopic observable" $Z(t)$.



Question = stability ?

S. Strogatz & RE Mirollo (1991), the incoherent state $Z = 0$ is unstable for $\varepsilon > \varepsilon_c$, but is marginally stable for $\varepsilon < \varepsilon_c$.
 (nonlinearly?)

exercise: consider more complicated $\Gamma(\gamma)$ such as

$$\Gamma(\gamma) = -A \sin \alpha (\sin \gamma + \beta \cos \gamma) + \frac{1}{4\pi} \sin 2\alpha (\sin 2\gamma + \beta \cos 2\gamma).$$

for integrate-and-fire networks with heterogeneity see

- Tsodyks et al.
- Abbott
- Kuramoto.

Lecture 14: Rhythmic oscillations in a network of inhibitory neurons

In the previous lectures, we discuss models for coupled neurons like phase-models or integrate-and-fire models. We have been concerned with oscillatory units and how such units in a network can become synchronized by excitatory connectivity (mutual excitation). This time we shall discuss rhythogenesis and synchrony in a population of exclusively inhibitory neurons.

In mammals, electroencephalography revealed several types of electrical brain waves during different stages of wakefulness and sleep.

fig. 1 shows some examples (α , θ , spindle, δ waves)

fig. 2 population rhythm versus single cell activity (θ -wave) we shall be focused on the spindle oscillation.

It consists of episodes of "10 Hz" (7-14 Hz) rhythmic activities that recur at a frequency of $\sim 0.1 \text{ Hz}$ (figs. 3-4). note the mostly subthreshold oscillation in thalamic relay cells. extensive experimental investigations since the 40's showed that the thalamus is a "pacemaker" of this neuronal oscillation synchronized over most parts of the cortex.

The thalamus consists of ~50 segregated nuclei,
figs. 5-6 e.g. LGN, MGN etc.; and the reticular nucleus that
(RTN)
is a thin sheet of neurons partly surrounding the (dorsal) thalamus.

P. Anderson: principal neurons in thalamic nuclei are endowed with a "post-inhibitory rebound" property. If they interact with a pool of inhibitory neurons, then a population rhythm may be generated in the way illustrated in fig. 7

- problem:
- no interneurons in many relay nuclei (e.g. VB) of rodents
 - no evidence for inter-nuclear fibers and yet major nuclei are synchronized during spindles.

M. Steriade provided evidence which suggested that RTN may supply the long-lasting inhibition and may synchronize various segregated nuclei because of its widespread projections. Some experiments even suggest that RTN alone can display the 10 Hz spindle oscillation with a high degree of population synchrony.

→ interesting question: RTN contains only GABAergic cells. Those cells have the PIR property, and are mutually coupled. How such a purely inhibitory network can generate synchronized oscillations?

modeling

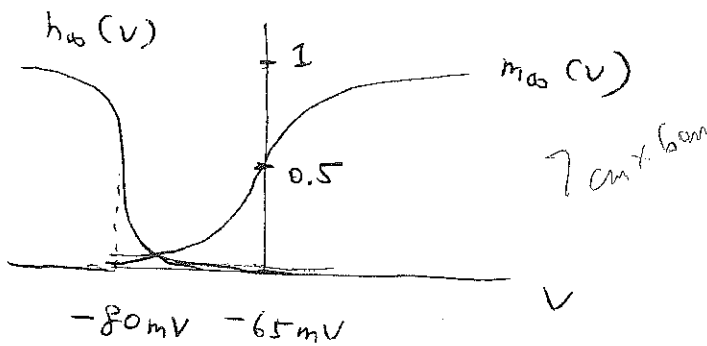
Step I : cellular basis of PIR

Llinás et al identified an intrinsic conductance as ionic basis of PIR in thalamic cells, the low-threshold (T-type) calcium current (I_T). Recent voltage-clamp data on I_T made it possible to construct a kinetic model of I_T . fig.8

$$I_T = g_T m^3 h (V - V_{Ca})$$

$$\frac{dm}{dt} = \frac{m_\infty(V) - m}{\tau_m(V)}$$

$$\frac{dh}{dt} = \frac{h_\infty(V) - h}{\tau_h(V)}$$



$h_\infty(V)$ is located far to the left of the resting membrane potential ($\sim -65 \text{ mV}$), so hyperpolarization is needed to increase it (for I_T to be

"de-inactivated". Since $\tau_h(V)$ is relatively large ($\gtrsim 30 \text{ ms}$), hyperpolarization

must be maintained for a long enough period of time.

Known I_T , the most parsimonious model of thalamic cell is with I_T and a leakage current

$$C_m \frac{dV}{dt} = -I_T - I_L + I_{app} \quad I_L = g_L (V - V_L)$$

Indeed, this is a simplest ion model of cell with PIR.

Figs. 8-11

Step II: 2-coupled cell.

let $m = m_\infty(V)$ (activation is fast), then each cell is described by only 2 variables (V, h). Consider 2 such cells coupled by a synaptic term,

$$C_m \frac{dV_i}{dt} = -g_T m_\infty^3(V_i) h_i (V_i - V_A) - g_L (V_i - V_L) - s_j g_{syn} (V_i - V_{syn})$$

$$\frac{dh_i}{dt} = (h_\infty(V_i) - h_i)/\tau(V_i)$$

$$\frac{ds_i}{dt} = S_\infty(V_i)(1 - s_i) - k_r s_i \quad k_r: \text{synaptic decay rate.}$$

the synaptic current $I_{syn} = g_{syn} s (V - V_{syn})$, s is the synaptic activation variable (= fraction of synaptic ion channels which are open). We suppose that

$$S_\infty(V) = \frac{1}{1 + e^{-(V - \theta_{syn})/k_{syn}}} \quad \theta_{syn} = \text{threshold.}$$

instantaneous synapse: $s_i = S_\infty(v_i) \rightarrow$ anti-phase (half-center)

oscillation. If $S_\infty(v)$ is very steep (k_{syn} small), then $s_i = S_\infty(v_i)$ is essentially either zero or one. Thus one can look at the (v, h) -phase plane with $s=0$ (free state) or $s=1$ (inhibited state). During a half-center oscillation, the 2 cells switch their states periodically in time. This picture suggests a way to do mathematical analysis by singular perturbation techniques.

Two mechanisms: release (fig. 12) } relevant to
escape (fig. 13) } central pattern generator systems
cf. R. Calabrese
TINS Sept. 1992

How to make the 2 cells synchronous? figs. 14-15

- synaptic current should outlast significantly the presynaptic burst $\rightarrow k_r$ should be sufficiently small.
- rebound excitation via escape rather than release $\rightarrow g_T$ should be sufficiently large

interpretation: $GABA_A$ $k_r \approx 20 \text{ ms}^{-1}$ $v_{syn} = v_L \approx -70$
 $GABA_B$ $k_r \approx 200 \text{ ms}^{-1}$ $v_{syn} = v_K \approx -80 \text{ to } -90$

Step III: N -coupled cells with global connectivity

$$C_m \frac{dV_i}{dt} = -I_T^i - I_L^i - \frac{1}{N} \sum_{j=1}^N g_{syn} s_j^i (V_i - V_{syn})$$

every cell receive exactly
the same input

$$g_{syn} s (V_i - V_{syn})$$

$$s = \frac{1}{N} \sum_{i=1}^N s_i^i$$

for $N \rightarrow \infty$, one can study separately the homogeneous limit

cycle (total synchrony) and the stationary state (total asynchrony)
uniform-phase distribution

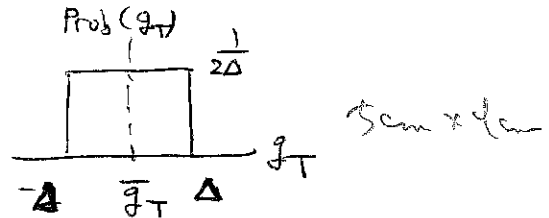
effect of heterogeneity: g_T is not a well known quantity, and
is likely a parameter value varying from one cell to another. Suppose
that we have a distribution of g_T . Then,

individual cells are no longer identical.

If they oscillate, they have different
frequencies & amplitudes. Do we still have population rhythms?

What are properties of population fluctuations?

"macroscopic variables" (1) $\langle s \rangle(t) = \frac{1}{N} \sum_{i=1}^N s_i(t)$; (2)
 $\langle V \rangle(t) = \frac{1}{N} \sum_{i=1}^N V_i(t)$; (3) # of cells $> \theta_{syn}$.



- small $\Delta \rightarrow$ synchrony persist

- moderate $\Delta \rightarrow$ clusters figs. 16-18

- large $\Delta \rightarrow$ asynchrony

BIORHYTHMS

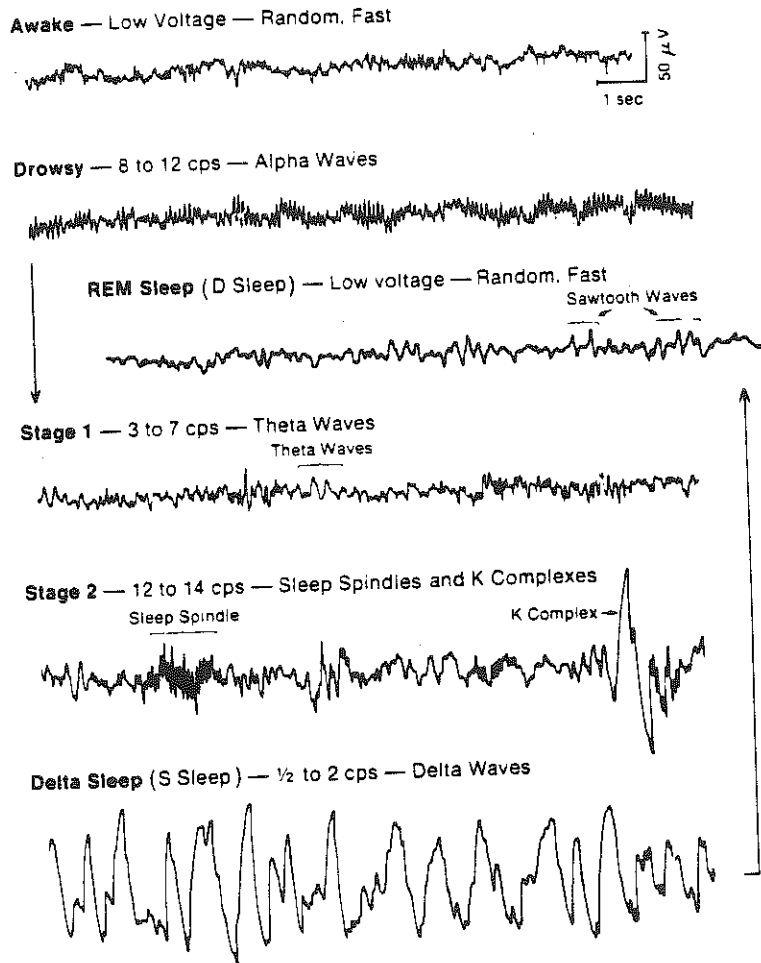


Fig. 25.10 Stages of sleep, as recorded in the electroencephalogram of the human. See text. (Modified from Hauri, 1977)

fig. 14.1

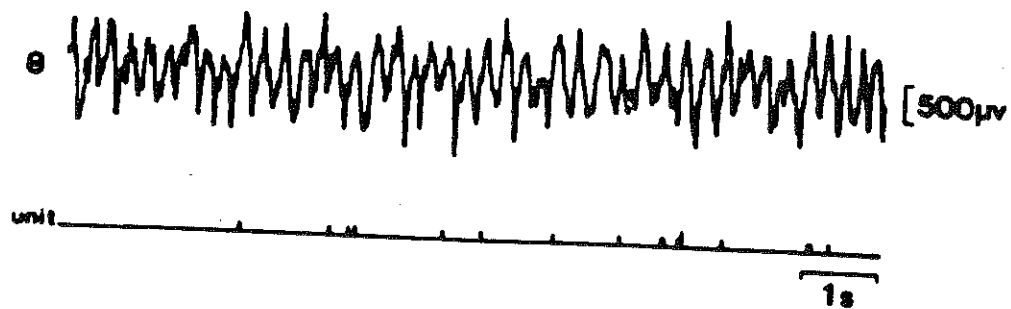
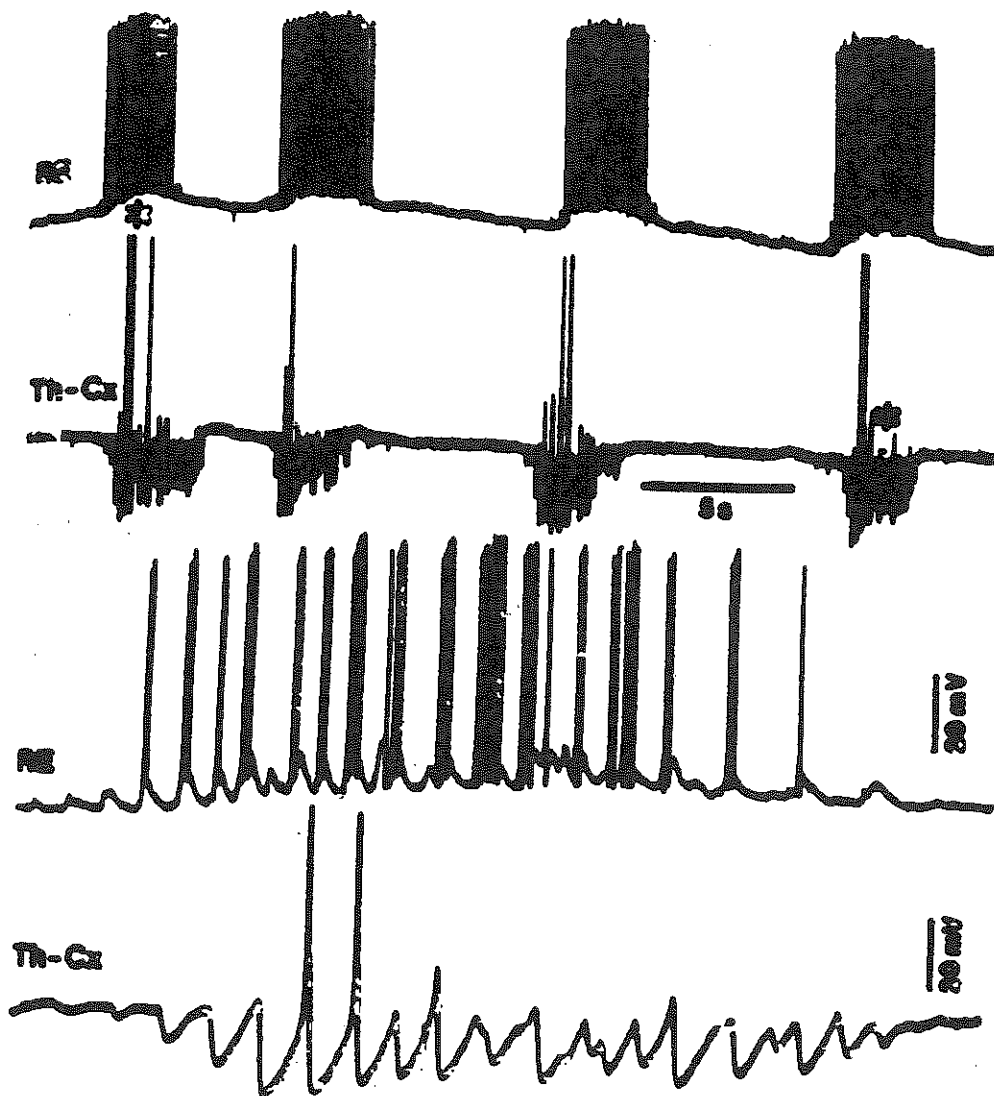
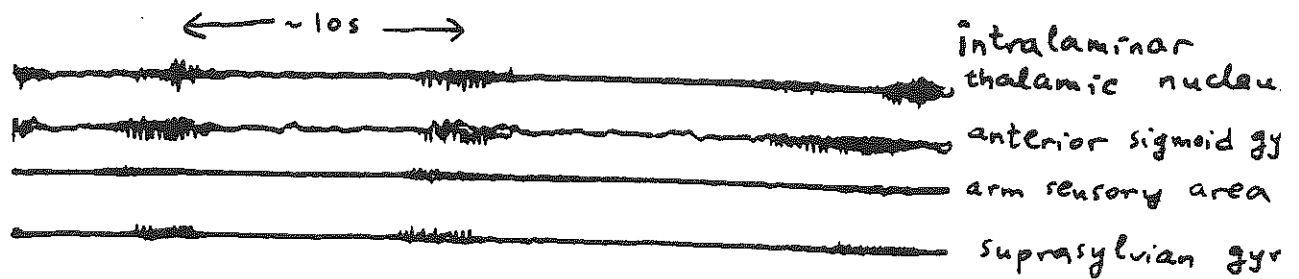


Figure 1.5. Simultaneous recording of theta activity and a single unit (neuron) in the rat entorhinal cortex. Note the apparently irregular firing of the unit. (From Alonso and Garcia-Austt, 1987b, with permission.)

fig. 14. 2



intraspindele bursting at 7-14 Hz

fig. 14.3

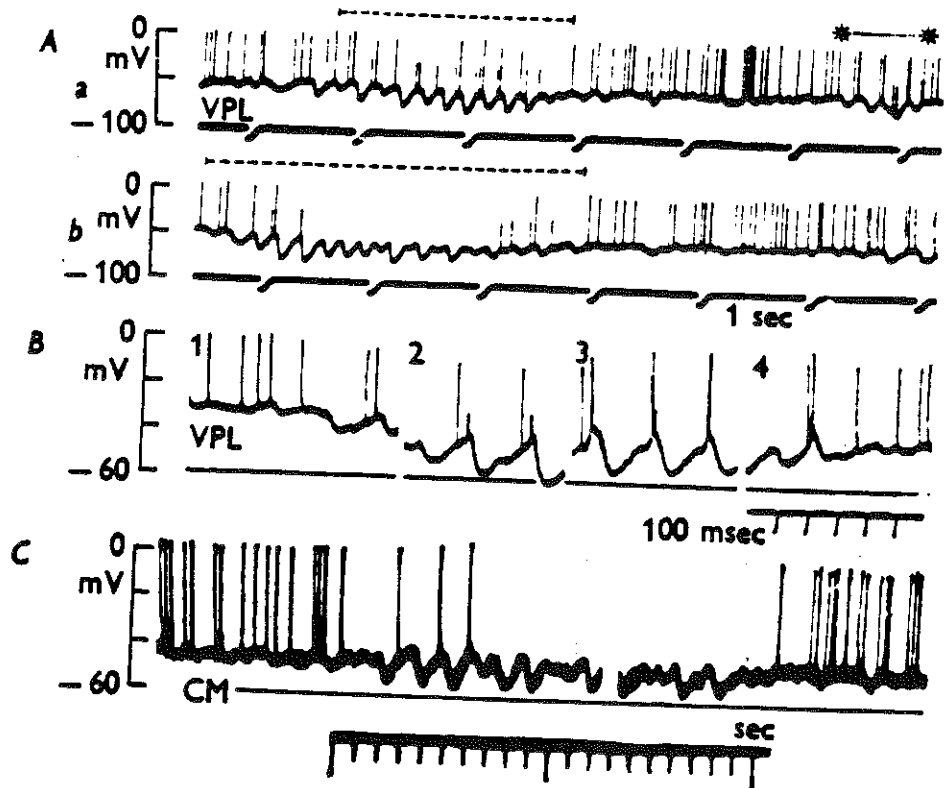


Fig. 3. Intracellular records of spontaneous thalamic spindles. All records are taken with a d.c.-coupled amplifier. *A.* *b* is the continuation of *a*. The time scale tracing also indicates the -100 mV level. Two spindles are indicated by broken lines, and an abortive spindle by two asterisks connected by an interrupted line. *B.* Excerpts of records taken with a d.c.-coupled amplifier at various stages during different spindles. 1 and 2 are two stages of the start of the spindle, 3 is from the middle, and 4, from the end of the spindle. *C.* Excerpts of records taken from a cell in the centre median (CM), the first showing the onset of a spindle, and the last, the end of another. Time scale, $\frac{1}{16}$ and 1 sec.

P. Andersen et al (1968)

Fig. 14. 4

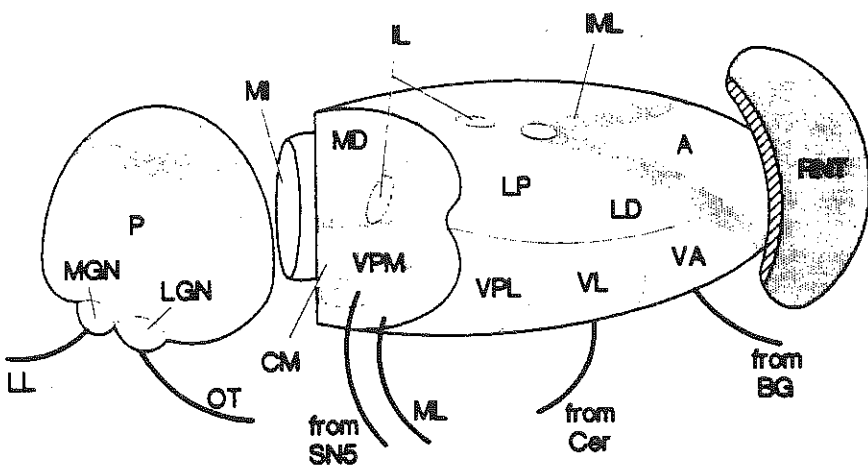


FIG. 8.1. Schematic three-dimensional view of right thalamus with many of its major nuclei. A cut is placed in the posterior part to reveal a representative cross section. Some of the important ascending afferents are also shown. To prevent obscuring of the dorsal thalamus, only the rostral tip of the reticular nucleus of the thalamus (RNT) is shown. Other abbreviations: A, anterior; BG, basal ganglia; Cer, cerebellum; CM, centromedian; IL, intralaminar nuclei; IML, internal medullary lamina; LD, lateral dorsal; LGN, lateral geniculate nucleus; LL, lateral lemniscus; LP, lateral posterior; MD, mediodorsal; MGN, medial geniculate nucleus; MI, midline nuclei; ML, medial lemniscus; OT, optic tract; P, pulvinar; SN5, main sensory and spinal nuclei of the 5th nerve; ST, spinothalamic; VA, ventral anterior; VPL, ventral posterolateral; VPM, ventral posteromedial. See E. G. Jones (1985) for details of connectivity of these nuclei. (Redrawn from Brodal, 1981.)

fig. 14.5

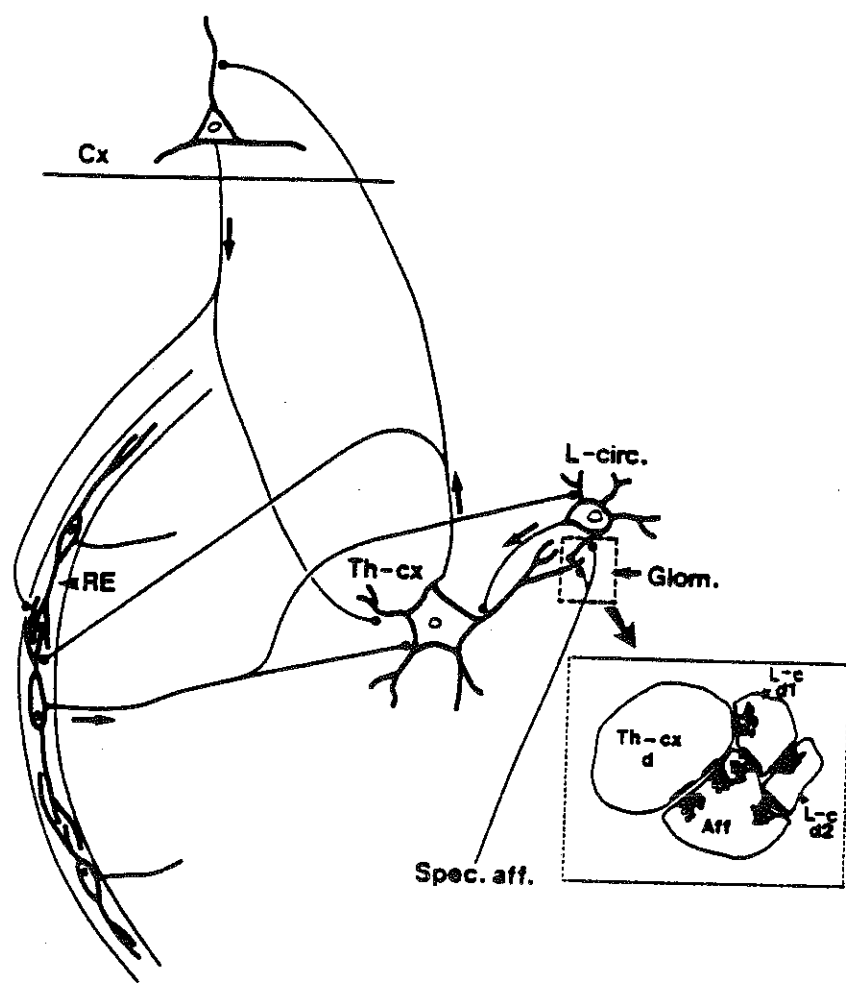


fig. 14.6

(14.7)

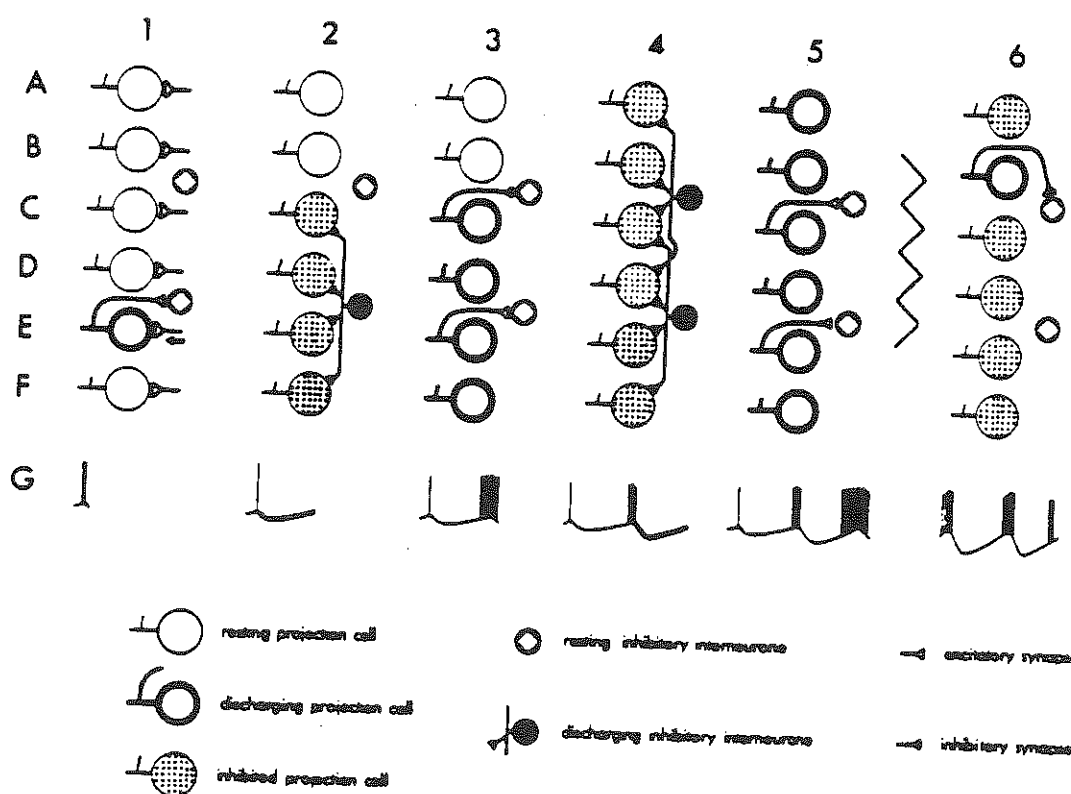
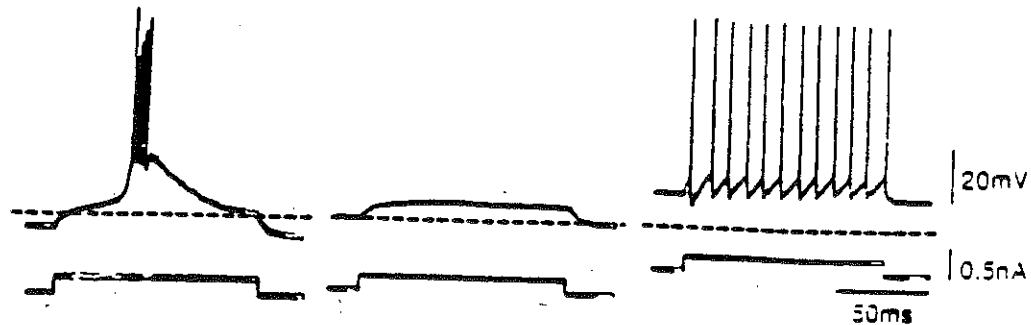


Fig. 14.7

Thalamic Neurons: 2 modes of activity (Llinás 1984)



Bursting

Repetitive Spiking



key cellular property: post-inhibitory rebound

ionic basis: T-type calcium channel I_T

fig. 14.8

(14.8)

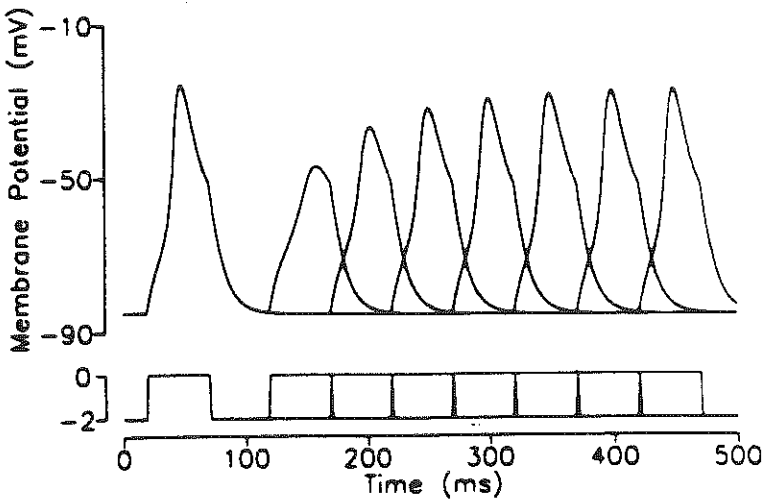


Fig.1. Release from a holding hyperpolarizing current produces an initial low threshold spike (LTS). A second release pulse of 50 ms is applied at increasing latencies. Near full recovery appears after a refractory time of about 100 ms. The unit of applied current is $\mu\text{A}/\text{cm}^2$. See Appendix for parameter values.

fig. 14.9

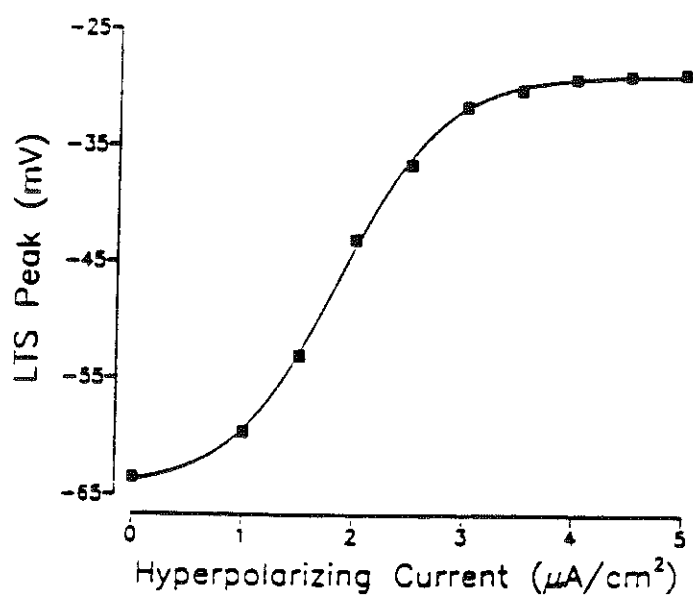
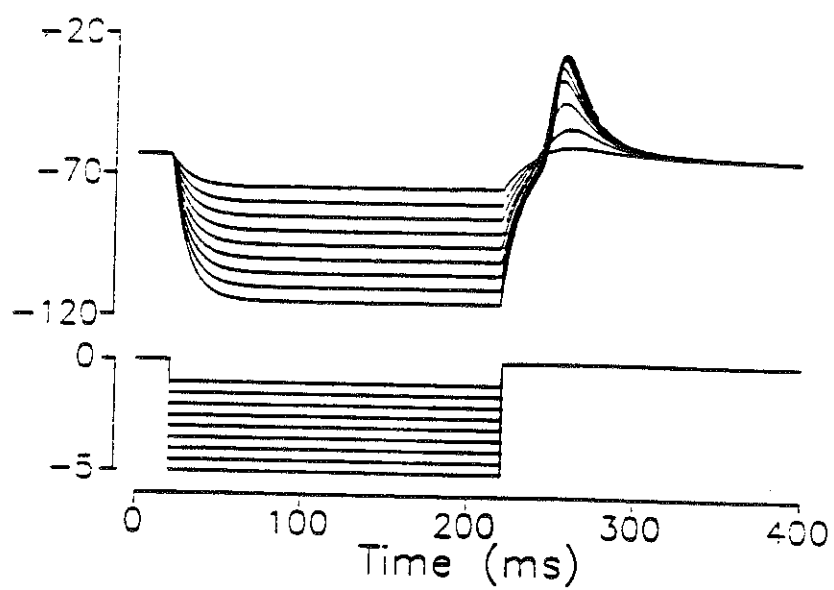


Fig. 14-10

(14.9)

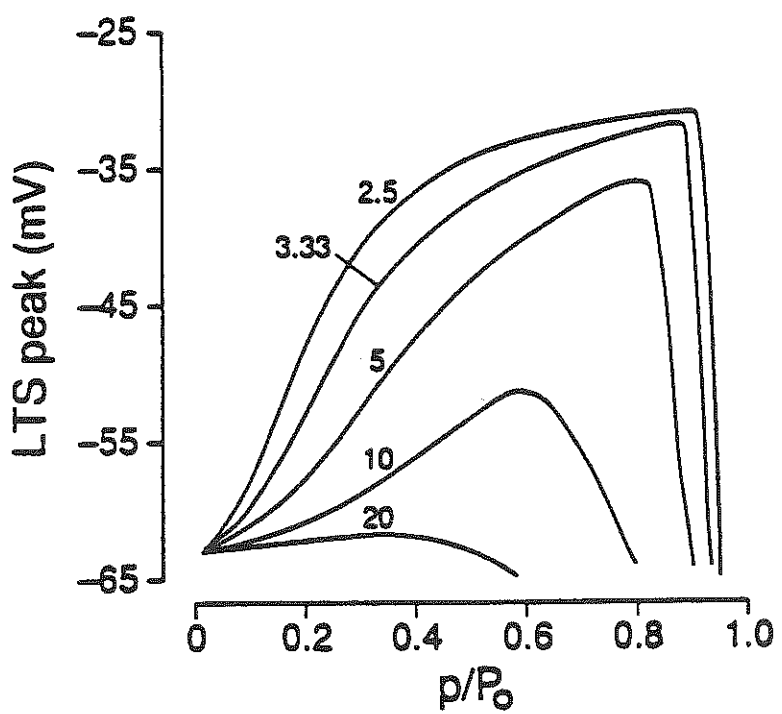
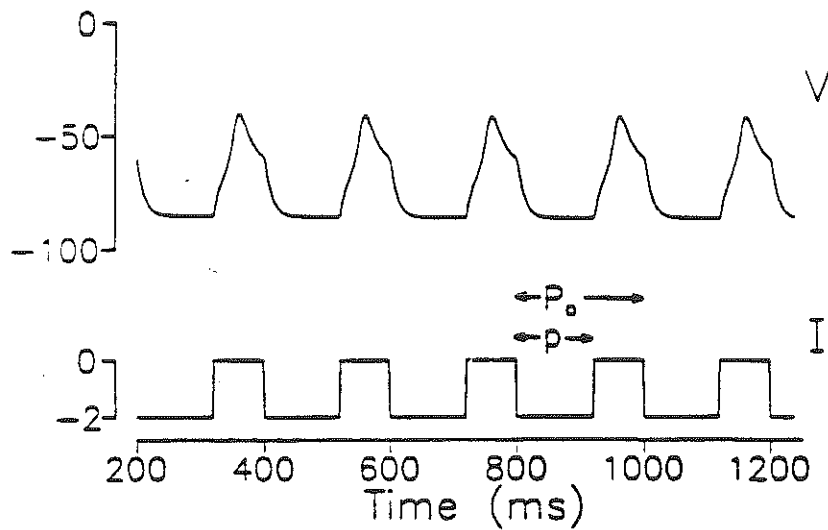


fig. 14.11

Instantaneous synapses: $s_i = S_{\infty}(v_i)$

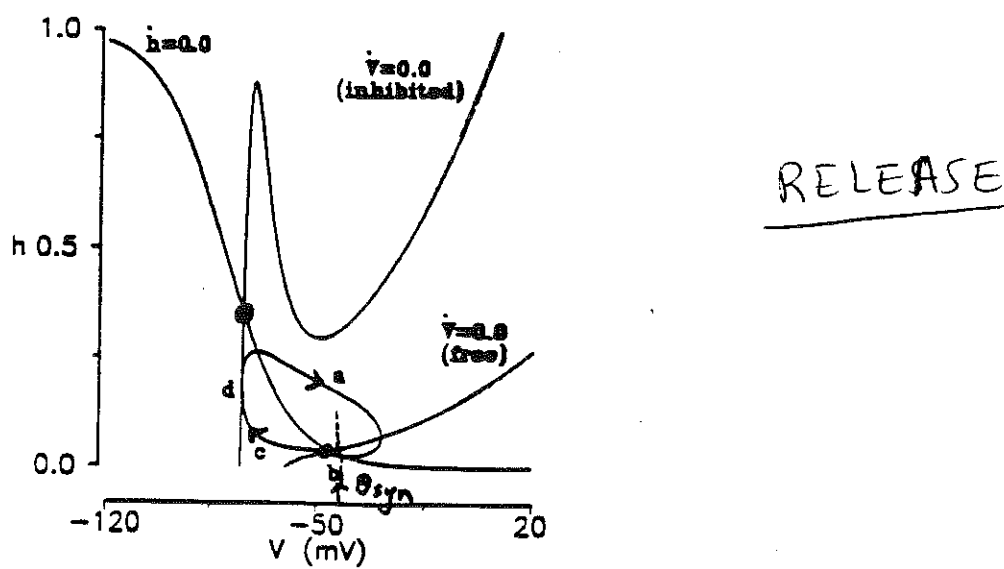
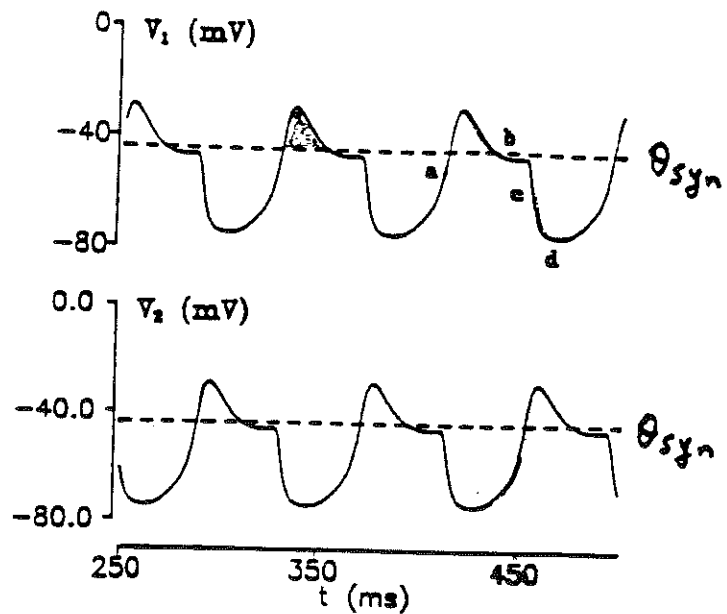


fig. 14.12

(14.10)

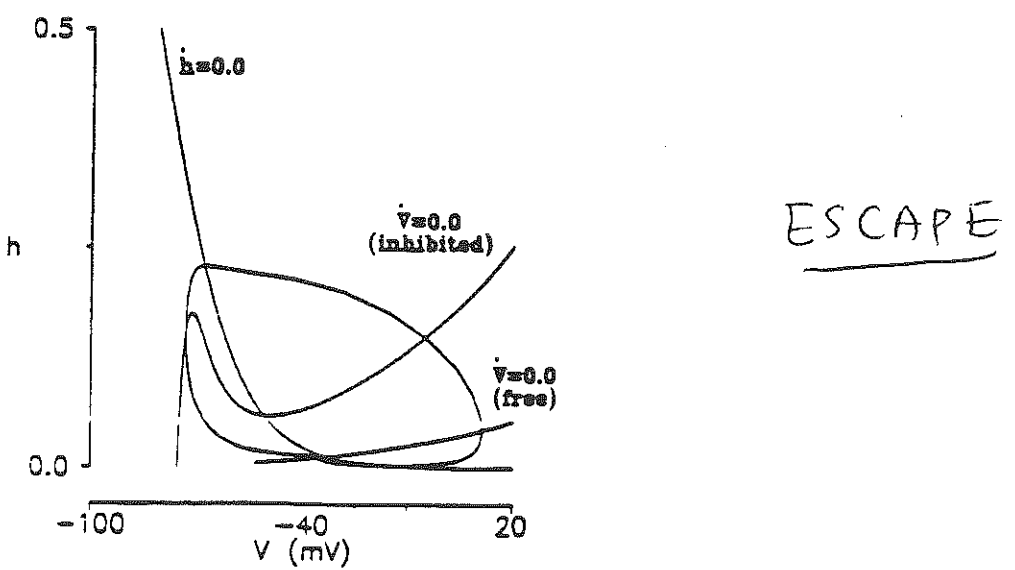
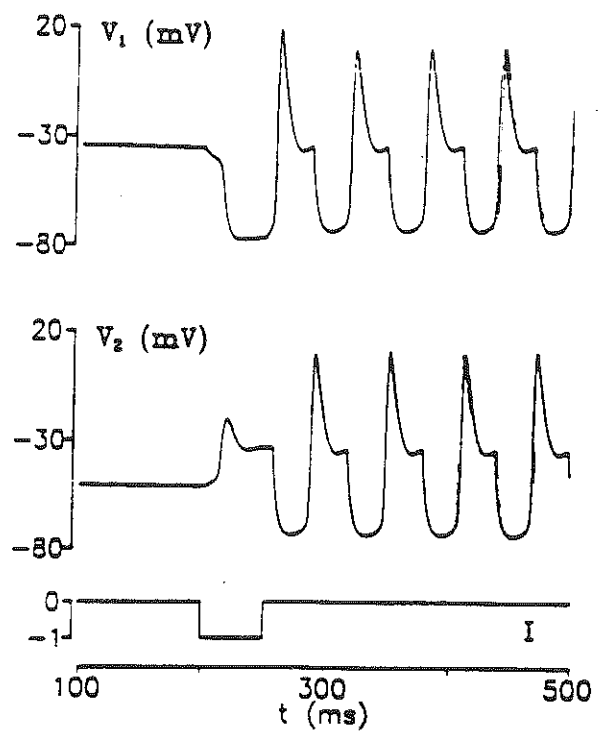


fig. 14.13

Synchronizing neurons by mutual inhibition

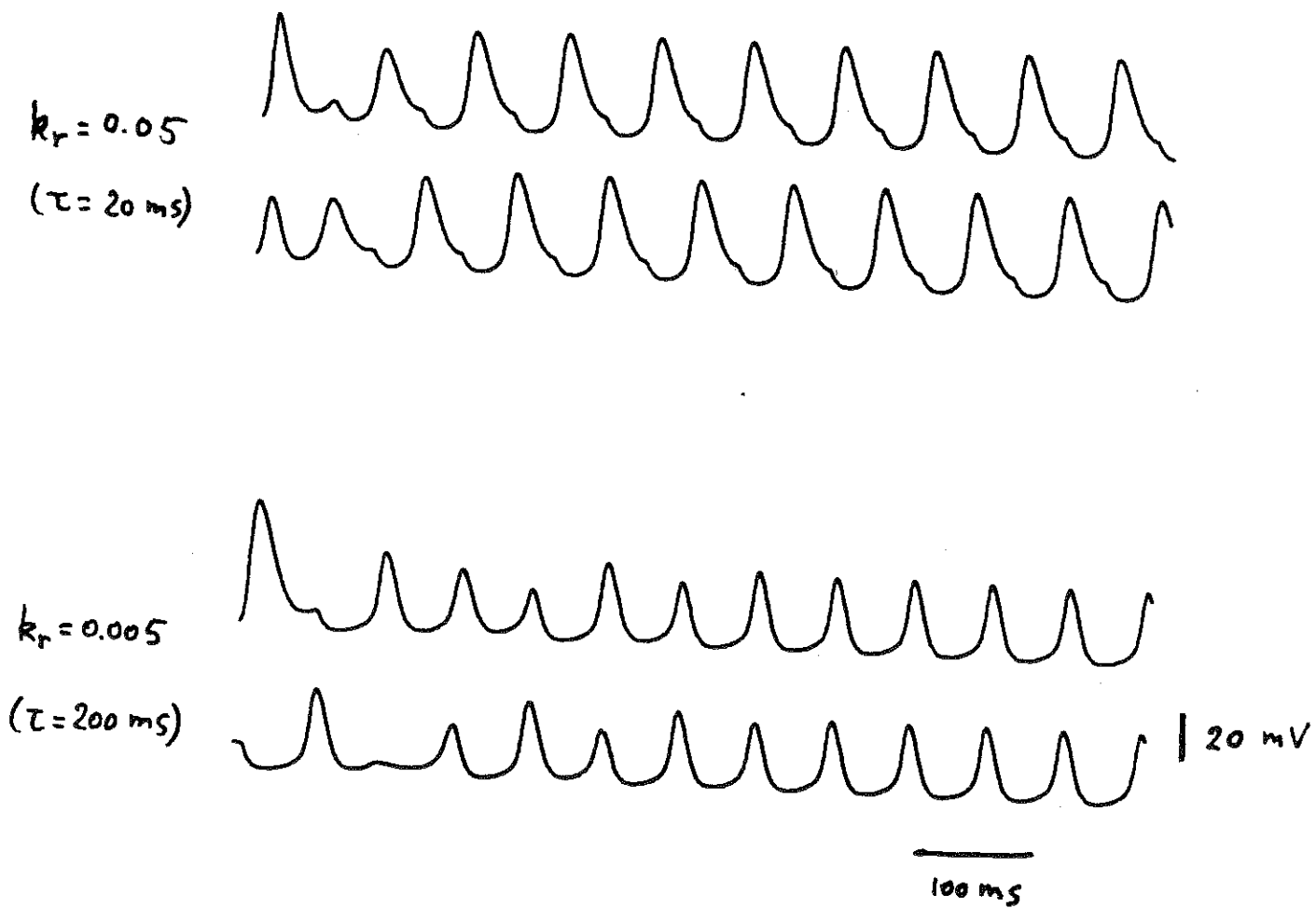


Fig.14.14

14.11

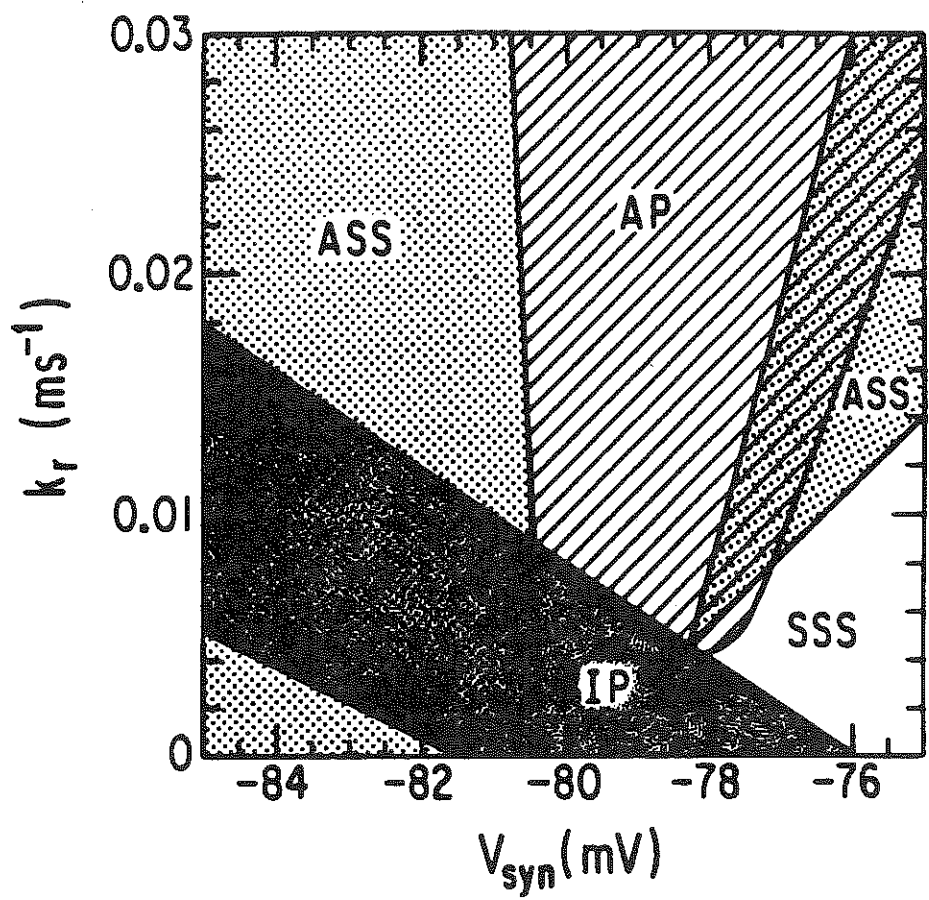
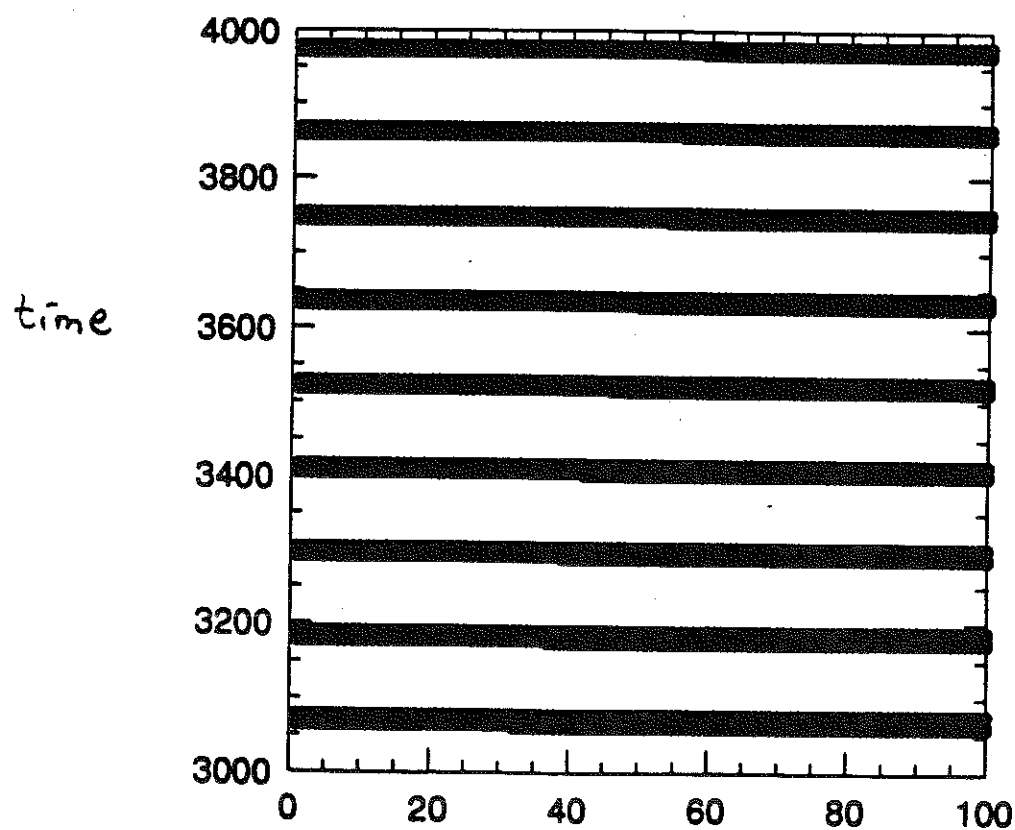
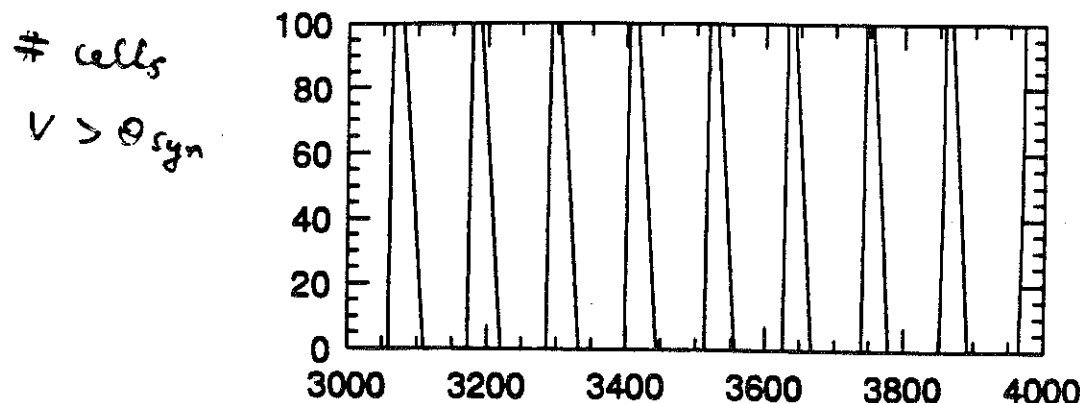


fig. 14.15

$$\bar{g}_T = 1.8 \quad \Delta = 0.01$$



cell label

N = 100

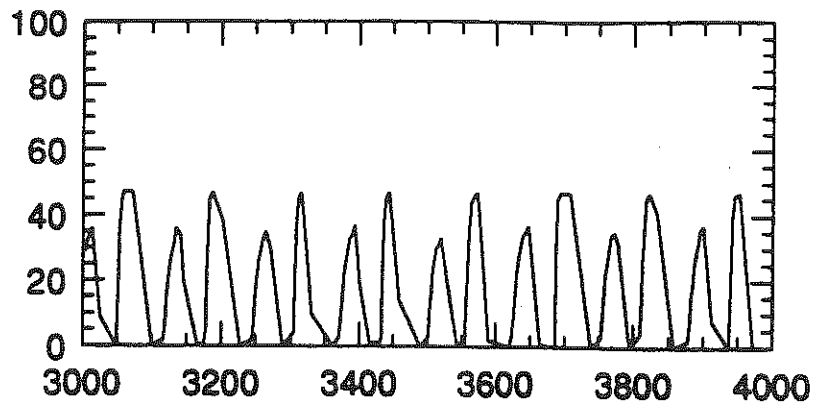
fig. 14, 16

(14.12)

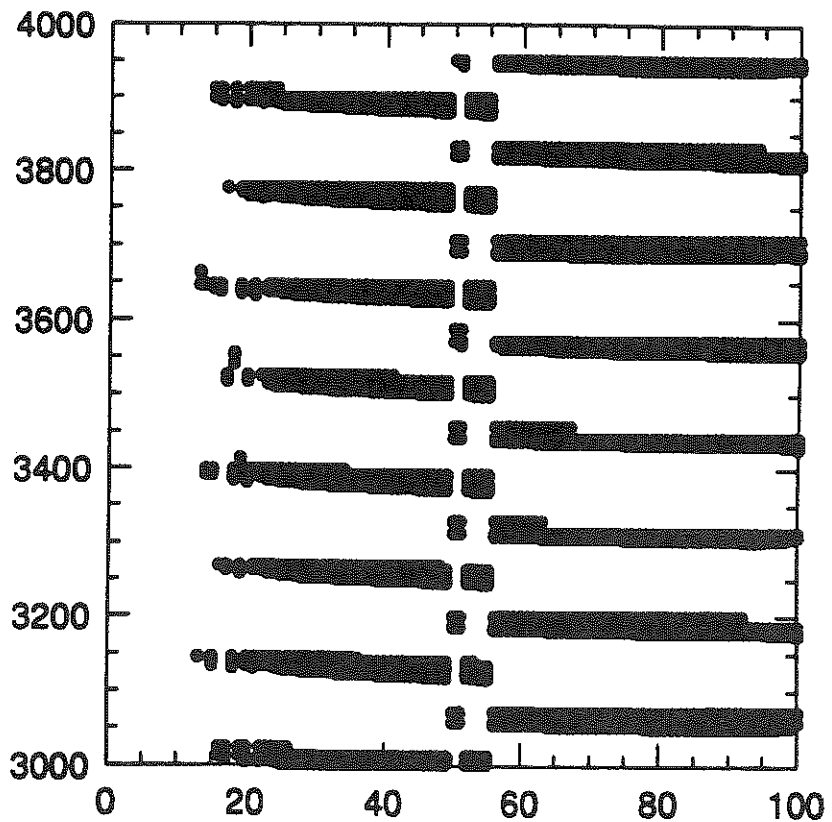
$$\bar{\sigma}_T = 1.8 \quad \Delta = 0.2$$

cells

$V > \theta_{syn}$



time

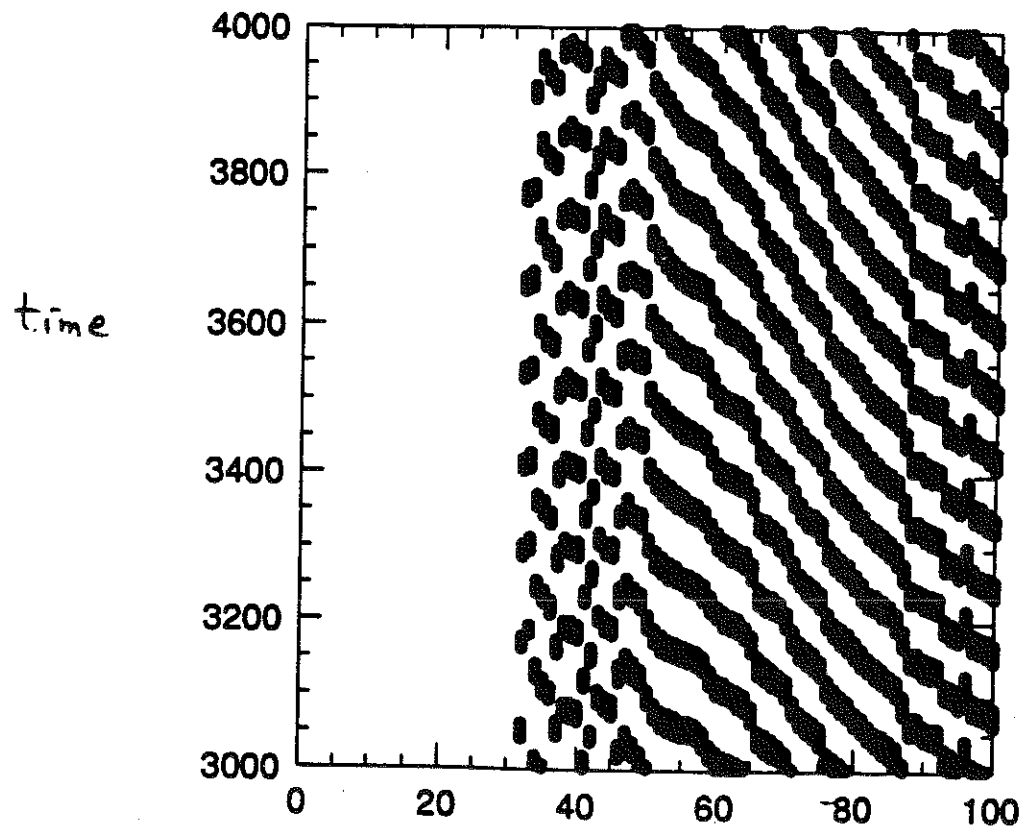
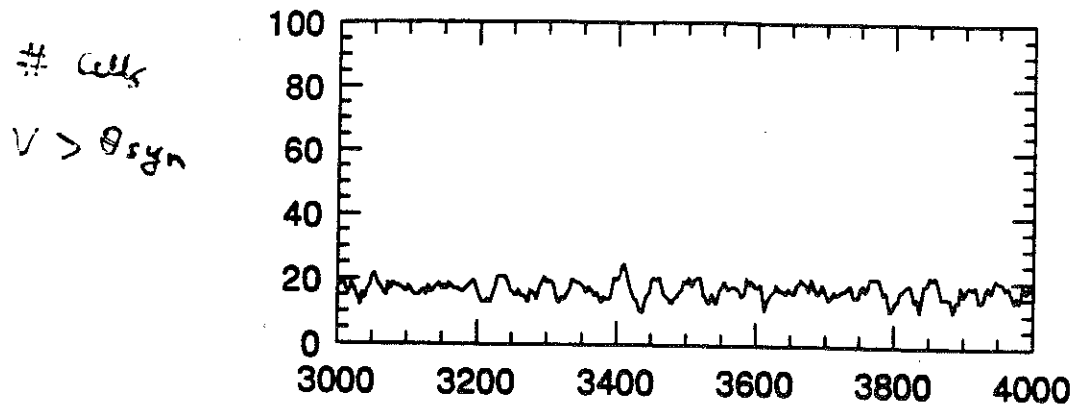


cell label

$N = 100$

fig. 14.17

$$\bar{g}_T = 1.8 \quad \Delta = 0.3$$



cell label

$N = 100$

Fig. 14. 18

Lecture 15: Large neural network with random connectivity

A distinguished characteristic of neural systems is that the network wiring and the strength of coupling between neurons are modifiable dynamically. This plasticity will be discussed in later lectures in connection with learning and memory. In this lecture, we shall discuss a very simple example, and introduce some notions and tools to describe such systems' dynamics when the network connectivity is more or less random.

(Sompolinsky et al 1988) Consider a formal neural network described by the equation

$$\frac{dv_i}{dt} = -\lambda v_i + \sum_{j=1}^N w_{ij} \sigma(v_j), \quad i=1, 2, \dots, N$$

where $\{v_i\}$ is the unit variable, w_{ij} the connectivity matrix, and $\sigma(v)$ the input-output function of a sigmoid type. We shall choose $\sigma(v) = \tanh(gv)$ with a gain parameter g . This system represents a bona fide "connectionist" model: each unit alone would merely relax to its rest $v_i = 0$ in a trivial way. When such units are connected by strong enough nonlinear interactions, however, collective dynamics and computational abilities can emerge in the network.

- Hopfield (1982), $w_{ij} = w_{ji}$ (see lecture 18)

- Amari (1972): one excitatory / one inhibitory subpopulation.

Here, we shall discuss the case studied by Sompolinsky et al (1988), where w_{ij} is completely random.

- w_{ij} independent, identical, with a Gaussian distribution.
- $[w_{ij}] = 0 \quad [w_{ij}^2] = J^2/N$.
- with a rescaling of v_i and t , the only (dimensionless) parameter is Jg . (For convenience we set $\lambda=1$).

Sompolinsky et al found, by a mean-field treatment, that as Jg is changed, two dynamically stable regimes were observed:

- if $Jg < 1 \quad v_i \equiv 0$
- at $Jg = 1 \quad v_i \equiv 0$ loses stability
- if $Jg > 1 \quad$ a chaotic state is stable.

This conclusion is exact in the limit of $N \rightarrow \infty$. In numerical simulations with finite N , the prediction was found to be essentially correct, but transition may not be direct (from a rest state to a chaotic state), and the transition point is not exactly at $Jg = 1$. (Fig. 1).

How to determine the stability of the rest state $v_i \equiv 0$?

If we apply our usual linear stability analysis to the system, the resulting infinite matrix has the elements

$$\boxed{M_{ij} = -\delta_{ij} + g J_{ij}} \quad i, j = 1, 2, \dots, N$$

This is a random matrix. Naively, we can imagine to calculate the eigenvalues of this matrix for each sampling of w_{ij} .

$$M e_i = \lambda_i e_i \quad i=1, 2, \dots, N$$

where $\{e_i\}$ are corresponding eigenvectors of M . Then we average $\{\lambda_i\}$ over the distribution of w_{ij} :

$$\bar{\lambda}_i = [\lambda_i]_w. \text{ The ensemble } \{\bar{\lambda}_i\} \text{ is the } \underline{\text{spectrum}} \text{ of } M$$

If all $\bar{\lambda}_i$ have negative real part, the fixed point is stable.

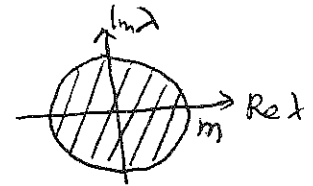
As $N \rightarrow \infty$, the spectrum of M becomes continuous usually. The fixed point is unstable when this spectrum is not confined to the left half of the complex plane.

The theory of random matrices was pioneered in the 1950s, but only recently it gained wide attention. We shall not be able to go into details here on this very interesting topic. For our purpose, we can simply apply a remarkable theorem due to E. Wigner (1958) which states as follows: If a random matrix of dimension N has as its elements independent Gaussian variables w_{ij}

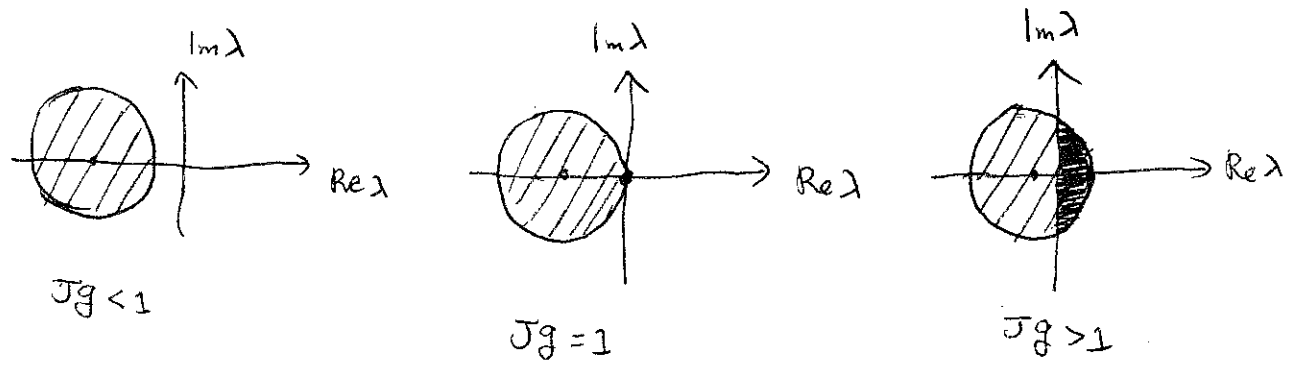
$$[w_{ij}] = 0 \quad [w_{ij}^2] = \frac{m^2}{N}$$

Then, the average density ρ of the eigenvalues in the limit $N \rightarrow \infty$ is

$$\rho(\lambda) = \begin{cases} \frac{1}{\pi m^2} & \text{if } |\lambda| < m \\ 0 & \text{otherwise} \end{cases}$$



Applying this result to our case, we conclude that if $Jg < 1$, the spectrum of M is strictly in the left-half of the complex plane, hence the fixed point $v_i \equiv 0$ is stable. As soon as $Jg > 1$, there are an infinity of eigenvalues with positive real part.



How to describe chaos for $Jg > 1$?

In lecture 8 we briefly mention deterministic chaotic phenomena, and introduce the notion of the Lyapunov exponent which describes the sensitivity to initial conditions.

(How nearby trajectories diverge in time due to chaos)

A second measure of aperiodicity is the exponential decay of correlation functions. Indeed, Sompolinsky et al showed that, in the limit $N \rightarrow \infty$, the original system is reduced to a dynamical mean-field equation of a single unit, which reads

$$\frac{dv_i}{dt} = -v_i + \eta_i(t)$$

where $\eta_i(t)$ is a nonMarkovian, Gaussian field, representing the ensemble average input from other units. Its auto-correlation function:

$$C(t) = \langle \eta_i(t) \eta_i(t+t) \rangle$$

is evaluated self-consistently within the mean field theory. Thus, the network behaves as if it consisted of independent units, embedded in a common field $\eta(t)$. For $gJ < 1$, $C(t) \equiv 0$, while for $gJ > 1$, $C(t)$ is nontrivial. $C(t)$ can be calculated explicitly when $\delta = gJ - 1 \ll 1$. We have $J^2 C(t) = \Delta - \tilde{\Delta}$ where

$$\Delta(t) = \langle v_i(t_0) v_i(t_0+t) \rangle \approx g \cosh^{-2} \left(\frac{st}{\sqrt{3}} \right).$$

This correlation function decays exponentially in time. The power spectrum of $v_i(t)$ is given by

$$S(\omega) = \sqrt{\frac{2}{\pi}} \int_0^\infty \cos(\omega t) \Delta(t) dt = \sqrt{\frac{6}{\pi}} \frac{\omega}{\omega_0} \sin^{-1} h \left(\frac{\omega}{\omega_0} \right)$$

where $\omega_0 = \frac{2\delta}{\sqrt{3}\pi}$. This is a continuous spectrum without sharp peaks, unlike regular, periodic or quasiperiodic states.

A third characterization is the dynamical entropy of the network. A chaotic flow generates "information", the entropy is the information production rate per unit time. For a finite-dimensional deterministic chaotic attractor, the dynamical entropy of Kolmogorov and Sinai (h_{KS}) is the sum of the positive Lyapunov exponents.

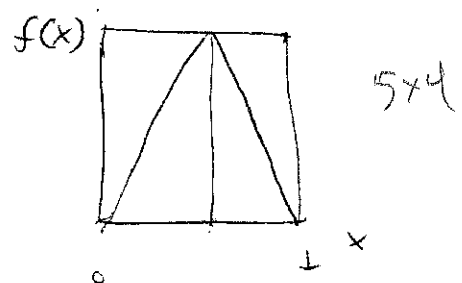
$$h_{KS} = \sum_{\lambda_i > 0} \lambda_i \quad (\text{Pesin})$$

So h_{KS} is positive if there is at least one positive Lyapunov exponent.

To illustrate this notion, let us consider a simple map

$$x_{n+1} = 2x_n \quad 0 \leq x_n \leq \frac{1}{2}$$

$$2(1-x_n) \quad \frac{1}{2} \leq x_n \leq 1$$



This is similar to the logistic map discussed in lecture 8, with $\mu=1$.

We can partition the unit interval into 2 subintervals

$0 = [0, \frac{1}{2}]$, $1 = [\frac{1}{2}, 1]$. Then one can see readily that each trajectory $(x_0, x_1, x_2, \dots, x_n, \dots)$ corresponds to a string of symbols $(w_0 w_1 w_2 \dots, w_n, \dots)$, $w_i = 0$ or 1 indicating which subinterval the i th iteration of the trajectory belongs to. By this symbolic dynamics a deterministic system with analog variables is mapped into a process with discrete states which is however stochastic. Suppose that the probability for a finite string $(w_0 w_1 \dots w_n)$ is $p(w_0 w_1 \dots w_n)$. The quantity $-\log_2 p(w_0 \dots w_n)$ denotes its information content. The average of this quantity, divided by the time n gives the information production rate

$$h_{KS} = \lim_{n \rightarrow \infty} \frac{1}{n} \sum_{(w_0 \dots w_n)} p(w_0 \dots w_n) \log_2 p(w_0 \dots w_{n-1})$$

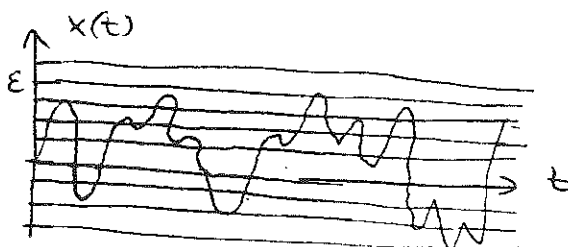
In the above example, we have simply $h_{KS} = 1$ bit/time unit.

In our case of a large neural network, as $N \rightarrow \infty$, the system is not of finite dimension. Indeed, if each unit is described by a Langevin equation

$$\frac{d u_i}{dt} = -u_i + \eta(t) \quad \text{where } \eta(t) \text{ is a continuous stochastic}$$

we have to extend the notion of dynamical entropy to continuous stochastic processes. A priori, the entropy of an analog signal $x(t)$ from a continuous stochastic process is infinite. However, its information generation rate is always bounded, if it is monitored by instruments with finite precision.

Shannon and Kolmogorov independently introduced the notion of " ϵ -entropy", calculated when the precision of measurement is limited by ϵ . For instance, the signal can be digitalized with a step ϵ .



One can show that:

- for low-dimensional chaos $h(\epsilon) \xrightarrow[\epsilon \rightarrow 0]{} h_{KS}$
- for Brownian motion $h(\epsilon) \underset{\epsilon \rightarrow 0}{\sim} \frac{1}{\epsilon^2}$
- for our Langevin equation, $h(\epsilon) \underset{\epsilon \rightarrow 0}{\sim} (\log_2 \frac{1}{\epsilon})^2$.

In this sense, the spontaneous activity of the neural network is neither chaos nor noise.

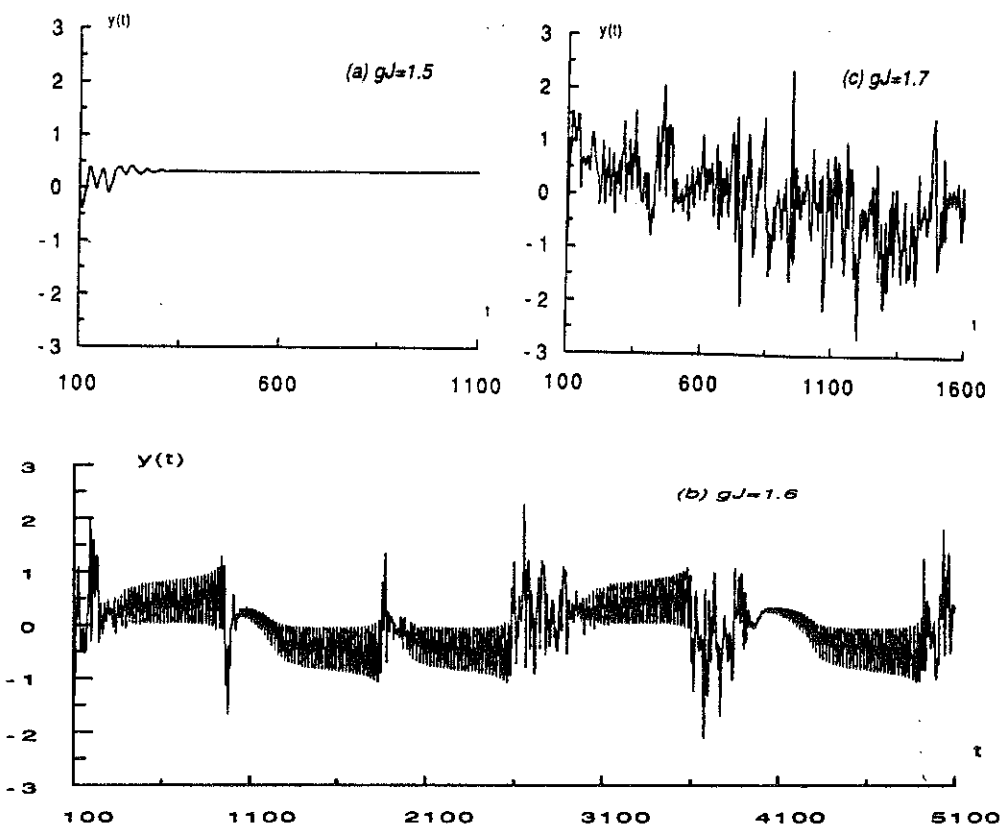


Fig.1. Numerical evidence of intermittency (b) near a transition from a fixed point (a) to a chaotic flow (c). The net Eq.(1) was simulated with $N = 500$ units, J_{ij} were randomly chosen, then fixed. Plotted here are the time evolutions of a single unit for different values of gJ . The intermittent behavior in (b) consists of long regular phases interrupted randomly by chaotic bursts.

fig. 15.1

Lecture 16: Activity-dependent synaptic plasticity

VII VI

Neuronal plasticity is considered as a cellular substrate for the brain's adaptive behaviors, learning and memory. According to a popular view, plasticity is expressed in the modifiability of the nervous network connectivity, in the activity-dependent changes of synapse.

D. Hebb's principle (1949): "When an axon of a cell A is near enough to excite cell B or repeatedly or persistently takes part in firing it, some growth or metabolic change takes place in both cells such that A's efficiency, as one of the cells firing B, is increased."

Let w_{AB} be the strength of a synapse between cell A & cell B, v_A, v_B their respective firing rate. Then the naive expression for the Hebb rule is

$$\frac{d w_{AB}}{dt} = \epsilon v_A v_B \quad \epsilon \ll 1$$

However, w_{AB} should decrease if cells A & B do not fire simultaneously

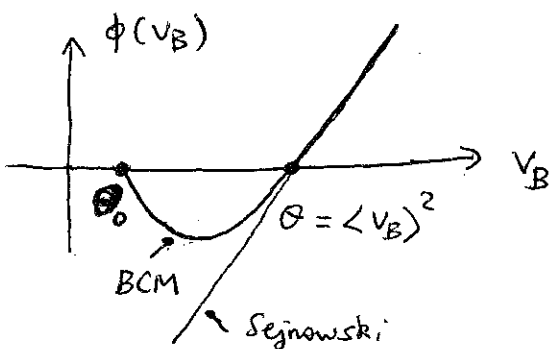
→ Sejnowski (1977)

$$\begin{aligned} \frac{d w_{AB}}{dt} &= \epsilon \langle v_A - \langle v_A \rangle \rangle \langle v_B - \langle v_B \rangle \rangle \\ &= \epsilon [\langle v_A v_B \rangle - \theta] \quad \theta = \langle v_A \rangle \langle v_B \rangle \end{aligned}$$

Bienenstock - Cooper - Munro (1982)

$$\frac{d w_{AB}}{dt} = \epsilon \phi(v_B, \langle v_B \rangle) v_A$$

where $\phi(v_B, \langle v_B \rangle)$ is of the form shown below



Thus, if the presynaptic cell A is active, then the synaptic strength is enhanced if the postsynaptic cell is also active; while it is reduced if the postsynaptic cell is not active. For the Sejnowski's covariance rule (not the BCM rule), the synaptic strength is also reduced if the postsynaptic cell is active while the presynaptic cell is inactive. In other words, correlated activity strengthens the coupling while uncorrelated activity weakens it.

An "Anti-Hebb" principle can be stated exactly as the Hebb's principle, with the last word "increased" replaced by "decreased".

The Hebb principle can probably be implemented by different mechanisms. In any case, it implicates synchronous/asynchronous activities & likely rhythmic activity in the plasticity, and learning.

Conceptually, therefore, one should bear in mind that the synaptic weights are dynamically modifiable, and we have 2 coupled systems with different time scales:

v_i : activity

w_{ij} : coupling

$$\frac{dv_i}{dt} = F(v_j, w_{ij})$$

$$\frac{dw_{ij}}{dt} = G(v_k, w_{mn})$$

Long-term potentiation (LTP): Bliss & Lomo (1973)

A high-frequency volley of pulses (100 Hz lasting 1 sec) was applied to the primary afferents of the dentate granule cells in the hippocampus. The response of the cell to a test stimulus was measured before and after the tetanus. It was found that the EPSP amplitude elicited by the test stimulus was significantly enhanced after the tetanus, and this change could persist for hours. If the granule cell is voltage-clamped to prevent depolarization at the postsynaptic site during the tetanus, however, the LTP effect did not occur (Fig. 1). This implies that LTP is essentially Hebbian.

Various types of LTP and LTD (long-term depression) are shown in Fig. 2. Glutamate is a major excitatory transmitter in the CNS.

According to experimental evidence, the LTP observed in the hippocampus is dependent on a particular subtype of Glutamate receptors, the N-methyl-D-aspartate (NMDA) receptors. The NMDA receptor-gated ion channel is normally blocked by Mg^{2+} . When the postsynaptic membrane is depolarized, this blockade by Mg^{2+} is removed. Therefore, the NMDA receptor subserves a molecular machine for Hebbian coincidence detection: it requires a simultaneous postsynaptic depolarization for the Mg^{2+} blockade to be removed, and presynaptic stimulus for the transmitter glutamate to be released to the postsynaptic site.

Furthermore, the NMDA receptor-gated channel is highly permeable to Ca^{2+} , unlike non-NMDA receptor-gated channels (e.g. AMPA). It has been shown that the increase of free intracellular Ca^{2+} is a necessary condition for the LTP induction. Probably, Ca^{2+} (as a second messenger) binds with the protein calmodulin (CaM), the $\text{Ca} - \text{CaM}$ complex can then trigger phosphorylation of certain protein kinases and lead to further cascade of biochemical processes resulting in the LTP.

A biophysical model of a Hebbian synapse : A. Zador et al

(PNAS 87, 6718 (1990)) present a model of electrical and Ca^{2+} dynamics following activation of NMDA receptors located on a dendritic spine (fig.3)

Most excitatory synapses are located on the spines.
(in the CNS)

- Large layer V pyramidal cell in the visual cortex
 $\sim 15,000$ spines . $2 \text{ spines}/\mu\text{m}$ of dendrite
- CA1 hippocampal pyramid. $1.5 \text{ spines}/\mu\text{m}$ of dendrite
- Purkinje cell $\sim 200,000$ spines. $14 \text{ spines}/\mu\text{m}$ of dendrite.

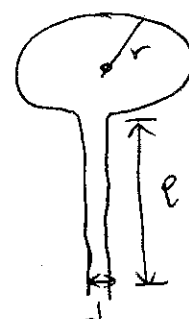
Spines are very small and separated from the dendritic shaft by a very slender neck.

CA1 pyramidal cell

$$l = 0.08 - 1.6 \mu\text{m}$$

$$d = 0.04 - 0.46 \mu\text{m}$$

$$\text{head volume} = 0.62 \pm 0.08 \mu\text{m}^3 \quad (\rightarrow r \approx 0.25 \mu\text{m})$$



Because of the extremely small volume, the spine head is very sensitive to ion concentration change.

e.g. If $[Ca^{2+}]_i = 80 \text{ nM}$ at rest

and $V = 0.05 \mu\text{m}^3 \rightarrow$ there are only 3 free Ca^{2+} ions.

In order for $[Ca^{2+}]_i$ to raise to $10 \mu\text{M}$, only an entry of 300 Ca^{2+} ions suffices. Imaging techniques permit now ~~or~~ direct measurement of $[Ca^{2+}]_i$ change in the spines.

The model of Zador et al. describes a spine with a NMDA synapse and a non-NMDA (AMPA) synapse. They are described by an α -function or α -like function

$$I_{AMPA}(t) = (E_{syn} - V) g_p \frac{\alpha(t)}{t_p} e^{-\frac{t}{t_p}}$$

$$t_p = 1.5 \text{ msec}, E_{syn} = 0, g_p = 0.5 \text{ nS} \quad (I_{AMPA} \text{ is fast})$$

$$I_{NMDA}(t) = (E_{syn} - V) g_n \frac{e^{-\frac{t}{\tau_1}} - e^{-\frac{t}{\tau_2}}}{1 + \eta [Mg] e^{-\delta V}}$$

$$\tau_1 = 80 \text{ msec}, \tau_2 = 0.67 \text{ msec}, \eta = 0.33 / \text{mM}, \delta = 0.06 / \text{mV},$$

$E_{syn} = 0, g_n = 0.2 \text{ nS}$ (I_{NMDA} decays slowly). The Mg-dependence is expressed in the voltage-dependent denominator.

The spine head and neck are each described as a cylinder. $R_m = 20 \text{ k}\Omega \text{ cm}^2$

$$R_i = 100 \Omega \text{ cm}$$

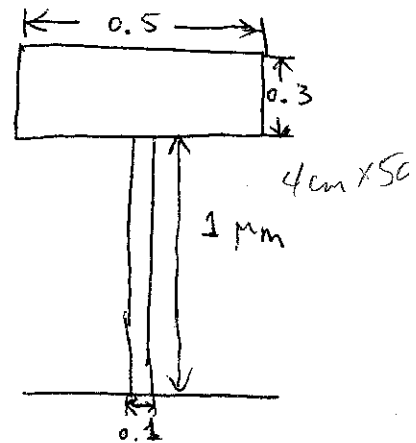
$$C_m = 1 \mu\text{F/cm}^2$$

spine axial resistance = $125 \text{ M}\Omega$

Spine head input resistance = $200 \text{ M}\Omega$.

see fig. 4.

The intracellular Ca^{2+} concentration changes due to several processes.



$$\frac{\partial [\text{Ca}^{2+}]}{\partial t} = \frac{\partial [\text{Ca}^{2+}]_{\text{NMDA}}}{\partial t} + \frac{\partial [\text{Ca}^{2+}]_{\text{pump}}}{\partial t} + \frac{\partial [\text{Ca}^{2+}]_{\text{buffer}}}{\partial t} + \frac{\partial [\text{Ca}^{2+}]_{\text{diff}}}{\partial t}$$

- Calcium current

$$\frac{\partial [\text{Ca}^{2+}]_{\text{NMDA}}}{\partial t} = -0.02 I_{\text{NMDA}} \frac{9 \text{ F Vol}}{2 \text{ F Vol}}$$

where F is the Faraday constant, Vol is the volume of the spine head.

The factor 0.02 reflects the estimate that 2% of the I_{NMDA} is carried by Ca^{2+}

- Calcium diffusion

$$\frac{\partial [\text{Ca}^{2+}]_{\text{diff}}}{\partial t} = D \frac{\partial^2 [\text{Ca}^{2+}]}{\partial x^2} \quad D = 0.6 \mu\text{m}^2/\text{msec}$$

- Calcium pump (described by a first-order Michaelis-Menton kinetics)

$$\frac{\partial [\text{Ca}^{2+}]_{\text{pump}}}{\partial t} = -K_{\text{max}} P_s \frac{A}{\text{Vol}} \frac{[\text{Ca}^{2+}]}{[\text{Ca}^{2+}] + K_d} + J_{\text{leak}} \frac{A}{\text{Vol}}$$

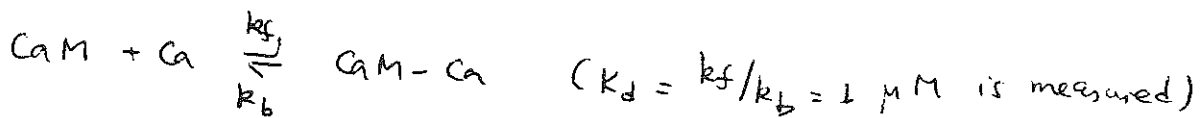
2-types: high-affinity ($K_d = 0.5 \mu\text{M}$) low-capacity ($P_s = 5 \times 10^{-16} \mu\text{mol}/\mu\text{m}^2$)

low-affinity ($K_d = 20 \mu\text{M}$) high-capacity ($P_s = 1-5 \times 10^{-15} \mu\text{mol}/\mu\text{m}^2$)

J_{leak} is set such that $\frac{\partial [\text{Ca}^{2+}]_{\text{pump}}}{\partial t} = 0 \rightarrow [\text{Ca}^{2+}] = [\text{Ca}^{2+}]_{\text{rest}}$

- calcium buffer by calmodulin (CaM)

If there was one binding site, the buffering kinetics can be assumed as



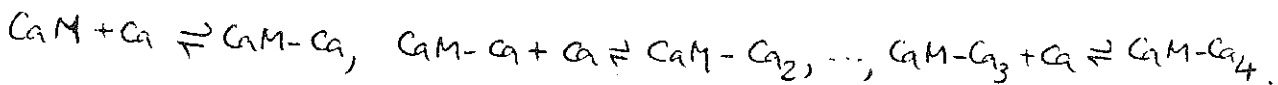
$$\frac{\partial [\text{Ca}^{2+}]_{\text{buffer}}}{\partial t} = \frac{\partial [\text{CaM}]}{\partial t} = k_b [\text{CaM-Ca}] - k_f [\text{Ca}^{2+}] [\text{CaM}]$$

$$[\text{CaM}] + [\text{CaM-Ca}] = [\text{CaM}]_T \text{ fixed } (\approx 3-30 \mu\text{M})$$

$$k_f = 0.5 / \text{MMmsec}, \quad k_b = 0.5 / \text{msec}$$

$$\rightarrow \frac{\partial [\text{Ca}^{2+}]_{\text{buffer}}}{\partial t} = \frac{\partial [\text{CaM}]}{\partial t} = k_b [\text{CaM}]_T - \{ k_b + k_f [\text{Ca}^{2+}] \} [\text{CaM}]$$

In fact, CaM has 4 Ca^{2+} -binding sites. Zador et al. assumed a sequential, non-cooperative kinetics

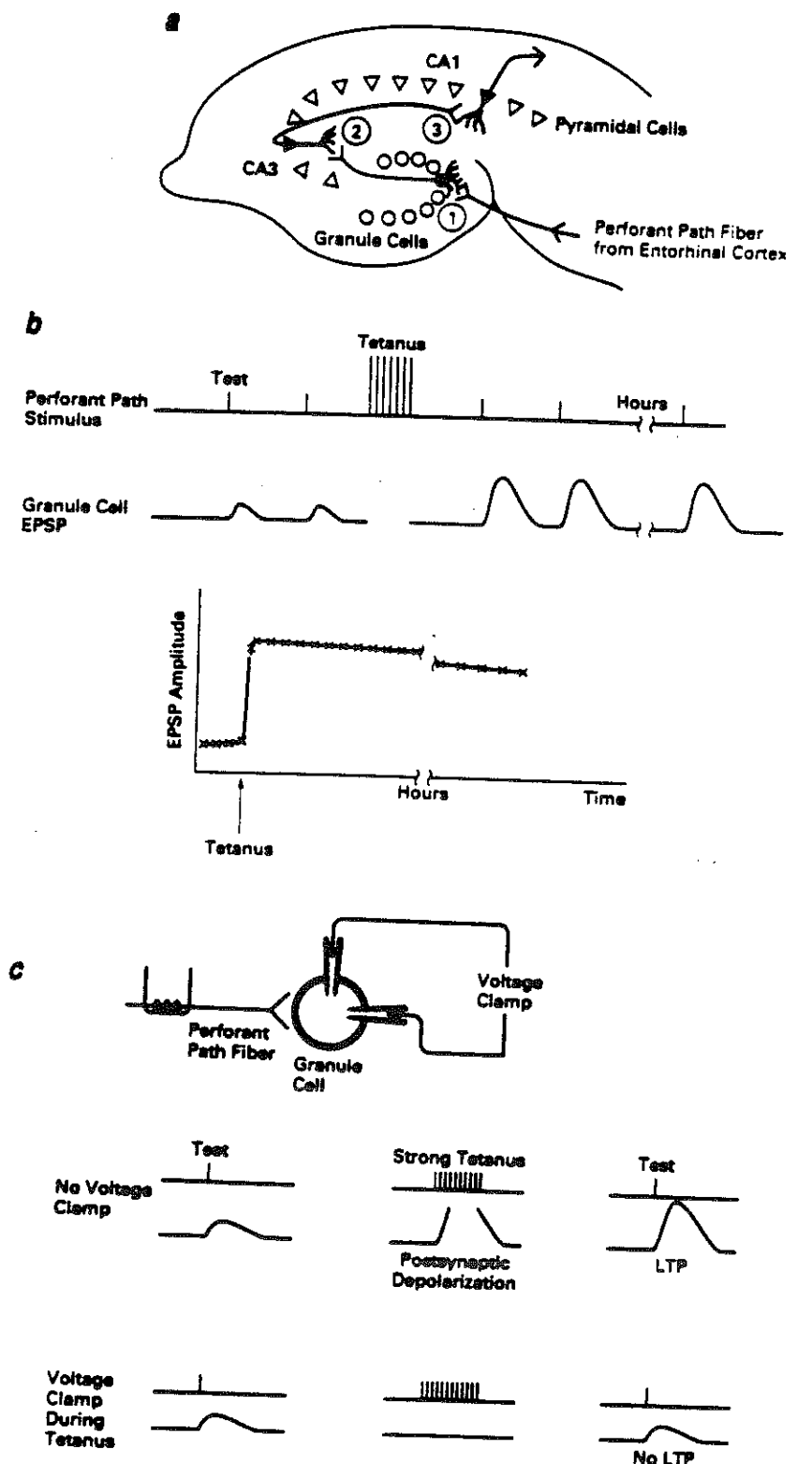


The synaptic enhancement is assumed to depend on $[\text{CaM-Ca}_4]$.

Results: see fig. 5 - fig. 6

The $[\text{CaM-Ca}_4]$ increase is Hebbian. Due to the nonlinear Ca^{2+} dynamics and buffering kinetics, the sensitivity to the postsynaptic depolarization is much sharper in $[\text{CaM-Ca}_4]$ than in NMDA-current.

The $[\text{Ca}^{2+}]$ and $[\text{CaM-Ca}_4]$ changes are largely confined to the spine head. The extremely thin spine neck does not allow Ca^{2+} diffusion efficiently. Also, Ca^{2+} pumps & buffers contribute to the chemical isolation of the spine head from the dendritic shaft.



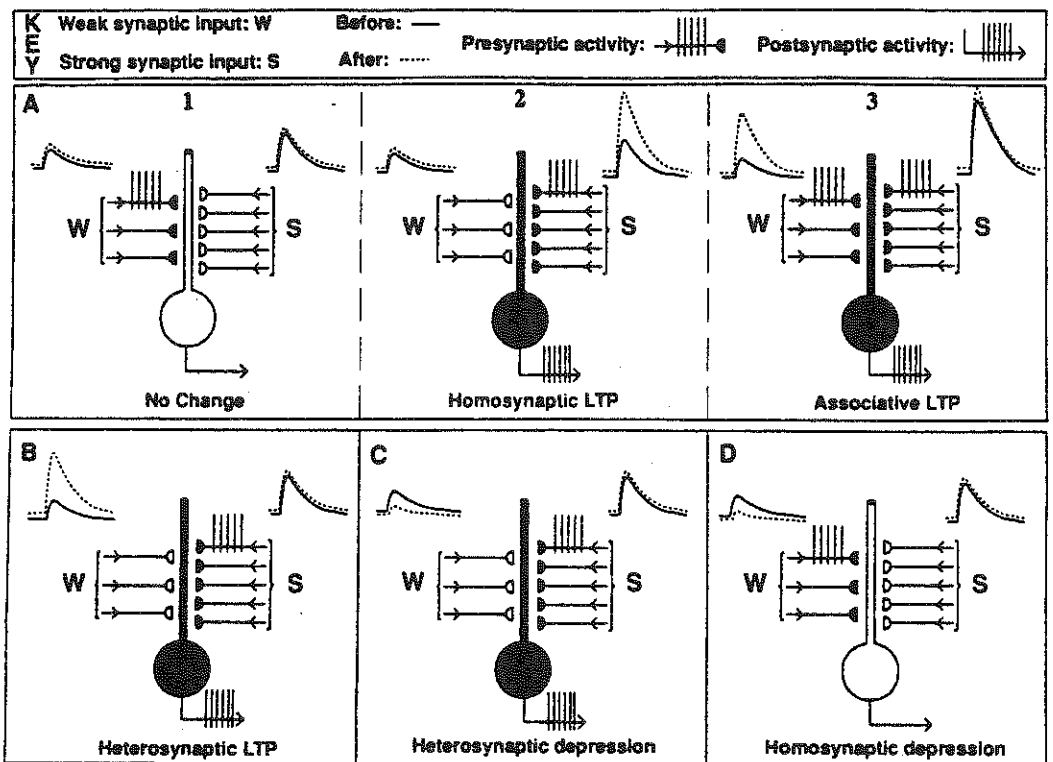


Figure 5.30 Use-dependent synaptic changes. Each neuron is shown receiving two sets of nonoverlapping synaptic inputs, one weak (W) and the other strong (S). The wave forms above each input illustrate schematically the excitatory postsynaptic potential produced by a single stimulation of that input before (solid curve) and after (broken curve) tetanic stimulation of one or both inputs. Filled elements indicate activity during the tetanic stimulation. (From Brown et al. 1990.)

Fig. 16.2

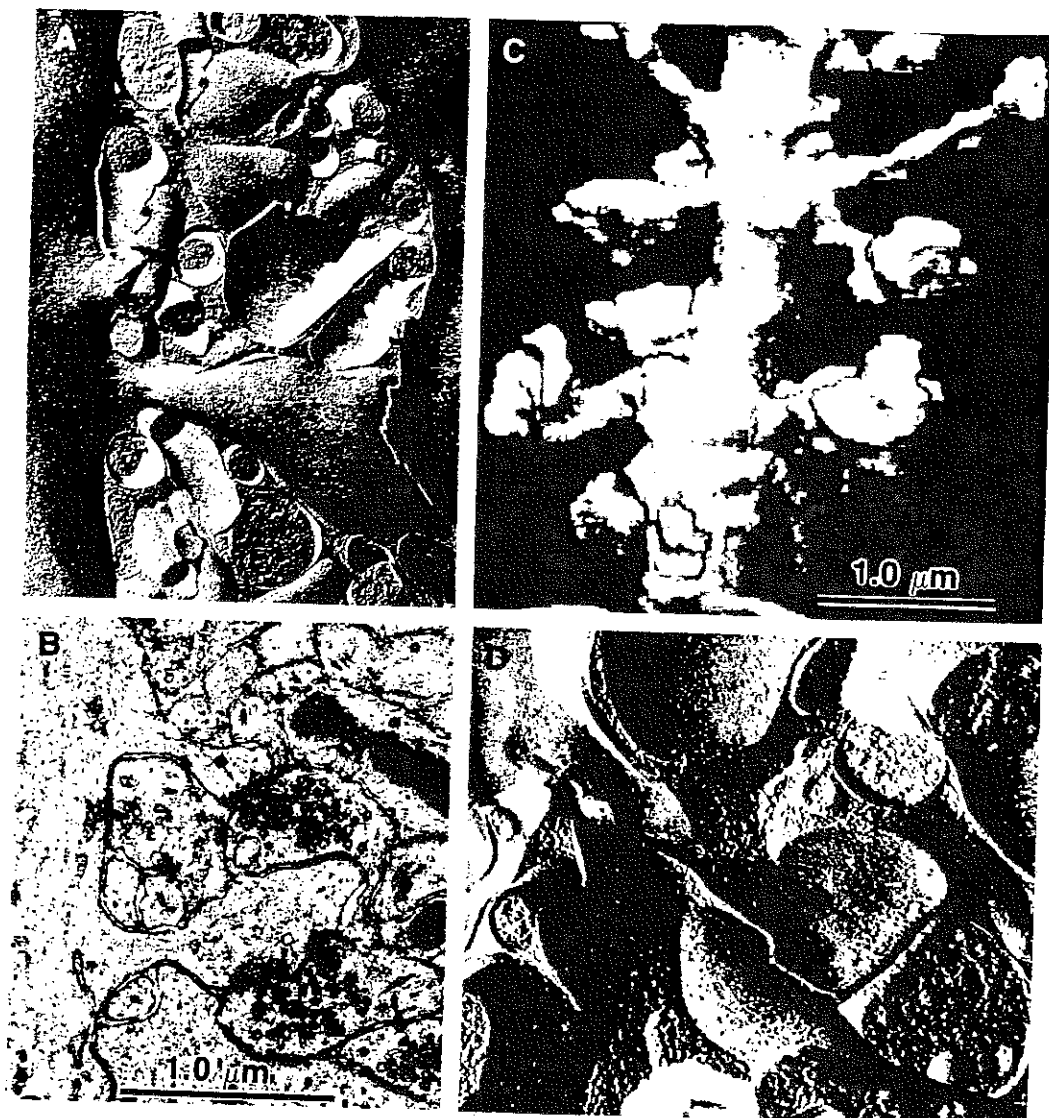


Fig. 2. Heterogeneity in the size and shapes of dendritic spines and their synapses in hippocampal area CA1. **(A)** Cytoplasmic profile (P-face) of a small, thin, or 'pedunculated' dendritic spine (filled square) revealed by freeze-fracture electron microscopy to be near to a large, mushroom-shaped dendritic spine (open square) of the same dendritic segment. **(B)** Thin-section view of two spines with similarly diverse shapes that also have different types of postsynaptic densities (PSDs). The smaller spine has a continuous, macular-shaped PSD (filled square), while the larger spine has an electron-lucent perforation in the PSD (open square). **(C)** Three-dimensional reconstruction of a segment of CA1 pyramidal cell dendrite revealing multiple spine shapes along its length. **(D)** Particle aggregate on the extracellular half of the membrane (E-face) at the site of a synapse on the head of a thin dendritic spine (filled square). [(A), (B) and (D) are modified from Ref. 18; (C) is modified from Ref. 19.]

Fig. 16. 3

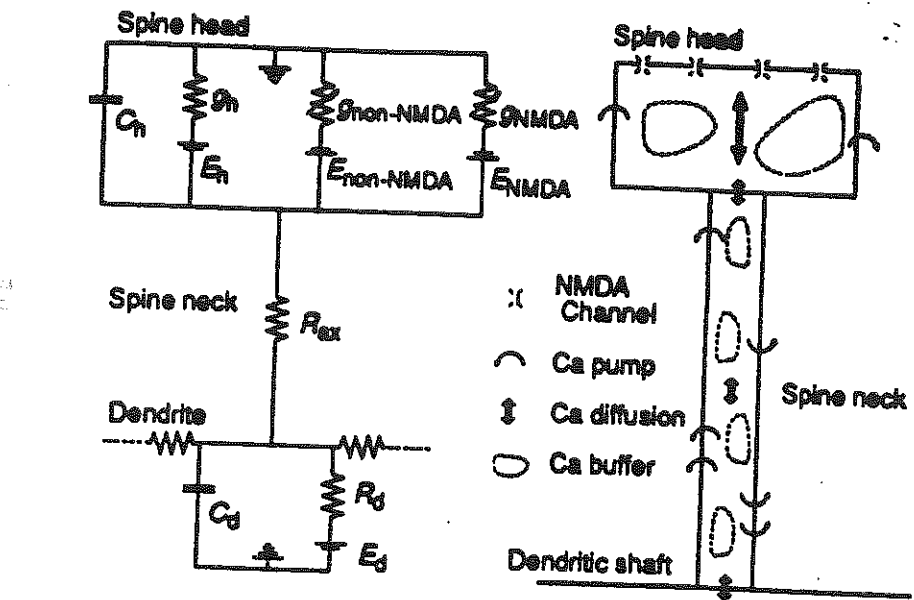


FIG. 1. The model. The electrical model (*Left*) of the spine included two separate conductances representing the distinct NMDA (Eq. 2) and non-NMDA (Eq. 1) components of the synaptic response. The dendritic compartment was connected to 27 other compartments representing the rest of the neuron. In the Ca^{2+} transport-buffering model (*Right*), Ca^{2+} entered the spine head through channels located only on the distal spine head and then diffused along the length of the spine to the dendritic shaft. Diffusion was limited by binding to saturable membrane pumps and cytosolic buffers.

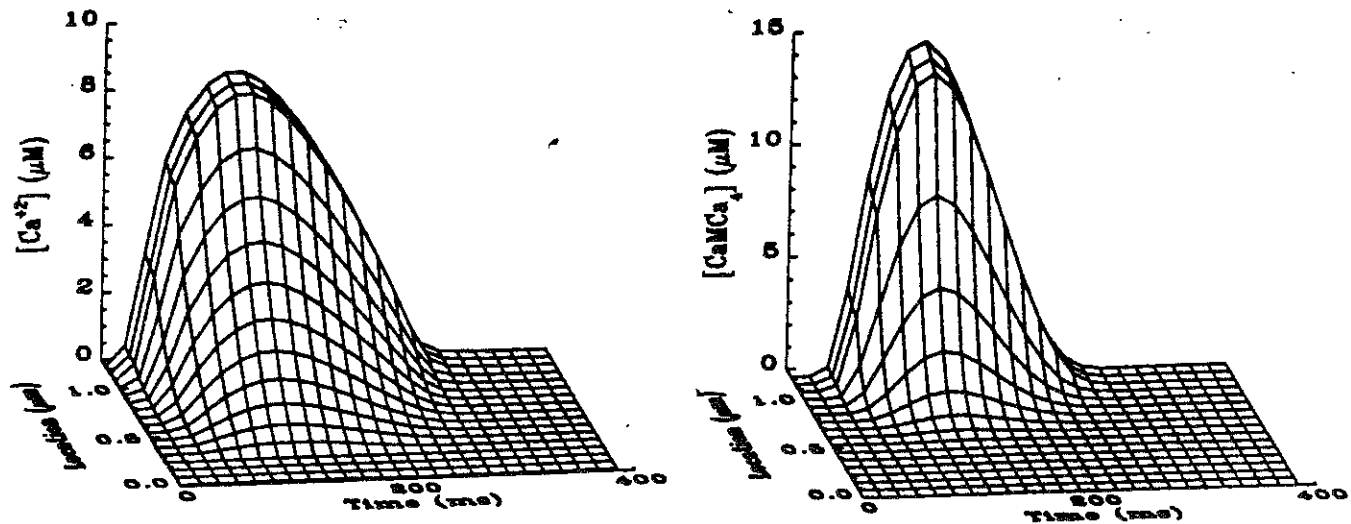


FIG. 2. Spatiotemporal dynamics of Ca^{2+} and CaM-Ca_4 . The time course of $[\text{Ca}^{2+}]$ (Left) and $[\text{CaM-Ca}_4]$ (Right) in a spine is shown. The axis labeled location indicates distance from dendritic shaft. A train of three presynaptic stimuli was applied at 100 Hz while postsynaptic voltage at the spine head was clamped to -40 mV . Changes in $[\text{Ca}^{2+}]$ and $[\text{CaM-Ca}_4]$ are restricted mainly to the spine head, where they are amplified. Note that the response of $[\text{CaM-Ca}_4]$ is sharper than that of $[\text{Ca}^{2+}]$.

Fig. 16.5

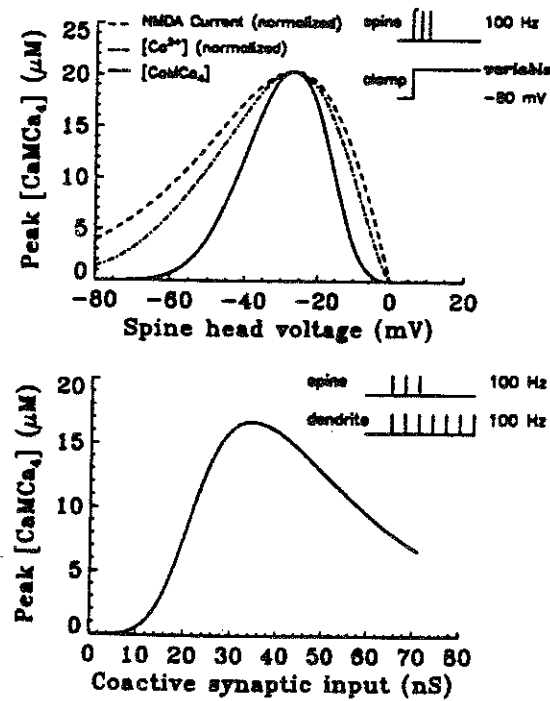


Fig. 16.6

FIG. 3. Effect of postsynaptic activity. Peak $[\text{CaM-Ca}_4]$ in the subsynaptic compartment is shown after a train of three presynaptic stimuli applied at 100 Hz. In the first type of simulation, the postsynaptic membrane was clamped to potentials ranging from -80 mV to 0 mV (Top). Peak $[\text{Ca}^{2+}]$ and NMDA current have been scaled to this graph. Note that $[\text{Ca}^{2+}]$ and $[\text{CaM-Ca}_4]$ are steeper functions of voltage than NMDA current. In the second kind of simulation, postsynaptic depolarization was provided by a coactive strong input (Bottom). The strong input consisted of a 100 Hz train of stimuli applied at synapses uniformly distributed on the same apical branch as the spine. The strength of the strong input stimulus, defined as peak total conductance of the coactive synapses, was varied from 0 nS to 75 nS. Note that for very low values of strong input activity (only weak input; see text), peak $[\text{CaM-Ca}_4]$ remains essentially unchanged from the resting value of $[\text{CaM-Ca}_4]$.

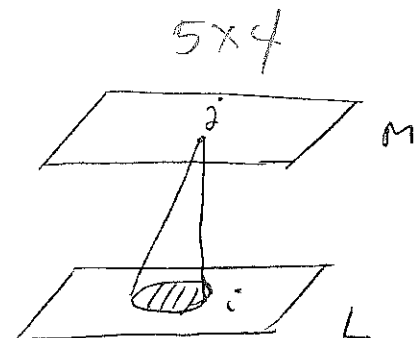
Lecture 17: Development of visual maps; Linsker's model

A fundamental question relates to mechanisms by which structured receptive fields emerge in the nervous system. For instance, from bipolar cells in the retina and on along the visual pathway, on-center & off-center cells are found (fig. 1), the primary visual cortex is organized into columns (of orientation selective cells) and hypercolumns (of ocular dominance) (figs 2-3), etc. How do they come into being during development?

Linsker's model: feed forward, linear. Density of synapses received by a neuron in layer M from layer L has a Gaussian distribution.

s_i^L : activity of cell i in layer L

$$\text{if } n = \# \text{ synapses chosen from } \frac{1}{\sqrt{2\pi A}} e^{-\frac{d(i,j)^2}{2A}}$$



$$s^M = \frac{1}{N} \sum_{i \in L} w_i s^L + a_1$$

$$\begin{aligned}
 &= \left[\int_{-\infty}^{\infty} \omega(x', y') s(x', y') g(x-x', y-y') dx' dy' \right] \\
 &\quad \text{Continuum limit} \\
 &\quad \text{Gaussian}
 \end{aligned}$$

$\{w_i\}$ evolve dynamically according to

$$\frac{dw_i}{dt} = \underbrace{(s^M - c_2)(s_i^L - c_1)}_{\text{Hebbian}} + c_3 = \left(\frac{1}{N} \sum_j w_j \cdot s_j^L + a_1 - c_2 \right) (s_i^L - c_1) + c_3$$

[or, in the continuum limit

$$\frac{dw(x,y)}{dt} = (s^M - c_2) (s^L(x,y) - c_1) + c_3$$

"unsupervised learning"

s_i^L varies much faster than $w_i \rightarrow$ ensemble average

$$\frac{dw_i}{dt} = \left\langle \left(\frac{1}{N} \sum_j w_j \cdot s_j^L + a_1 - c_2 \right) (s_i^L - c_1) + c_3 \right\rangle$$

$$= \frac{1}{N} \sum_j [Q_{ij}^L + \bar{s}_j^L (s_i^L - c_1)] w_j + (a_1 - c_2) (\bar{s}_i^L - c_1) + c_3$$

where

$$Q_{ij}^L = \langle (s_i - \bar{s}_i) (s_j - \bar{s}_j) \rangle$$

$$\text{assume } \bar{s}_i^L = \bar{s}^L$$

$$\rightarrow \boxed{\frac{dw_i}{dt} = \frac{1}{N} \sum_{j \in L} (Q_{ij}^L + k_2) w_j + k_1}$$

$$\text{where } k_2 = \bar{s}^L (\bar{s}^L - c_1)$$

$$k_1 = (a_1 - c_2) (\bar{s}^L - c_1) + c_3$$

(17.2)

$$\text{let } \bar{k} = -\frac{k_1}{k_2} \quad \lambda = -\frac{k_2}{N}$$

$$E = -\frac{1}{2} w^T Q w + \frac{\lambda}{2} (\bar{k} N - \sum_j w_j)^2$$

$$\rightarrow \frac{dw_i}{dt} = -\frac{\partial E}{\partial w_i}$$

$$\frac{dE}{dt} = + \sum_i \frac{\partial E}{\partial w_i} \frac{\partial w_i}{\partial t} = - \sum_i \left(\frac{dw_i}{dt} \right)^2 \leq 0$$

$$\frac{dE}{dt} = 0 \Leftrightarrow \frac{dw_i}{dt} = 0$$

If there was no 2nd term $\frac{dE}{dt} \Leftrightarrow w^T Q w = \sum_{ij} w_i Q_{ij} w_j$ to be

maximized, because $-\frac{\partial^2 E}{\partial w_i \partial w_j} = Q_{ij}$ is positively defined.

(proof): Since $Q_{ij} = Q_{ji}$ and $Q_{ij} = \langle (s_i - \bar{s})(s_j - \bar{s}) \rangle$ is
of the outer product form, for any vector r , $r^T Q r = \langle r^T (\bar{s} - \bar{s})(\bar{s} - \bar{s})^T r \rangle = \langle ((\bar{s} - \bar{s})r)^2 \rangle \geq 0 \rightarrow Q \text{ is positively defined}.$

Therefore, the rule consists of maximizing the output covariance
provided that a constraint (the 2nd term) is satisfied. However,

Linsler requires that, for the 1st transformation from layer A to
layer B, such an extremum does not exist.

Suppose that the 1st layer consists of uncorrelated inputs, $Q_{ij} = \delta_{ij}$.

$$\frac{dw_i}{dt} = \frac{w_i}{N} + k_1 + \frac{k_2}{N} \sum_j w_j$$

some negative
some positive only if
 $\frac{k_2}{N} \sum_j w_j + k_1 = o(\frac{1}{N})$

$$= \frac{w_i}{N} + k_2 \left[\frac{1}{N} \sum_j w_j - \bar{k} \right]$$

Let $1 \leq w_i \leq -1$

$$\rightarrow w_i \equiv 1 \quad \text{if } k_2 > 0 \quad \bar{k} < -1 \quad \text{or } k_2 < 0 \quad \bar{k} > 1$$

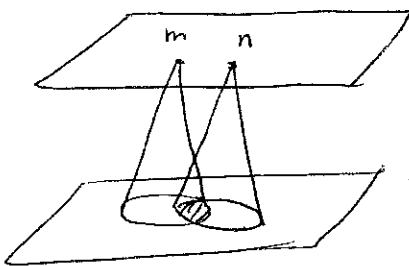
$$w_i \equiv -1 \quad \text{otherwise.}$$

Ansatz: choose $w_i \equiv 1$ ($k_2 < 0, \bar{k} > 1$)

\rightarrow in 2nd layer, 2 cells have a Gaussian correlation.

Eq 4.4

$$S_m = \int_A g(x_m - x', y_m - y') \underbrace{s(x', y')}_{\delta(x', y')} dx' dy'$$



$$S_n = \int_A g(x_n - x', y_n - y') \underbrace{s(x', y')}_{\delta(x', y')} dx' dy'$$

$$Q_{mn} = \langle (S_m - \bar{s})(S_n - \bar{s}) \rangle$$

$$\delta(x' - x'') \delta(y' - y'')$$

$$= \int_A g(x_m - x', y_m - y') \int_A g(x_n - x'', y_n - y'') \underbrace{\langle (S^g(x', y') - \bar{s})(S^g(x'', y'') - \bar{s}) \rangle}_{\delta(x', x'') \delta(y', y'')} dx' dy' dx''$$

$$Q_{mn} \propto g_{2A}(x_m - x_n, y_m - y_n)$$

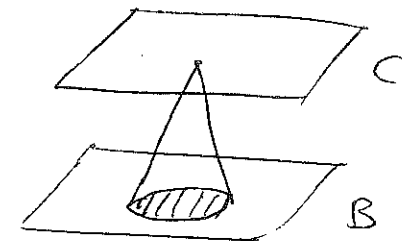
hinter: same transformation for several layers A, B, C, ... G,
with some what different parameter values.

$$B \rightarrow C \quad Q^B(r, r') = g_\sigma(r - r') \quad \Sigma = (x, y) \quad \sigma = 2A$$

$$\frac{dw(r)}{dt} = \int (Q^B(r, r') + k_2) g_B(r') w(r') dr' + k_1$$

$$k_1 > 0 \quad k_2 < 0$$

$$A/B = 1/3$$



Cells spatially close in layer B \rightarrow fire together.

In the central region $Q^B(r, r') > |k_2| \quad \frac{dw}{dt} \uparrow$

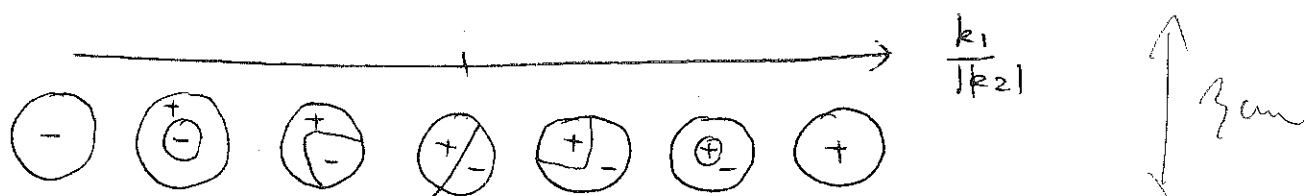
In the periphery $Q^B(r, r') < |k_2| \quad \frac{dw}{dt} \downarrow$
sufficiently to overcome k_1

$\rightarrow w(r)$ distribution yields On-center receptive field of layer C cells

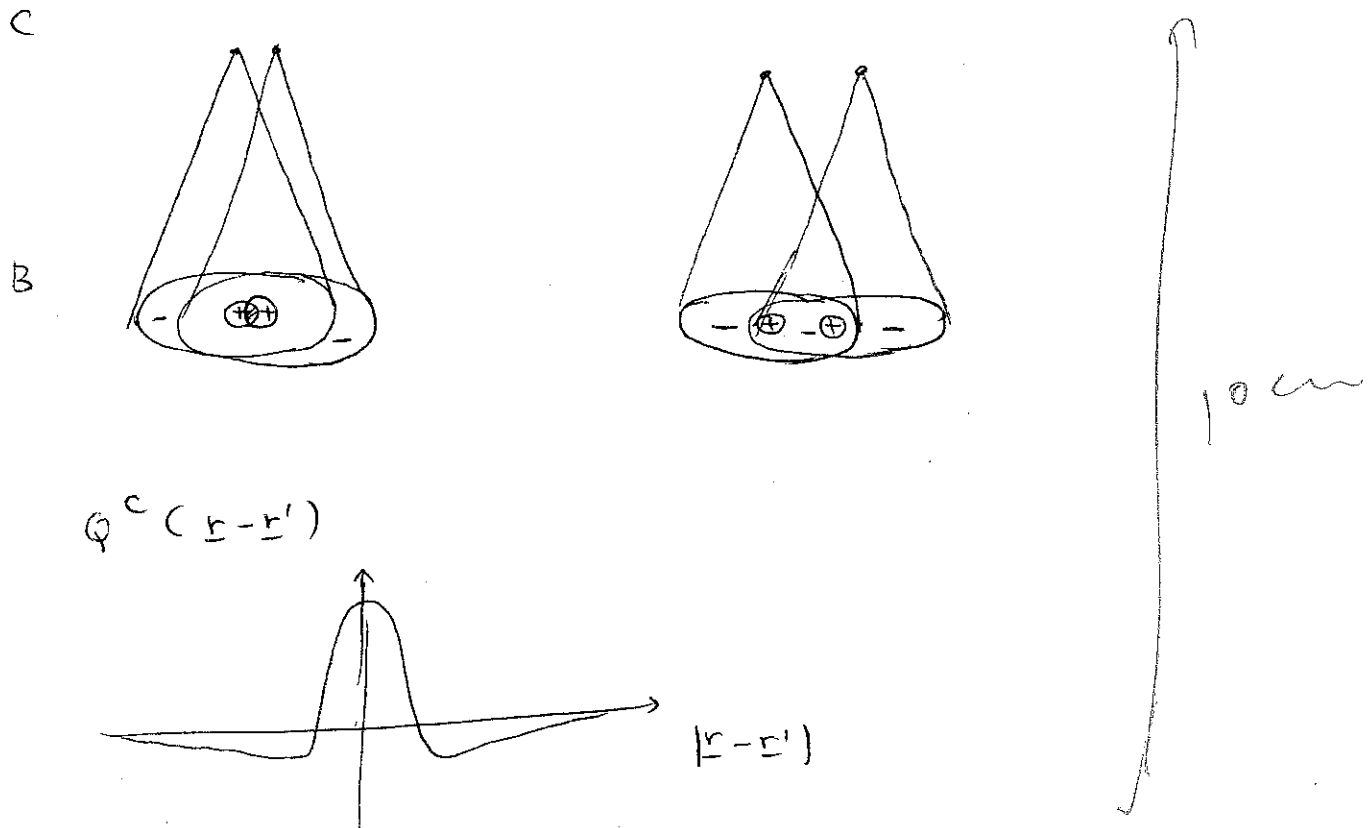
if k_1 negative enough \rightarrow Off-center

"

(fig. 4)



→ covariance in layer C is of the Mexican hat form



$C \rightarrow D \rightarrow E \rightarrow F$: sharper mexican hat correlations, deeper negative trough

$F \rightarrow G$: cells in G has wider receptive field \rightarrow orientation selective
(bilevel fig. 5)

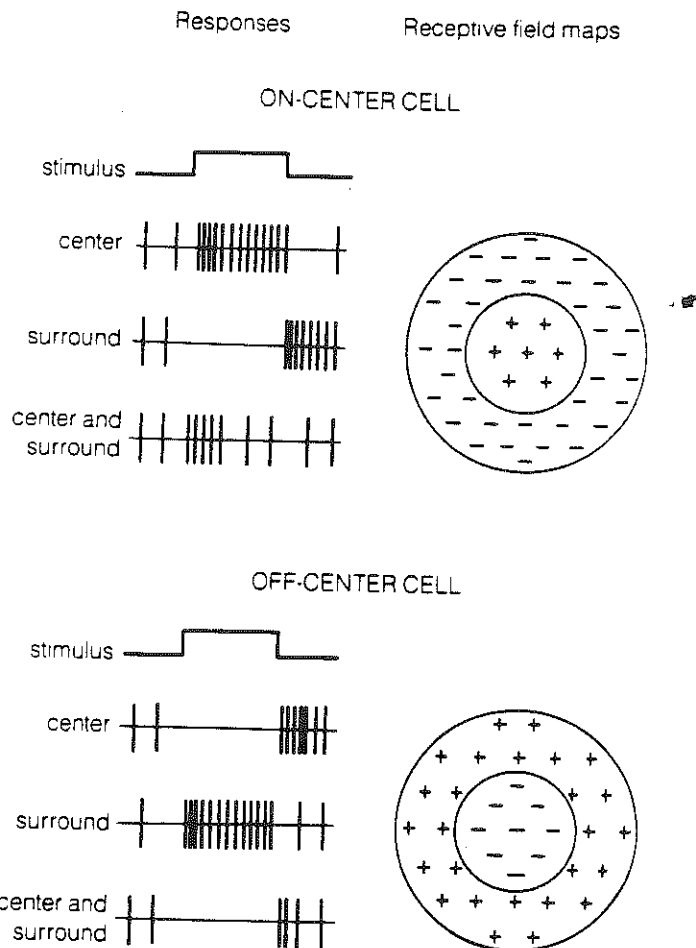
add local lateral connections \rightarrow smooth variation of orientational preference across the output layer (fig. 6)

Note : why $A \rightarrow G$? ad hoc.

$A \rightarrow B \rightarrow C \rightarrow D \rightarrow E \rightarrow F \rightarrow G$

input \rightarrow photoreceptor \rightarrow bipolar cells \rightarrow ganglion \rightarrow LGN \rightarrow stellate \rightarrow simple cells
(layer IV)

2.13 Idealized responses and receptive field maps for on-center (top) and off-center (bottom) contrast-sensitive ganglion cells. The drawings on the left represent hypothetical responses to a spot of light presented in the center of the receptive field, in the surround of the receptive field, or in both the center and surround regions of the receptive field. A + symbol on the receptive field map indicates an increase in the firing rate of the cell, that is, excitation; a - symbol indicates a decrease in the firing rate, that is, inhibition.



2.14 Idealized responses and a receptive field map for a direction-sensitive ganglion cell. Such cells respond with a burst of impulses at both the onset and termination of a spot of light presented anywhere in the cell's receptive field. This response is indicated by = symbols all over the map. Movement of a spot of light through the receptive field in the preferred direction (open circles) elicits firing from the cell that lasts for as long as the spot is within the field. Movement of a spot of light in the opposite (null) direction (open squares) causes inhibition of the cell's maintained activity for as long as the spot is within the receptive field.

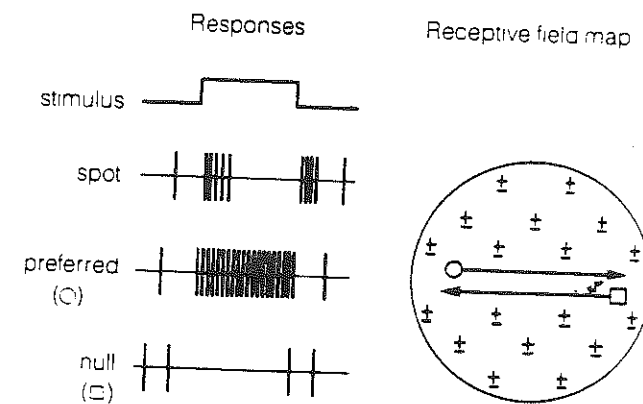


fig. 17.1

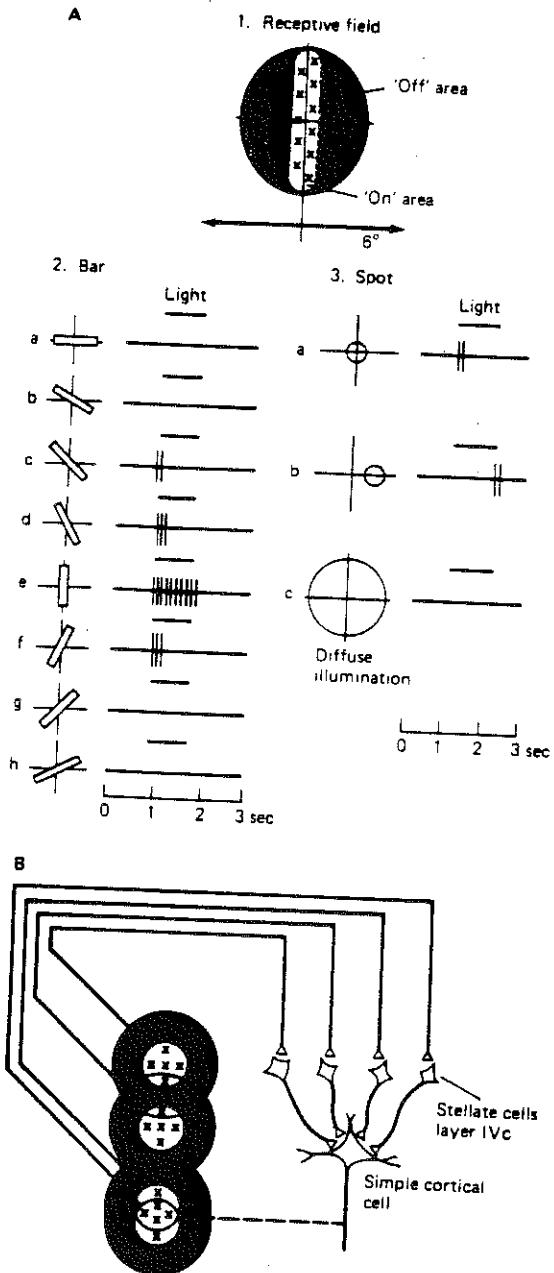


Figure 4.9 Diagram illustrating the receptive field properties of a simple cell in the primary visual cortex. (A) 1. The receptive field has a narrow central excitatory area flanked by symmetrical inhibitory areas. 2. The best stimulus for this cell is a vertically oriented light bar ($1^\circ \times 8^\circ$) in the center of its receptive field. Other orientations are less effective in driving the cell. 3. In contrast to a vertical bar, a small spot of light in the excitatory center of the field (a) gives only a weak excitatory response. A small spot in the inhibitory area (b) gives a weak inhibitory response. Diffuse light (c) is ineffective. (B) Hubel and Wiesel's (1962) hypothesis to explain how center-surround cells could be connected to a simple cell so that the latter responds selectively to bars of light in a particular orientation. (From Kandel 1985; adapted from Hubel and Wiesel 1962.)

17.5

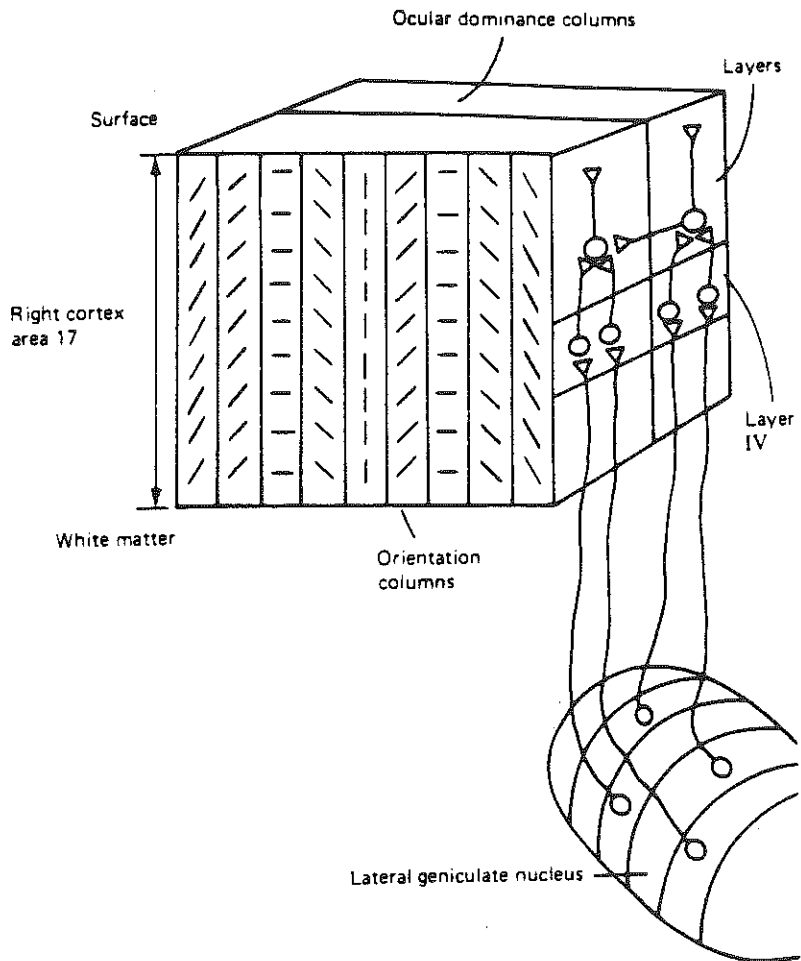


Figure 4.13 Schematic diagram showing cortical columns containing cells with a response preference for stimuli in a particular orientation. (Based on Hubel and Wiesel 1962; reprinted from Kandel and Schwartz 1985.)

fig. 17.3

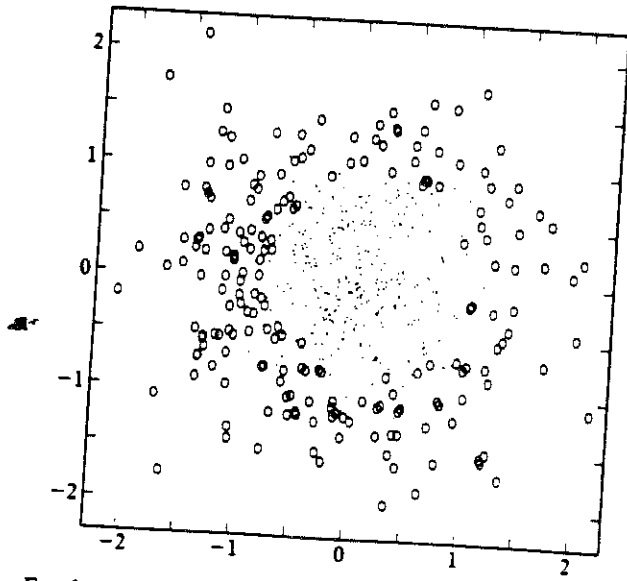


FIG. 2. Synaptic positions and mature connection strengths for a single cell of layer C having 600 synapses. Parameter values are $k_1 = 0.45$, $k_2 = -3$, $r_C/r_B = 3^{1/2}$, and each c value is allowed to range between -0.5 and $+0.5$. Random initial c values are chosen from uniform distribution on the interval -0.5 to $+0.5$. Values of Q_{ns}^B are appropriate to random placement of A-to-B and B-to-C synapses; layer uniformity is not assumed (see text). At maturity, every c reaches an extreme value: 0.5 (indicated by an oval) or -0.5 (dot). Axes are labeled by distance from cell center (in units of r_C).

R. Linsen PNAS 83, 7508 (1986)

fig. 17.4

(17.6)

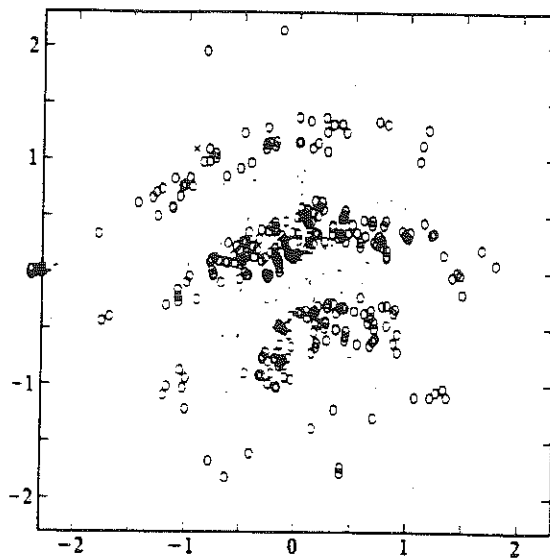


FIG. 1. Synaptic positions and connection strengths at maturity for a single cell of layer G having 600 synapses, placed randomly according to a two-dimensional Gaussian distribution. Parameter values are $n_{EG} = 0.5$, $r_G/r_F = 4$, $k_1 = 0$, $k_2 = -3$. Connection strengths are indicated as ovals, for $c = -0.5$, and dots, for $c = +0.5$; x represents intermediate c (one point only). Axis values are in units of r_G .

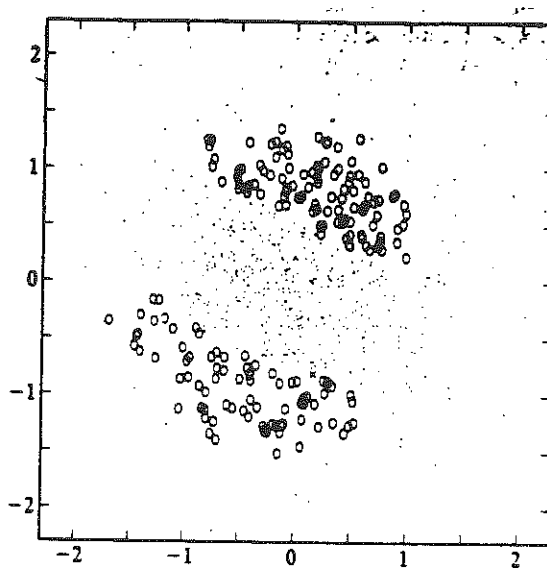


FIG. 2. A bilobed G cell. Parameter values are $n_{EG} = 0.5$, $r_G/r_F = 1.8$, $k_1 = 0.6$, $k_2 = -3$. Symbols are as in Fig. 1.

fig. 17.5

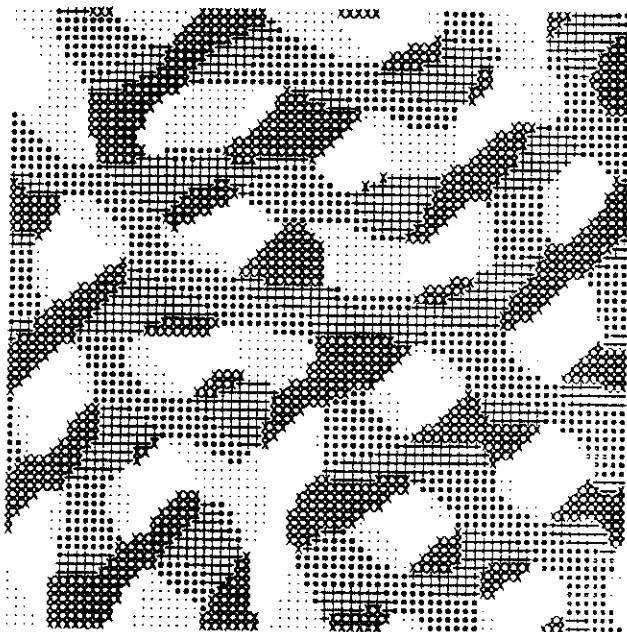


FIG. 2. A nearly Hebb-optimal solution for an array of orientation cells. Each cell is "stained" according to its orientation preference θ (measured counterclockwise from the vertical): $9-45^\circ$ (dot); $45-81^\circ$ (small circle); $81-117^\circ$ (+); $117-153^\circ$ (x); $153-189^\circ$ (blank). Adjacent grid positions are separated by distance $0.1493r_G$. The function $\rho(d)$ (see Eq. 8) is taken proportional to $\exp(-d^2/d_0^2)$ for $d_0 = 1.194r_G$ (= 8 grid positions). Array is 72 by 72 with periodic boundary conditions. [Qualitatively similar patterns result if $\rho(d)$ is constant out to, for example, 11 grid positions and zero beyond that, or if an 80-by-80 array is used.]

fig. 17. 6

Lecture 18: Associative memory - Hopfield's net. Willshaw's net.

Consider a net of McCulloch-Pitts neurons

$$x_i(t+1) = H \left(\sum_{j \neq i}^N J_{ij} x_j(t) - \theta_i \right)$$

$H(x) = 0$	$x < 0$
1	$x > 0$

- 3 aspects of memory:
 - learning
 - storage
 - retrieval

- Desirable properties
- distributed
 - content-addressable
 - high storage capacity

Hopfield (PNAS 79, 2554 (1982)), the net is recurrent, "learning"

& "storage" are prescribed. Question: what is the storage capacity of memorized patterns which can be retrieved reliably?

- feedback loops are essential \rightarrow attractors
- asynchronous updating
- $J_{ij} = J_{ji} \rightarrow E = -\frac{1}{2} \sum_{i \neq j} x_i J_{ij} x_j + \sum_i \theta_i x_i$

\therefore a Lyapunov function, if $J_{ii} \geq 0$.

Proof: for each time step $x_i(t) \rightarrow x_i(t+1)$

$$\Delta E = E(t+1) - E(t) = - \left[\sum_{j \neq i} J_{ij} x_j - \theta_i \right] \delta x_i \leq 0$$

Hebbian prescription: Suppose we want to store P patterns
(due to L. Cooper)

$$\{x_i^{(n)}\}_{n=1, \dots, P} \text{ . Let } J_{ij} = \frac{1}{N} \sum_{n=1}^P (2x_i^{(n)} - 1)(2x_j^{(n)} - 1)$$

$$\rightarrow J_{ij} = J_{ji} \quad \text{assume } J_{ii} = 0, \theta_i = 0.$$

Question: How many patterns can be stored as true attractors?

A particular pattern $\{x_j^{(n)}\}$ is a fixed point iff

$$x_i^{(n)} = 1 \rightarrow \sum_{j \neq i} J_{ij} x_j^{(n)} > 0$$

$$= 0 \rightarrow < 0$$

$$\begin{aligned} H_i^{(n)} &= \sum_{j \neq i} J_{ij} x_j^{(n)} = \frac{1}{N} \sum_n (2x_i^{(n)} - 1) \sum_{j \neq i} (2x_j^{(n)} - 1) x_j^{(n)} \\ &= \frac{1}{N} \sum_{j \neq i} (2x_i^{(n)} - 1) x_j^{(n)} (2x_j^{(n)} - 1) + \frac{1}{N} \sum_n \sum_{j \neq i} x_j^{(n)} (2x_i^{(n)} - 1) (2x_j^{(n)} - 1) \\ &= \frac{N-1}{2N} (2x_i^{(n)} - 1) \end{aligned}$$

sum of $\frac{(P-1)(N-1)}{2}$
random bits of ± 1 .

$$\underset{N \rightarrow \infty}{\rightarrow} \sim \frac{1}{2} [(2x_i^{(n)} - 1) + \text{noise}]$$

Standard deviation $\sigma = \left[\frac{(P-1)(N-1)}{N^2} \right]^{\frac{1}{2}}$

$$\boxed{\sigma^2 = P/N.}$$

$\rightarrow \{x_i^{(n)}\}$ is a fixed point if the noise is small enough.

If $x_i^{(n)} = 1$

$$\Pr\{H_i^{(n)} > 0\} = \frac{1}{\sqrt{2\pi}\sigma} \int_{-1}^{\infty} e^{-\frac{x^2}{2\sigma^2}} dx = \frac{1}{2} [1 + \operatorname{erf} \sqrt{\frac{1}{2\sigma^2}}]$$

where $\text{erf}(x) = \frac{2}{\sqrt{\pi}} \int_0^x e^{-y^2} dy$.

If $\sigma < 1$ $\frac{1}{\sigma} \gg 1$

$$\text{erf}(x) \underset{x \rightarrow \infty}{\sim} 1 - \frac{1}{\sqrt{\pi}} x e^{-x^2}$$

$$\Pr \{ H_i^{(n)} > 0 \} \approx \frac{1}{2} + \frac{1}{2} \left[1 - \frac{\sigma}{\sqrt{\pi/2}} e^{-\frac{1}{2\sigma^2}} \right] \simeq 1 - \sqrt{\frac{\alpha}{2\pi}} e^{-\frac{1}{2\alpha}}$$

$$\alpha = \frac{\beta}{N}$$

same
if $x_i^{(n)} = 0$ since $\int_{-\infty}^1 e^{-\frac{x^2}{2\sigma^2}} dx = \int_{-\infty}^0 e^{-\frac{x^2}{2\sigma^2}} dx$

\rightarrow

$$\Pr \{ \text{pattern is a fixed point} \} \simeq \left[1 - \sqrt{\frac{\alpha}{2\pi}} e^{-\frac{1}{2\alpha}} \right]^N$$

$$\text{Let } \alpha = (2\beta \ln N)^{-1} \rightarrow N \sqrt{\frac{\alpha}{2\pi}} e^{-\frac{1}{2\alpha}} = N \sqrt{\frac{1}{4\pi\beta \ln N}} e^{-\beta \ln N}$$

$$\left[1 - \sqrt{\frac{\alpha}{2\pi}} e^{-\frac{1}{2\alpha}} \right]^N = \left[1 - \frac{1}{N} \left[\frac{1}{\sqrt{4\pi\beta \ln N}} N^{1-\beta} \right] \right]^N$$

$$\underset{N \rightarrow \infty}{\approx} e^{-\frac{1}{\sqrt{4\pi\beta \ln N}} N^{1-\beta}} \underset{N \rightarrow \infty}{\rightarrow} 1 \quad \text{if } \beta \geq 1$$

therefore, at maximum $\beta = 1$ $\alpha_c = \frac{1}{2 \ln N}$

$$\beta_c = \frac{N}{2 \ln N}$$

If we require that the probability for every bit of all p patterns to be wrong goes to zero, we shall have

$$P_n \sim [1 - \sqrt{\frac{2}{2\pi}} e^{-\frac{1}{2\alpha}}]^{PN} \rightarrow \beta > 2$$

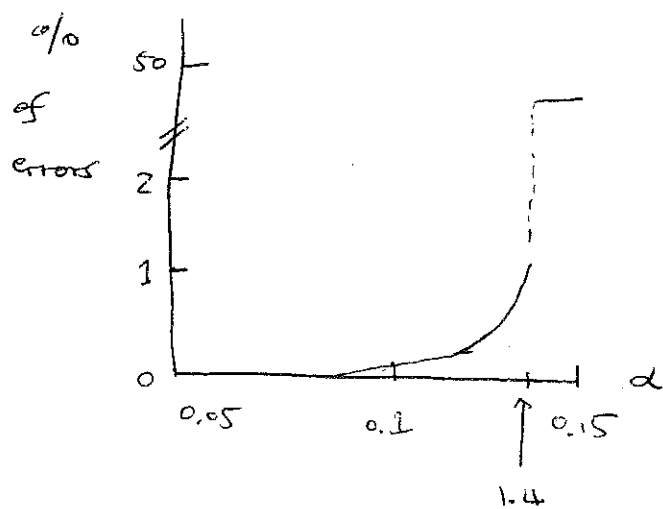
$$\rightarrow P_C = \frac{N}{4 \ln N}$$

If we allow that the net has stable state not necessarily exactly identical to the stored patterns, but within less than 1% of errors

$$\rightarrow P_C \approx 0.14 N$$

(very hard result from statistical mechanics of spin glasses)

Cf. D. Amit et al Phys Rev Lett 55, 1530 (1985)



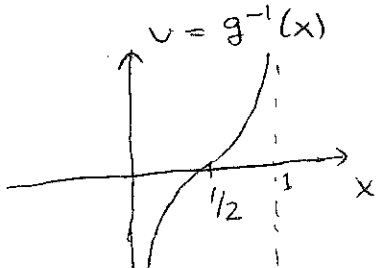
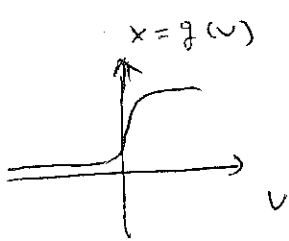
Note: there may be also "spurious states", i.e., attractors which are not stored patterns.

Digression: analog neurons.

$$C \frac{dV_i}{dt} = \sum_j J_{ij} g(V_j) - \frac{V_i}{R_i} + I_i$$

V_i = state (membrane potential)

$x_i = g(V_i)$ out put ("short term firing rate")



e.g. $g(v) = \frac{1}{1+e^{-\lambda v}}$

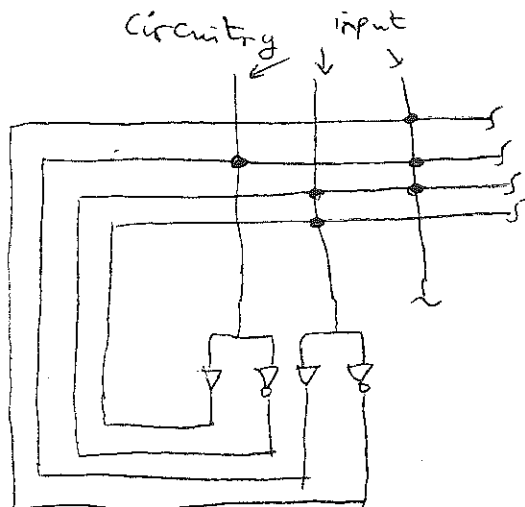
$$g^{-1}(x) = \frac{1}{\lambda} \ln\left(\frac{x}{1-x}\right)$$

intrinsic time constant = $R_i C$

▷ amplifier

▷ inverting amplifier

register $|J_{ij}| = \frac{1}{R_{ij}}$



$$E = -\frac{1}{2} \sum_{ij} J_{ij} x_i x_j + \sum_i \frac{1}{R_i} \int_0^{x_i} g^{-1}(x) dx - I_i x_i \quad J_{ij} = J_{ji}$$

is a Lyapunov function

note: $J_{ii} \geq 0$ not required

Proof: $\frac{dE}{dt} = - \sum_i C \left[g^{-1}(x_i) \right]' \left(\frac{dx_i}{dt} \right)^2 \leq 0$

$$\frac{dE}{dt} = 0 \Leftrightarrow \frac{dx_i}{dt} = 0 \quad \forall i \quad (\text{steady state})$$

In the high gain limit, $\lambda \rightarrow \infty$, the 2nd term in E is proportional to $\frac{1}{\lambda} \rightarrow 0$. Also $x_i \rightarrow 0$ or 1.

example: analog / digital converter

cf. D. Tank & J. Hopfield IEEE Trans on Circuits & Systems

33, 533 (1986)

4 bit converter $[0] = \sum_{k=0}^3 2^k x_k \quad 0 \leq x_k \leq 1$

$$-0.5 < \sigma < 15.5$$

minimize $E = \frac{1}{2} (\sigma - \sum_{k=0}^3 2^k x_k)^2 - \frac{1}{2} \underbrace{\sum_{k=0}^3 2^k x_k (x_i - 1)}_{\text{no guarantee for the minima to be at the corners}}$

minimal if $x_i = 0$ or 1

$$\Rightarrow E = -\frac{1}{2} \sum_{i \neq j} (-2^{i+j}) x_i x_j - \sum_{k=0}^3 (2^k \sigma - 2^{2k-1}) x_k + \cancel{\frac{1}{2}}$$

$$J_{ij} = -2^{(i+j)}, \quad I_i = 2^i \sigma - 2^{2i-1}.$$

Note: if $J_{ij} \neq J_{ji}$, then time-dependent states (e.g. oscillation / chaos) are possible. cf. H. Sompolinsky et al. Phys Rev Lett 61, 259 (1988) and lecture 15.

back to memory storage.

for a stored pattern $\{x_i^M\}$ $x_i = 0, 1$

$$\text{Let } f = \frac{\sum_{i=1}^N x_i^M}{N} = \text{fraction of active units}$$

Let $P = \#$ of stable stored patterns (with zero error)

h = information content per pattern

H = information capacity of the network $= hP$

example: Hopfield net $f = \frac{1}{2}$

$$P = \frac{N}{2 \ln N}$$

$$h = N$$

$$H = \frac{N^2}{2 \ln N}$$

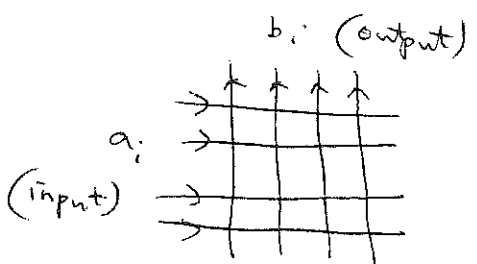
By comparison, let us consider another net (due to Willshaw) which has much higher storage capacity (large P) and sparser activity (low f).

This is a linear associative memory device.

$$b_i = \sum_j J_{ij} a_j$$

Learning: introduce

$$\{a_i^M\} \quad \{b_i^M\} \quad J_{ij} = 1 \quad \text{if } a_i^M = b_i^M = 1 \quad \text{for any } \mu = 1, 2, \dots, P.$$



$$\text{Let } M = \sum_{i=1}^N a_i = \sum_{i=1}^N b_i, \quad f = \frac{M}{N} \ll 1$$

q = fraction of active synapses

$$\rightarrow 1-q = (1-f^2)^P = e^{P \ln(1-f^2)} \approx e^{-P f^2} \rightarrow P = -\frac{N^2}{M^2} \ln(1-q)$$

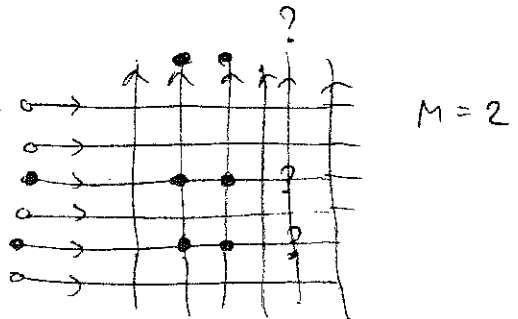
retrieval: set the threshold = $M = Nf$. Consider a learned pattern $\{a_i\}_M$ \rightarrow correct $b_i = 1$ (there are M of them). Consider $(N-M)$ other output lines. Each may receive M inputs with probability q^M , hence reaches the threshold.

$$\rightarrow \# \text{ of incorrect output bits} = (N-M) q^M$$

if $M \leq N$ let us require $Nq^M \leq 1$

$$\rightarrow M \geq \frac{-\ln N}{\ln q}$$

$$M_C = \frac{-\ln N}{\ln q}$$



correlated patterns: $\binom{N}{M}$ possible patterns

$$\rightarrow h = \log_2 \binom{N}{M} \approx M \log_2 N$$

$$H = Ph \approx + \frac{N^2}{M^2} \ln(1-q) \ln q \quad \text{maximal if } q = \frac{1}{2}$$

$$\rightarrow H_{\max} = (\ln 2) N^2$$

$$f = \frac{\log_2 N}{N}$$

$$P \approx \left(\frac{N}{\log_2 N}\right)^2 \ln 2$$

$$h = (\log_2 N)^2$$

Lecture 19: The problem of the cortical code

Cortical code = firing patterns used to represent objects or features of the environment. (or synaptic w_{ij} patterns for memory.)

Observations: along a sensory pathway e.g. visual pathway (fig. 1), the number of cells is drastically increased (fig. 2); the firing rate is significantly decreased (data available at least for spontaneous activity fig. 3; and for Abeles' experiment, fig. 4).

Cells are found to be "feature detectors" e.g. orientation, motion direction, color, disparity etc. It can be argued that cells in higher levels along the pathway would respond to more complex objects (i.e. code) or features. It was found, for instance certain cell groups in the inferotemporal cortex respond predominantly to faces. Those cells are likely less often excited than those cells responding to simple / nonspecific features such as edges, hence fire at a lower average rate. Furthermore, it may be argued that in early stages a great many cells are used to code incoming data, while in later stages less and less cells are involved (they "integrate" information and show more specificity). Note that from a naive point of view of "information preservation", it also makes sense since there are much more cells at higher levels.

On the other hand, there is strong evidence for a population code or distributed code. For instance, the face cells respond to a range of face-like stimuli, and a great number of them are active for one particular cell. As far as memory is concerned, lesion experiments of Lashley indicated its nonlocality, and the associative property, gradual degradation reliability also indicate its distributed nature.

Therefore, the code is probably a population but sparse code, sparse both in terms of firing rate in individual cells and in terms of the fraction of the population involved. In other words, the spatial-temporal firing patterns of neurons are sparse and intermittent.

How sparse? firing rate can be as low as 0.002, unknown for the population fraction but may be of the same order of magnitude. (e.g. burst rate of Abeles)

Another relevant example relate to space cells in the hippocampus. These cells fire at particular location in space of environment. Again, the firing pattern involves a distributed but small subpopulation of cells, and their firing rate is very low (fig. 5).

Are cells involved in a perception task dynamically correlated?
 Recurrence of some stereotyped firing patterns is occasionally observed (fig. 6)
 There are two interesting lines of thought on this important issue.

H. Barlow observed that sensory inputs are redundant. He argued that neurons should try to reduce this redundancy so that unexpected features become detectable easily. A simplest ^(possibility) would be that neurons are statistically independent in their responses across all input patterns. Then, the probability of a firing pattern (coding a conjunction of features) is the product of the probabilities of ^(the) individual units. Thus redundancy would be eliminated. There is a single information-theoretic argument for this.

Suppose that a set of states is given, A_j their probabilities ($\sum A_j = 1$). Suppose that each state is to be coded by (mapped to) a binary string of length N , j th state $\leftrightarrow \{b_{ij}\}_{i=1}^N$, $b_{ij} = 0$ or 1 ($\sim N$ binary neurons).

$$\text{Let } E(A) = - \sum_j A_j \log A_j$$

p_i = Prob. of the i th bit taking the value 1, summed over N .

$$= \sum_j A_j \quad q_i = 1 - p_i \\ b_{ij} = 1$$

$$E(A, b) = - \sum_i p_i \log p_i - \sum_i q_i \log q_i$$

b is called a functional code if $A_j = \prod_{b_{ij}=1} p_i \prod_{b_{ij}=0} q_i$

Theorem (Watanabe): $e(A, b) \geq E(A)$. $e(A, b) = E(b)$ iff b is factorial.

Proof:

$$\begin{aligned} e(A, b) - E(A) &= -\sum_i p_i \log p_i - \sum_i q_i \log q_i + \sum_j A_j \log A_j \\ &= -\sum_{\substack{i \\ b_{ij}=1}} \left(\sum_j A_j \right) \log p_i - \sum_{\substack{i \\ b_{ij}=0}} \left(\sum_j A_j \right) \log q_i + \sum_j A_j \log A_j \\ &= -\sum_j A_j \log \left(\frac{\pi_j}{A_j} \right) \geq -\sum_j A_j \left(\frac{\pi_j}{A_j} - 1 \right) = \sum_j A_j - \sum_j \pi_j \\ &\quad \text{for } x > 0 \\ &= 1 - 1 = 0 \end{aligned}$$

$\prod_i (p_i + q_i)$

Equality only if $x=1$

Conclusion: if \exists factorial code, $e(A, b)$ is to be minimized.

Note: factorial code has dimension N

sets of A_i with $\sum A_i = 1$ has dimension $2^N - 1$.

Proposition (Mitchison): if $A_j = k \alpha^j$ $\alpha < 1$ $j = 1, 2, \dots, 2^N$, then

A has a factorial code. Example: keyboard characters

On the other hand, cells that are excited simultaneously and involved in a same task are likely correlated. In fact, it is suggested that transient correlations between active cells may subserve as a mechanism of binding different features of an object into a whole entity. This idea obtained some support from the Gray-Singer experiment on 40 Hz synchronous oscillations in cat visual cortex (figs. 7-8).

If one argues that "synchrony" may be realized by rare and random events of coincidence, then the nerve system should be viewed as operating in terms of sparse spatiotemporal activity patterns are rare coincidence phenomena.

4.17 Summary diagram correlating the synaptic organization of the vertebrate retina with some of the intracellularly recorded responses from the mudpuppy retina. This figure attempts to show how the receptive field organization of the hyperpolarizing bipolar cells, off-center ganglion cells, and on-off ganglion cells is established. The responses occurring in the various neurons upon illumination (bar) of the retinal receptor are indicated.

The hyperpolarizing bipolar cells and off-center ganglion cells (G_1) respond to direct central illumination (left side) by hyperpolarizing, to indirect (surround) illumination (right side) by depolarizing. Note that the switch from hyperpolarizing to depolarizing potentials along the surround illumination pathway occurs at the horizontal-bipolar junction.

The on-off ganglion cell (G_3) receives strong inhibitory input from amacrine cells; the figure suggests that these cells receive their excitatory input from both amacrine and bipolar cells. Inhibitory feedback synapses from amacrine cells onto the bipolar terminals are also indicated.

R receptors, H, horizontal cell; B, bipolar cells; A, amacrine cells; G, ganglion cells. + with open circles represents excitatory synapses; - with filled circles represents inhibitory synapses. Modified from Dowling (1970) with permission of J. B. Lippincott Company.

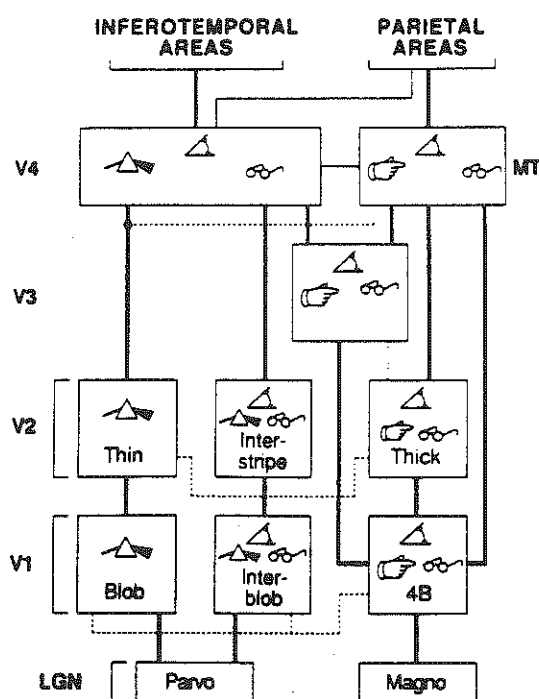
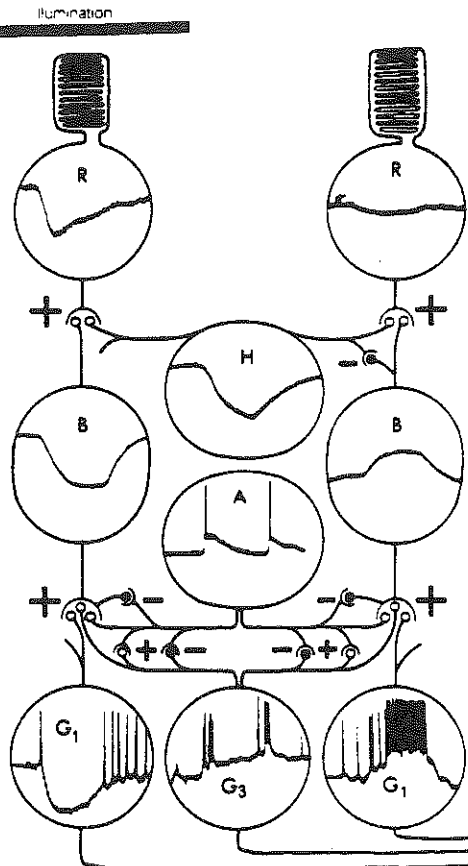


Fig. 19.1

Figure 4.11 The major anatomical connections and neuronal response selectivities in early visual areas of the macaque monkey. Icons symbolize response preference of many cells in that area: prism = wavelength; angle = orientation; pointing finger = direction; spectacles = binocular disparity. (Reprinted from DeYoe and van Essen [1987]. Concurrent processing streams in monkey visual cortex. *Trends in Neurosciences* 11: 219–226.)

Table I

LEVEL :-	EARLY	MIDDLE	HIGH
No. of cells	10^6	$10^{7.5}$	10^9
Av.No. active	5×10^5	10^5	6.8×10^4
Av. proportion active	0.5	0.003	0.00007
Av. bits per active cell	1	8.2	14
Av. bits per inactive cell	1	4.8×10^{-3}	1×10^{-4}
Total bits for active cells	5×10^5	8.8×10^5	9.2×10^5
Total bits for inactive cells	5×10^5	1.4×10^5	8×10^4
Total for all cells	10^6	10^6	10^6

Note: This shows the informational balance sheet for a transformation such as that of Figure 6. To demonstrate the principle, it is assumed that no information is lost, and the third line shows the result of calculating what proportion of the cells need to be active, on average, in order to carry this unchanged amount of information. The consequence of the reduced a priori probability of being active is that the information conveyed *when it is active* is greatly increased, as shown in the fourth line, even though the average information conveyed by a high-level cell obviously decreases as the numbers increase.

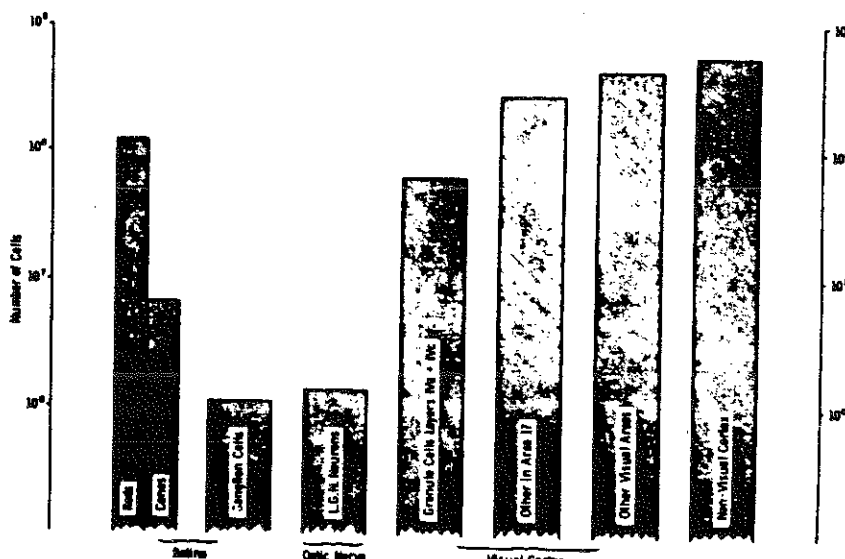


Figure 5. Histogram showing that, after the level of retinal ganglion cells, the number of neurons available to carry the representation of a visual image increases at least 100 times (data collated from various sources by Barlow, 1981).

Fig. 19.2

Tabelle

Mittlere Entladungshäufigkeit von Neuronen des ascendierenden optischen Systems bei Dunkelheit.
Entladungen pro Sekunde, 3–20 min dauernde Ableitungen. Mittelwert und mittlerer Fehler
des Mittelwertes

Ableiteort	Zahl der Neurone	Reaktionstyp				Gesamt
		on	off	on-off	A-Neurone ¹	
Cortex	145	5,7 ± 1,34	2,8 ± 0,4	8,7 ± 1,99	4,5 ± 0,68	5,7
Corpus geniculatum laterale	24	13,2 ± 3,7	9,8 ± 4,4	17,4 ± 5,8		14,0
Tractus opticus	13	39,2 ± 4,0	24,0 ± 6,0	34,2 ± 4,2		35,5

¹ Neurone, die auf Licht keine Reaktion zeigen (s. JUNG u. Mitarb. 1952 [25]).

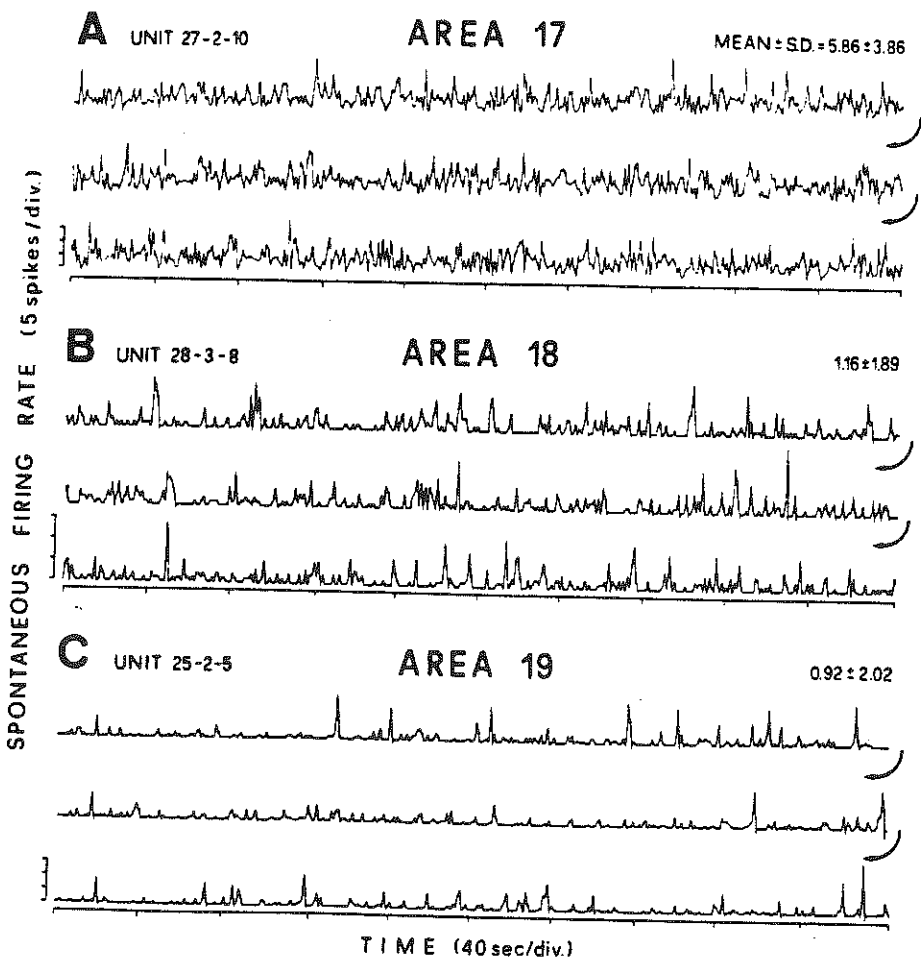


Fig. 2. Maintained single unit activity recorded from the visual areas 17 (A), 18 (B) and 19 (C) over an uninterrupted period of 20 min. Tracings in A, B and C are, respectively, continuous recordings as indicated by arrows. The firing rate was measured on 1-sec counts. The mean values of the firing rate with the standard deviation (S.D.) for each unit are reported on the right. Note how the grouped activity recognizable in this kind of record by more or less isolated peaks is particularly evident in A-18 (B) and A-19 (C). This type of unit firing, when observed on photographed records, is characterized by groups of 2–10 spikes in A-18 and 1–3 spikes in A-19 with short interspike intervals, and each group is separated from the successive one by intervals of variable duration.

fig. 19.3

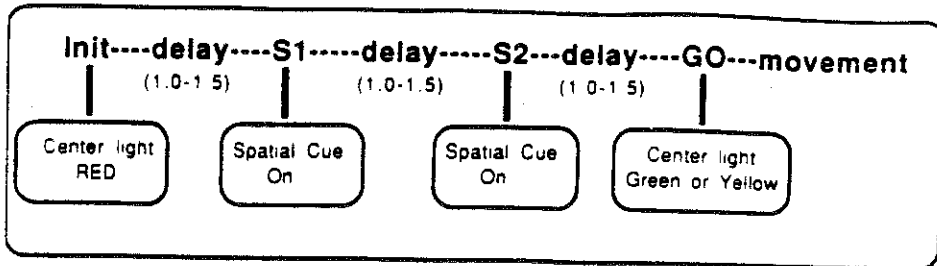


Fig. 11.4. The sequence of events from trial initiation to the behavioral response in the localizing task

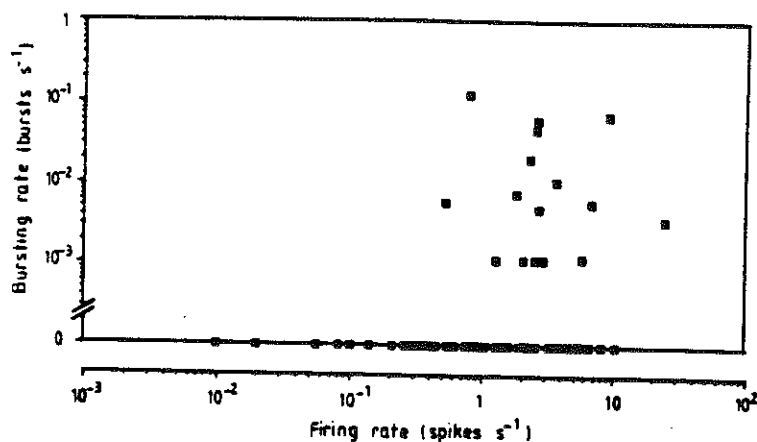


Figure 1. Relations between bursting rates and firing rates for 70 units. Each point represents data for one neuron. The abscissa describes the averaged firing rate of the neuron. The ordinate describes the averaged rate of high-frequency bursts of the neuron. Most neurons did not burst at all. They are represented by the points on the zero bursts s^{-1} line.

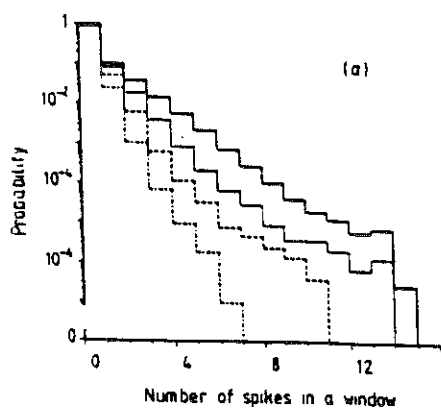
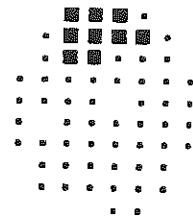


fig.17.4

19.5



A

B

Figure 4. A. The place field of a CA1 pyramidal unit, mapped on a radial-arm maze. Place fields (defined by unit firing more than 3 SD above the grand mean firing rate) are indicated by solid squares, and background activity in all other areas visited by small dots. B. The place field of the same unit, mapped in an enclosed drum. Note that the locations of the 2 fields in the 2 environments are unrelated. Most units tested in different environments had no place field in at least one of them.

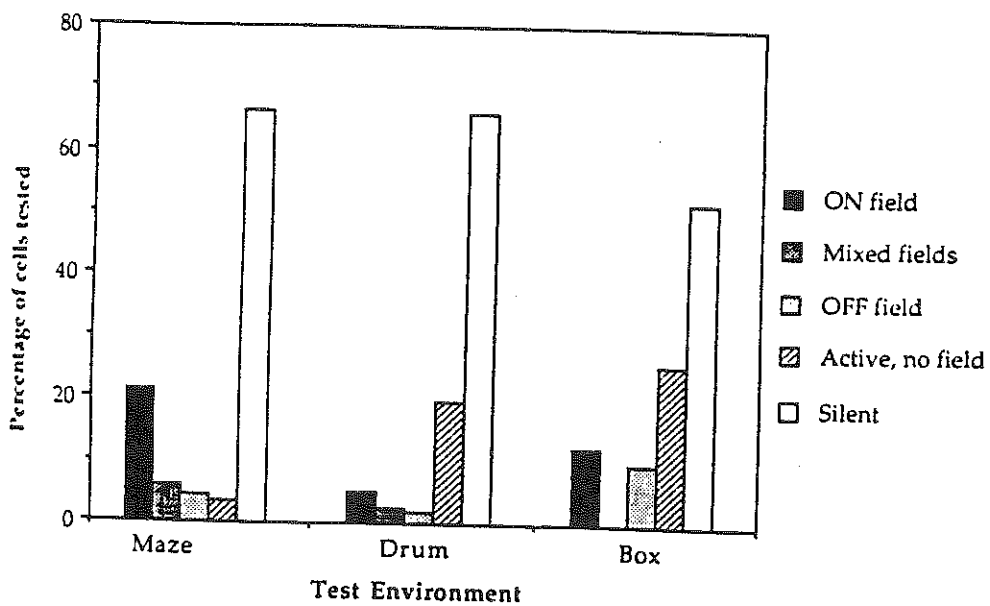


Figure 5. Proportions and types of place fields and proportions of non-place field activity observed during testing in 3 different spatial environments. Silent cells never exhibited place field activity in any of the environments tested. Identified place cells frequently had no place field activity in some environments. More units had place fields when tested on the radial-arm maze than in either of the simpler environments.

Figure 6. The mean firing rates (in Hz, plotted on a log scale) of hippocampal place cells when rats were exploring non-place field environments (i.e., ones not containing place fields, open circles) and environments containing place fields. Both the spontaneous firing rates (i.e., the rate across the entire environment, including the place field, filled triangles) and the background firing rates (i.e., the rate, excluding place fields, squares) were higher in environments containing place fields than was the spontaneous firing rate of the same cells in environments in which they had no place fields. A rightward shift in the mean firing frequency occurs in environments in which place field activity is found.

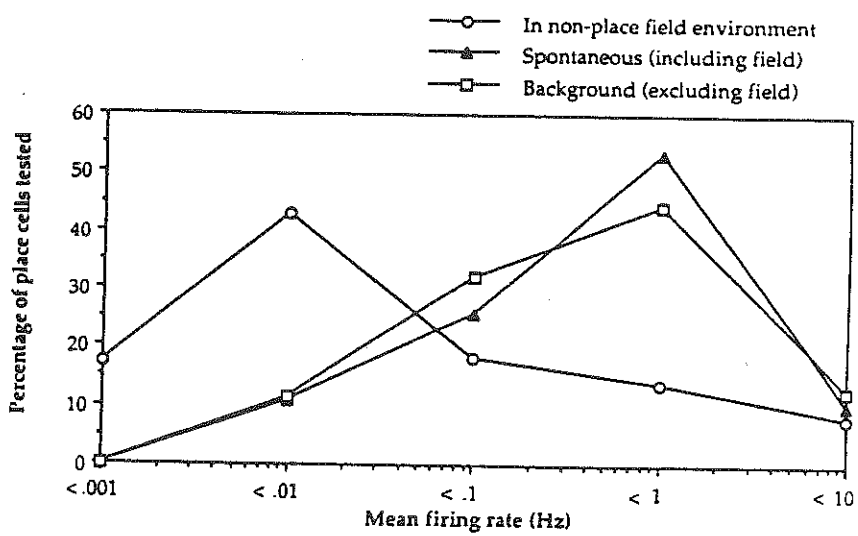


fig. 19.5

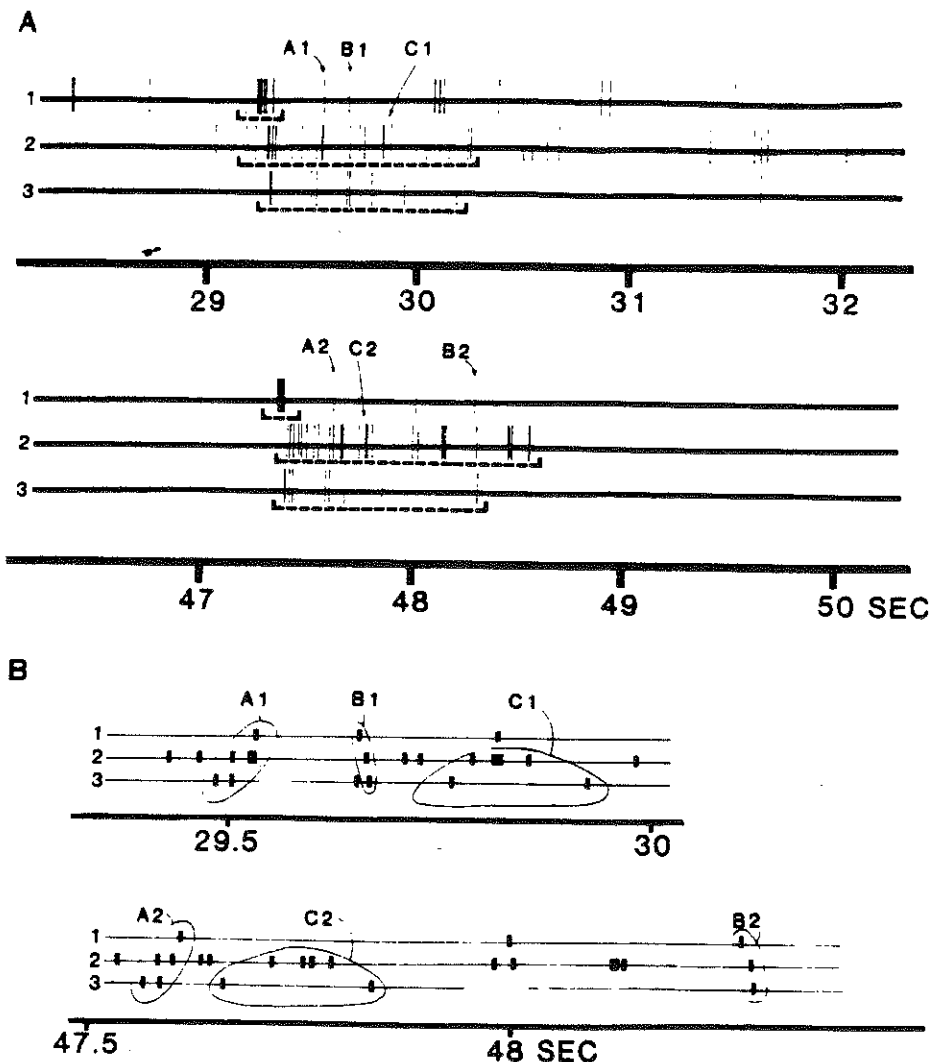


FIG. 8. Example of recurrence of a three-neuron pattern of bursts. **A:** recurrence of bursts in coarse outline. Display shows two segments of a three-neuron spike train, each about 4 s long; bottom segment was recorded about 18 s later than top segment (see time scales). Spike trains of three neurons are numbered at left. Average spike rates are 4.0 spikes/s (neuron 1), 3.9 spikes/s (neuron 2), and 0.9 spikes/s (neuron 3). Bursts of interest are bracketed. Neuron 2 emits a large burst in each segment ($S = 26.0$, $S = 24.4$), both bursts have same number of spikes (27 spikes, including first and last). Neuron 3 emits smaller bursts ($S = 13.2$, $S = 12.2$) accompanying these, having nearly equal spike counts (10 spikes and 9 spikes), and neuron 1 emits even smaller bursts ($S = 11$, $S = 9.2$) with not widely differing spike counts (9 spikes and 6 spikes), similar in their briskness and their time relation to other bursts. Last spike on neuron 3, bottom, is excluded from burst by burst-detecting program, as it slightly decreases the Poisson surprise, and is included here as a correction. **B:** similarity in fine structures of two burst triplets. Display shows part of same segments as shown in **A**, but with the time scale expanded 4 times (see time scales), and spikes drawn in heavier lines for clarity of display. Six sets of spikes, marked $A1$, $B1$, $C1$, $A2$, $B2$, $C2$ in both figure portions, are circled. $A1$ is seen to be roughly similar to $A2$, also $B1$ to $B2$, and $C1$ to $C2$. Neurons 2 and 3 were recorded by one electrode; neuron 1 was recorded by another electrode 2 mm away.

fig 196

19.6

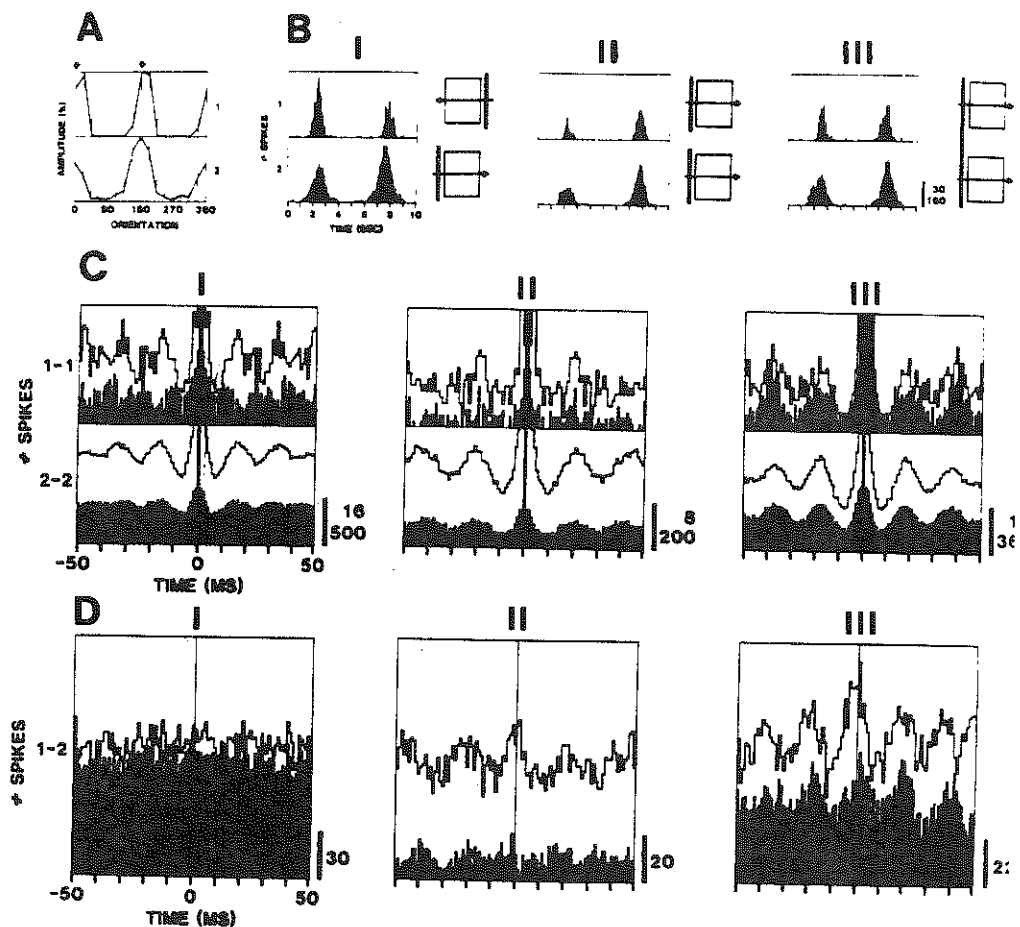


Fig. 8.5. Long-range oscillatory correlations reflect global stimulus properties. A Orientation tuning curves of neuronal responses recorded from two electrodes (1, 2) separated by 7 mm show a preference for vertical light bars (0 and 180°) at both recording sites. B Post-stimulus time histograms of the neuronal responses recorded at each site for each of three different stimulus conditions: (I) two light bars moved in opposite directions, (II) two light bars moved in the same direction and (III) one long light bar moved across both receptive fields. A schematic diagram of the receptive field locations and the stimulus configuration used is displayed to the right of each post-stimulus time histogram. C, D Auto-correlograms (C, 1-1, 2-2) and cross correlograms (D, 1-2) computed for the neuronal responses at both sites (1 and 2 in A and B) for each of the three stimulus conditions (I, II, III) displayed in B. For each pair of correlograms except the two displayed in C (I, 1-1) and D (I), the second direction of stimulus movement is shown with unfilled bars. Numbers on the vertical calibration correspond to the number of coincident events (spikes) in the respective auto- and cross-correlograms. From (Gray et al. 1989)

fig. 19.7

40Hz : SYNCHRONIZATION

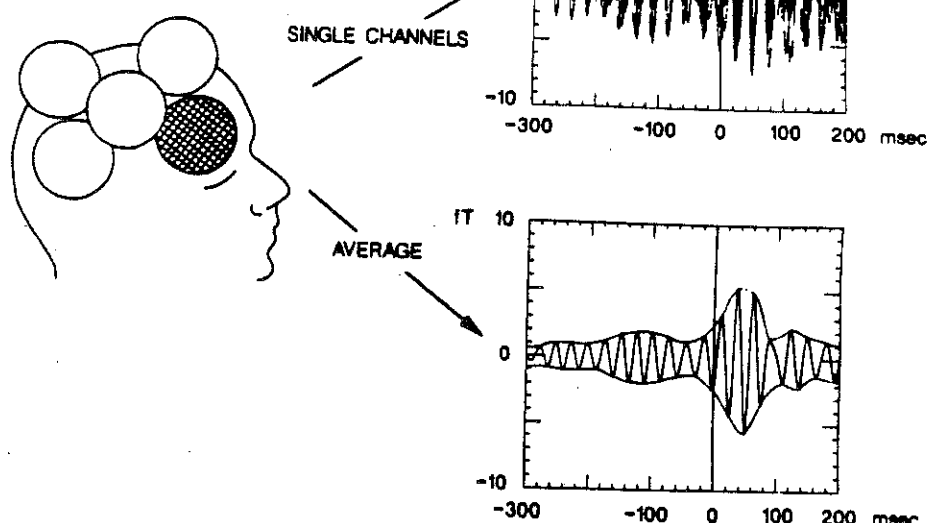


Fig. 4. Synchronization of human magnetic 40-Hz oscillatory activity during auditory processing within seven single channels of one probe placed over lower frontal areas. The graph on the top right indicates a superimposition of 40-Hz activities, time locked to the stimulus onset, recorded from the seven channels. The graph on the lower right indicates an average of the seven individual channels, demonstrating synchronization over a large area (around 25 cm²). Reproduced from Llinás and Ribary.⁵⁷

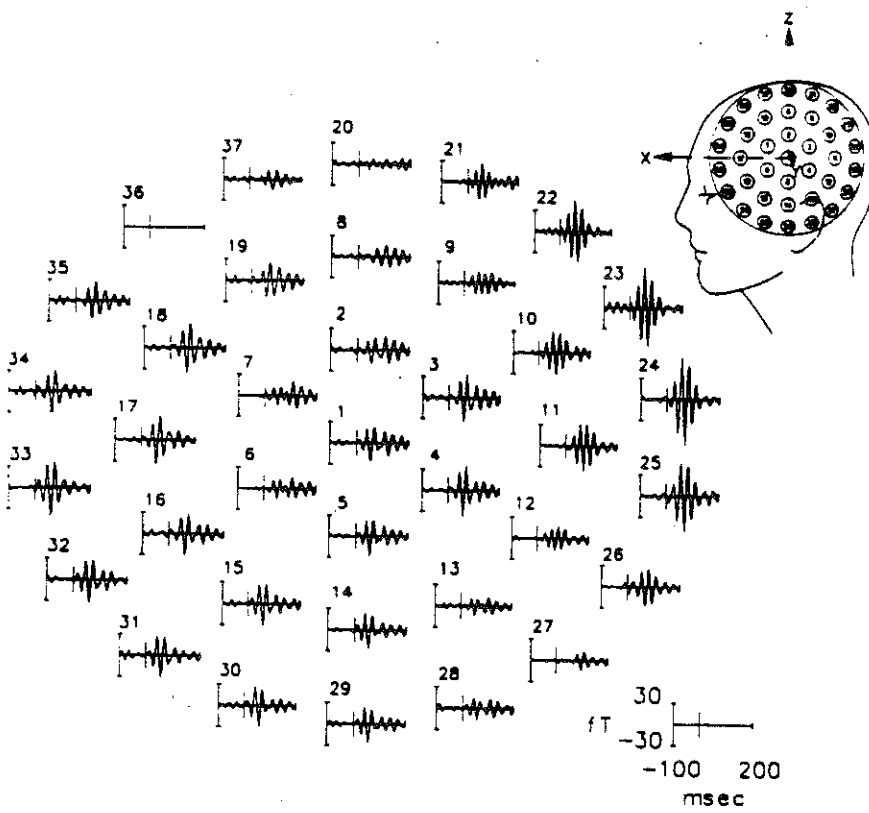


FIG. 3. Grand average of three data blocks ($n = 384$) from the same subject and under the same experimental conditions as described in Fig. 1, after digital band-pass filtering between 28 and 48 Hz with a 2-pole Butterworth filter with zero phase shift.